

Understanding the Thermo-Mechanical Behaviour of Thermal Piles in Sand

by

Amin Rafiei

A thesis submitted in partial fulfilment for the
degree of Doctor of Philosophy

Department of Civil, Environmental and Geomatic Engineering
University College London (UCL)

Supervisors: Dr Chanakya Arya & Dr Raul Fuentes

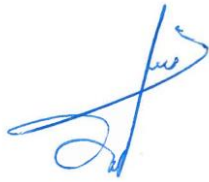
September 2016

Declaration of authorship

I, Amin Rafiei, confirm that the work presented in this thesis is the result of my investigations. Where information has been derived from other sources, I confirm that this has been indicated in the thesis.

Amin Rafiei

30.09.2016

A handwritten signature in blue ink, consisting of a stylized 'A' followed by 'rafiei'.

Acknowledgements

Firstly, I would like to thank Dr Chanakya Arya and Dr Raul Fuentes for their encouragement and valuable advice during the project and providing me with the opportunity to conduct this research.

Secondly, I would like to thank my family for their unconditional love, support and patience during my studies. Completion of my PhD would not have been possible without them.

I would like to thank my girlfriend, Niloofar, who has been patient with me during the entire process and encouraged me to carry on my PhD during some difficult times.

I would like to thank all the civil engineering laboratory staff, in particular, Mr Ben Boorman for being patient and helpful throughout my laboratory works.

I would also like to thank Professor Stephen James from Cranfield University and Dr Ricardo Correia from the University of Nottingham for providing me with the equipment and advice during the project.

Finally, I would also like to thank all my friends and colleagues who supported me in any way in the completion of the project.

Abstract

Thermal piles are piled foundations that can be used both to extract heat at shallow depth from the ground and to transfer load from the structure to the ground. Despite an increased number of applications of thermal piles in recent years, knowledge of the thermo-mechanical behaviour of thermal piles is still limited. The literature reveals that additional thermal loading results in considerable induced axial load and stress along the pile, that can lead to a reduction in safety factor down to 1. Also, there are inconsistencies in the literature regarding the thermo-elastic/plastic, reversible/irreversible response of thermal piles and also on the effects of cyclic thermal loading on the side shear friction at the soil–pile interface. Moreover, the framework proposed in the Thermal Pile Standard (Ground Source Heat Pump Association, 2012) has not been tested for various soils conditions. In this study, the effect of thermo-mechanical loading on the mechanical performance of thermal piles and the soil–pile interface is investigated. A 1g laboratory model was developed using a stainless steel model pile embedded in medium-dense, dry sand. Strain and temperature along the pile were monitored using multiplexed fibre Bragg grating sensors. A 2D finite difference heat transfer model was developed in Matlab, predicting the temperature profiles within the soil. Findings from the numerical model were used to design the location of the temperature sensors in the soil. Laboratory tests were divided into five scenarios, involving both shaft resisting and shaft and base resisting piles. It was found that under thermo-mechanical loading, up to 68.4% of the maximum induced load was transferred to the pile toe for the shaft resisting pile, compared to virtually none under mechanical loading. It was further found that the level of restraint caused by medium-dense sand with a relative density of 57% was rather limited in the absence of surcharge load and the degree of freedom varied between 0.97 and 1.0. Moreover, it was found that the location of the null point shifts during each heating/cooling period. For a shaft and base resisting pile heated up to 50°C, the maximum induced thermal load was found to be 90% of the ultimate capacity of the pile. The maximum induced stress remained below the BS 8004:1986 (British Standards Institution, 1986) recommendations. Irreversible settlements were observed for both types of pile. The load threshold, where the limit to thermo-elastic behaviour was observed, was found to be up to 18% of the ultimate pile capacity, while this value was up to 31% in the case of shaft and base resisting pile. Despite an increase in the side friction during heating periods (up to 32% compared to the friction under ultimate state mechanical loading), the subsequent cooling periods seemed to reduce the friction level, and cyclic skin friction degradation and accumulation of pile settlement were observed in the heating and cooling cycles. The results also show deviations from the proposed framework for a model pile in sand mainly due to a variable friction angle at the soil–pile interface.

Contents

Declaration of authorship.....	2
Acknowledgements.....	3
Abstract.....	4
Table of Figures.....	10
List of Tables.....	15
Abbreviations.....	16
Chapter 1. Introduction.....	17
1.1 Research significance.....	17
1.2 Aim and objectives.....	18
1.3 Applied methodology.....	19
1.4 Thesis structure.....	19
Chapter 2. Literature review.....	21
2.1 Introduction.....	21
2.1.1 An introduction into the ground source heat pump (GSHP) system.....	21
2.1.2 Thermal piles in the UK.....	23
2.1.3 The working mechanism of thermal piles.....	24
2.1.4 Chapter structure.....	25
2.2 Load transfer mechanisms in thermal piles.....	25
2.2.1 Proposed load transfer mechanism.....	25
2.2.2 Piles under thermal loading.....	33
2.2.3 Piles under thermo-mechanical loading.....	35
2.3 Analysis of thermal pile cyclic loading.....	35
2.4 Thermo-mechanical behaviour of thermal piles.....	37
2.4.1 Full-scale testing.....	37
2.4.2 Physical 1g models.....	53
2.4.3 Centrifuge models.....	56
2.4.4 Numerical modelling.....	60
2.5 Thermodynamic aspects of thermal piles.....	63

2.5.1	Heat transfer in thermal piles	63
2.5.2	Thermal capacity of thermal piles	65
2.5.3	Design aspects of thermal piles	66
2.6	Summary of the literature review	68
Chapter 3.	Experimental methodology	72
3.1	Introduction.....	72
3.2	Physical modelling of a thermal pile.....	73
3.2.1	Dimensional analysis	73
3.2.2	Size effects and boundary conditions.....	78
3.3	Experimental materials and set-up.....	80
3.3.1	General arrangement	80
3.3.2	Tank design	80
3.3.3	Pile design	85
3.3.4	Loading assembly.....	85
3.3.5	Temperature control system.....	85
3.4	Monitoring instrumentation	85
3.4.1	Instrumentation layout	85
3.4.2	Monitoring using fibre optic sensors.....	89
3.5	Sand characteristics tests.....	95
3.5.1	Grain size distribution	95
3.5.2	Specific gravity	96
3.5.3	Limiting densities.....	96
3.5.4	Direct shear test.....	96
3.6	Test programme	98
3.7	Test procedure.....	99
3.7.1	Scenario 1.....	99
3.7.2	Scenario 2.....	100
3.7.3	Scenario 3.....	101
3.7.4	Scenario 4.....	104

3.7.5	Scenario 5.....	104
Chapter 4.	Thermo-mechanical behaviour of shaft resisting pile	106
4.1	Introduction.....	106
4.2	Ultimate shaft resistance of model pile.....	106
4.3	Scenario 1	107
4.3.1	Temperature and strain sensitivity of FBGs.....	107
4.3.2	Thermal expansion coefficient of the model pile.....	113
4.4	Scenario 2	116
4.5	Scenario 3	118
4.5.1	Pile temperature profiles	118
4.5.2	Strain profiles	119
4.5.3	Degree of freedom.....	123
4.5.4	Thermally induced axial force and stress in the pile	123
4.5.5	Pile head displacement	125
4.5.6	Mobilised friction at the soil–pile interface	125
4.5.7	Comparison with the framework.....	126
4.6	Scenario 4	128
4.6.1	Pile temperature profiles	128
4.6.2	Strain profiles	131
4.6.3	Degree of freedom.....	142
4.6.4	Thermally induced axial force and stress in the pile	145
4.6.5	Pile head displacement	148
4.6.6	Mobilised friction at the soil–pile interface	152
4.6.7	Comparison with the framework.....	158
Chapter 5.	Thermo-mechanical behaviour of shaft and base resisting pile	159
5.1	Introduction.....	159
5.2	Shaft and base resistant capacity – Scenario 5.....	159
5.3	Pile temperature profiles	162
5.4	Strain profiles.....	165

5.4.1	Observed strain.....	165
5.4.2	Restrained strain.....	170
5.5	Degree of freedom	172
5.6	Thermally induced axial force and stress in the pile.....	172
5.7	Pile head displacement.....	178
5.8	Mobilised friction at the soil–pile interface	181
5.9	Comparison with the framework	190
Chapter 6.	Discussion on the laboratory results.....	194
6.1	Ultimate load-bearing capacity of the model pile.....	194
6.2	Pile temperature profiles	195
6.3	Strain profiles.....	198
6.3.1	Observed strain.....	198
6.3.2	Restrained strain.....	202
6.4	Degree of freedom	206
6.5	Thermally induced axial load and stress in the pile	208
6.6	Pile head displacement.....	212
6.7	Mobilised friction at the soil–pile interface	217
6.7.1	Observed response	217
6.7.2	Sand–pile interface.....	218
6.7.3	Assessing the assumption of cyclic compression-tension for thermal piles.....	221
6.8	Comparison with the framework	222
6.9	Error analysis	224
Chapter 7.	Conclusions and recommendations for future works	226
7.1	Conclusions.....	226
7.2	Recommendations for future works	230
References.....		233
Appendices.....		243
Appendix A.	Numerical model	243
Appendix B.	Temperature profiles.....	245

Appendix C. Matlab code	248
Appendix D. Sieve analysis test results	251
Appendix E. Specific gravity test results	252
Appendix F. Limiting densities test results.....	253
Appendix G. Scenario 2- Temperature and strain profiles	254
Appendix H. Mobilised shaft friction- Scenario 4.....	255
Appendix I. Load-bearing capacity of piles.....	263
Appendix J. Temperature variations in sand.....	265

Table of Figures

Figure 2-1. The amplitude of subsurface temperature fluctuations with a depth that represents typical Swedish conditions, resulting from an annual temperature variation of 20°C at the surface and based on data cited by Rosen et al. (2001) (Banks, 2008) (Permission to reproduce this has been granted by John Wiley and Sons Inc).....	22
Figure 2-2. Typical ground temperature profile for different seasons in the UK (Preene and Powrie, 2009) (Permission to reproduce this has been granted by ICE Publishing)	22
Figure 2-3. Thermal pile arrangement (Olgun and McCartney, 2014) (Permission to reproduce this has been granted by Taylor & Francis)	23
Figure 2-4. The number of installed energy piles and the estimated carbon dioxide savings between 2005 and 2010 based on data provided by Amis at Geothermal International Ltd (Laloui and Di Donna, 2011) (Permission to reproduce this has been granted by ICE Publishing)	24
Figure 2-5. A closed-loop working mechanism for heating (De Moel et al., 2010) (Permission to reproduce this has been granted by Elsevier).....	25
Figure 2-6. Cyclic thermal loading in thermal piles	36
Figure 2-7. Thermo-mechanical analysis of an in-situ thermal pile: (a) mechanical, thermal and thermo-mechanical loading in Test 7 (b) induced thermal load in Tests 2 to 7 (Laloui, 2011) (Permission to reproduce this has been granted by ASCE)	40
Figure 2-8. Mobilised shaft friction: (a) Test 1 – thermal loading (Laloui et al., 2003), (b) Test 7 – thermo-mechanical (Laloui, 2011) (Permission to reproduce this has been granted by (a) NRC Research Press, (b) ASCE)	41
Figure 2-9. Axial load profiles: (a) Lambeth College – cooling, (b) Lambeth College – heating, (c) Lausanne test (Amatya et al., 2012) (Permission to reproduce this has been granted by ICE Publishing).....	44
Figure 2-10. Mobilised friction under heating-only: (a) Lambeth College (b) Lausanne test, and under thermo-mechanical loading, (c) Lambeth College, (d) Lausanne test (Amatya et al., 2012) (Permission to reproduce this has been granted by ICE Publishing)	46
Figure 2-11. Induced thermal stress (a) Foundation A, (b) Foundation B (Murphy and McCartney, 2014) (Permission to reproduce this has been granted by Springer).....	48
Figure 2-12. (a) Axial load profile for two heating-cooling cycles under a constant load of 200N, (b) mobilised shaft friction along the pile under thermal loading (Tang et al., 2013) (Permission to reproduce this has been granted by John Wiley and Sons).....	55
Figure 2-13. (a) Axial thermal strain along the pile during heating and cooling periods for numerical and in-situ installations, (b) additional induced thermal stress in the pile (Laloui and Nuth, 2009) (Permission to reproduce this has been granted by Prof.Laloui).....	61

Figure 2-14. Thermally induced pile head displacement at constant load (Suryatriyastuti et al., 2015) (Permission to reproduce this has been granted by John Wiley and Sons)	63
Figure 2-15. Heat transfer procedures in a thermal pile system (Adopted from Loveridge and Powrie, 2013) (Permission to reproduce this has been granted by ICE Publishing)	65
Figure 2-16. Different pipe configurations used by Gao et al. (2008) (Permission to reproduce this has been granted by Elsevier)	67
Figure 2-17. (a) Installation of coil-shaped polybutylene pipes in a thermal pile (Lee et al., 2013), (b) schematic view of a thermal pile with coils (Man et al., 2010) (Permission to reproduce this has been granted by Elsevier)	68
Figure 3-1. A schematic view of dimensional analysis steps.....	73
Figure 3-2. A Schematic view of Scenarios 1 to 4 test set-up (dimensions in mm)	80
Figure 3-3. A schematic view of Scenario 5 test set-up (dimensions in mm).....	81
Figure 3-4. (a) container, (b) model pile, (c) loading plate.....	81
Figure 3-5. Temperature profiles at different heating periods using a 2D FDM model	84
Figure 3-6. A schematic view of FBGs installed on the pile surface.....	87
Figure 3-7. A schematic view of FBGs installed in sand.....	87
Figure 3-8. (a) LVDT calibration apparatus (b) LVDT dimensions	88
Figure 3-9. LVDT calibration	89
Figure 3-10. (a) FBG strain and temperature sensors mounted on the pile surface, (b) Temperature sensors for use in the sand	90
Figure 3-11. Refractive index change of a FBG (Correia, 2008) (Adopted from Zhao, 2001) ..	91
Figure 3-12. Bragg wavelength at different levels along the pile surface- Test S3T1.....	92
Figure 3-13. (a) FBG protection using Araldite epoxy adhesive, (b) Plastic tubes protection(c) Aluminium tape protection	93
Figure 3-14. (a) Extra protection on the pile head, (b) Fibre optic connector cleaning instrument, (c) Opening of the fibre optic cleaner	94
Figure 3-15. (a) Laser box and interrogator, (b) Interrogator channels	95
Figure 3-16. Schematic view of the data acquisition	95
Figure 3-17. Sand grading curve.....	96
Figure 3-18. Shear stress vs. horizontal displacement- shear box test.....	97
Figure 3-19. Shear stress vs. normal stress for peak and critical shear states.....	97
Figure 3-20. (a) Pile head support, (b) & (c) Pile base support	100
Figure 3-21. (a) Latex protection, (b) Scenario 3 test set-up, (c) Scenario 4 test set-up.....	103
Figure 3-22. Installation of FOS in the sand bed, dimensions in mm.....	104
Figure 4-1. Load-Displacement curve for a shaft resistant pile	107
Figure 4-2. Variations in wavelengths with temperature – S1T1	109

Figure 4-3. (a) Shift in total wavelength vs time, (b) shift in the wavelength of temperature FBGs during heating-cooling cycles, (c) compensated observed strain along the pile at different levels, (d) observed strain at various depths at the end of heating and cooling	111
Figure 4-4. Variation in the wavelength with changes in the compensated strain – S1T1	112
Figure 4-5. (a and b) Absolute temperature and temperature changes along the pile for high and low levels of noise in the data, (c) variations in the coefficient of thermal expansion along the pile – S1T1	115
Figure 4-6. (a and b) Temperature distribution along the pile, (c and d) observed strain along the pile – Scenario 2.....	117
Figure 4-7. Temperature distribution: (a and b) along the pile surface, (c and d) in the soil....	121
Figure 4-8. (a and b) Observed strain, (c and d) restrained strain at the end of each heating-cooling period – Scenario 3	122
Figure 4-9. (a and b) Variation of DoF, (c and d) induced axial load and stress – Scenario 3 .	124
Figure 4-10. (a and b) Pile head displacement, (c and d) mobilised friction at the end of each heating-cooling period – Scenario 3	127
Figure 4-11. Temperature distribution and temperature changes along the pile surface – Scenario 4	130
Figure 4-12. Observed mechanical strain and acting axial load along the pile – Scenario 4....	136
Figure 4-13. Observed strain during two heating-cooling cycles – Scenario 4	138
Figure 4-14. Observed strain at the end of each heating-cooling period – Scenario 4	139
Figure 4-15. Restrained strain at the end of each heating-cooling period – (a) to (d): S4TM1-S4TM5; (e) to (f): S4TM6-S4TM8.....	141
Figure 4-16. Variation of DoF along the pile length – Scenario 4.....	144
Figure 4-17. Induced thermal force in the pile – Scenario 4.....	147
Figure 4-18. Pile head displacement vs time – Scenario 4	151
Figure 4-19. Mobilised shaft friction under mechanical loading in four zones along the pile – Scenario 4.....	154
Figure 4-20. Mobilised shaft friction vs pile head displacement – Scenario 4 – S4TM1	155
Figure 4-21. Mobilised friction along the pile at the end of each heating and cooling period – Scenario 4.....	157
Figure 5-1. Load-displacement curve: S5M1–S5M4.....	161
Figure 5-2. Temperature distribution along the pile surface – Scenario 5	163
Figure 5-3. Changes in temperature along the pile surface – Scenario 5.....	164
Figure 5-4. Observed mechanical strain and acting axial load along the pile before thermal loading– Scenario 5.....	167
Figure 5-5. Observed thermal strain during the entire test period – Scenario 5	168
Figure 5-6. Observed thermal strain along the pile – Scenario.....	169

Figure 5-7. Restrained thermal strain along the pile – Scenario 5	171
Figure 5-8. Variation of the DoF along the pile length – Scenario 5.....	173
Figure 5-9. Induced thermal load and stress in the pile – Scenario 5	176
Figure 5-10. Axial load along the pile under both mechanical and thermal loading – Scenario 5	177
Figure 5-11. Pile head displacement – Scenario 5.....	180
Figure 5-12. Mobilised friction along the pile at the end of mechanical loading – Scenario 5	184
Figure 5-13. Mobilised shaft friction vs pile head displacement – Scenario 5 – S5TM1	185
Figure 5-14. Mobilised shaft friction vs pile head displacement – Scenario 5 – S5TM2.....	186
Figure 5-15. Mobilised shaft friction vs pile head displacement – Scenario 5 – S5TM3.....	187
Figure 5-16. Mobilised shaft friction vs pile head displacement – Scenario 5 – S5TM4.....	188
Figure 5-17. Mobilised friction along the pile at the end of each heating and cooling period – Scenario 5.....	189
Figure 5-18. Comparison of restrained strain along the pile surface between Scenario 5 tests and the proposed framework	192
Figure 5-19. Comparison of mobilised shaft friction along the pile surface between Scenario 5 tests and the proposed framework.....	193
Figure 6-1. Temperature changes along the pile surface at the end of the: (a) first heating period and (b) first cooling period – Scenarios 3 to 5	196
Figure 6-2. Comparison between the 1 st and 24 th hour of thermal loading: (a) heating and (b) cooling	202
Figure 6-3. Comparison between restrained strain profiles at the end of each heating and cooling period – Scenarios 3 to 5.....	205
Figure 6-4. Location of the minimum DoF – (a) Scenarios 3 and 4 and (b) Scenario 5.....	208
Figure 6-5. Maximum induced thermal load at the pile toe compared to the maximum induced load along the pile during the two heating-cooling cycles.....	209
Figure 6-6. The location and magnitude of the maximum induced thermal load during the two cycles of heating and cooling.....	210
Figure 6-7. Rate of induced stress per degree change in temperature vs maximum induced stress over allowable stress – Scenarios 3 to 5	211
Figure 6-8. The rate of induced stress per degree change in temperature during the heating and cooling periods – Comparison between the results from Scenarios 3 to 5 and the literature ...	212
Figure 6-9. Normalised pile head displacement – Scenarios 3 to 5.....	214
Figure 6-10. Rate of pile head displacement – Scenarios 3 to 5	215
Figure 6-11. Changes in the safety factor due to two heating-cooling cycles – Scenarios 4 and 5	216

Figure 6-12. Normalised pile head displacement – Comparison between Scenarios 3 to 5 with the literature	217
Figure 6-13. Comparison between restrained strain profiles for the shaft resistance pile and the proposed framework	225

List of Tables

Table 2-1. Four scenarios considered in the framework	27
Table 2-2. Expected pile responses to different loading conditions (Thermal Pile Standard, 2012)	28
Table 2-3. Adopted from the framework proposed by Bourne-Webb et al. (2013) (Permission to reproduce this has been granted by ICE Publishing)	29
Table 2-4. A summary of findings from thermal pile in-situ studies (Adopted from Olgun and McCartney, 2014)	52
Table 2-5. A summary of findings from thermal pile physical models (Adopted from Olgun and McCartney, 2014)	59
Table 3-1. Physical and thermal variables and dimensions of the study.....	75
Table 3-2. Dimensionless groups and scaling factors of DA for a pile under an axial load	76
Table 3-3. Dimensionless groups and scaling factors of DA for a pile under thermal loadings.	78
Table 3-4. Scaling effect recommendations between the pile diameter and sand grain size	79
Table 3-5. Summary of the monitoring instruments used in this study (read in conjunctions with Figures 3.2 and 3.3)	86
Table 3-6. Test Programme - Scenarios 1 to 5.....	99
Table 4-1. Temperature sensitivity of FBGs.....	108
Table 4-2. Strain sensitivity of FBGs.....	110
Table 4-3. Variations in the coefficient of thermal expansion during heating-cooling cycles (10^{-6} m/m. K).....	114
Table 4-4. Changes in pile head settlement under heating and cooling cycles – Scenario 4 tests	149
Table 5-1. Comparison between various test layouts in Scenario 5.....	160
Table 5-2. Temperature readings for Scenario 5 tests (°C).....	162
Table 5-3. Difference between maximum heating and cooling strain values – Scenario 5	166
Table 5-4. Location of maximum strain value along the pile surface – Scenario 5.....	166
Table 5-5. Changes in pile head settlement under heating and cooling cycles – Scenario 5 tests	179
Table 6-1. Comparison between changes in the pile temperature for previous studies	198
Table 6-2. Maximum induced stress per degree change in temperature (kPa/°C) – Scenarios 3 to 5	212

Abbreviations

AR	Aspect ratio
API	American petroleum institute
BSI	British standards institution
DA	Dimensional analysis
DG	Dimensionless group
DoF	Degree of freedom
FBG	Fibre Bragg grating
FDM	Finite difference method
FOS	Fibre optic sensor
GSHP	Ground source heat pump
GSHPA	Ground source heat pump association
HDPE	High-density polyethylene
LVDT	Linear variable differential transformer
PDE	Partial differential equation
PVC	Polyvinyl chloride
RHI	Renewable heat incentive
SPF	Seasonal performance factor
WDM	Wavelength–division-multiplexed

Chapter 1. Introduction

1.1 Research significance

To meet its constantly growing energy demand, the UK's target is to provide 15% of the total energy demand and 12% of the heat demand from renewables by 2020 (Department of Energy & Climate Change, 2013). In 2015, only 5.6% of heating and cooling were produced by renewable sources and a fast uptake in the use of renewables is required to achieve the 2020 target (Department for Business, Energy & Industrial Strategy, 2016). Geothermal energy is considered one of the renewable energy options but, in 2015, heat pumps and deep geothermal energy contributed only 1.0% of the total renewable energy produced in the UK compared to 20.8% and 70.7% for wind energy and bioenergy respectively. Despite the small proportion supplied by geothermal energy, its use has increased in recent years. Thus, the energy produced by geothermal energy and heat pumps in 2015 was equivalent to 169000 tonnes of oil compared to the equivalent of only 1000 tonnes of oil in 2000 (Department for Business, Energy & Industrial Strategy, 2016). A ground source heat pump (GSHP) system is a shallow geothermal energy system that utilises the stored energy in the ground at shallow depths. A thermal pile is a type of closed-loop GSHP system that carries the structure's weight and, at the same time, utilises the stored energy in the ground. Application of thermal piles to major projects, particularly commercial buildings, has increased considerably in recent years since the initial installations in the UK in 2001 (Nicholson, 2012). However, despite an increased number of installations, knowledge of thermal pile behaviour under combined thermal and mechanical loading is still rather limited.

Despite the stable ground temperature, particularly 5m below ground level, thermal piles experience seasonal fluctuations in winter and summer that result in cyclic compressive and tensile forces (Bourne-Webb et al., 2013). Understanding the behaviour of thermal piles under combined thermo-mechanical loading has become a major issue in recent years. A considerable amount of research has been carried out on thermal piles recently, including full-scale testing (Laloui et al., 2006; Bourne-Webb et al., 2009), numerical modelling (Knellwolf et al., 2011; Suryatriyastuti et al., 2015), centrifuge tests (Ng et al., 2015; Goode et al., 2014) and laboratory 1g models (Wang et al., 2011; Kalantidou et al., 2012). According to the studies mentioned above, additional thermal loading is expected to induce considerable axial load and stress on the pile, up to three times the initial mechanical loading, reducing the factor of safety to 1 (Laloui et al., 2006). Moreover, due to pile movement during heating and cooling periods, a considerable friction is mobilised during these heating and cooling periods. However, a few contradictions can be noticed in the findings, such as both reversible and irreversible settlements (Bourne-Webb et al., 2009; Yavari et al., 2014) after thermal cycles are seen. Similarly, both decreases (Wang et al., 2011) and increases (McCartney and Rosenberg, 2011) in side shear resistance are observed for piles

embedded in sand and silt respectively. Moreover, the applicability of Bourne-Webb et al.'s (2013) proposed framework—which has been adopted by the Thermal Pile Standard (2012)—to other soils has not been provided as yet. In addition to the additional compressive loads, tensile forces have been observed for concrete piles that are susceptible to cracking.

Inconsistencies found in the literature on the thermo-mechanical performance of thermal piles and the lack of a comprehensive design guide have resulted in the adoption of an inefficient method for thermal pile design. At the moment, thermal piles are designed by considering the maximum induced load for a situation where least movement is allowed for the pile; maximum pile settlement is also assumed at the least level of restraint. These are both extreme conditions that lead to a low-efficient design with the need for higher safety factors. This results in a less cost-effective design. Knowledge of thermal pile response under various soil and end-bearing conditions will help optimise the design, reduce the cost and, therefore, promote this technology. Limitations exist for in-situ installations, mainly the lack of control of boundary conditions and the difficulty of applying significant mechanical loadings close to the ultimate state. It is also suggested by Bourne-Webb et al. (2013) that controlled physical experiments could help to understand the response of thermal piles under cyclic thermal loading.

1.2 Aim and objectives

The main aim of the research is to investigate the effects of combined thermo-mechanical loading on the pile response compared to conventional mechanical loading. Within the context of the research aim, the following objectives will be explored:

- To determine the additional stress on the pile compared to the allowable stress limits given by BS 8004:1986 (British Standards Institution, 1986).
- To determine the differences in the response of shaft resisting piles versus base and shaft resisting piles. Moreover, the effects of end bearing on the thermal pile response will be investigated.
- To determine the limits of elastic or plastic behaviour of thermal piles and to define the threshold for thermo-elastic behaviour.
- To determine the variations in the factor of safety under thermo-mechanical loading.
- To quantify the degree of freedom (DoF) imposed by the surrounding soil and the mechanical loading on the pile head (the DoF of thermal piles is considered to be a defining parameter for the response of thermal piles).
- To assess the assumption of considering cyclic thermal loading of thermal piles as two-way cyclic loading presented in the literature.

- To look at the effect of higher magnitudes of mechanical loading closer to the ultimate capacity of the pile. If cyclic degradation is to be seen, the piles need to be loaded close enough to the ultimate shaft capacity, which is not possible within the field.
- To assess the reliability of the proposed framework by the Thermal Pile Standard (2012) for various end-bearing conditions and magnitudes of loadings and to assess the reliability of the proposed location of the null point along the thermal pile surface.

1.3 Applied methodology

To investigate the thermo-mechanical behaviour of thermal piles, a 1g small-scale model is developed using a stainless steel model pile embedded in medium-dense, dry sand. To monitor the temperature and strain changes along the pile surface, FBGs are used at five points along the surface. Additionally, to capture the temperature variations in the surrounding soil, a set of four FBGs are installed at five levels in the sand bed. Experiments are divided into five scenarios, mirroring those defined in the framework adopted by the Thermal Pile Standard (2012). Both shaft resisting piles and shaft and base resisting piles are examined. Two heating-cooling cycles are applied to the pile for 24 hours each. Thermal loading is applied under various magnitudes of mechanical loading on the pile head. Changes in the pile head displacement during thermo-mechanical loading are measured. The model pile response under mechanical, thermal and thermo-mechanical loading is investigated to determine the aim and objectives mentioned above.

1.4 Thesis structure

The thesis consists of six more chapters:

- Chapter 2 – Initially, an introduction to a GSHP system is given. This is followed by the introduction to thermal piles and a brief description of their working mechanism. The load transfer mechanism adopted for the design of thermal piles is described. The assumption of considering the behaviour of thermal piles under seasonal heating-cooling cycles as a pile under two-way cyclic loading is presented afterwards. Previous works done on thermal piles are then presented, starting with the effects of thermo-mechanical loading on the mechanical performance of thermal piles. A brief description of the heat transfer process in thermal piles is given as a necessary tool to understand the behaviour of thermal piles. A summary of the literature review is provided at the end of the chapter, followed by an introduction of the research question.
- Chapter 3 – This chapter presents the methodology used to develop the laboratory model and testing schedule. Firstly, a dimensional analysis (DA) done for a model thermal pile is presented. It is followed by a description of the experimental model and the monitoring fibre optic sensors used in this study. Moreover, a brief description of the numerical model used to

predict the temperature profiles is given. Test results of sand characteristics test are presented. At the end, the test schedule and the test procedure for five scenarios are presented.

- Chapter 4 – Results of the experimental study on the shaft resisting thermal pile are presented in this chapter. Initially, the load capacity tests that were performed to assess the ultimate shaft resistance of the pile are presented. These are used to determine the required magnitude of mechanical loading on the pile head. Initially, the reference test results, Test S1T1, are presented. The effects of mechanical-only, thermal-only and thermo-mechanical loading on a single pile with varying end bearings but no soil are studied in Scenarios 1 and 2. This is followed by Scenario 3 results, which are for a shaft resisting pile embedded in sand and undergoing heating-cooling cycles without any constant mechanical load on the pile head. Scenario 4 test results are presented at the end of this chapter, where the pile is under thermo-mechanical loading. Test results are also compared with the proposed framework by the Thermal Pile Standard (2012).
- Chapter 5 – This chapter presents the results for the base and shaft resisting pile. The main difference from Chapter 4 is the different set-up used in the Scenario 5 tests, which present the more common working situation of a thermal pile embedded in the soil.
- Chapter 6 – This chapter deals with the discussion of the laboratory tests. Results are compared with the findings in the literature, and a discussion on the possible reasons for the observed behaviour is presented.
- Chapter 7 – This chapter presents the conclusions drawn from this study, followed by the recommendations for future works, as well as recommendations that need to be considered in the design of thermal piles.

Chapter 2. Literature review

2.1 Introduction

2.1.1 An introduction into the ground source heat pump (GSHP) system

At the moment, the UK's commitment for 2020 is to provide 15% of total energy demand and 12% of heat demand from renewable sources (Department of Energy & Climate Change, 2013). In 2015, heating and cooling produced by renewable sources were just 5.6% of the total produced heating and cooling (Department for Business, Energy & Industrial Strategy, 2016). The application of microgeneration technologies has been introduced by the Renewable Heat Incentive (RHI) and is defined as the generation of low or zero carbon heat and power by individuals, small businesses and communities (Baker et al., 2009). Heat pumps, including ground, air and water sources, are included in RHI microgeneration technologies. The GSHP, which utilises the geothermal energy stored in the ground, is of interest in this study.

Geothermal energy is defined as a percentage of the earth heat that can be recovered and exploited by man (Dickson and Fanelli, 2004). In another definition, Batchelor (2005) describes geothermal energy as all forms of heat extracted from the earth. Geothermal resources are usually classified into three categories based on delivery temperature (Batchelor, 2005):

- $>150^{\circ}\text{C}$: Mainly for power generation.
- $40\text{--}150^{\circ}\text{C}$: Large-scale heating and power generation with low efficiency.
- $<40^{\circ}\text{C}$: Mostly used with heat pumps to provide heating, cooling and hot water.

The third category, shallow geothermal, is of interest in this study. Alternatively, a term called 'thermogeology' is defined by Banks (2008) as the study of the storage and transfer of low-enthalpy heat ($<30^{\circ}\text{C}$) in a relatively shallow geological environment ($<200\text{m}$). A GSHP is a type of shallow geothermal energy technology that is considered low-carbon emission technology. Despite seasonal fluctuations in temperature, ground temperature below a depth of 5m remains relatively stable, which helps to increase the efficiency of GSHP systems (see Figure 2.1). Preene and Powrie (2009) state that the mean annual air temperature in the UK varies between 10°C and 14°C (see Figure 2.2). Moreover, the annual average surface temperature is within the range of 9°C and 12°C , which is also reflected in subsurface temperature (Banks, 2008).

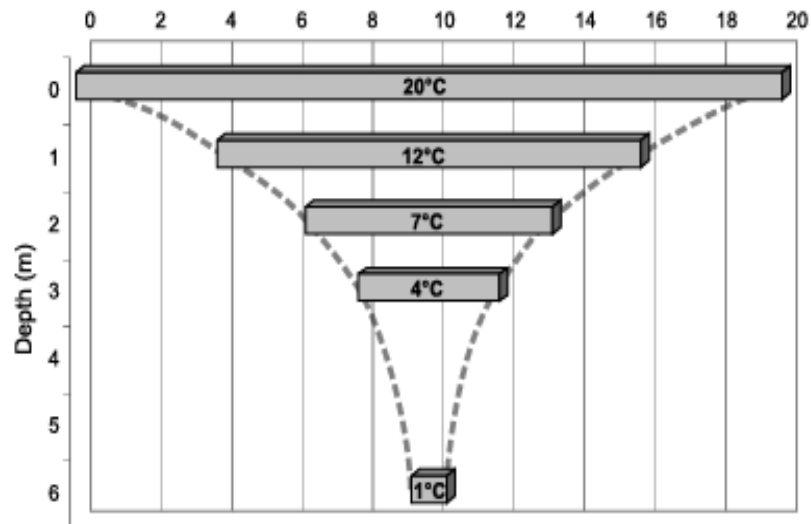


Figure 2-1. The amplitude of subsurface temperature fluctuations with a depth that represents typical Swedish conditions, resulting from an annual temperature variation of 20°C at the surface and based on data cited by Rosen et al. (2001) (Banks, 2008) (Permission to reproduce this has been granted by John Wiley and Sons Inc)

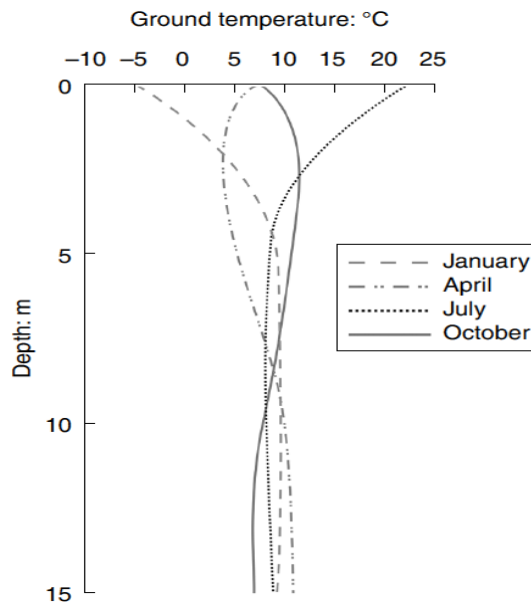


Figure 2-2. Typical ground temperature profile for different seasons in the UK (Preene and Powrie, 2009) (Permission to reproduce this has been granted by ICE Publishing)

There are two main types of GSHP systems: open-loop and closed-loop. The applied system depends on various parameters, including soil conditions, thermal conductivity and the availability of water and land space. For an open-loop system, the source is usually groundwater or surface water, and water is extracted from the source using boreholes. The groundwater is then transferred through the heat transfer system (which is usually a heat pump) and, at the end, it is disposed of as waste or re-injected back into the ground. This study investigates the behaviour of the closed-loop system. Closed-loop systems are installed both vertically and horizontally. The

three main types of closed-loop systems are: horizontal trenches, vertical boreholes and thermal piles.

2.1.2 Thermal piles in the UK

A thermal pile is a type of closed-loop GSHP system that is called different names, including ‘heat exchanger foundation’, ‘geo-pile’, ‘thermo-active pile’ and ‘energy pile’. At the moment, its generic name in the UK is ‘thermal pile’, which has been used in the Ground Source Heat Pump Association’s (GSHPA’s) Thermal Pile Standard, published in 2012. A schematic diagram of a thermal pile is shown in Figure 2.3, where geothermal loops or pipes are installed in or around the reinforcement cage of the pile.

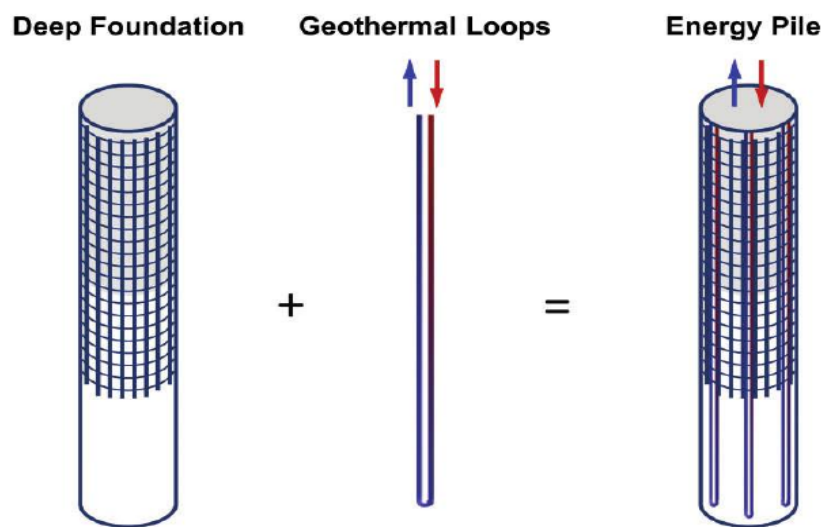


Figure 2-3. Thermal pile arrangement (Olgun and McCartney, 2014) (Permission to reproduce this has been granted by Taylor & Francis)

It is stated by Brandl (2006) that, since the beginning of the 1980s, there has been greater application of geothermal energy in foundation elements in Austria and Switzerland, with the first installations of structural piles in 1984. Nicholson (2012) states that thermal piles were established in the UK in 2001, with early installations in 2002. In 2005, Cementation Skanska gave the trademark term ‘energy piles’ to heat exchanger foundations. In terms of the UK, rapid growth in the number of installed units between 2005 and 2010 has been reported (see Figure 2.4). The main reasons for this rapid increase of thermal pile installations are:

- This technology uses stored energy in the ground as a clean and renewable source.
- The high thermal storage capacity of the concrete is a bonus.
- The dual application of thermal piles – which already exist in buildings as part of the structural foundation – results in a reduction of the initial cost. A comparison between the initial installation cost of conventional vertical boreholes and the initial installation cost of prestressed high-strength concrete thermal piles that use a coil-type fluid carrier was done by

Lee et al. (2013). A cost reduction of 16.3% in the cost is reported for the thermal piles compared to the vertical boreholes. In a similar study by Sekine et al. (2006), it is found that the initial cost of construction per unit for heat extraction and rejection is approximately \$0.79/W for thermal piles, and \$3.0/W for existing standard boreholes. Emission of borehole drilling cost is the main benefit in the cost analysis of thermal piles. Other studies also confirm the benefits of using thermal piles instead of vertical boreholes as heat exchangers (Hamada et al., 2007; Wood et al., 2009).

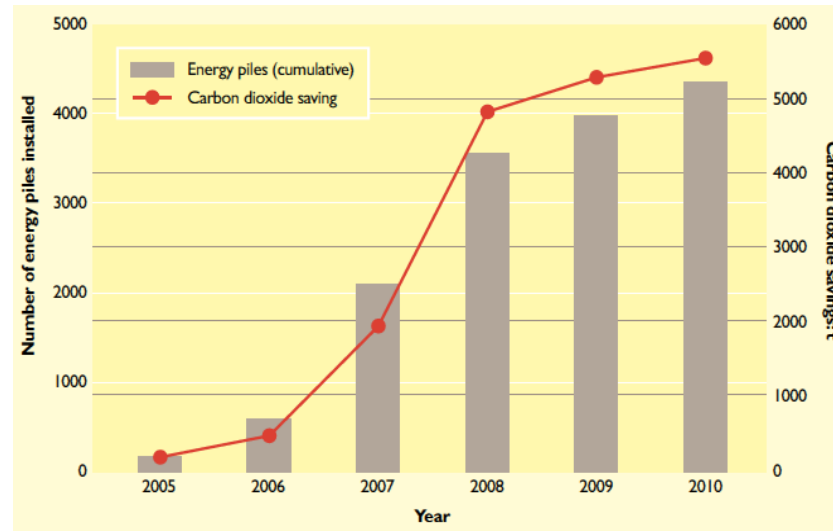


Figure 2-4. The number of installed energy piles and the estimated carbon dioxide savings between 2005 and 2010 based on data provided by Amis at Geothermal International Ltd (Laloui and Di Donna, 2011) (Permission to reproduce this has been granted by ICE Publishing)

2.1.3 The working mechanism of thermal piles

The working mechanism of thermal piles is similar to other types of closed-loop systems, which mainly consist of primary and secondary circuits. In the primary circuit, source side, a fluid is circulated through a loop of pipes buried in the ground. It then goes through the heat transfer system on the surface (the heat pump) and, at the end, it is recirculated using the buried ground loop to exchange heat with the soil (Preene and Powrie, 2009). The secondary circuit, load side, consists of a network of closed-loop pipes carrying the fluid for the heating and cooling of buildings. This network of pipes is embedded in the floors, walls, bridge decks or any other element that is meant to be heated up or cooled down (see Figure 2.5). Primary and secondary circuits are connected via a heat pump. Heat pumps are used to adapt the temperature of the upper ground level fluid to the acceptable level required for heating the building. Electrical heat pumps are the most common type of heat pumps. The refrigerant cycle inside the heat pump is also shown in Figure 2.5. This cycle consists of four steps. The refrigerant gets to the evaporator and the temperature rises. It is then sent to the compressor, in which the pressure is increased, and the temperature rises as well. The condenser cools down the refrigerant and sends it through the

expansion valve in a cyclic process. The compressor is a mechanical device and is mainly powered by electricity. If a renewable power supply is provided for the compressor, then the GSHP – and, consequently, thermal pile system – would be a fully renewable energy source.

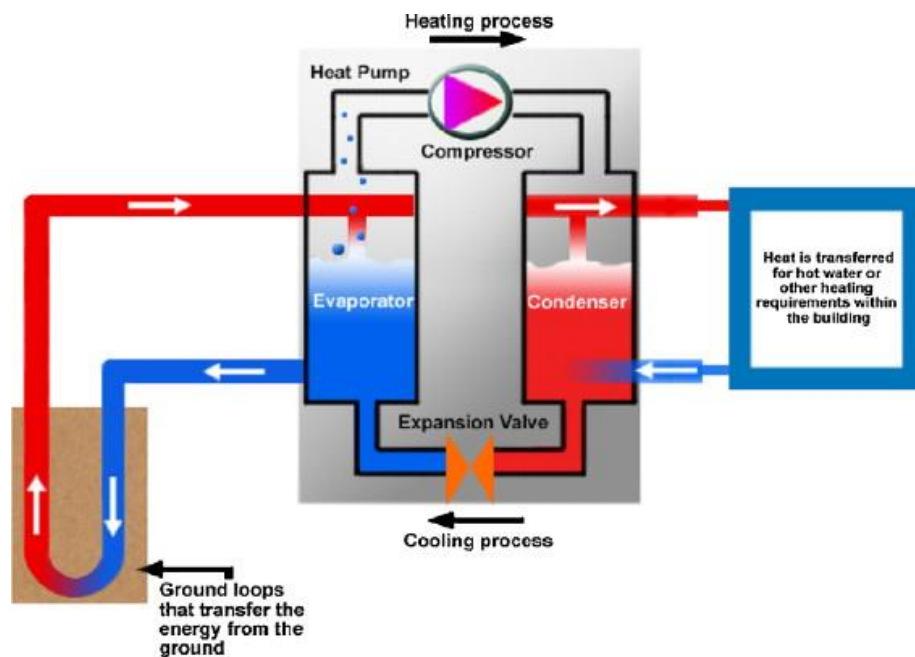


Figure 2-5. A closed-loop working mechanism for heating (De Moel et al., 2010) (*Permission to reproduce this has been granted by Elsevier*)

2.1.4 Chapter structure

The load transfer mechanism used in this study is adopted from the Thermal Pile Standard (GSHPA, 2012), which is based on the framework given by Bourne-Webb et al. (2009; 2013). The applied load transfer mechanism is described in Section 2.2. Thermal piles experience cyclic seasonal heating and cooling loads, and the effects of cyclic loading on a typical pile are discussed in Section 2.3. In general, the literature on thermal piles is divided into two main parts:

- Part 1: Understanding the performance of thermal piles under additional thermal loading.
- Part 2: Thermodynamic aspects of thermal piles.

A brief summary of heat transfers and the parameters involved in the heat transfer of thermal piles is given in Section 2.5; this is useful to better understand the working mechanism of thermal piles. A summary of the literature review is given in Section 2.6, and it is followed by a description of the research question.

2.2 Load transfer mechanisms in thermal piles

2.2.1 Proposed load transfer mechanism

The load transfer mechanism used for the design of thermal piles, as well as in this study, is based on the framework given by Bourne-Webb et al. (2013) and is adopted by the Thermal Pile Standard (GSHPA, 2012). This load transfer mechanism is based on two in-situ studies done by

Bourne-Webb et al. (2009) and Laloui et al. (2006). In general, the temperature influence on pile behaviour is presented using the following parameters:

- Axial thermal strains
- Pile head displacement
- Induced axial load and stress
- Mobilised shaft friction

Pile responses under singular thermal loading, heating or cooling, and combined thermo-mechanical loading are described below. The framework presented in this section provides a helpful tool for the prediction of strain and mobilised shaft resistance behaviour. The results obtained in the laboratory will be compared with the framework to assess the applicability of this framework under different boundary conditions. The framework is validated by Bourne-Webb et al. (2013) based on in-situ tests conducted at Lambeth College London, and École Polytechnique Fédérale de Lausanne by Laloui et al. (2006). Some assumptions are considered in the simplified model (Bourne-Webb et al., 2013):

- The pile load is resisted on the shaft alone.
- The resistance generated is uniform along the length of the shaft – that is, there is a constant rate of change in strain with depth.
- An idealised soil with uniform strength is considered. The model is developed for single profile uniform soil.
- There is a linear elastic pile and a constant cross-sectional area, which will cause linear variations in the load and strain along the pile.
- Temperature variations are uniform over the length of the pile.
- The null point is located at the mid-depth of the pile.

The sign agreement used in this analysis assigns a positive sign to the compressive stress and strain caused by thermal expansion and upward shaft resistance. It is also considered that compressive strain is caused by heating, and tensile strain caused by cooling. Both free and perfectly restrained end-bearing conditions are considered. Loading conditions are categorised into five categories:

1. Mechanical
2. Cooling
3. Heating
4. Mechanical and heating
5. Mechanical and cooling

Loading conditions 4 and 5 are the actual loading conditions for thermal piles, but an understanding of pile behaviour under single mechanical or thermal loading is necessary, as it helps to differentiate the effects caused by thermal loading. Four different scenarios are described in Table 2.1, based on variations in the end-bearing condition, surrounding soil restraint and loading condition.

Table 2-1. Four scenarios considered in the framework

Scenario no.	End-bearing	Soil restraint	Loading
Scenario 1	Free ends	No	Thermal
Scenario 2	Fully restrained	No	Thermal
Scenario 3A	Free ends	Yes	Thermal
Scenario 3B	Fully restrained	Yes	Thermal
Scenario 4A	Free ends	Yes	Thermal + mechanical
Scenario 4B	Partially restrained	Yes	Thermal + mechanical
Scenario 4C	Fully restrained	Yes	Thermal + mechanical

In Scenario 1, a single pile with no end and side restraints is heated and cooled. In Scenario 2, the pile is heated and cooled with both ends restrained. Restraints caused by pile ends in Scenario 2 cause an additional induced load in the pile. In Scenario 3A, no end restraints are considered for the pile, but side resistance from the surrounding soil is considered. Heating and cooling will result in pile displacement, resulting in the mobilisation of shaft friction. Due to the assumption of no base support in Scenario 3, the pile load is meant to be carried entirely on the pile shaft. In Scenario 3B, the end restraints are applied on the pile, and this results in an increase in the induced thermal load. The location of maximum induced thermal load and stress in Scenarios 3A and 3B is assumed to be at the mid-depth of the pile as a null point. Bourne-Webb et al. (2013) state that a higher magnitude of thermal loading or stiffer soil will result in an increase in the mobilised shaft friction and restrained strain. During the cooling period, tensile force is expected to develop, which is unfavourable for concrete piles. The existence of end restraints in Scenario 3B will result in the reduction of pile head displacement and, eventually, in less mobilised friction.

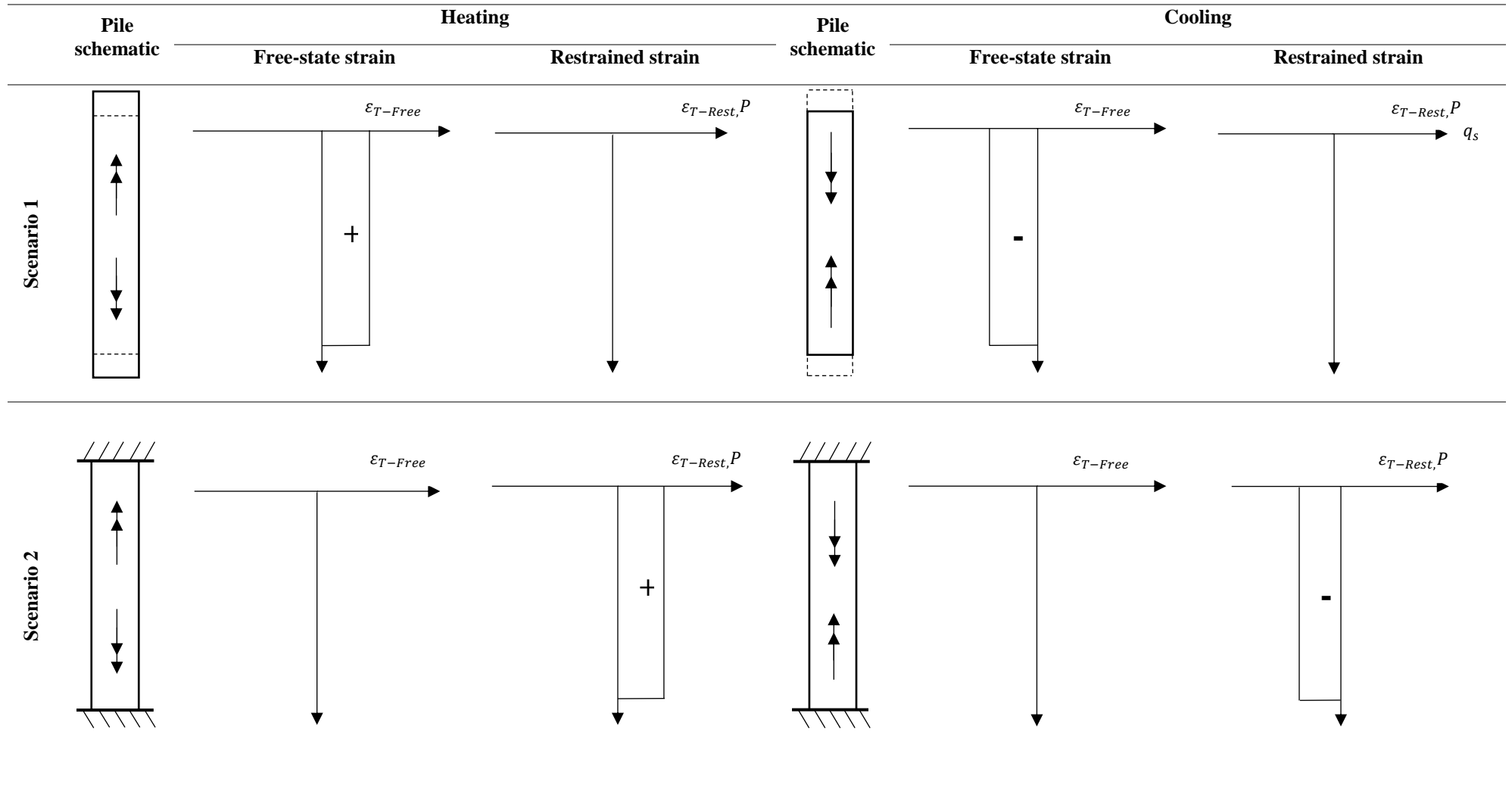
In Scenario 4, both mechanical and thermal loading are applied on the pile, which represents the actual working condition of a typical thermal pile. Mechanical loading is expected to induce a certain level of restraint, depending on the magnitude of mechanical loading, which results in an increase in the induced thermal load and stress on the pile. Moreover, during the heating period, the upper half of the pile heaves less compared to Scenario 3, resulting in less mobilised friction. In the bottom half of the pile, the reverse procedure occurs. In Scenario 4B, where the pile is rested on stiff soil and is considered to be an end-bearing pile, the level of restraint caused by the pile bottom is expected to be higher than the level of restraint caused by mechanical loading. This

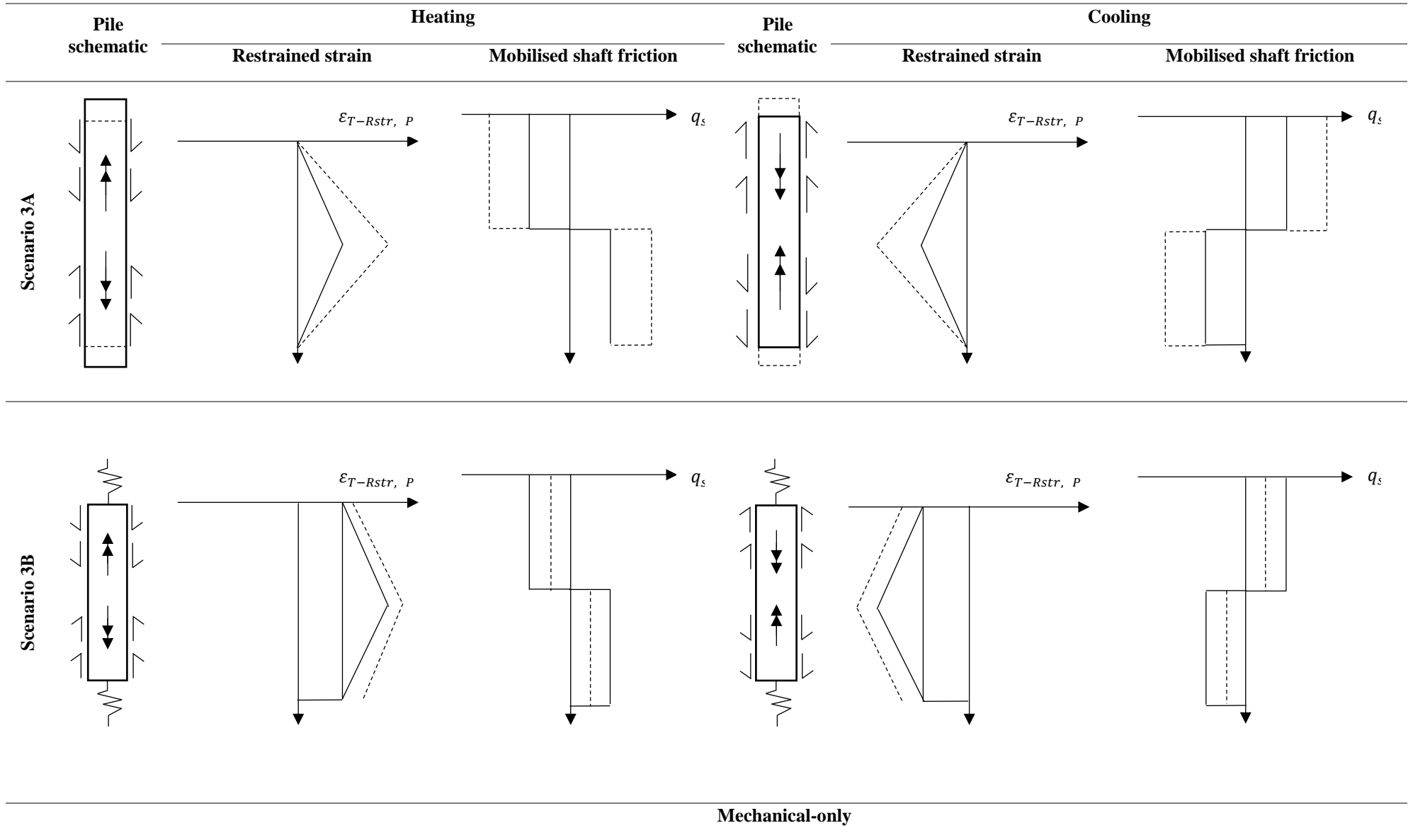
results in a higher magnitude of induced thermal load at the pile toe. In Scenario 4C, it is assumed that the pile is already being restrained at both ends, and the level of induced stress is mainly dependent on the level of restraint caused by the end supports. A schematic preview of scenarios mentioned above is given in Table 2.3. Additionally, the expected pile responses under different loading conditions are given in Table 2.2.

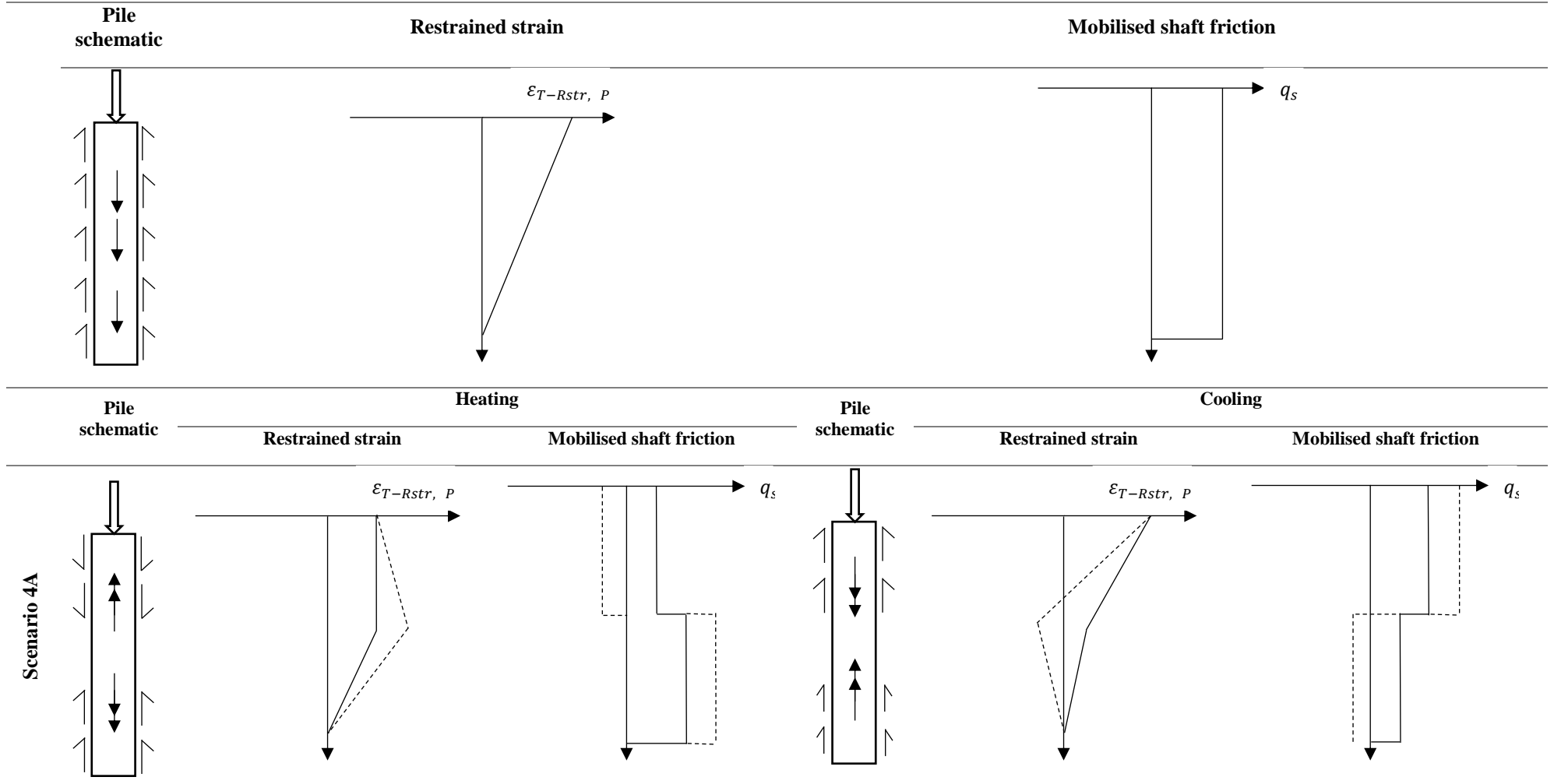
Table 2-2. Expected pile responses to different loading conditions (Thermal Pile Standard, 2012)

Loading condition	Pile response
Mechanical	The pile is under compression.
	It moves downward, into the soil.
	Shaft resistance acts in an upward direction, opposing the load.
Cooling–Free ends	Restraints on the pile shaft result in the development of tensile stress within the pile.
	The resulting shear stress on the soil–pile interface is in the same direction as shear stress mobilised by compression loading in the upper part of the pile, and in the opposite direction in the bottom of the pile.
	Tension can potentially result in the cracking of concrete piles.
Heating–Free ends	Shaft resistance causes additional compressive stress in the pile.
	The resulting shear stress on the soil–pile interface is in the opposite direction as the shear stress mobilised by compression loading in the upper part of the pile, and in the same direction in the lower part of the pile.
Mechanical and cooling	Axial loads become less compressive at the mid-point, and may become tensile in the lower part of the pile.
	The mobilised shaft resistance increases in the upper part of the pile and decreases in the lower part of the pile.
Mechanical and heating	Axial loads become more compressive.
	Restraints on the pile shaft result in compressive stress in the pile. This may lead to compressive failure of the pile.
	The mobilised shaft resistance decreases in the upper part of the pile, but increases in the lower part of the pile.

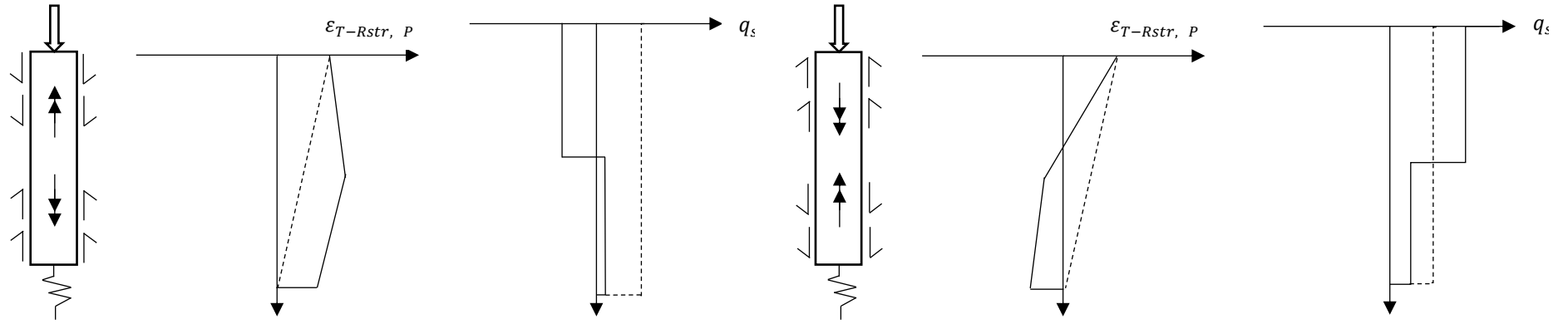
Table 2-3. Adopted from the framework proposed by Bourne-Webb et al. (2013) (Permission to reproduce this has been granted by ICE Publishing)



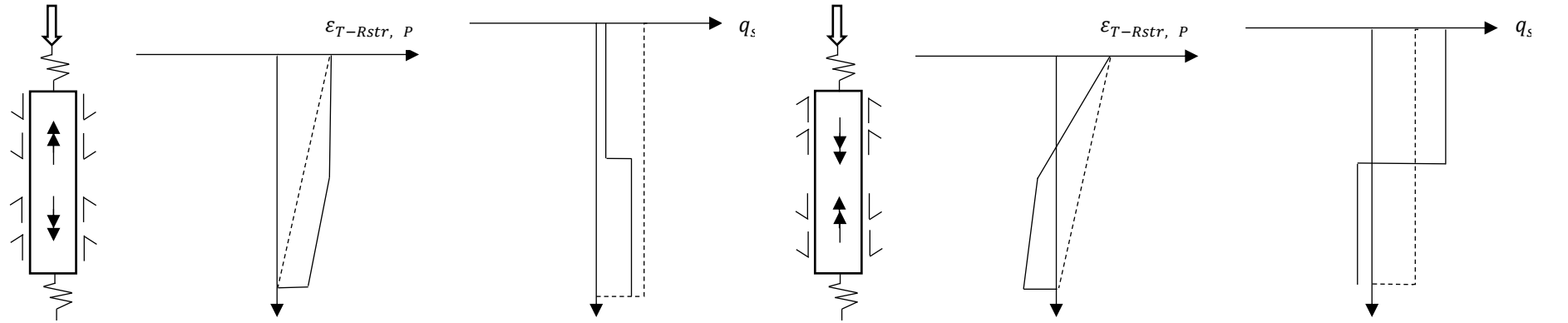




Scenario 4B



Scenario 4C



2.2.2 Piles under thermal loading

Using the above load transfer mechanism, the following procedure is used to determine the effect of thermal and thermo-mechanical loading on thermal piles. For a pile with no restrictions from pile ends and the surrounding soil, heating and cooling will result in expansion and contraction of the pile respectively. This is proportional to the coefficient of thermal expansion of the pile and the magnitude of change in temperature. Free thermal strain is then achieved by:

$$\varepsilon_{T-Free} = \alpha \Delta T \quad (2.1)$$

Where:

ε_{T-Free} : Free-state strain (μE)

α : Coefficient of thermal expansion ($10^{-6}/\text{K}$)

ΔT : Temperature variations ($^{\circ}\text{C}$)

The pile is elongated and shortened under heating and cooling respectively:

$$\Delta L = L_0 \varepsilon_{T-Free} \quad (2.2)$$

Where:

ΔL : Change in pile length due to thermal loading (mm)

L_0 : Initial pile length (mm)

The axial force inside the pile is calculated using the following equation:

$$P = EA \varepsilon_{T-Free} \quad (2.3)$$

Where:

E : Young's modulus of the pile (GPa)

A : Cross-sectional area (m^2)

The free-state condition stated above is not achievable in practice, and a certain degree of restraint exists in the field either as structural weight on the pile head or from the surrounding soil. Due to the presence of restraints, part or all of the pile deformation is blocked. A term called 'degree of freedom' (DoF) is defined as the ratio of observed strain over free strain:

$$n = \frac{\varepsilon_{T-Obs}}{\varepsilon_{T-Free}} \quad (2.4)$$

Where:

n : DoF

ε_{T-obs} : Observed strain collected in the field or laboratory

The value of the DoF varies between 0 and 1. Two possible extreme cases are:

- Case 1: Perfectly restrained body: $n = 0 \rightarrow \varepsilon_{T-obs} = 0$
- Case 2: Completely free body: $n = 1 \rightarrow \varepsilon_{T-obs} = \varepsilon_{T-Free}$

The value of the DoF varies along the pile length. For instance, in the analysis done by Bourne-Webb et al. (2013), perfect restraint is assumed for the pile ends and the minimum DoF is seen in the middle of the pile, which is called the null point. The null point is considered a point where zero thermal-induced axial displacement occurs (Di Donna and Laloui, 2014). In the absence of thermal loading, the null point definition does not apply (Mimouni, 2014).

Determining the value of the DoF is considered one of the main challenges in the analysis of the stress and strain behaviours of thermal piles. Laloui et al. (2003) have done in-situ tests to determine the value of the DoF as a function of depth in order to locate the null point on the pile surface. To understand the effect of the DoF, a term called ‘restrained strain’ is used, which is the result of restraints from the ends or the surrounding soil. The restrained strain is the difference between the free-state strain and the observed strain:

$$\varepsilon_{T-Rstr} = \varepsilon_{T-Free} - \varepsilon_{T-obs} \quad (2.5)$$

Where:

ε_{T-Rstr} : Restrained thermal strain

When combining Equations 2.4 and 2.5, ε_{T-Rstr} is calculated using Equation 2.6 as a function of the DoF:

$$\varepsilon_{T-Rstr} = (n - 1) \cdot \varepsilon_{T-Free} \quad (2.6)$$

Assuming linear elastic behaviour, the induced stress caused by thermal loading in the pile is a proportion of the restrained strain:

$$\sigma_{th} = \varepsilon_{T-Rstr} \cdot E = (n - 1) \cdot \alpha \cdot \Delta T \cdot E \quad (2.7)$$

The induced thermal loading is also determined using the following equation:

$$P_T = E \cdot A \cdot \varepsilon_{T-Rstr} = E \cdot A \cdot \alpha \cdot \Delta T \cdot (n - 1) \quad (2.8)$$

The induced thermal load is a concern in the design of thermal piles, as it is applied approximately evenly on the entire length of the pile and the pile toe carries a large amount of the load (unlike conventional friction piles, where almost no load is carried by the pile toe (Laloui et al., 2006). Thermal loading causes pile displacement with respect to the ground, which results in the mobilisation of side friction at the soil–pile interface. To determine the value of mobilised shaft resistance, Laloui (2011) uses a formula taken from previous works by Bustamante et al. (1991) and Vulliet and Meyer (1999):

$$q_s(z) = \left(\frac{A(z) \cdot E_{pile}}{\Pi \cdot D(z)} \right) \left(\frac{\Delta \varepsilon(z)}{dz_i} \right) \quad (2.9)$$

Where:

$q_s(z)$: Mobilised shear stress at depth z (kPa)

D : Pile diameter (mm)

dz_i : Thickness of layer 'i' (mm)

$\Delta\varepsilon(z)$: Strain difference between the bottom and the top of the layer

To understand the effect of thermal loading on shaft resistance of the pile, the mobilised friction under thermal loading should be compared with mobilised friction under ultimate mechanical loading.

2.2.3 Piles under thermo-mechanical loading

The addition of mechanical loading means the addition of strain caused by mechanical loading:

$$P_M = E \cdot A \cdot \varepsilon_M \quad (2.10)$$

Where:

ε_M : Mechanical strain ($\mu\varepsilon$)

P_M : Mechanical load (N)

The total strain caused by thermo-mechanical loading is the sum of strains caused by mechanical and thermal loadings:

$$\varepsilon_{Total} = \varepsilon_M + \varepsilon_{T-obs} \quad (2.11)$$

Similarly, the total load applied on the pile is the sum of mechanical and thermal loadings:

$$P_{Total} = P_M + P_T = E \cdot A \cdot [\varepsilon_M + \varepsilon_{free}(n - 1)] \quad (2.12)$$

2.3 Analysis of thermal pile cyclic loading

For a thermal pile operating in both heating and cooling modes, seasonal heating and cooling loads are applied. Cyclic expansion and contraction of thermal piles can be considered as cyclic axial thermal loading. The applied load on a typical thermal pile under working condition can be considered a combination of static axial mechanical loading and cyclic thermal loading (see Figure 2.6). To understand the possible detrimental effects of cyclic axial thermal loading, its type needs to be first identified. Cyclic axial loadings are divided into one-way and two-way. One-way cyclic axial loading involves applying one type of loading, tension or compression in a cyclic manner on the pile head. Two-way cyclic axial loading involves applying both compression and tension in the cycles. Two-way cyclic axial loading has more potential to damage the pile compared to one-way cyclic loading. The behaviour of thermal piles can be considered as two-

way cyclic axial loading, undergoing cyclic compression and tension under heating and cooling periods respectively. This assumption seems reasonable due to the small ratio of the pile diameter compared to the pile length. It is assumed that the radial movement of the thermal pile under thermal loading is neglected compared to the axial movement (Suryatriyastuti et al., 2013). This assumption is assessed in the laboratory tests in Chapters 4 and 5.

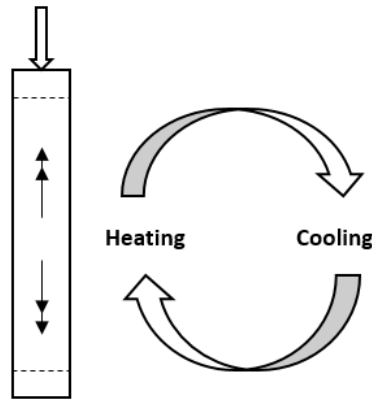


Figure 2-6. Cyclic thermal loading in thermal piles

Before examining previous work in the literature on the behaviour of thermal piles under cyclic thermal loading, the behaviour of a typical pile under cyclic mechanical loading is discussed. The possible failure mechanisms are related to the type of cyclic loading (Poulos, 1989):

1. Accumulation of permanent displacement for one-way cyclic loading.
2. Degradation of skin friction and base resistance for two-way cyclic loading.

For a thermal pile operating in both heating and cooling modes, degradation of skin and base resistance is expected to be seen. In general, there are three parameters that could reduce the load-bearing capacity of a pile (Poulos, 1989):

- Skin friction degradation
- Base resistance degradation
- Soil modulus degradation

Poulos (1989) states that base resistance degradation from cyclic loading can be ignored in the analysis. Moreover, in the case of model piles in a sand container, load carried by the pile base is usually neglected due to its small contribution to the overall capacity. It is stated by Suryatriyastuti et al. (2013) that the soil is not affected by thermal volumetric variations and the ground temperature equilibrium remains constant in two soil conditions. The first situation is where sandy soil exists and the groundwater flows away quickly. The second situation is where significant groundwater flow exists (>35 m/year). If these two cases are present, the pile will only undergo thermal variations, and the analysis is limited to soil–pile interaction. Moreover, it is suggested by Poulos (1989) that the effects of sand modulus degradation are not significant and can be

ignored compared to the significant impact caused by clay degradation modulus. The only parameter that seems to be applicable for this study is the degradation of skin friction, but this needs to be assessed using laboratory data. Degradation factors are affected by the following parameters (Lee, 2004):

- Type of cyclic loading: Poulos (1989) states that the effect of two-way cyclic loading is greater than that of one-way cyclic loading.
- The amplitude of cyclic loading: In this case, higher changes in temperature could result in more detrimental effects.
- A number of cycles: It is expected that greater degradations will be observed in a higher number of cyclic loadings.
- Type of soil and pile.

A centrifuge model is developed by Li et al. (2012) to investigate the cyclic axial behaviour of piles and pile groups in sand. It is found that pile head stiffness reduces with an increase in the number of cycles at a decreasing rate. It is also found that a majority of the reduction takes place in the first few cycles. This observation aligns with Poulos' (1989) findings. A summary of previous works' findings on the cyclic behaviour of a single pile is given by Lee (2004) and shows the reduced load-bearing capacity of piles, as well as the accumulation of pile displacement under cyclic axial loading. Moreover, sudden failure of a micropile under cyclic axial loading is observed depending on the magnitude of cyclic loading. The effect of cyclic thermal loading on mobilised shaft friction and accumulated displacement will be studied in Chapters 4 and 5.

2.4 Thermo-mechanical behaviour of thermal piles

2.4.1 Full-scale testing

Despite the successful installation of thermal piles worldwide and a considerable amount of research in recent years, information on the performance of thermal piles under thermo-mechanical loading is still rather limited. Material found in the literature regarding the thermo-mechanical behaviour of thermal piles is divided into four main types: in-situ installations, laboratory 1g models, centrifuge testing with different gravity levels, and numerical models. Full-scale studies are divided into two main categories:

1. To study the thermal performance and efficiency of thermal piles, as well as to look at heat transfer from thermal piles to the surrounding soil (Hamada et al., 2007; Gao et al., 2008; Wood et al., 2009; Jalaluddin et al., 2011; Wang et al., 2012; Ozudogru et al., 2012; Loveridge and Powrie, 2013).
2. To understand the effect of thermo-mechanical loading on the structural performance of thermal piles. This is further divided into two main categories:

- Axial loading applied on the pile from the superstructure according to different temperature changes (Brandl, 2006; Laloui et al., 2006; Laloui and Nuth, 2006; Bourne-Webb et al., 2009; Laloui, 2011; Amatya et al., 2012; Murphy and McCartney, 2012; Murphy and McCartney, 2014).
- Wang et al. (2012; 2013) use the Osterberg cells (O-cells) embedded in thermal piles to characterise the changes that happen in the side shear resistance of thermal piles.

A summary of in-situ tests found in the literature is presented in Table 2.4. The two main in-situ studies – which are the basis of other research studies on thermal piles – are conducted by Laloui et al. (2006) and Bourne-Webb et al. (2009). Findings are mainly divided into six main categories: thermal strain, pile head displacement under thermal loading, induced thermal loading, the DoF, the magnitude of mobilised shaft friction due to heating and cooling, and the influence of end restraints on pile behaviour.

An instrumented test pile was installed as part of a new structure at the Swiss Federal Institute of Technology, Lausanne (Laloui et al., 2003; 2006; Laloui, 2011). Details of the soil profile and pile properties are given in Table 2.4. Seven tests were performed at different stages of this construction. In Test 1, where the pile head is free to expand, the pile is heated up for 12 days with $\Delta T=21^{\circ}\text{C}$ (Laloui et al., 2006) and then cooled for 16 days. In another publication by Laloui (2011), $\Delta T=22^{\circ}\text{C}$ is mentioned for Test 1. In Tests 2 to 7, the pile head is partially restrained by the building's weight depending on the stage of construction. In Tests 2 to 7, the pile is initially loaded mechanically, after which a thermal load with a magnitude of $\Delta T=15^{\circ}\text{C}$ (which is less than in Test 1) is applied. The maximum applied mechanical load is 1300kN in Test 7. Following observations are made:

- The deformation of the pile is thermo-elastic in both radial and axial directions. Displacement caused by heating is recovered during cooling.
- The maximum observed strain is seen at the pile head, reducing towards the pile bottom with a sudden increase at the bottom of the pile. This could be mainly due to the presence of stiffer soil at that level, giving more freedom to the pile to expand. Non-uniform strain profiles during the heating period are also related to changes in friction along the pile shaft in this study by Laloui et al. (2006). Linear behaviour is approximately seen along the pile for the observed strain at the end of the cooling period.
- Radial heat transfer is seen from the pile towards the soil.
- Temperature distribution along the pile is not completely uniform, with $\pm 2^{\circ}\text{C}$ variations.
- The radial strain is also measured, and it is observed that there is still contact between the soil and the pile after the thermal cycle. Residual strain is seen at the end of the heating-cooling

cycle, which is mainly due to the pile temperature not returning to its original value and which is why the behaviour is considered thermo-elastic.

- When the observed strains at the pile head and at the toe are compared, it is seen that the level of restraint caused by the building's weight is higher than the level of restraint caused by the soil at the pile toe.
- An upward movement of approximately 4mm is recorded by optical fibres during the heating period. The thermally induced displacement at the pile head is significant compared to the settlement caused by the mechanical loading on the building. An upward displacement of 1mm is recorded for the pile during heating, which is equivalent to the settlement caused by a mechanical loading of 600kN.
- Maximum and minimum induced vertical stresses caused by restraints from surrounding soil are seen at the pile's mid-depth and the pile head respectively. This is mainly due to the differences in soil stiffness. Maximum and minimum induced stresses for $\Delta T=13.3^{\circ}\text{C}$ are approximately 2.9 and 1.6MPa.
- In Test 7, where maximum mechanical load (equal to 1300kN) is applied on the pile head, the maximum vertical stress is equal to 1.3MPa at the pile head and reduces to zero at the pile toe. In contrast, a more uniform induced stress is applied on the pile head during thermal loading, with a maximum of 2.3MPa at the middle of the pile. The pile toe usually carries the least load in a friction pile, but it underwent heavy loading due to the nature of thermal loading.
- A temperature increase of 1°C results in an additional 100kN induced thermal load.
- A significant increase in the induced stress is seen at the mid-depth of the pile, where approximately 2.2MPa is induced by thermal loading compared to approximately 0.8MPa caused by mechanical loading. This means that induced thermal stress is 2.75 larger than mechanical stress.
- The induced strain from the surrounding soil under thermal is rather limited and does not affect the effective stress.
- Under service load condition in Test 7 – where the thermal cycle is applied on the pile with mechanical loading on the pile head – the magnitude of the induced load from heating is two times the mechanical loading. This takes the overall load from approximately 1200kN to 3690kN (see Figure 2.7-a). Thus, it changes the safety factor from 3 to approximately 0.75 (Laloui and Di Donna, 2011).
- The maximum thermal loads in Tests 2 to 7 are shown in Figure 2.7-b. Here, it can be seen that a direct relationship exists between the magnitude of induced thermal load and changes in temperature. For instance, despite there being a stronger restraint on the pile head in Test 7 compared to other tests, a lower induced load is seen due to a lower increase in temperature

in Test 7 compared to Tests 3 to 6. This means that the effect of the magnitude of temperature change is greater than the effect of the level of restraint caused by mechanical loading on the pile head.

- Average induced stress at the pile head is dependent on the magnitude of mechanical loading on the pile head, where average induced stress in Test 1 is $-50\text{kPa}/^\circ\text{C}$, is increased to $-150\text{kPa}/^\circ\text{C}$ in Test 2 and further increased in Tests 3 to 7.
- There are changes in the DoF for all seven tests. The maximum DoF, approximately 0.85, is seen at the pile head in Test 1, where there is no restraint on the pile head. The DoF reduces towards the bottom of the pile, with an increase in the last layer of soil due to the existence of sandstone.
- The maximum restraint is seen in Test 6, while the maximum load is applied to the pile head in Test 7. The lowest magnitude of the DoF is seen in Test 4, at a 23m depth for a magnitude of approximately 0.42.

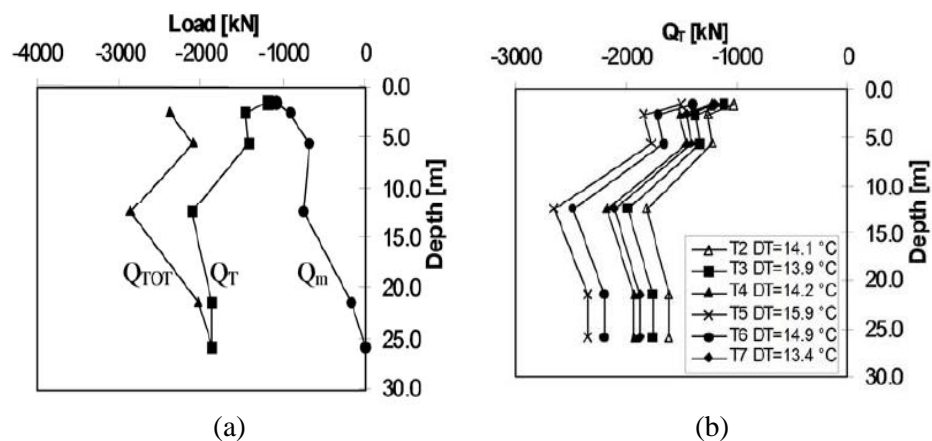


Figure 2-7. Thermo-mechanical analysis of an in-situ thermal pile: (a) mechanical, thermal and thermo-mechanical loading in Test 7 (b) induced thermal load in Tests 2 to 7 (Laloui, 2011) (Permission to reproduce this has been granted by ASCE)

- Due to the opposite movements of the pile during mechanical loading and heating, it is seen that friction resistance is not much affected. The magnitude and the sign of mobilised friction are dependent on the type of soil layer and pile depth.
- Under mechanical loading, positive friction is seen in three layers, mainly due to the downward movement of the pile. Maximum mobilisation happens in layer C, where least displacement is seen at approximately 35kPa. In the same layer in the thermal-only test, the maximum mobilised friction is approximately 30kPa. Considerable negative skin friction is seen in the other layers for Test 1 (see Figure 2.8-a).
- In Test 7, an increase in mobilised friction is seen in layer C with a positive sign (see Figure 2.8-b). It is observed that mobilised friction remains at below-limit values.

- Mobilised shaft friction is unlikely to cause damage to the thermal pile. The main reason is the combined influence of the adverse effects caused by thermal loading (uplift) and settlement caused by static loading: these are said to neutralise each other.

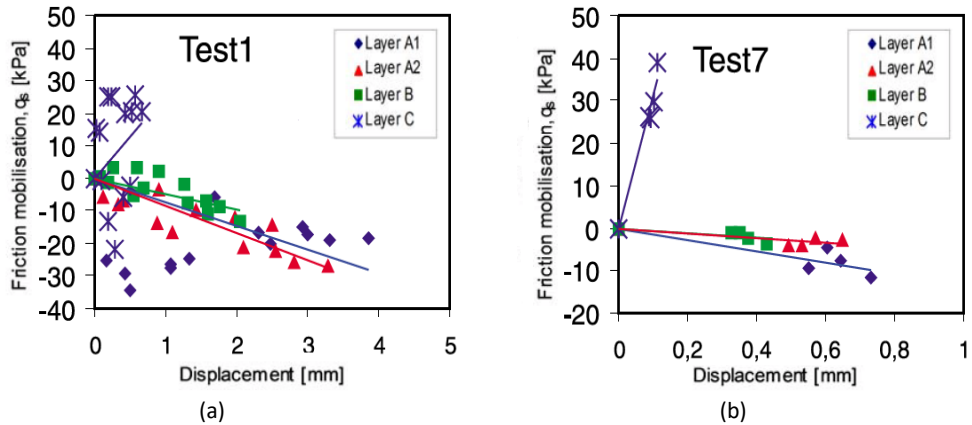


Figure 2-8. Mobilised shaft friction: (a) Test 1 – thermal loading (Laloui et al., 2003), (b) Test 7 – thermo-mechanical (Laloui, 2011) (Permission to reproduce this has been granted by (a) NRC Research Press, (b) ASCE)

Another full-scale in-situ study, conducted at Lambeth College, is reported by Amis et al. (2008), Bourne-Webb et al. (2009) and Amatya et al. (2012) (see Table 2.4). In this study, two sets of optical fibres are used: one to measure the strain and another to measure the temperature. This is similar to what is done in this current study and will be described in Chapter 3. For thermo-mechanical loading with a constant load of 1200 kN, working load, the pile is cooled for $\Delta T = -19^\circ\text{C}$ and heated for $\Delta T = +10^\circ\text{C}$. This is while in Laloui et al. (2006), test T1 is heated for $\Delta T = 22^\circ\text{C}$ and tests T2 to T7 are heated up for $\Delta T = 15^\circ\text{C}$. The magnitude of thermal loading is one of the parameters that can affect the induced thermal loading which is discussed later when all the results are compared.

In the operational range, the temperature is usually expected to vary between -1°C and $+38^\circ\text{C}$ (Amis et al., 2008) or $+30^\circ\text{C}$ (Bourne-Webb et al., 2009). Initial mechanical loading includes loading-unloading cycles in the order of 1200 and 1800 kN. It is while the maximum induced mechanical loading in Laloui et al. (2006) is equal to 1300 kN for Test 7. The test period was 53 days, in which the 1200 kN mechanical loading was maintained for 46 days. The pile is cooled for 31 days and heated for 12 days, and then cooled and heated in daily cycles. This is while the pile is heated up for 12 days and then cooled for 16 days by Laloui et al. (2006). It means that similar heating period is applied in both studies while the cooling period in Bourne-Webb et al. (2009) is two times greater than Laloui et al. (2006). Another difference in the thermal loading is existed between these two studies. The pile is initially cooled and then heated in Bourne Webb et al. (2009), while the reverse procedure is applied by Laloui et al. (2006). Results are compared with the framework proposed by Amatya et al. (2012). The ultimate load is 3600 kN, which is three times greater than the working load. The following results are reported:

- The temperature increase in the heat sink pile is $\Delta T = +29.4^\circ\text{C}$ and $\Delta T = +10^\circ\text{C}$ for the pile with the load frame on top, compared to $\Delta T = +20.9^\circ\text{C}$ for the pile in the Lausanne test.
- A symmetrical uniform radial distribution of heat is seen in the soil. This is in line with the observations made by Laloui et al. (2006).
- Similar to Laloui et al. (2006), the pile temperature is not completely recovered after the heating-cooling cycle, mainly due to improvements in the thermal capacity of the soil.
- The behaviour of the pile is thermo-elastic, similar to Laloui et al. (2006).
- The authors state that the pile floats on the ground with few restraints on pile movement at both ends. This could be seen as a contradiction to Laloui et al.'s (2003) pile end considerations.
- At the end of the cooling phase, the strain variation in the upper part is minimum, but there is a significant reduction from 6m to 14m (in terms of depth) and, near the bottom of the pile, the strain becomes close to zero and moves towards tension.
- Following cooling, the pile is then heated. At the end of this heating phase, the mobilised strain is larger than it would be in a situation without any temperature change. The maximum induced load in the pile is larger than the mechanical load (Amatya et al., 2012).
- The observed strains at the top and bottom of the pile are close to 100% of the free-state strain, while the observed strain at mid-depth is approximately half of the free-state strain. This differs from Test 1 in Laloui et al.'s (2006) study, where the location of the minimum observed strain is at a depth of approximately 20m. Moreover, the maximum observed strain in Laloui et al. (2006) reaches only 70% of the free-state strain. The larger strain values observed by Bourne-Webb et al. (2009) are mainly due to the higher temperature increases in the pile and less restraints at the ends.
- The pile head displacement after four weeks of cooling is 4.8 mm, which is two times the settlement caused by the service working load of 1200kN at 2.4 mm (Amis et al., 2008). Despite the considerable increase in the settlement during the cooling cycle, approximately 83% of it is recovered during the heating period, taking the pile head settlement to 2.8mm. It means that, after cooling-heating cycles, a 17% increase in the pile head settlement is seen. The maximum pile head displacement under an ultimate load of 3600kN is approximately 10mm.
- Pile head displacement under 1800kN (which is 1.5 times the service working load) is equal to 3.2mm. This means that the magnitude of additional settlement caused by cooling-heating cycles is half of the settlement caused by an addition of mechanical loading and is equal to half of the service working load.
- Pile heave due to heating is 40% of the theoretical value for a 27°C increase in temperature. For cooling, it is seen that the contraction of the pile head is 60% of the theoretical value.

- At the end of the heating period, after initial settlement due to heating, a 1.63mm pile heave is seen. This shows an approximately 70% recovery of pile head displacement caused by cooling in the previous step.
- A reduction in the axial load becomes tensile in the lower third of the pile.
- In terms of combined mechanical and cooling loads, tensile forces are developed in the lower part of the pile (see Figure 2.9-a). It is suggested by Bourne-Webb et al. (2009) that the tensile stresses do not exceed design limits and there is no need for extra reinforcement to protect the pile from possible cracking, but further investigation in this area is also recommended. The maximum tensile force and stress during the cooling period are 500kN and 2MPa respectively.
- The location of the maximum induced thermal load along the pile changes during each heating and cooling period.
- Unlike Laloui et al.'s (2006) study, the magnitude of the compressive induced load from thermal loading at the pile toe is not significant (see Figure 2.9-b). Moreover, a lower increase in the axial thermal load is seen at the pile head, which is 70% higher than the mechanical load. The main reason is the difference between the restraint levels in the two studies. The Lausanne test's pile seems nearly perfectly restrained, while the Lambeth College test's pile has only partial restraint. The lower induced load in the Lambeth College test – compared to in Laloui et al.'s (2006) study – could be due to the load control mechanism used, which produces lower restraints than a completed structure.
- Findings for induced thermal load distribution in the pile by Bourne-Webb et al. (2009) and Laloui et al. (2006) show the effects of restraints on the pile axial response.
- Heating increases the ratio of compressive stress over ultimate concrete strength by 71% (it changes from 0.14 to 0.24). It remains below the limit of 0.25 under the working load given by BS 8004:1986 (British Standards Institution, 1986).
- The thermally induced axial load profile shows the negligible effect of end restraints on the pile in this study (which is contradictory to findings by Laloui et al. (2006)). The maximum induced thermal load is just below the mid-depth and is equal to 1550kN, which is approximately 1.3 times the working load on the pile head.
- The maximum rate of increase for the induced stress from heating is $-192\text{kPa}/^{\circ}\text{C}$, and is 56% of the ultimate theoretical induced stress. This rate of increase is approximately two times bigger than the rate of increase in Laloui et al.'s (2006) study, which shows $104\text{kPa}/^{\circ}\text{C}$ (36% of the ultimate theoretical induced stress). During the cooling period, the maximum additional stress in the Lambeth College test is $177\text{kPa}/^{\circ}\text{C}$ which is close to the value found in the heating period. Despite there being a negligible increase in the induced stresses at the top and the bottom of the pile in Bourne-Webb et al.'s (2009) study, the rates of increase in induced

stress with temperature change at the top and the bottom of the pile in the Lausanne test are equal to $-87\text{kPa}/^\circ\text{C}$ and $-50\text{kPa}/^\circ\text{C}$ respectively, showing partial restraints at both ends.

- In thermo-mechanical loading, similar to the heating-only condition, a lower magnitude of induced stress is seen in the Lausanne test compared to the Lambeth College test. This is mainly due to the softer soil used in the Lausanne test (with a lower level of restraint) compared to the stiff soil used in the Lambeth College test. The maximum induced stress with constant load on the pile head is between $-267\text{kPa}/^\circ\text{C}$ and $-329\text{kPa}/^\circ\text{C}$ in the Lambeth College installation, while this value is lower (at $-147\text{kPa}/^\circ\text{C}$ to $-153\text{kPa}/^\circ\text{C}$) for the Lausanne test.

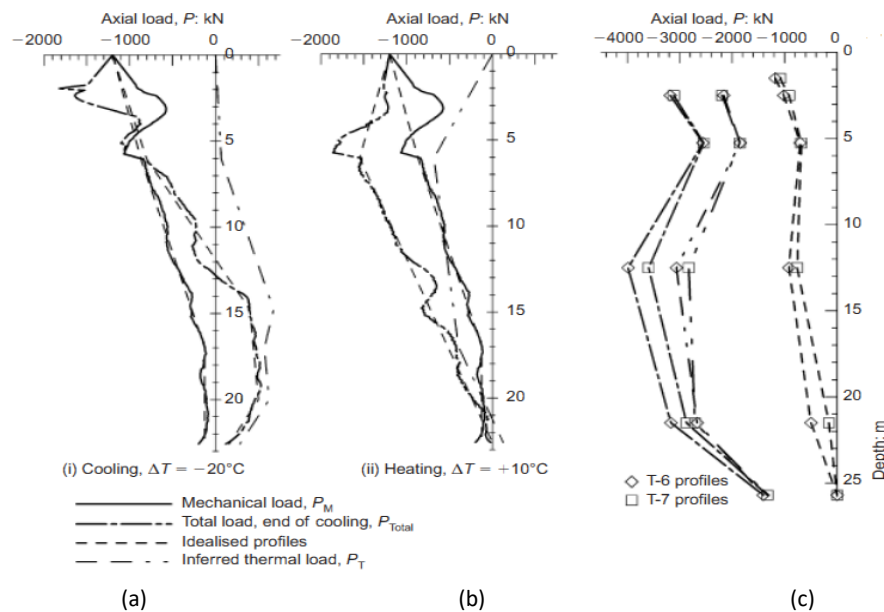


Figure 2-9. Axial load profiles: (a) Lambeth College – cooling, (b) Lambeth College – heating, (c) Lausanne test (Amatya et al., 2012) (Permission to reproduce this has been granted by ICE Publishing)

- The mobilised shaft resistance for the mechanical test of 1200kN is approximately uniform and equal to 30kPa (Bourne-Webb et al., 2009). During the cooling period with constant load on the pile head, the mobilised friction profile is similar to the proposed framework in Section 2.2. For a combination of mechanical loading and cooling, additional shaft resistance equal to 60kPa is seen in the upper part of the shaft. This value is two times higher than the mobilised friction by mechanical loading (see Figure 2.10-c).
- Ultimate shaft resistance is measured at 90kPa under the ultimate load of 3600kN. This means that the mobilised friction during cooling is two-thirds of the ultimate mobilised friction. Moreover, reduced mobilised friction is seen at the bottom of the shaft close to the value of mobilised shaft by mechanical loading.

- Despite determining that mobilised friction is within limits, it is suggested that further study is required to understand the effects of mobilised friction, as higher temperatures might have a damaging impact on the pile.
- Radial expansion of the pile is seen during heating, which may contribute to the observed increase in shaft friction. By comparing the results by Bourne-Webb et al. (2009) and Laloui et al. (2006), it is found that soil type is a dominant parameter for changes in the shaft friction caused by temperature changes.
- In the Lausanne test, the ultimate average shaft resistance achieved by applying a mechanical load three times larger than the working load is equal to 120kPa. Under thermal loading, the average mobilised frictions at the upper and lower halves of the pile are -50kPa and +75kPa respectively, which are 41.6% and 62.5% of the ultimate friction respectively (see Figure 2.10-b). In the Lambeth College test, a linear increase in the shaft resistance with temperature at an average value of 2.1-2.5kPa/°C is seen. In contrast, in the Lausanne test, this value changes from 0.5kPa/°C to 1.5kPa/°C depending on the soil layer.
- Mobilised friction under working load is 40kPa, which is half of the value seen due to cooling. The average mobilised friction per degree decrease in the cooling period is 2.1kPa/°C compared to an average value of 2.1kPa/°C to 2.5kPa/°C in the heating period. In the lower part of the pile, negative skin friction is seen with an average value of -4kPa/°C. In the subsequent heating period, due to the upward movement of the pile, negative skin friction is seen.
- A higher magnitude of mobilised friction is seen during the heating period in constant mechanical loading compared to mechanical-only loading. For the Lambeth College test, maximum friction is mobilised during the cooling period in constant mechanical loading.
- The trends for both tests during heating look similar: negative shaft friction is mobilised at the upper section of the pile and positive friction is mobilised at the lower half.
-

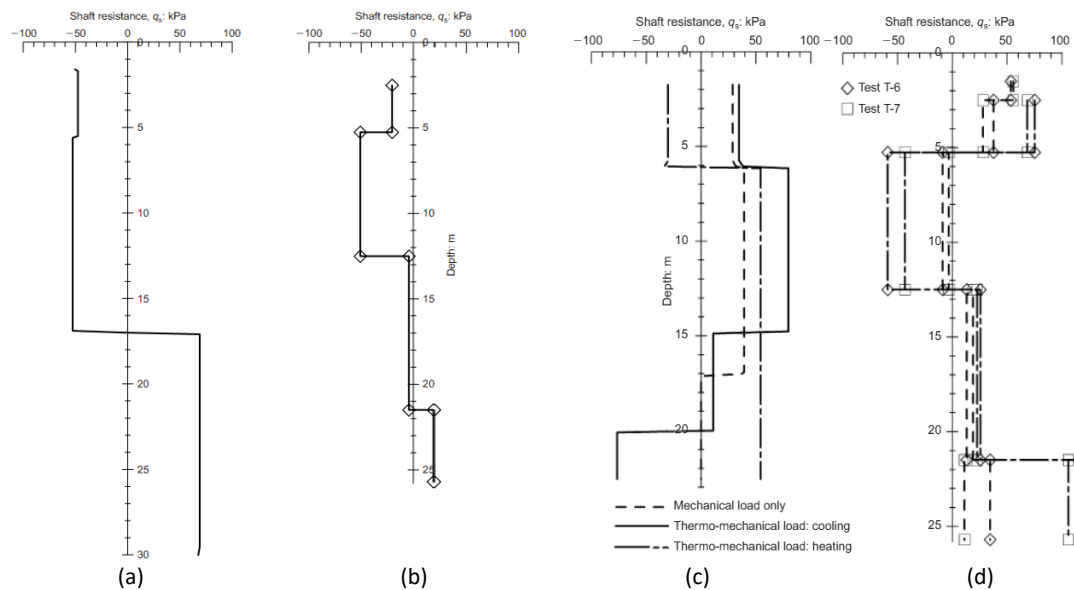


Figure 2-10. Mobilised friction under heating-only: (a) Lambeth College (b) Lausanne test, and under thermo-mechanical loading, (c) Lambeth College, (d) Lausanne test (Amatya et al., 2012) (Permission to reproduce this has been granted by ICE Publishing)

Another in-situ study is reported by Murphy and McCartney (2012) and Murphy and McCartney (2014). Two out of 60 installed piles for an eight-storey building were converted into thermal piles at the new Denver Housing Authority Senior Living Facility in Denver, Colorado (see Table 2.4). The maximum change in temperature during cooling and heating periods are -5°C to $+14^{\circ}\text{C}$. The thermo-mechanical behaviours of the piles are monitored under constant building loads of 3840kN and 3640kN, which are more than three times the mechanical loads applied by Laloui et al. (2006) and Bourne-Webb et al. (2009). Findings by Murphy and McCartney (2012) for ΔT variations between $+5^{\circ}\text{C}$ and -3°C are as follows:

- The thermo-elastic behaviour of thermal piles is seen during the first year of heating and cooling, but this behaviour changes to thermo-plastic during the second cycle. It is unlike the observed behaviour by Laloui et al. (2006) and Bourne Webb et al. (2009).
- The maximum induced thermal load is seen at the bottom and the top of the pile due to the existence of soil restraint and mechanical loading on the pile head. It is in contrast with Laloui et al. (2006) where the maximum induced thermal load is seen at the pile mid-depth. Larger magnitude of mechanical loading is used by Murphy and McCartney (2012) which is approximately 3 times greater than those used by Laloui et al. (2006). It means that the magnitude of mechanical loading on the pile head can be a defining parameter to determine the location of maximum induced thermal load/stress along the pile. The maximum induced stress under thermo-mechanical loading is 10MPa (considered within the allowable limit) and is found close to the pile toe in Foundation A and close to the pile head in Foundation B. Foundation B is 1.4m shorter in length and has four heat exchange tubes installed, compared to the three tubes in Foundation A. Differences in the axial stress profiles could be due to the

higher rate of heat transfer caused by the presence of an additional tube (see Figures 2.11-a and 2.11-b). It means that there could be a direct relationship between the magnitude of thermal loading and induced thermal stress. In terms of practical applications, it can be an indicator that additional pipings can only be used in thermal piles when excessive induced thermal load caused by additional pipes does not exceed the load bearing capacity of thermal piles.

- In the heating phase, the minimum and maximum induced thermal stresses during temperature variations for both piles are seen in the upper part and lower part of the pile respectively. The difference comes from variations in the soil profile, where fill, sand and gravel are present in the upper half with a lower degree of restraint compared to the claystone present at the bottom of the pile with a higher level of restraint. Moreover, it shows that, despite considerable mechanical load at the pile head, a higher level of restraint is caused by the soil – as compared to head restraint – which results in a lower DoF in the lower half of the pile. A similar observation is made for mobilised shear stress. It means that soil layers has the potential to provide more restraints than applied mechanical loading depending on the soil profile constituents and magnitude of mechanical loading as a percentage of thermal pile load bearing capacity.
- Induced thermal load and stress, pile head displacement and strain values are all within the required limits, possibly due to the low level of temperature changes.
- The maximum increase in the induced axial stress is $285\text{kPa}/^{\circ}\text{C}$ (Olgun and McCartney, 2014), which is higher than the values given by Laloui et al. (2006). It means that despite lower magnitude of temperature changes compared with Laloui et al. (2006) and Bourne Webb et al. (2009), stiff soil layers has resulted in a considerable induced stress in the pile per degree change in the temperature. This again shows the importance of soil stiffness on the overall thermal pile response to thermal loading.
- A non-linear profile is achieved for mobilised shear stress. Unlike Laloui et al. (2006) and Bourne-Webb et al. (2009), positive mobilised friction is seen at the top one-third of the pile, followed by negative mobilised friction in the rest of the pile. The magnitude of maximum mobilised friction is approximately 140kPa , which gives an average increase of $10\text{kPa}/^{\circ}\text{C}$ in mobilised friction.

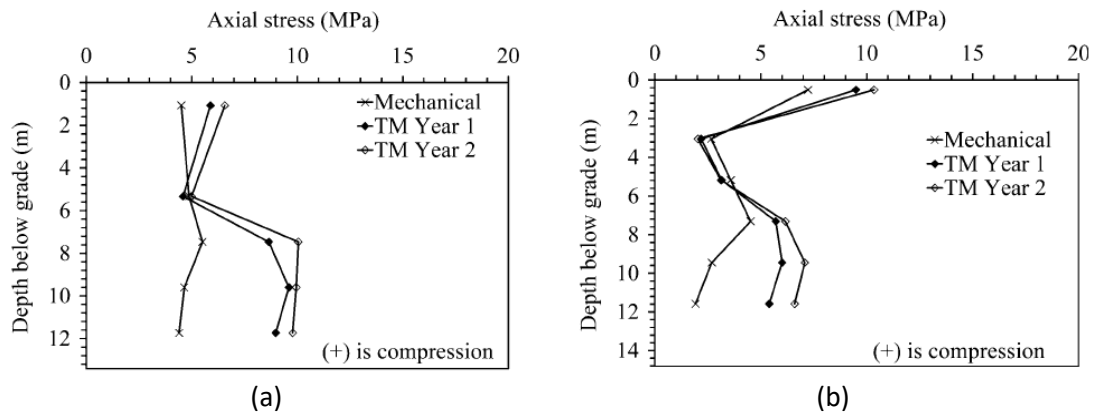


Figure 2-11. Induced thermal stress (a) Foundation A, (b) Foundation B (Murphy and McCartney, 2014)
(Permission to reproduce this has been granted by Springer)

In another in-situ study by Murphy et al. (2014), eight thermal piles were used for a new, one-storey building at the US Air Force Academy. The soil beneath the building is an unsaturated sandstone deposit. Only three out of the eight thermal piles are instrumented by strain gauges and thermistors. In this study, unlike Murphy and McCartney (2014), the pile is not cooled below the ambient air. The maximum mechanical load from the building's weight is 833kN. The observations are as follows:

- Approximately linear thermo-elastic behaviour of piles during heating and cooling is observed in dry sandstone. It is in line with the observations made by Bourne Webb et al. (2009) and Laloui et al. (2006).
- Maximum strain is observed near the top and the bottom of the pile. This means that the minimum level of restraint exists at the top and the bottom of the pile. It is similar to the observation made by Murphy and McCartney (2012) and unlike the observation made by Laloui et al. (2006) and Bourne Webb et al. (2009).
- For an 18°C increase in temperature, the maximum induced stress (4.0 to 5.1MPa) is seen at the normalised depth of 0.72 to 0.78. This is approximately equal to 25% of concrete compressive strength. Differences in the location of the maximum induced stress in the different studies are mainly due to variations in soil stiffness and the magnitude of thermal loading. Similarly, the magnitude of induced stress remained within the limits in Laloui et al. (2006) and Bourne Webb et al. (2009).
- The maximum pile head upward movement under thermo-mechanical loading is equal to between 1.4mm and 1.7mm.

Another full-scale study is done by Sutman et al. (2015) in Richmond, Texas, where three thermal piles (TP1–TP3) were tested with and without a constant mechanical load on the pile head (see Table 2.4). An average increase of 8°C is seen along the piles. Both fibre optics and strain gauges are used to monitor strain and temperature variations along the pile. For test TP1, in the absence

of mechanical loading, it is seen that there is no compressive stress induced on the pile head. With an increase in the pile length, the magnitude of induced thermal stress is increased until it reaches the maximum value of 2.04MPa at the normalised depth of 0.65. This is then followed by a slight reduction in the magnitude of induced thermal load. The existence of dense sand results in an increase in the induced thermal stress in the lower half of the pile. The results of TP2 and TP3, where the respective mechanical loads of 378kN and 1056kN are applied on the pile head, are given by Olgun and McCartney (2014):

- The application of 378kN does not result in a considerable reduction of pile heave, but the application of 1056kN mechanical loading results in an approximately 31% reduction of pile heave, showing the impact of mechanical loading as partial pile restraint.
- Similarly, the addition of mechanical loading does not result in significant changes to induced stress, and maximum induced stresses of 2.14, 2.22 and 2.44MPa are seen in TP1 to TP3 respectively.
- The location of the null point in TP2 and TP3 shifts upwards compared to TP1. This is mainly due to the existence of mechanical loading on the pile head. It is unlike the assumption used by Thermal Pile Standard (Ground Source Heat Pump Association, 2012) where the location of the null point under any type of loading condition is considered at the pile mid-depth.

Another in-situ study is done by Wang et al. (2013) on a bored thermal pile at Monash University campus in order to investigate the effects of thermo-mechanical loading on the capacity of a thermal pile. No groundwater is seen during the installation of the pile. The results by Wang et al. (2013) contradict the results by Laloui et al. (2006) and Bourne-Webb et al. (2009). Wang et al. (2013) state that the pile's shaft capacity increases up to 14% after heating, and returns to its initial state when the pile is cooled.

A comparison between described in-situ studies is provided in Table 2.4. Various soil profiles and pile properties are used in six listed studies. A summary of the main observations for in-situ studies are given below:

- The adopted framework by the Thermal Pile Standard (Ground Source Heat Pump Association, 2012) is mainly based on two in-situ studies done by Laloui et al. (2006) and Bourne-Webb et al. (2009). The main assumption in the framework is the location of the null point which is considered to be at the pile mid-depth. This is observed in the fully restrained condition by Laloui et al. (2006) and free-state condition by Bourne Webb et al. (2009). It is while the location of the null point is observed at the nominal depth of 0.78 from the pile head by Murphy and McCartney (2012) and Murphy et al. (2014) which is in contrast with the assumption of having the null point at the mid-depth. Also, it is seen by Sutman et al. (2015) that the location of the null point is located at the nominal depth of 0.65. It shows that further

investigation is required to determine the applicability of the assumption used by the Thermal Pile Standard for all soil and loading conditions. The effect of magnitude of mechanical loading on the location of the null point can only be determined with using different magnitudes of mechanical loading on the pile.

- The main shortcoming in the Lausanne test is that only the pile is tested for the heating period. Moreover, in both tests, there are limitations regarding the number of cyclic loadings, repetition in tests to validate the data, and testing the most extreme cases.
- In all above six studies, thermo-elastic behaviour of the thermal pile is reported based on the comparison between original and final strain levels. Small differences are neglected in their conclusion of the pile behaviour. However, permanent pile displacement is observed during heating-cooling cycles based on the magnitude of thermal loading and pile restraints.
- It is shown in all in-situ studies that additional stress is induced in the pile due to thermal loading. In Laloui et al. (2006) and Bourne Webb et al. (2009), it is observed that the magnitude of additional induced stress is approximately equal to the maximum allowable induced stress in the concrete which is 25% of the concrete compressive strength. Higher level of restraint on the pile and excessive temperature changes can result in passing this limit. Moreover, additional tensile force could cause additional stress in the pile resulting in cracks along the pile. Quantifying the amount of induced thermal stress will help to avoid passing the BS limits for compressive and tensile stresses.
- Various magnitudes of induced stress per degree change in the temperature is recorded in above in-situ studies. The maximum induced stress per degree change in the temperature in Laloui et al. (2006) is equal to 153kPa/°C for fully-restrained condition while this value is more than doubled in Bourne Webb et al. (2009). Values between 210kPa/°C and 285kPa/°C is recorded in other studies. The magnitude of induced stress per degree change in the pile temperature in the pile is mainly dependant on the restraint level on the pile or in other words DoF. It is only in Laloui et al. (2003) that DoF is quantified and lack of quantifying the DoF is seen in other studies. Using DoF along the pile in various soil and pile conditions will help the thermal pile designers to estimate the maximum induced stress on the pile. It shows the importance of knowledge on DoF values at various depths along the pile.
- All the piles used above for in-situ studies are base and shaft resisting piles. In practice, most of the piles are shaft and base resistant and it is difficult to determine what proportion of the load is carried by load or base. Unlike in-situ installations, it is possible to carry out both shaft-resisting tests and shaft and base resisting tests in the laboratory. It is crucial to determine the proportion of the load carried by shaft/base for thermal piles and subsequent provisions needs to be considered in the design.

- It is seen by Laloui et al. (2006) that due to the induced thermal loading, the factor of safety is reduced from 3 to 1. Similar reduction in factor of safety is seen in other in-situ studies caused by additional thermal loading. The reduction in safety factor is seen to be dependant on pile restraints and magnitude of thermal loading.

Table 2-4. A summary of findings from thermal pile in-situ studies (Adopted from Olgun and McCartney, 2014)

Reference	Soil profile	Pile properties	Temp. variations (°C)	Mechanical load (kN)	Null point location	$\Delta\sigma/\Delta T$ (kPa/°C)	Pile displacement (mm)
Laloui et al. (2003; 2006)	0.0–5.5m Very soft alluvial clay 5.5–12m Very soft alluvial clay 12.0–21.7m Loose sandy and gravelly moraine 21.7–25.3m Stiff ‘bottom moraine’ >25.3m Sandstone Soil initial temp. =10°C	D=880mm L=25.8m E=29.2GPa $\alpha=10(\mu\epsilon/^\circ\text{C})$	T1: +20.9 T7: +18.0	1300	T1: 0.83 T7: 0.48	T1: 104 T7: 153	T1: -4.2
Amis et al. (2008), Bourne-Webb et al. (2009)	0.0–1.5m Made ground (granular) 1.5–4.0m Sand and gravel >4.0m Stiff, silty clay Soil initial temp. =18°C	D=600mm L=23m and 30m E=40GPa $\alpha=8.5(\mu\epsilon/^\circ\text{C})$	Free: +29.4 Restrained: -19.0 to +10.0	1350	Free: 0.57 Restrained: 0.26	Free: 192 Restrained: -177 to +329	Restrained: +4.0 to -2.0
Murphy and McCartney (2012)	0.0–3.0m Fill 3.0–7.6m Sand and Gravel >7.6m Claystone Soil initial temp. =9–10°C	D=910mm L=14.8m and 13.4m E=30GPa $\alpha=10(\mu\epsilon/^\circ\text{C})$	-5.0 to 14.0	3840 3640	0.78	285	+0.4 to -0.8
Wang et al. (2013)	<3m Clayey fill >3m Fine to coarse, very dense clayey sand and sand Soil initial temp. =17–18°C	D=600mm L=16.1m $\alpha=10(\mu\epsilon/^\circ\text{C})$	0.0 to 25.0	1885	Approx. 0.4	N/A	Upper section – Short-term heating: -4.5 Long-term heating: -10.5
Murphy et al. (2014)	0–1m Sandy fill with silt and gravel 1–2m Dense sand, silt, gravel 2–12+ Sandstone	D=610mm L=26.3m E=30GPa $\alpha=12(\mu\epsilon/^\circ\text{C})$	18.0 to 19.0	833	0.78	210 to 268	-1.4 to -1.7
Sutman et al. (2015)	~0.0–5.0m Silty clay ~5.0–6.0m Silty sand ~6.0–8.2m Silty clay ~8.2–9.8m Sandy clay ~9.8–15.0m Sand	D=460mm L=15.2m, 9.1m, 15.2m E=36GPa	-6.0 to +8.8	TP1: 0 TP2: 378 TP3: 1056	0.65	TP1: -271 to 214 TP2 and TP3: -213 to +244	TP1: -5.8 to +2.5 TP2: -6.1 to +1.8 TP3: -4.0 to +1.8

2.4.2 Physical 1g models

The data provided by in-situ studies offer good insight into the behaviour of thermal piles, but there are limitations for these full-scale studies, such as no precise control over boundaries and limits regarding critical testing where thermal or mechanical loads could be taken to the ultimate stage. A few small-scale laboratory studies are available in the literature, and a summary of their findings is presented below.

Wang et al. (2011; 2012) investigate variations in shaft resistance before and after thermal loading using a laboratory model (see Table 2.5). To study only the shaft resistance, mechanical loading is applied upwards from the bottom of the pile. Temperature variations are 20°C to 40°C to 20°C in Wang et al. (2011; 2012) and 20°C to 60°C to 20°C in Wang et al. (2012). The first soil tested is fine silica sand: N50 fine sand, with moisture content of 0%, 2% and 4%. The second soil tested is 300WQ Silica flour with moisture content of 21.5% and 24% (see Table 2.5). Pre-heat load-unload cycles are applied to reach the peak residual shaft load resistance, and post-heat load-unload cycles are applied to investigate changes after thermal loading. Mechanical loads are applied with different durations, as presented below:

- Pre-heat load-unload cycles are applied for around one hour.
- Thermal loading is applied for approximately 24 hours for each sample.
- Post-heat load-unload cycles are applied for around 45 minutes.

It is found that:

- After thermal loading, shaft resistance for silica sand with $w=0.5\%$ is reduced by 60%. For the 300WQ Silica flour samples, 10% and 50% reductions are seen for $w=21.5\%$ and $w=24\%$ respectively.
- Unlike the studies above, Wang et al. (2012) show that there is no change in the maximum shaft resistance for $w=0\%$, while there is a reduction of shaft resistance for $w=2\%$ and $w=4\%$.
- Wang et al. (2012) investigate the effect of the magnitude of temperature change on the shaft friction for N50 sand with 2% moisture content. Three different samples are left at three different temperatures of 20°C, 40°C and 60°C for 24 hours. It is seen that higher thermal loading results in greater reduction in shaft friction, as well as sharper drops in moisture content.
- Tests on the samples with 4% moisture content are performed by Wang et al. (2012) and no significant change in friction resistance is seen compared to samples with $w=2\%$.
- In another test by Wang et al. (2012), a single sample with 2% moisture content is subjected to both heating and cooling cycles. It is seen that, although shaft resistance is significantly reduced during the heating process, it is partially recovered after the cooling process such that it is close to the initial peak values.

Another laboratory study was carried out by Kalantidou et al. (2012). Compared to Wang et al. (2011; 2012), the pile in this study is smaller in diameter but more than three times bigger in length. Similarly, both model piles are closed-ended. The model pile used by Wang et al. (2011; 2012) is a shaft resisting pile and is made of stainless steel, while Kalantidou et al.'s (2012) model pile has shaft and base resistance and is made of aluminium with a lower thermal expansion coefficient than stainless steel. Soil used in this study is dry Fontainebleau sand (see Table 2.5). Unlike Wang et al. (2011; 2012), mechanical loading is applied using dead weights on top of the pile. These weights range between 0N and 500N. Mechanical loading is applied through the progressive loading technique in Wang et al. (2011; 2012), while dead weights are used by Kalantidou et al. (2012), which is a better presentation of the working load mechanism applied on a pile due to the building's weight. Four tests are designed with different axial mechanical loads – in the order of 0N, 200N, 400N and 500N – with an ultimate bearing capacity of 525N. This means that mechanical loads are 0%, 38%, 76% and 95% of the ultimate capacity. Applied temperature for the heating-cooling cycle is 25°C to 50°C to 25°C. Two thermal cycles are applied for each test. The results are summarised as follows:

- The thermo-elastic behaviour of the model pile is observed under heating-cooling cycles for mechanical loading up to approximately 40% of the ultimate resistance. For this mechanical loading, the pile head settlement remains below 1% of the pile diameter.
- For mechanical loading higher than 40% of the ultimate capacity, additional settlement is seen due to thermal loading as a result of additional induced load in the model pile. This results in larger displacement at the pile toe and causes irreversible strain.
- Creep behaviour is seen during the second thermal cycle of all tests, where the pile settlement curve lies below the first cycle. It is also expected that further settlements will be seen in forthcoming cycles.

Another similar study is done by Tang et al. (2013), with minor modifications to Kalantidou et al.'s (2012) experiment set-up. The main difference is the loading mechanism, where progressive loading is adapted using a water tank. The results are as follows:

- Despite having different loading mechanism, similar results are found in this study as those reported by Kalantidou et al. (2012).
- Additionally, it is found that heating-cooling cycles result in an increase in the axial forces along the pile. The axial force profile for the model pile under a 200N constant load on the pile head is shown in Figure 2.12-a.

- Minimum increase in the axial force is seen during the first heating period. The location of the maximum axial force during both heating periods is at the normalised depth of 0.16 from the pile surface. It shifts to mid-depth of the pile during both cooling periods.
- The maximum axial force under combined thermo-mechanical loading with a constant load of 200N is equal to approximately 270N, which shows a 35% increase in the magnitude of the maximum axial load compared to mechanical-only loading.
- The maximum mobilised friction along the pile surface under mechanical loading is seen close to the pile bottom. Under thermo-mechanical loading, a significant change in the mobilised friction is seen, where the direction of the mobilised friction in the upper half of the pile changes. Moreover, the direction of the mobilised friction changes during the cooling and heating periods (see Figure 2.12-b).
- The maximum mobilised friction in Zone 4 at the bottom of the pile under thermo-mechanical loading is three times higher than the maximum friction under a constant mechanical load of 200N alone.

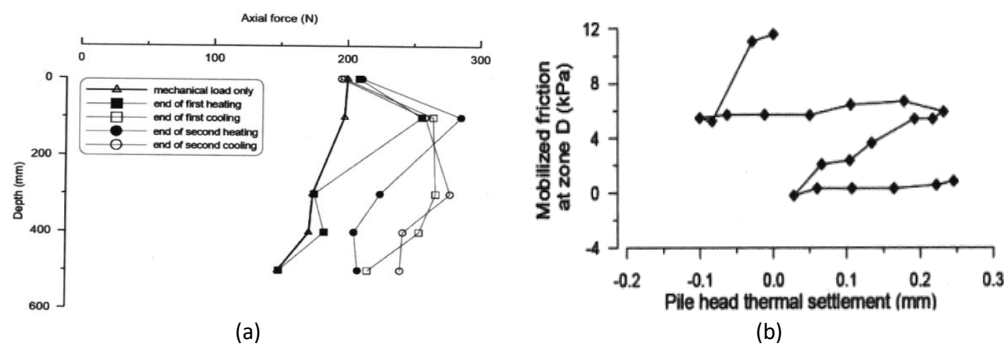


Figure 2-12. (a) Axial load profile for two heating-cooling cycles under a constant load of 200N, (b) mobilised shaft friction along the pile under thermal loading (Tang et al., 2013) (*Permission to reproduce this has been granted by John Wiley and Sons*)

Another laboratory model is provided by Kramer and Basu (2014), where a precast 100mm concrete pile is embedded in standard F50 Ottawa sand (known as fine silica sand) with the properties given in Table 2.5. The thermal performance of the model pile under a heating load of $\Delta T = +21^\circ\text{C}$ for seven days is investigated. Mechanical loading tests are performed before and after thermal loading, and it is found that:

- Pile thermal expansion is close to free-state expansion. This shows very limited restraint caused by the surrounding soil and the pile head.
- A small increase, less than 10%, in the pile capacity is seen with heating. The pile head stiffness also decreases after the heating period. This is similar to the findings by McCartney and Rosenberg (2011), but contradicts the findings by Wang et al. (2011; 2012).

- Assuming the negligible effect of thermal loading on the sand's properties, the main reason for an increase in the pile capacity is believed to be the partial restraint of pile movement during thermal loading.

The main focus of laboratory studies mentioned above is to determine the changes in the pile bearing capacity under combined thermal and mechanical loading. Piles are basically designed to carry the load of the structure to the ground and additional loading will be applied to the pile during heating-cooling cycles. Understanding the changes on the bearing capacity of thermal piles is one of the most important factors for a thermal pile designer. A contrast is seen in the laboratory and centrifuge studies. Decrease in the side shear resistance is reported by Wang et al. (2011; 2012) while no change is seen in the pile ultimate capacity by Goode et al. (2014). Unlike mentioned studies, an increase in the side shear resistance is seen by Tang et al. (2013), McCartney & Rosenberg (2011) and Ng et al. (2015). It is while in all studies, except McCartney & Rosenberg (2011), sand with relatively similar properties with small differences in the compaction ratio and moisture content are used. Also, most of the piles used in the laboratory studies are base and shaft resisting piles whereas the model pile used by Wang et al. (2011; 2012) is a shaft resisting pile which has seen a reduction in the side shear resistance with heating. In five 1g physical models given in Table 2.5, in two tests the pile is made of stainless steel, in two tests made of aluminium and in one test the pile is made of precast concrete. The model pile made of precast concrete (Kramer & Basu, 2014) has seen an increase in the pile capacity while reduction/no change in the piles made of stainless steel and aluminium is observed.

In the laboratory studies given in Table 2.5, comparison between their results and the proposed framework by the Thermal Pile Standards is not covered which will be considered in this study. Also, considerable variations in the mobilised friction is observed where it is seen that under thermal loading the maximum mobilised friction reaches three times higher than the maximum friction under a constant mechanical load of 200N (Tang et al. (2013)). It is a huge change in the mobilised shaft friction that needs to be studied under different loading conditions and compared with mechanical loading only state. Other aspects of thermo-mechanical behaviour of thermal piles such as induced stress under thermal loading is only covered by (Tang et al. (2013) and lack of sufficient data to determine the pile response under thermal loading is apparent.

2.4.3 Centrifuge models

In addition to laboratory models, centrifuge modelling has also been used to investigate the thermo-mechanical behaviour of thermal piles. A centrifuge model is developed by McCartney and Rosenberg (2011) using a precast concrete model pile embedded in compacted silt (see Table 2.5). The pile is heated from 15°C to 50°C and 60°C. The semi-floating pile, with its top free and its bottom laid on the silt bed, is used to understand the effect of thermal loading on the ultimate

resistance of the pile. The pile is loaded mechanically after thermal loading and then compared with the initial mechanical loading results before thermal loading. It is found that the side shear resistance increases by 40% when the pile is heated from 15°C to 60°C. This method of determining the ultimate capacity of the pile does not represent the real working condition of a thermal pile, where mechanical loading is constant on the pile head.

Another centrifuge test is done by Goode et al. (2014) using a precast concrete model pile embedded in dry Nevada sand (see Table 2.5). Similar to McCartney and Rosenberg (2011), a semi-floating pile – with the same loading order and smaller magnitudes of thermal loading equal to $\Delta T = +7, +12$ and $+18^\circ\text{C}$ – is tested. It is seen that:

- The ultimate pile capacity is not sensitive to temperature, unlike in McCartney and Rosenberg's (2011) results. This could be mainly due to the differences in the soil types.
- The strain profiles in all tests seem to be relatively linear and close to the free-state strain. This means that the sand offers low-level restraint.
- The minimum induced axial stress is seen at the pile head, while the maximum induced stress is seen just below the mid-depth of the pile.
- It is seen that an increase in the temperature does not result in a notable change in the location of the null point.
- The findings are different from McCartney and Rosenberg (2011): in the dry Nevada sand, the shear strength is expected to increase with depth, while in unsaturated silt, uniform shear strength with depth is observed.

In another centrifuge model by Ng et al. (2015), an aluminium model pile is tested in medium-dense, saturated sand. Tests with three temperatures of 22°C, 37°C and 52°C are performed, and it is found that the pile capacity increases by 13% and 30% under the respective temperature increments of 15°C and 30°C. Moreover, the null point is initially at the mid-depth of the pile, but moves downwards with an increase in temperature.

Similar to 1g models, a contrast between the findings in centrifuge modelling is also observed. An increase in the side shear resistance is seen with an increase in the pile temperature by McCartney & Rosenberg (2011) and Ng et al. (2015) while no change in the ultimate capacity with heating is observed by Goode et al. (2014). Relevance of material type to the pile response cannot be recognised as precast concrete is used in both McCartney & Rosenberg (2011) and Goode et al. (2014) but different responses are observed. In Goode et al. (2014), the maximum temperature increase has reached up to 18°C whereas in McCartney & Rosenberg (2011) the pile has experienced temperature increase of 41°C. It means that in the studies with similar pile material, the pile which is heated up to 41°C has seen an increase in the mobilised shaft friction

while the pile which is heated up to only 18°C above the room temperature has not experienced any change in the side friction. Also, in terms of the soil type, Bonny silt-compacted soil with water content of 13.2% is used in McCartney & Rosenberg (2011) while Dry Nevada sand with relative density of 60% is used by Goode et al. It means that increase in the side shear resistance is seen in the study where silty soil with higher temperature changes are used and no change in the study carried out on sand with lower values of change in the pile temperature. Similar to 1g studies, most of the focus on the centrifuge studies are on variations in the side shear resistance under thermal loading and less attention is given on other aspects of thermal pile response that highlights the lack of sufficient 1g and centrifuge studies on the behaviour of thermal piles.

Table 2-5. A summary of findings from thermal pile physical models (Adopted from Olgun and McCartney, 2014)

Reference	Gravity level	Soil profile	Pile properties	Temp. Variations (°C)	Findings
Wang et al. (2011)	1g	N50 fine sand $w=0.5\%$	Stainless steel tube D=25.4 mm t=1.2 mm	20	60% decrease in side shear resistance with heating
		300WQ Silica flour $w=21.5\%$ & 24%			10% and 50% decrease in side shear resistance with heating for $w=21.5\%$ and 24% respectively
Wang et al. (2012)	1g	N50 fine sand $w=0, 2$ and 4%	Stainless steel tube D=25.4 mm t=1.2 mm	20 & 40	$w=0\%$: no change in side shear resistance $w=2\%$ & 4%: reduction in side shear resistance
Kalantidou et al. (2012)	1g	Dry Fontainebleau sand $D_{50}=0.23\text{mm}$ $D_r=46\%$	Aluminium tube L=800mm D=20 mm t=2 mm	± 25	Irreversible settlement for mechanical loading higher than 40% of ultimate pile capacity
Tang et al. (2013)	1g	Dry Fontainebleau sand $D_{50}=0.23\text{mm}$ $D_r=46\%$	Aluminium tube L=800mm D=20 mm t=2 mm	± 25	Significant change in the mobilised friction with changes in the direction of mobilised friction
Kramer & Basu (2014)	1g	F50 Ottawa sand $D_{50}=0.28\text{mm}$ $D_r=75\%$	Precast concrete D=100 mm L=1.22 m	20	Less than 10% increase in pile capacity with heating
McCartney and Rosenberg (2011)	24g	Bonny silt- compacted $w =13.2\%$ $\phi' =32^\circ$	Precast concrete D=76.2 mm (1.8 m) L=381 mm (9.1 m)	29 & 41	40% increase in side shear resistance with heating
Goode et al. (2014)	24g	Dry Nevada sand $D_r=60\%$ $D_{60}=0.16\text{mm}$	Precast concrete D=63.5 mm (1.5 m) L=342.9 mm (8.2 m)	7 & 12 & 18	No change in ultimate capacity with heating
Ng et al. (2015)	40g	Saturated Toyoura sand $D_{50}=0.17\text{mm}$ $D_r=67\%$ to 89%	Aluminium tube D=22 mm (0.88m) L=600 mm (24 m)	15 & 30	13% and 30% increase in pile capacity with $\Delta T=15$ and 30°C respectively

2.4.4 Numerical modelling

In addition to in-situ installations and physical models, numerical modelling is also used in the literature to assess the thermo-mechanical behaviour of thermal piles. A single vertical thermal pile is modelled by Laloui et al. (2006) and Laloui and Nuth (2009) using the thermo-hydro-mechanical finite element method. The pile length in the numerical model is 26m and the diameter is 0.5m, with the same soil profile as the in-situ profile given by Laloui et al. (2006) (see Table 2.4). Thermal loading consists of 12 days of heating and 16 days of cooling. The heating period consists of heating up to nearly 3°C for five days, and then a temperature increase of 21°C is applied to the pile for seven days. During the cooling process, the pile is initially cooled by around 10°C for three days, and then cooling is continued at a slower rate for another 13 days by less than 10°C. Two end-bearing conditions are applied to the pile:

- Case 1: Thermal-only, where the pile head is free to move with no mechanical loading.
- Case 2: Thermal and mechanical loading (structure weight) as partial restraint.

It is found that:

- Uniform temperature change is seen along the pile (unlike Laloui et al.'s (2006) study, which observes variations of temperature along the pile length for in-situ installations).
- A non-uniform thermal strain profile is achieved during a heating period, where maximum strain is seen at the pile head and minimum strain is seen at the normalised depth of 0.77 (see Figure 2.13-a). The main reason for the difference between the strain profiles of in-situ and numerical models could be the numerical model's overestimation of friction at the bottom of the pile.
- It is seen that the pile toe carries a large amount of induced stress, unlike in the mechanical-only loading case. It is in line with the observations made by Laloui et al. (2006) and Bourne-Webb et al. (2009).
- The maximum induced stress from mechanical loading is equal to approximately -1.3MPa at the pile head and nearly zero at the pile tip. For $\Delta T=13.4^\circ\text{C}$ increase in temperature, it is seen that the maximum induced stress occurs at the normalised depth of 0.83 and is equal to approximately -2.3MPa. The overall stress increases from -1.3MPa under the mechanical-only condition to -2.6MPa under thermo-mechanical loading, which means that thermal loading doubles the induced stress. The maximum induced stress under thermo-mechanical loading in the numerical model is approximately 70% of that obtained by Laloui et al. (2006) in the in-situ results. This shows an underestimation of the maximum stress by the numerical model (see Figure 2.13-b).

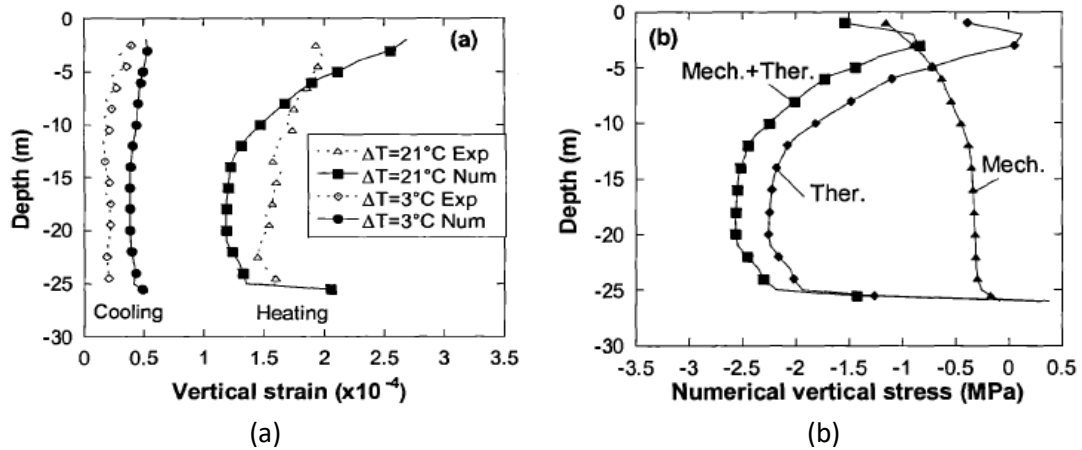


Figure 2-13. (a) Axial thermal strain along the pile during heating and cooling periods for numerical and in-situ installations, (b) additional induced thermal stress in the pile (Laloui and Nuth, 2009) (*Permission to reproduce this has been granted by Prof.Laloui*)

Another numerical model is developed by Knellwolf et al. (2011) to assess the effects caused by temperature changes in pile behaviour. The method is validated using in-situ data provided by Laloui et al. (2003; 2006) and Bourne-Webb et al. (2009). Assumptions and the methodology are described in Knellwolf et al. (2011). The measured strain values obtained through this technique show small errors compared to the in-situ data presented by Laloui et al. (2003; 2006). This model shows that an increase in the pile temperature will induce additional compressive force in the pile, and will also increase mobilised shear stress. Moreover, cooling will result in the development of tensile stress in the pile and in the partial or complete release of mobilised shaft friction.

Another numerical model is developed by Suryatriyastuti et al. (2012) using the finite difference method (FDM) to study the effects of the contact surface between the pile and the soil on the mechanical behaviour of thermal piles. Two possible contact surfaces are considered: (a) perfect contact and (b) sliding. The methodology used in this model is based on the simulation of a thermal pile under static thermal loading in different seasons, assuming that the pile is free to move at both ends. Results are summarised as follows:

- The temperature-induced behaviour of thermal piles is strongly related to contact conditions between the pile and soil. It is seen that there is a higher magnitude of stress and displacement for perfect contact surfaces compared to sliding surfaces.
- For single-mode operations, a slight effect on the mechanical behaviour of the thermal pile is seen due to thermal loading, but for seasonal performed systems where the annual thermal loads are applied in cycles, the effects are remarkable.
- The null point is seen in the middle of the pile. This could be mainly due to the assumption of homogenous soil, which is impossible to achieve in in-situ and laboratory studies. It is in

line with the assumption used in the Thermal Pile Standard where the null point location under all end restraint conditions is considered at the mid-depth of the pile.

- Model pile behaviour is compared with the results published for in-situ tests at the Lambeth College and at Lausanne. The same trend is seen with regard to mobilised friction along the pile, while the end-bearing conditions are different.

Another numerical study is done by Suryatriyastuti et al. (2015) on the behaviour of a single thermal pile, as well as on the behaviour of a single thermal pile in a group of thermal piles. For a single pile under 12 heating-cooling cycles, which represents 12 years of thermal pile operation, it is found that:

- The pile capacity degrades under repetitive stress reversals. It is while only 12 cycles are modelled in this study and a typical thermal pile will experience more cycles which can lead to further degrade in the pile capacity.
- The state of the soil after mechanical loading considerably affects the results from the thermal cyclic loading.
- After the heating period and due to expansion, the bearing stress increases due to the movement of the pile towards the pile base. On the other hand, there is a reduction in the bearing stress due to cooling, as there are contractions and the base moves upward. Similarly, Mimouni (2014) states that, for contraction, the contact between the pile base and soil may be broken and this will result in significant pile displacement.
- Regarding pile head settlement, in situations where there is only mechanical loading on the pile head and thermal cycles are applied, a higher magnitude of settlement is seen compared to heaves during cooling, accounting for -5% and +30% respectively.
- No pile heave is seen in the fifth cycle (see Figure 2.14) and only settlement is observed during both heating and cooling periods. This is an unsatisfactory finding in terms of thermal pile design, as pile heave could partially recover the settlements caused during the cooling periods.
- After five cycles, strain ratcheting occurs due to the softening of soil–pile resistance.
- At the end of all 12 cycles, the magnitude of the pile head settlement is 29% more than it was before the heating-cooling cycles. After 12 cycles, there is an average increase of 2.41% in this pile head settlement compared to the mechanical settlement.
- The rate of settlement from the second cycle onwards seems to be quicker than what is suggested by Lee (2004) for cyclic loading.

None of the above numerical studies has focused on the framework given by the Thermal Pile Standards (GSHPA, 2012). It is shown by Suryatriyastuti et al. (2015) that after 5 cycles, pile heave completely disappears and only pile settlement is observed. This can become a significant

problem for a thermal pile with a long lifetime period that will experience at least 1 cycle of heating and cooling each year. Also, it is shown in all numerical studies above that the pile toe will carry a significant amount of thermal loading unlike the condition where the pile is only under mechanical loading. Considerable cyclic degradation of pile capacity is mentioned by Suryatriyastuti et al. (2015) unlike the numerical model developed by Laloui et al. (2006). In none of the studies given above the effect of magnitude of mechanical loading on overall thermal pile behaviour is observed. Also, none of them have determined the pile behaviour with respect to the proposed framework by Bourne Webb et al. (2013).

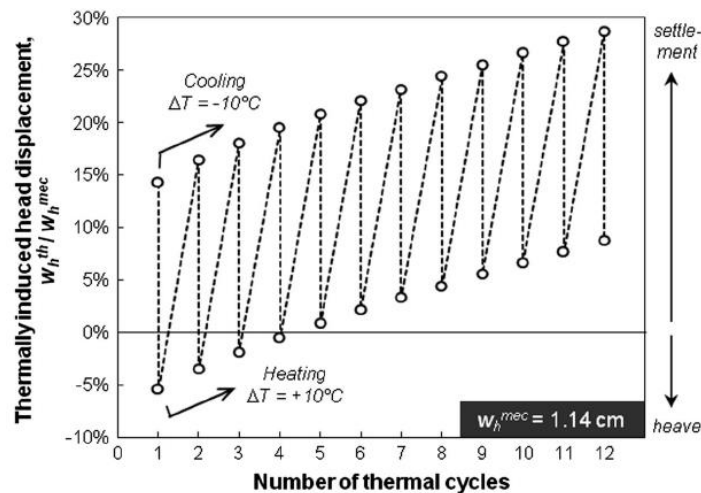


Figure 2-14. Thermally induced pile head displacement at constant load (Suryatriyastuti et al., 2015) (Permission to reproduce this has been granted by John Wiley and Sons)

2.5 Thermodynamic aspects of thermal piles

2.5.1 Heat transfer in thermal piles

Understanding the heat transfer process in thermal piles and the surrounding soil will help to better understand the behaviour of thermal piles under thermal loading. A brief description of heat transfer in the thermal pile is given here. This is followed by a description of the capability of thermal piles to provide required heat demand, and design aspects are considered.

Heat transfer analysis in thermal piles is usually based on methods used for the heat transfer analysis of boreholes, comprehensively provided by Ghasemi-Fare and Basu (2013). Despite the widespread use of this technique, Loveridge and Powrie (2013) state that the analysis of heat transfer in thermal piles has more complexities than a heat analysis of single or double U-shaped vertical boreholes. Heat transfer in a thermal pile system is a combination of steady and transient states. Heat transfer inside the thermal pile is considered as steady-state, and the transient state governs the heat transfer between the pile and the surrounding soil (see Figure 2.15). In general, heat transfer in a thermal pile system is categorised into three phases:

- Convection at the pipe-fluid boundary.
- Steady conduction through heat transfer pipes and the pile's concrete.
- Transient conduction through soils.

Convection is the first heating process that occurs between the fluid inside the pipes and the pipe walls. The governing equation is Newton's law of cooling (see Equation 2.13):

$$\frac{Q}{A} = h(T_{pi} - T_f) \quad (2.13)$$

Where:

Q/A : Rate of heat transfer per unit area (W/m^2)

h : Heat transfer coefficient ($W/m^2 \cdot K$)

T_f : Fluid temperature

T_{pi} : Inner pipe wall temperature

In soils, heat is transferred through porous media via different mechanisms, including convection, conduction, radiation and heat transfer due to water phase change (which is called the latent heat of vaporisation) (Rees et al., 2000). The equation for total heat transfer in the soil is formulated by Rees et al. (2000):

$$q_{soil} = q_{cond} + q_{conv} + q_{lat} \quad (2.14)$$

Radiation has the least effect and it is usually neglected. Moreover, it is assumed that the soil has a solid, dry structure in this study and convection does not exist. In this study, due to the absence of groundwater flow, conduction is considered the main heating transfer mechanism. The theory of heat transfer through conduction was established by Fourier and it states that the rate of heat flow (Q_x) is proportional to the thermal conductivity of the material (λ), area of the flow (A) and the temperature gradient in the direction of the flow (dT/dx):

$$Q_x = -\lambda A \frac{dT}{dx} \quad (2.15)$$

Brandl (2006) states that thermal conductivity is the most important thermal soil parameter to consider in the design of a thermal pile system. Additionally, specific heat capacity, S_c , is also considered an important parameter to determine the thermal behaviour of soil. Specific heat capacity is defined as the medium's (i.e. solid, liquid or gas) ability to store heat (Banks, 2008). In other word, it is the amount of heat locked in the medium for every degree Kelvin of temperature. It is shown by Hamdhan and Clarke (2010) that dry sand has a high value for heat capacity – around 800J/K. Kg – but does not have high thermal conductivity values. This means that a large amount of heat can be stored in sand but not easily transferred.

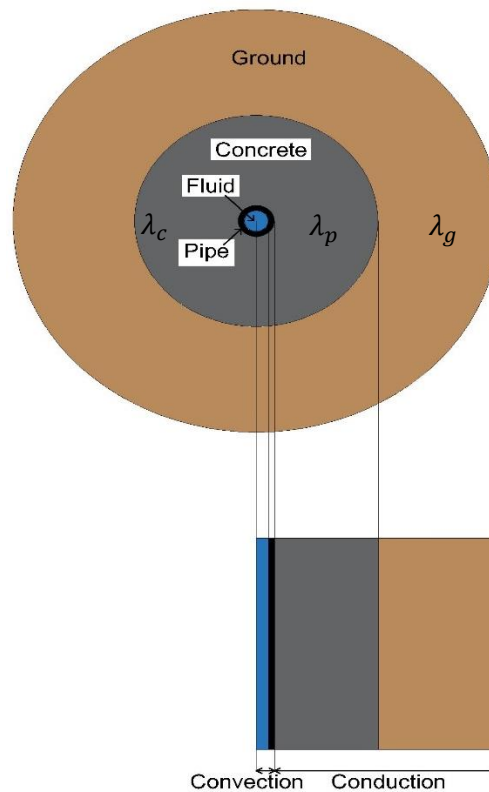


Figure 2-15. Heat transfer procedures in a thermal pile system (Adopted from Loveridge and Powrie, 2013)
(Permission to reproduce this has been granted by ICE Publishing)

2.5.2 Thermal capacity of thermal piles

At the early stages of thermal pile development, there were concerns over the capability of thermal piles to carry the required thermal load of a building. A very early in-situ investigation was done by Morino and Oka (1994) on a thermal pile made of steel to measure the quantity of heat exchanged between the carrier fluid and the soil in the short-term. A steel thermal pile with the length of 20m and a diameter of 400mm is chosen. The piping material is polyvinyl chloride (PVC) with a 25mm diameter for water circulation. It is found that the amount of heat collected from the soil by the fluid in the pile is three times larger in the short-term operation compared to the long-term operation, but the collected heat is sufficient to support the building's thermal needs. Another study is done by Sekine et al. (2006) on a cast-in-place concrete pile using U-shaped pipes, and it is found that the coefficient of performance of the system is 4.89 in the cooling mode, which is 1.7 times larger than a typical air source heat pump system. Moreover, the effect of temperature variations of the ground on the efficiency of heat pumps for thermal piles is studied by Wood et al. (2009). The study is based on the heating-only operation mode in winter for a residential building, and the results are found to be satisfactory, with the Seasonal Performance Factor (SPF) of the heat pump at approximately 3.62. It is mentioned that the SPF has not changed significantly during the entire operation period. The capability of thermal piles to provide sufficient thermal loading seems to be mainly dependent on the thermal load of the building and

how the thermal piles are utilised to benefit from ground energy. If it is not possible to provide for the entire heating demand from thermal piles alone, a combination of thermal piles with other renewable or conventional systems could be used.

2.5.3 Design aspects of thermal piles

Different analytical, numerical and in-situ studies have been done on the design parameters needed in the early stages of thermal pile design, including the selection of pipe and fluid material, as well as the number, dimensions and arrangement of pipes. The aim is to increase the efficiency of thermal piles by applying efficient design parameters.

2.5.3.1 *Material selection*

To benefit to the maximum from concrete's high thermal storage capacity, high-density polyethylene (HDPE) plastic pipes are used to carry fluid. Regarding the material for thermal piles, most of the in-situ studies on thermal piles use concrete thermal piles and only a few use steel thermal piles (Jalaluddin et al., 2011; Morino and Oka, 1994; Lennon et al., 2009). The thermal performance of thermal piles with regard to concrete's constituent materials is investigated by Patel and Bull (2011). In this laboratory study, a 150x150x150mm concrete cube is cast, and a U-shaped copper pipe is inserted into it. Three different concrete mixes using cement-replacing materials are tested. The best thermal performance is achieved when ordinary Portland cement with 30% pulverised fuel ash is used.

2.5.3.2 *Fluid selection*

Water is the cheapest and most widely available option but, in winter, due to the possibility of freezing, antifreeze must be added. For this, water-based antifreeze solutions are the best choice. The most appropriate option is a fluid with a small coefficient of expansion, low viscosity, high thermal capacity, low freezing point, high boiling point, not flammable preferably and non-toxic in cases of pipe leakage. In the study done by Patel and Bull (2011), three circulating liquids are examined:

- A. Water only
- B. Water and 50% ethylene glycol
- C. Water and 3.5% saline solution

It is found that water with 50% ethylene glycol is the best choice regarding thermal properties, which means that it can absorb increased heat in the shortest time. Water having a saline solution and water only come in second place and third place respectively. It is stated by Banks (2008) that using carrier fluids with a freezing point between -10°C and -20°C is acceptable. Changing the concentration level of antifreeze can adjust the freezing point to meet the required climatic conditions of where the pipe is installed. It is stated by Brandl (2006) that the glycol-water mixture has proved to be the most suitable medium used in pipes due to the additives inside the fluid, which help to prevent the corrosion in the header blocks of the valves or the heat pump.

2.5.3.3 Pipe configuration

The most common type of pipe configuration is the U-shaped thermal pile with HDPE as piping material. A full-scale in-situ study on a steel thermal pile is done by Jalaluddin et al. (2011) in order to investigate the thermal performance of thermal piles with different pipe configurations. A 20m steel pile is installed in soil consisting of clay from 0m to 15m and sandy clay from 15m to 20m with varying water content of 30% to 150%. Pipe flow rates of 2, 4, and 8 l/min are tested in addition to double-tube, U-tube and multi-tube pipe configurations. It is found that:

- The heat exchange rate is the highest in the double-tube configuration, followed by multi-tubes.
- Increasing the flow rate increases the heat exchange rate of thermal piles. In high flow rates, the application of multi-tube and double-tube is more highly recommended.

In study by Gao et al. (2008), different pipe configurations and fluid flow rates are examined to find the most efficient one (see Figure 2.16). Using both numerical predictions and in-situ results, the W-shaped pipe with moderate flow rate is shown to be the most efficient set-up.

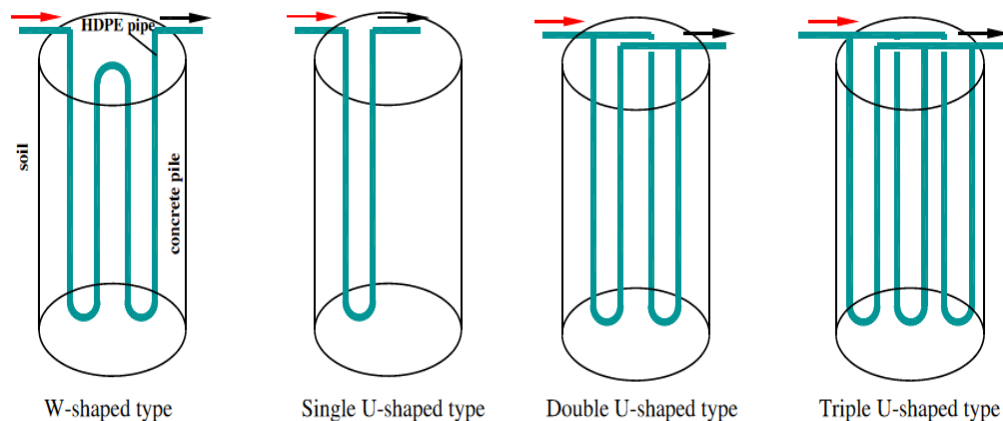


Figure 2-16. Different pipe configurations used by Gao et al. (2008) (*Permission to reproduce this has been granted by Elsevier*)

In addition to the above-mentioned configurations, it is suggested by Lee et al. (2013) that the coil-type heat exchanger will improve the efficiency of thermal piles by increasing the heat transfer surface between the pipes and the pile (see Figure 2.17). It is found that the efficiency of the system in the cooling mode ranges from 3.9 to 4.3, which is close to, but less than, that of the vertical borehole system.

Another construction aspect of thermal piles is studied by Lee and Lam (2013), who investigate the order and spacing of pipe connections in thermal piles with multiple pipe connections. A simplified 3D numerical model is developed using the FDM. It is found that the most efficient

model regarding thermal performance is when the pipes are connected consecutively in series with equal spacing between them.



Figure 2-17. (a) Installation of coil-shaped polybutylene pipes in a thermal pile (Lee et al., 2013), (b) schematic view of a thermal pile with coils (Man et al., 2010) (Permission to reproduce this has been granted by Elsevier)

2.6 Summary of the literature review

In the first part of the literature, an introduction and a background is given to GSHP technology and the thermal pile system:

- The UK's 2020 target is to supply 12% of the heat demand through renewable sources. In 2015, only 5.6% of heating and cooling were produced by renewable sources (Department for Business, Energy & Industrial Strategy, 2016).
- The GSHP system is considered an efficient system because the temperature in the ground remains relatively constant below the topsoil. A thermal pile is a type of closed-loop GSHP system that utilises the stored energy in the ground for existing building foundations.

This background is followed by a theoretical background on the possible behaviour of thermal piles under seasonal temperature variations. Moreover, the proposed qualitative framework by Bourne-Webb et al. (2013) is presented and will be used in Chapter 3 to develop the programme for laboratory tests.

Previous work carried out on thermal piles is divided into two main parts:

- Part 1: Thermo-mechanical performance of thermal piles.
- Part 2: Thermodynamic aspects of thermal piles.

In Part 1, the effects of combined thermo-mechanical loading on thermal piles are investigated. A summary of findings is listed below:

- Thermo-mechanical loading includes additional stresses and strains inside the pile, as well as mobilised shaft friction, which affects soil properties, the pile structure (due to increased axial

load and stress on the pile), and the soil–pile interface. Additional stresses and strains can potentially reduce the safety margin of the conventional pile design, which does not consider thermal loading. This can cause undesirable consequences, including additional building settlement, a significant increase in the compressive stresses and the mobilisation of shaft resistance to limits close to ultimate resistance.

- Thermal loading is more uniformly distributed along the pile surface compared to mechanical loading, where maximum loading is applied on the pile head and reduced towards the pile toe (which is expected to carry a null load under mechanical loading). Moreover, it is seen that the magnitude of thermal loading could be larger than mechanical loading (Laloui et al., 2006).
- The pile toe carries the least load under mechanical loading, but a considerable load is applied to the pile toe under thermal loading. This needs to be considered in the design.
- In the models used to develop the proposed framework, due to the limitations in each test (such as testing only one soil profile, providing mechanical loadings well below the ultimate state, and a lack of control over the boundary conditions), there is a need to assess the applicability of the models in a more controlled environment, such as laboratory.
- In-situ studies by Bourne-Webb et al. (2009) and Laloui et al. (2006) confirm that the magnitude of detrimental effects caused by additional thermal loading on the pile is a function of the pile’s characteristics, the amount of changes in the thermal load per unit degree increase in temperature, and the level of restraint applied to the pile ends and by the soil. Both studies find that the response of the thermal pile to temperature changes is thermo-elastic.
- It is suggested by Bourne-Webb et al. (2013) that controlled physical experiments to examine the effects of end restraint and varying shaft resistance are required to bound the behaviours and confirm the recently developed descriptive framework.
- Thermal piles undergo seasonal heating-cooling cycles, and the pile is assumed to experience cyclic compressive and tensile forces. So-called two-way cyclic loading could result in the degradation of skin friction (Poulos, 1989). The assumption of considering two-way cyclic loading for thermal piles will be assessed in this study.

In Part 2, the heat transfer procedure in thermal piles is described, and the initial design parameters for thermal capacity of the thermal piles are reviewed. It is found that:

- The dominant heat transfer process for the model pile and soil in this study is conduction.
- Thermal piles can be used as the sole or joint provider of heating or cooling for a building, depending on the required thermal load.
- HDPE pipes are the most common material used to transfer fluid (Brandl, 2006).

- The favourable fluid used in the pipes must have a small coefficient of expansion, low viscosity, high thermal capacity, low freezing point and high boiling point (Banks, 2008). The glycol-water mixture has been proven to be the most suitable medium for use in pipes to date (Brandl, 2006).
- It seems that the heat exchange rate is the highest in the double-tube pipe configuration, followed by multi-tube and single U-tube configurations. In addition, increasing the flow rate increases the heat exchange rate of thermal piles (Gao et al., 2008; Jalaluddin et al., 2011).

At the moment, the design of thermal piles is based on an inefficient method, where maximum induced load and pile head displacement are considered and large safety factors are used to cover the uncertainties. The Thermal Pile Standard (GSHPA, 2012) has recommended the proposed framework by Bourne-Webb et al. (2013), but it is clear from differences in the findings in the literature that the proposed framework needs to be assessed for different soil conditions and end-bearing conditions. Significant induced thermal loads up to three times larger than mechanical loading are reported by Laloui et al. (2006) and could cause severe defects in buildings and reduce the safety factor. This can result in considerable structural defects and reduction in the safety factor that is considered as a main concern for thermal pile designers. It was seen in most of the in-situ studies that the amount of induced thermal stress reaches close to the safety margin given by BS 8004:1986 (British Standards Institution, 1986) for induced stress on the concrete and higher temperatures or greater restraint from the surrounding soil can result in passing the BS limits. One of the main advantages of laboratory studies is the ability to reach close to the ultimate state loading to experience the most critical state of loading which is not achievable for in-situ studies. Moreover, it is seen that an additional tension load could arise in the pile that could potentially result in cracking in the concrete and reducing the pile strength. For thermo-mechanical behaviour of thermal piles, it is observed that the pile response is mainly dependant on the level of restraint caused by the surrounding soil and the mechanical loading on the pile head. Determining changes in DoF along the pile during different loading conditions will help in understanding the behaviour of thermal piles. There are limitations and shortcomings with the previous works done in-situ, and there is a strong need to study thermal pile behaviour in a more controlled environment by going beyond the scope of previous works. Additionally, discrepancies found in the literature regarding the behaviour of thermal piles have resulted in the adoption of conservative methods for thermal pile design. According to reasons above, this study has focused on understanding the thermo-mechanical behaviour of a model thermal pile under seasonal heating-cooling cycles. Changes in pile capacity will be assessed, as will the applicability of the proposed framework by Bourne-Webb et al. (2013) for different scenarios. If cyclic degradation

is to be seen, the piles need to be loaded close enough to the ultimate shaft capacity, which is not possible in the field but is carried out in this study. Moreover, in the literature, it is clearly stated that there is an absence of a database that includes different situations regarding end-bearing conditions and the restraint caused by the surrounding soil in different temperature variations. Furthermore, the outcome will be an observational set of data, which could be used to validate cyclic behaviour predictions for thermal piles. One of the main concerns for the thermal pile designers is to determine if the induced thermal load has the potential to pass the elastic limit or not. In most of the literature, the focus has been on the type of pile response, elastic or plastic, rather than the threshold where elastic behaviour ends. A parametric study where various levels of mechanical loading is applied on the pile will help to determine this threshold. In the context of the research question, other objectives are expected to be covered that are directly related to the research question. These objectives are described in the aims and objectives in Chapter 1. To carry out this research, a laboratory model is developed, which will be described in Chapter 3.

Chapter 3. Experimental methodology

3.1 Introduction

To understand the behaviour of piles, various techniques may be utilised including the full-scale testing and physical modelling, both have been used for many years. Full-scale tests are costly, time-consuming and also lack sufficient control of boundary conditions. Due to such difficulties, physical models, and in particular laboratory models, are currently widely used in the field of geotechnics. The art and science of the physical modelling of soil are defined by Mayne et al. (2009) as “the ability to consistently predict soil behaviour using the simplest possible model by considering the limitations and extent of the validity of the results generated by the physical model”. According to Mayne et al. (2009), there are five types of physical modelling:

- 1g small-scale models and tests
- 1g large-scale models and tests
- Calibration chambers
- 1g shaking tables
- Geotechnical centrifuge

In this study, a 1g small-scale physical model is designed and constructed because of the following reasons:

- Reduced disturbance to instruments due to the ease and control of installation, resulting in more accurate data.
- Data obtained from physical models is more reliable for numerical modelling and back analysis (Muir Wood, 2004).
- Unlike full-scale models, boundary conditions are well defined and controlled.
- The cost of the 1g small-scale model is low.
- Trends in behaviour can be investigated more rapidly.
- Parametric studies and repeatable tests can be conducted easily and quickly using 1g small-scale models.

Translation from small-scale models to a real prototype scale situation using scaling laws is difficult due to the need to scale down all the elements involved (Altaee & Fellenius, 1994). An alternative solution is to use dimensional analysis (DA); comparing the results independently of the scaling laws for similarity analysis. A brief description of the DA method used in this study is provided below. Moreover, this chapter also describes the full design and development of the laboratory model including the application of a novel monitoring technique using optical fibre sensors. The tests undertaken in this study are divided into five scenarios. At the end of this chapter, the test programme and procedure for each scenario is described.

3.2 Physical modelling of a thermal pile

3.2.1 Dimensional analysis

3.2.1.1 An introduction to dimensional analysis

Dimensional analysis (DA), also known as non-dimensional analysis, is a tool to aid the design of experiments and characterise certain aspects of a system. Buckingham's (1914) 'Pi' theorem is presented; however, it was later found that conditions stated in the theorem are necessary, but not sufficient (Butterfield, 1999). Hence, more recently, a systematic approach has been developed and is described by Butterfield (1999) for the application of DA in geotechnics. The outcome of DA is a set of dimensionless groups (DG) or normalised parameters called 'Pi' factors (Π_i) that apply to basic dimensions characterising the physics of the problem. In order to have a small-scale model similar to the prototype, instead of similarity between all parameters, a combination of parameters in the form of DGs needs to be similar.

Assume that there are 'n' variables in the study $V = (V_1, V_2, \dots, V_n)$ and a total of 'm' independent primary dimensions $D = (D_1, D_2, \dots, D_m)$ (i.e. mass, length, time, temperature, voltage, etc.). It is stated by Buckingham (1914) that the number of variables can be reduced to a minimum number of DGs, N , where $N = n - m$. However, this theorem does not provide any guidance on how to select or combine the variables in each of the groups. A revised algorithm is described by Butterfield (1999) presenting two further conditions to achieve a complete solution (see Figure 3.1). A limitation exists for DA of thermal pile where it is not possible to achieve only one set of DGs due to the presence of two completely distinct governing equations. Parameters, units, notations and dimensions of each parameter involved in the DA of model thermal piles are given in Table 3.1. The aim of carrying out this dimensional analysis is to determine the equivalent of the pile tested in this study to the pile size in real life. Also, this can provide a detailed DA procedure for future experimental studies on thermal piles.

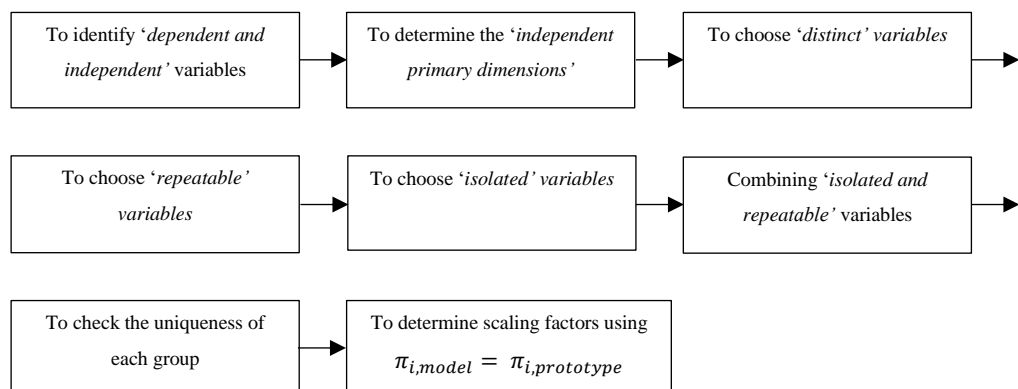


Figure 3-1. A schematic view of dimensional analysis steps

3.2.1.2 Dimensional analysis - bearing capacity of a model thermal pile

The DA for a pile under mechanical loading consists of the following steps (Butterfield,1999):

- Step 1: To identify the number of dependant and independent variables governing the system behaviour, n . This includes the combination of parameters affecting the pile capacity (see Appendix I) including the pile geometry and mechanical properties, soil properties and parameters affecting the friction at the soil–pile interface:

$$V = \{D, l, E_p, G_p, w, \rho, E_s, \nu_s, e, \gamma_s, \tan\delta, \phi_f, \phi_c, k, \sigma_v, \tau\} \rightarrow n = 16 \quad (3.1)$$

- Step 2: To determine the number of independent primary dimensions. In this case, there are three primary dimensions: Length (L), Mass (M), Time (T):

$$D = \{M, L, T\} \quad : \quad m = 3 \quad (3.2)$$

- Step 3: To choose a set of Distinct Variables, R , noting the following restrictions:
 - Not to choose dimensionless variables (e.g. e, φ).
 - Not to choose variables with similar dimensions (e.g. l, D).
 - Not to choose variables that are powers of another variable (e.g. l, D, A).

Applying above restrictions to a set of variables, n , gives:

$$R = \{l, \rho, E_s, \gamma_s\} \quad (3.3)$$

- Step 4: To choose a set of Repeatable Variables, Q . The only condition that needs to be satisfied is that the chosen parameters do not constitute a DG alone. The number of parameters needed for ‘ Q ’ depends on the ‘ m ’ value, which is 3 in our case. After trying 4 possible options from ‘ R ’, the following set of repeatable variables are chosen which satisfy the aforementioned conditions:

$$Q = \{l, \rho, E_s\} \quad (3.4)$$

- Step 5: To choose the Isolated Variables as the difference between ‘ V ’ and ‘ Q ’:

$$V - Q = \{D, w, E_p, G_p, \nu_s, e, \gamma_s, \tan\delta, \phi_f, \phi_c, K, \sigma_v, \tau\} \quad (3.5)$$

- Step 6: To arrive at the DG groups, repeatable variables $\{l, \rho, E_s\}$ are used in all groups and one Isolated Variable found above is used for each group resulting in 13 DGs (see Table 3.2).
- Step 7: The variables in each DG are combined to find a dimensionless group, Π_i . Only 1 DG can be constructed from each group resulting in 13 DGs (see Table 3.2).
- Step 8: For an appropriate model, the following condition must be satisfied:

$$\pi_{i,model} = \pi_{i,prototype} \quad (3.6)$$

The scale factor is defined as the ratio of the property of the model to the prototype (see Table 3.2).

Table 3-1. Physical and thermal variables and dimensions of the study

Quantity	Notation	Dimensions	Derived units
Pile diameter	D	L	m
Pile embedded length	l	L	m
Elastic modulus of pile	E_p	$ML^{-1}T^{-2}$	$kg.m^{-1}.s^{-2}$
Shear modulus of pile	G_p	$ML^{-1}T^{-2}$	$kg.m^{-1}.s^{-2}$
Pile axial displacement	w	L	m
Soil density	ρ	ML^{-3}	$kg.m^{-3}$
Elastic modulus of soil	E_s	$ML^{-1}T^{-2}$	$kg.m^{-1}.s^{-2}$
Void ratio	e	1	
Unit weight of the soil	γ_s	$M.L^{-2}.T^{-2}$	kN/m^3
Friction angle at pile-soil interface	$\tan\delta$	1	-
Friction angle at failure	ϕ_f	1	-
Friction angle at critical state	ϕ_c	1	-
Coefficient of lateral earth pressure	k	1	-
Applied stress	σ_v	M/LT^2	kPa
Shear stress	τ	M/LT^2	kPa
Poisson ratio of soil	ν_s	1	-
Heat capacity per unit volume	C_p	$ML^{-1}T^{-2}\theta^{-1}$	$J.m^{-3}.K^{-1}$
Thermal conductivity	λ	$MT^{-3}L\theta^{-1}$	$W.m^{-1}.K^{-1}$
Thermal diffusivity	α	L^2T^{-1}	m^2s^{-1}
Heat source (pile) radius	r	L	m
Radius of heat propagation	R	L	m
Quantity of heat	Q	ML^2T^{-2}	J
Time	t	T	s
Temperature change	ΔT	θ	K

Table 3-2. Dimensionless groups and scaling factors of DA for a pile under an axial load

Group	Variables	Π group	Group name	Scaling factor
DG1	l, ρ, E_s, D	D/l	Pile's AR	$S_D = S_l$
DG2	l, ρ, E_s, w	w/l	Normalised displacement	$S_w = S_l$
DG3	l, ρ, E_s, E_p	E_p/E_s	Modular ratio	$S_{E_p} = S_{E_s}$
DG4	l, ρ, E_s, ν_s	ν_s	Poisson ratio of soil	$S_\nu = 1$
DG5	l, ρ, E_s, e	e	Void ratio	$S_e = 1$
DG6	l, ρ, E_s, γ_s	$\gamma_s \cdot l / E_s$	Normalised unit weight of soil	$S_{\gamma_s} \cdot S_l = S_r^2$
DG7	$l, \rho, E_s, \tan\delta$	$\tan\delta$	Friction at soil–pile interface	$S_{\tan\delta} = 1$
DG8	l, ρ, E_s, ϕ_f	ϕ_f	Friction coefficient at failure state	$S_{\phi_f} = 1$
DG9	l, ρ, E_s, ϕ_c	ϕ_c	Friction coefficient at critical state	$S_{\phi_c} = 1$
DG10	l, ρ, E_s, k	k	Coefficient of lateral earth pressure	$S_k = 1$
DG11	l, ρ, E_s, σ_v	σ_v / E_s	-	$S_{\sigma_v} = S_{E_s}$
DG12	l, ρ, E_s, τ	τ / E_s	-	$S_\tau = S_{E_s}$
DG13	l, ρ, E_s, G_p	G_p / E_p	Normalised modulus	$S_{E_p} = S_{G_p}$

In addition to the DGs found in the previous section, the necessity of correct modelling of pile axial stiffness is emphasised in the literature by Muir Wood (2004) and Bradshaw (2012). It is shown by Muir Wood (2004) that to have a reasonable comparison between the model and the prototype, the ratio $(G_p/E_p)(\sqrt{l/r_0})$ needs to be similar where r_0 is the radius of the pile. Using the 13 DGs and the stiffness condition mentioned above would help to more accurately compare the model and prototype results. It is not possible to achieve complete similarity, and the aim of conducting a DA is to provide a set of DGs to compare the results, rather than a prototype simulation. With regards to the stiffness ratio given by Muir Wood (2004), the model pile used in this study has a pile diameter and length of 28mm and 530mm respectively, and is made of stainless steel, surrounded by sand. This could then be compared to a concrete pile with a diameter and length of 1m and 5.73m respectively with similar sand surrounding the pile. As mentioned in Section 3.2.1.1, the main aim of DA done in this section is to determine the equivalent of tested pile in the real life. Moreover, it was shown that in order to compare a set of results from laboratory studies with in-situ installations, there is no need to find similarity in every element of

a physical model. A combination of parameters has to be similar in the form of dimensionless groups. DA carried out for the heat transfer process in thermal piles is described below.

3.2.1.3 Dimensional analysis- Heat transfer in a model thermal pile

In this study, the model pile is designed to support both mechanical and thermal loadings. In the second part of the DA, heat transfer in the soil is the governing equation (see Equations 2.13 and 2.15). Due to the existence of two distinct governing equations for thermal piles, load bearing capacity under mechanical loading and heat transfer under thermal loading, DA for the heat transfer needs to be carried out separately. A summary of variables involved: units, notations and dimensions, are presented in Table 3.1. A brief description of the DA of the heat transfer procedure is presented below:

- Step 1: Variables are chosen based on Equation A.3 (see Appendix A), a transient heat transfer equation, and the geometry of the study:

$$V = \{C_p, \lambda, \alpha, r, R, l, Q, t, \Delta T\} \rightarrow n = 9 \quad (3.7)$$

- Step 2: For DA of heat transfer, temperature is added as the 4th primary dimension:

$$D = \{M, L, T, \theta\} \rightarrow m = 4 \quad (3.8)$$

Based on Buckingham's π theorem, the minimum number of DGs is 5.

- Steps 3, 4 and 5: Similar to Section 3.2.1.2:

Distinct variables:

$$R = \{C_p, \lambda, \alpha, r, Q, t, \Delta T\} \quad (3.9)$$

Repeatable variables:

$$Q = \{\lambda, \alpha, r, Q\} \quad (3.10)$$

Isolated variables:

$$V - Q = \{C_p, R, l, t, \Delta T\} \quad (3.11)$$

- Steps 6, 7 and 8: Similar procedure as Section 3.2.1.2 is followed, and five DGs and scale factors are formed (see Table 3.3).

Dimensionless group 1 is known as the Fourier number, Fo , and is a common dimensionless number used in heat transfer. It is defined as the ratio of the heat conduction rate to the rate of thermal energy storage in a solid. It is also used as a dimensionless measure of time in transient heat conduction. The Fourier number also provides an indication of the time remaining to reach a steady-state condition. In addition to the previously described DA, a set of additional recommendations for a 1g model must be satisfied, which are presented in Section 3.2.2.

Table 3-3. Dimensionless groups and scaling factors of DA for a pile under thermal loadings

Group	Variables	Π group	Group name	Scaling factor
DG1	λ, α, r, Q, t	$\alpha \cdot t / r^2$	Fourier number ($ Fo $)	$ S_{\alpha} \cdot S_t = S_r^2 $
DG2	λ, α, r, Q, l	$ r / l $	Heating source's AR	$ S_l = S_r $
DG3	λ, α, r, Q, R	$ R / r $	Normalised radial distance	$ S_R = S_r $
DG4	$\lambda, \alpha, r, Q, \Delta T$	$ \alpha \cdot \lambda \cdot \Delta T / r \cdot Q $	-	$ S_Q = \frac{S_{\alpha} \cdot S_{\lambda} \cdot S_{\Delta T}}{S_r} $
DG5	$\lambda, \alpha, r, Q, C_p$	$ C_p \cdot r^4 / \alpha \cdot \lambda $	-	$ S_r = \sqrt[4]{\frac{S_{\alpha} \cdot S_{\lambda}}{S_c}} $

3.2.2 Size effects and boundary conditions

In addition to the DA carried out in this study, a more conventional approach is also used in Section 3.2.2 where the chosen dimensions are compared with recommended values in the literature. There are 4 boundary conditions that are compared with the literature values:

- Ratio between the pile and container diameter
- Aspect ratio
- Scaling of soil particle size
- Thermally induced boundary conditions

A brief description of each comparison is provided below.

3.2.2.1 Ratio between the pile and container diameters

The ratio between the pile diameter and the container diameter should be selected in such a way as to minimise boundary effects. In the laboratory model, the container has an external diameter of 500mm and a wall thickness of 3mm. The pile has an external diameter of 28mm. As such, the ratio between the diameter of the container and model pile is 17.85. According to Kraft (1991), the lateral boundaries of the soil container affect both the stress and displacement patterns in the sand. The zone of influence is defined as the zone in which the soil will be affected due to pile loading or the pile installation method and depends on soil density and pile installation method. Recommendations found in the literature are as follows:

1. Al-Mhaidib and Edil (1998):

$$R \text{ (Zone of influence)} = 3D \text{ to } 8D \text{ (Pile diameter)}$$

For the laboratory model:

$$3D = 84\text{mm} < R < 8D = 224\text{mm}$$

The container diameter is 500mm and meets the above criterion.

2. Randolph and Wroth (1978):

$$R \text{ (Zone of influence)} = 0.9L \text{ - } 1.4L \text{ (Embedded pile length)}$$

For the laboratory model:

$$0.9L=351\text{mm} < R < 1.4L=546\text{mm}$$

The embedded pile length and container diameter used in this study is 390mm and 500mm respectively which is close to the high range of recommendations. Most recommendations are based on a specific method of pile installation, which disturbs the surrounding soil; however, in this study, the pile is installed before the sand and hence, the effects are expected to be much lower.

3.2.2.2 Aspect ratio

For the pile design, there is a ratio between the length of the pile and the diameter, which is called the Aspect Ratio (AR). In the field, the recommended ratio ranges between 10 to 50. In this study, the AR is equal to 18.92 when considering the entire pile length, and it is equal to 13.92 when considering the pile length embedded in sand, both of which are within the recommended limit.

3.2.2.3 Scaling of soil particle size

The size of the sand grains is not scaled down along with the rest of the system. However, several recommendations are found in the literature based on the relationship between the pile diameter and median grain size ' D_{50} '. In the laboratory model, the pile diameter and sand median size are equal to 28mm and 0.18mm respectively, and the ratio of D/D_{50} is equal to 155.5, which is greater than all recommendations given in Table 3.4. This suggests that the effect of soil particle scaling should not significantly affect the results of this study.

Table 3-4. Scaling effect recommendations between the pile diameter and sand grain size

King et al. (1985)	Weinstein (2008)	Franke and Muth (1985)	Garnier and Konig (1998)	Fioravante (2002)
$D/D_{50} > 35$	$D/D_{50} > 100$	$D/D_{50} > 30$	$D/D_{50} > 100$	$D/D_{50} > 50$

3.2.2.4 Thermally induced boundary conditions

For thermally induced boundary conditions, recommendations are given by Tang et al. (2013):

- Choose a container diameter large enough to ensure that no boundary effects are induced by either the container's wall or base. In this study, this condition is checked by the temperature and strain sensors on the container wall.
- The container walls and base should be well insulated, and we also need to consider the heat transfer at the soil surface. In this study, all sides of the container bottom, wall and top are insulated, as described in Section 3.3.2.

3.3 Experimental materials and set-up

3.3.1 General arrangement

The apparatus consists of a steel container, a stainless steel tube, a water circulator, water flowing pipes and monitoring equipment. Schematic views of the test set-ups used are shown in Figures 3.2 and 3.3. Descriptions of the design of each element are provided below.

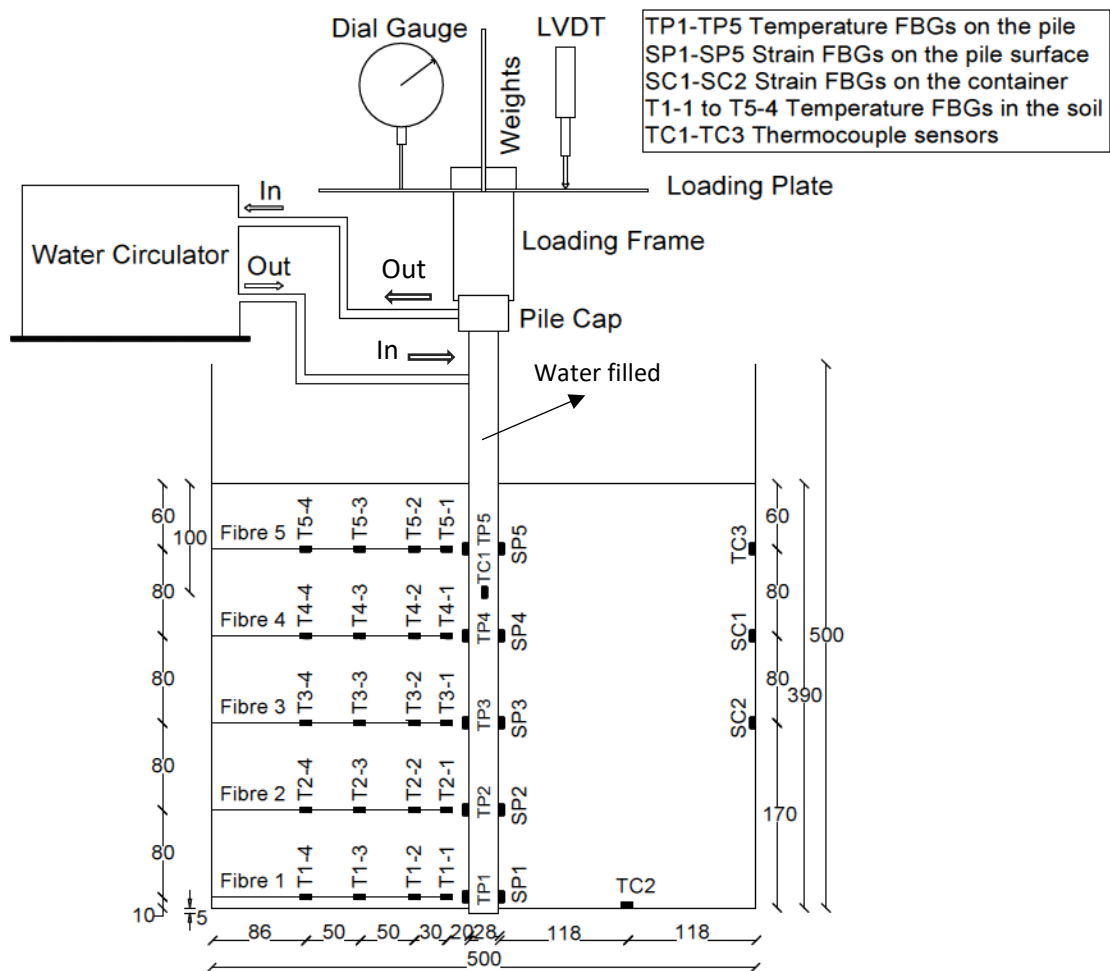


Figure 3-2. A Schematic view of Scenarios 1 to 4 test set-up (dimensions in mm)

3.3.2 Tank design

A cylindrical steel tank is used as the soil container in this study. Initially, a 1580mm x 500mm steel sheet with steel grade S275 is cut and delivered to the laboratory as a rolled tube. It is then tack welded, according to EN 10025-1:2004 (British Standards Institution, 2004) for weldable structural steels, to achieve $D=500\text{mm}$, $H=500\text{mm}$ and 3mm thickness, with a resultant volume of 0.0981m^3 (see Figure 3.4-a). Steel grade S275 is chosen due to the suitability for welding. The procedure followed to determine the minimum required size of the container is described below. A hole is located at the bottom centre with a diameter of 33mm, which is slightly larger than the pile diameter, and which allows the pile to run through the hole for shaft resistant tests. A

fibreglass insulation jacket with a thermal conductivity of 0.04w/m.k and thickness of 80mm is placed around the container and on top of the sand to minimise heat losses. The container is placed on top of a steel box to allowed sufficient space for the pile to travel downwards.

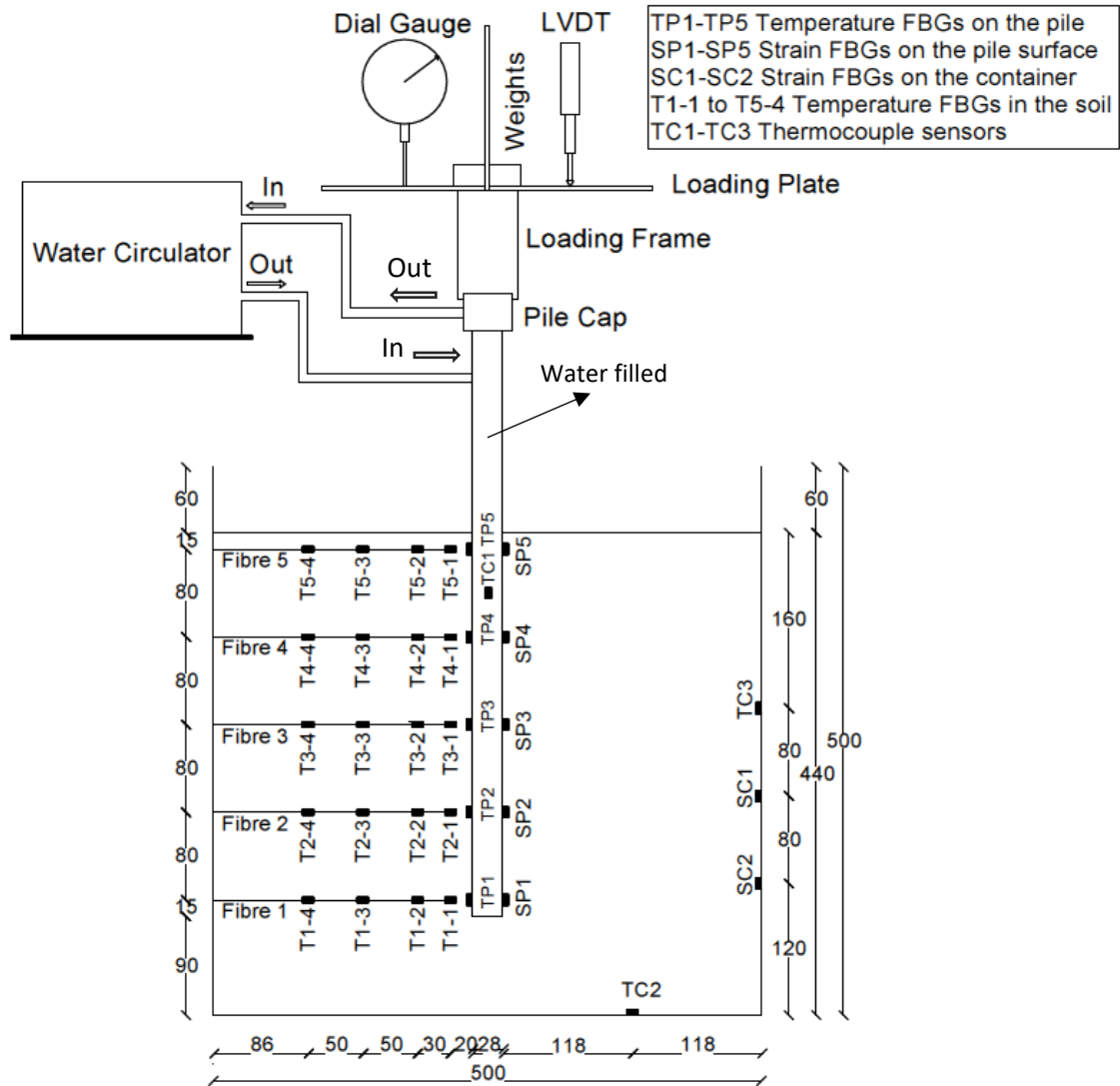


Figure 3-3. A schematic view of Scenario 5 test set-up (dimensions in mm)

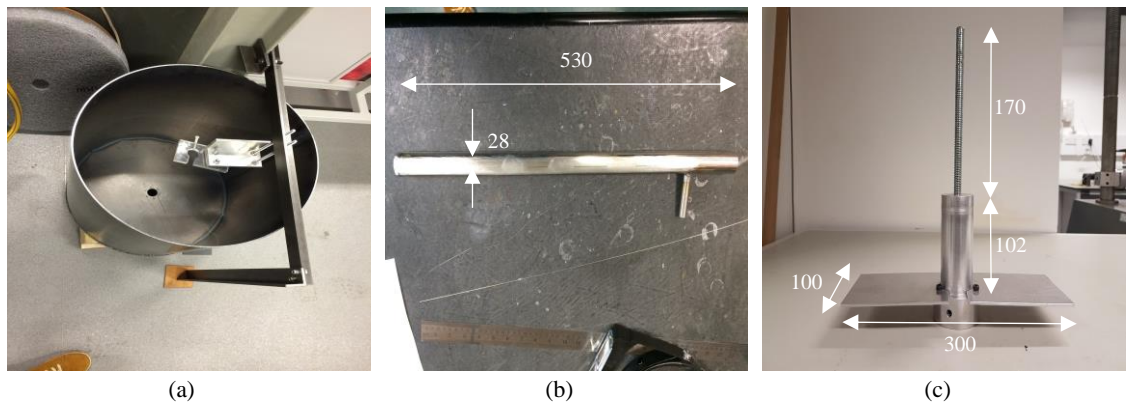


Figure 3-4. (a) container, (b) model pile, (c) loading plate

To determine the required size of the container, changes in the soil temperature due to heating of the pile are simulated using a two-dimensional FDM in Matlab. The governing equation and properties of materials used in the model are given in Appendix A. The Matlab code used to develop the model is given in Appendix C. Dimensions used in the model are the same as those used in the laboratory model for the shaft resisting pile. The thermal conductivity of sand is considered as a constant value of 0.15W/m.K in both horizontal and vertical directions based on the value given by Hamdhan and Clarke (2010) for fine sand. A few assumptions are considered in developing the numerical model which are listed below:

- Effects of groundwater flow and mechanical superstructure loading is not included.
- Conduction is assumed to be the dominant process.
- A finite heat source with a constant temperature of the heat source is considered. The horizontal axis on all 4 plots in Figure 3.5 starts from 0.014mm which is the pile surface. Small discipation of heat, i.e. change in the temperature, is seen between the pile core and pile surface.
- The thermal conductivity of concrete and convection that happens in the pipes are neglected.
- Sand bed is assumed as a solid and homogeneous medium.

A summary of the boundary conditions and initial values given in the finite difference model is provided below:

- Only half of the container is modelled due to the assumption of symmetrical heat flow.
- The radius of the container, soil height and heat source diameter is equal to 250mm, 390mm and 28mm respectively.
- Fixed temperature Dirichlet boundary conditions are used. Pile temperature is considered at a constant value of 50°C and the temperature inside the soil and on the boundaries including top, bottom, left and right is considered as 22°C.
- 80mm Fibreglass insulation is used for the insulation of top and bottom of the soil.
- For the numerical resolution of the model, the computational mesh consists of 400 rows and 400 columns.
- The temperature field is considered at consecutive time steps with a time increment of 1 second.

Temperature readings are collected at 0.02, 0.05, 0.1 and 0.15m away from the pile surface which is similar to the location of FBG sensors in the laboratory model.

Temperature profiles at the end of 1st, 4th, 12th and 24th hour of heating are provided in Figure 3.5. Temperature profiles for intermediate time periods and also heating period up to 1 month are given in Appendix B. The results show that heat transfer from thermal pile to the surrounding soil is mostly a radial phenomenon (especially ignoring the pile ends) which is in agreement with findings by Ghasemi-Fare and Basu (2013). The insulation level at the top and bottom of the

container are shown by a dashed line. The thermal influence zone after 24 hours of heating extends 215mm away from the pile surface which is approximately 15 times the pile radius. In this study, the container diameter is chosen as 250mm to make sure that the least disturbance to the soil is caused by the boundaries.

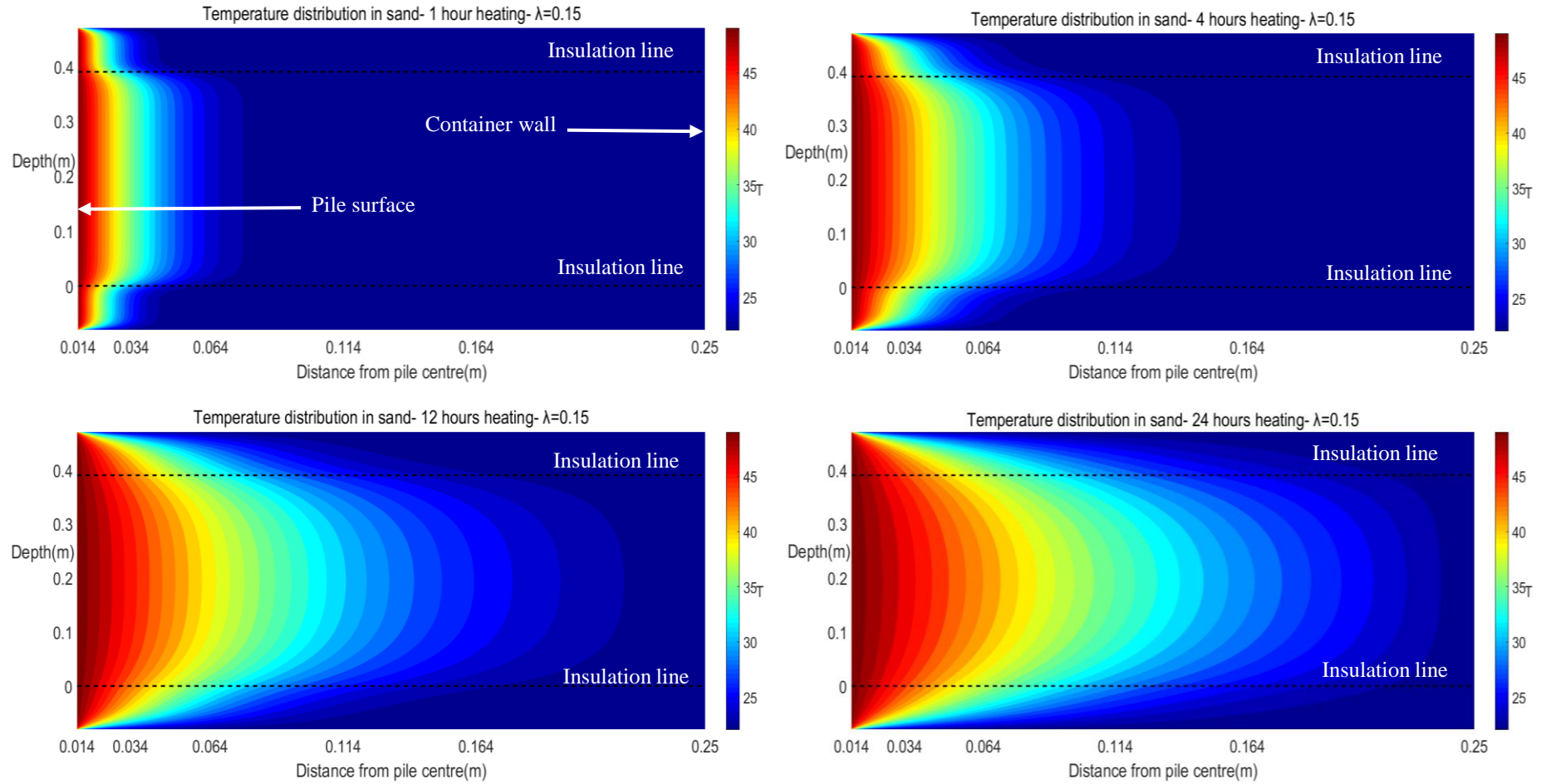


Figure 3-5. Temperature profiles at different heating periods using a 2D FDM model

3.3.3 Pile design

A bright polished closed-end stainless steel tube model 1.4301, also known as the US grade 304, is used as the model pile (see Figure 3.4-b). The physical properties of the model pile are in line with EN 1993-1-4:2006 (British Standards Institution, 2006) having Young's modulus, yield strength and tensile strength equal to 200GPa, 210MPa and 520MPa respectively. The external diameter, height and thickness of the model pile are 28, 535 and 1.5mm respectively. The model pile is sealed by welding a plate made from the same material as the tube. This allows the water to be stored and circulated inside the pile. An external pile cap is also manufactured using the same material with a rod attached to the centre to carry the water to the pile bottom. Two additional stainless steel rods are welded to the pile cap and surface, with external diameter of 12mm to connect the inlet and outlet water pipes from the water circulator to the pile.

3.3.4 Loading assembly

In this study, dead weights are used because they provide a more realistic representation of mechanical loading steps that occur during the construction of a building. Thermal piles carry the structural load, which is considered as a dead load, in addition to the thermal load caused by seasonal heating and cooling cycles. Mechanical loads of 1kg or 2kg are applied on the pile head and increased depending on the final required load. A loading frame is attached to the pile head consisting of a circular hollow steel tube, a loading plate and a long rod to keep weights in position (see Figure 3.4-c). The loading plate is made of steel with a length, width and thickness of 300, 100 and 2mm, and is attached to the pile head to place on it the Linear Variable Differential Transformer (LVDT) and dial gauge. The loading plate is levelled before any test commences using a spirit level.

3.3.5 Temperature control system

A water circulator is used to circulate thermostatically-controlled water through tubes connected to the pile head. The circulator is Techne model C-400, with manual temperature adjustments up to +80°C. The circulator is used for heating purposes only to raise the water temperature to 50°C, but during the cooling period, the pile is allowed to cool down naturally.

3.4 Monitoring instrumentation

3.4.1 Instrumentation layout

Schematics of the apparatus used for Scenarios 1-4 and five tests across all monitoring instruments installed are shown in Figures 3.2 and 3.3 respectively. The instrumentation used in the two set-ups consist of 4 main parts, used for:

1. Strain and temperature monitoring of the pile
2. Temperature monitoring in the sand bed
3. Pile head movement monitoring

4. Container wall and bottom monitoring

Optical Fibre Bragg Gratings (FBGs) are optical fibre sensors and are used for temperature and strain monitoring. FBG sensing technology is described in Section 3.4.2. A summary of the instruments used in this study is given in Table 3.5.

Table 3-5. Summary of the monitoring instruments used in this study (read in conjunctions with Figures 3.2 and 3.3)

Monitoring instrument	Number of sensors
FBG Temperature sensors on the pile	5
FBG strain sensors on the pile	5
FBG strain sensors on the container wall	2
FBG Temperature sensors in the soil	20 in 5 levels
Thermocouples on the container wall and bottom	2
Thermocouples on the pile surface	1
LVDT	1
Dial gauge	1

3.4.1.1 Strain and temperature monitoring of the pile

Changes in temperature and strain along the pile surface are monitored using two sets of optical fibre sensors. Each optical fibre cable contains 5 Wavelength-Division-Multiplexed (WDM) FBG sensors, with adjacent sensors separated by 80mm (see Figure 3.6). FBG strain sensors are bonded to the pile surface and labelled as SP1, located 15mm above the bottom of the pile, to SP5, located 60mm below the sand surface. Similarly, FBG temperature sensors mounted on the pile surface are labelled from TP1 to TP5. A thermocouple type *T*, TC1, is placed on the pile surface between TP4 and TP5 sensors as an extra measuring tool to support the FBG temperature readings.

Thermocouple Type-T, composed of a pair of copper and constantan wires, is a low-cost temperature monitoring instrument with a measurable range between -270 to +400°C (American Society for Testing and Materials, 1993). It is also considered as the most frequent choice for geotechnical applications with an accuracy of $\pm 1^\circ\text{C}$ (Dunncliff and Green, 1988). The thermocouple is calibrated using an ice bucket where one end is placed inside the bucket, and the other end is attached to the data logger. It is found that the measured temperature is within the range of 0 to 0.5°C, which is in the range of $\pm 1.0^\circ\text{C}$ accuracy of thermocouples recommended by Dunncliff and Green (1988). Thermocouple data is collected using an eight channel Pico-TC 08 data logger from Pico technology, measuring from -270°C to +1820°C. Picologger software is used to convert voltage into temperature, recording frequencies of 60 seconds.

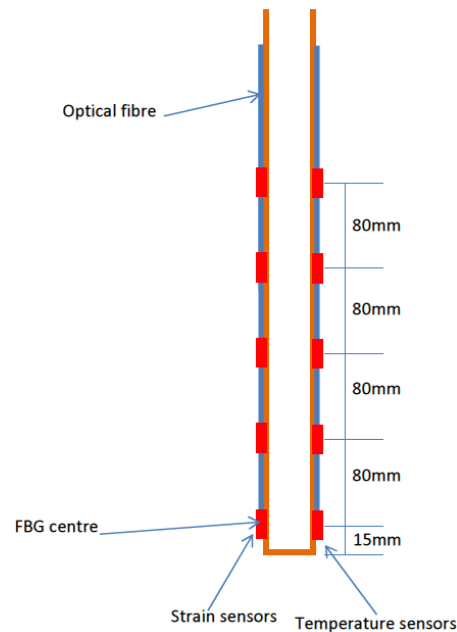


Figure 3-6. A schematic view of FBGs installed on the pile surface

3.4.1.2 Temperature monitoring in the sand bed

Five layers of soil are monitored using 4 FBG temperature sensors in each layer (see Figure 3.7). To optimise the positioning of FBGs in the sand, temperature profiles developed by the numerical model and shown in Figure 3.5 are used. Using the numerical model, it is found that despite having a large influence zone after 24 hours of heating, the major area affected by pile heating is 150mm from pile surface. It is approximately 11 times the pile radius, where temperatures ranging from 49.9 to 30°C are recorded. Therefore, two FBGs are placed next to the pile within 50mm of the pile surface, and the other two FBGs are placed at 50mm intervals up to 150mm away from the pile surface (see Figure 3.7).

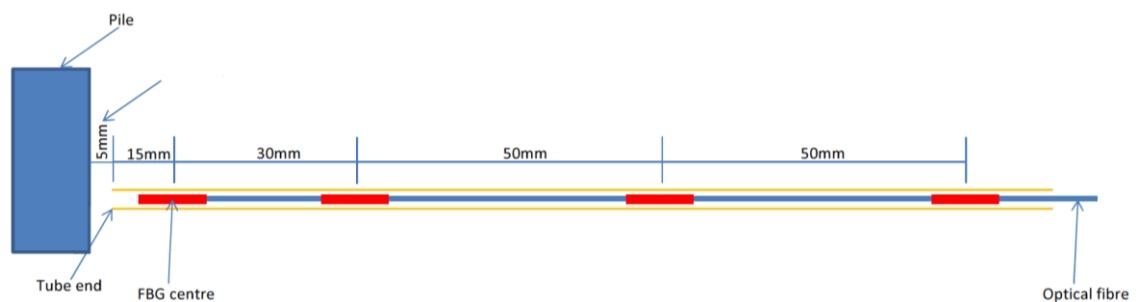


Figure 3-7. A schematic view of FBGs installed in sand

3.4.1.1 Pile head movement monitoring

The pile head movement is monitored using a LVDT placed on the loading plate (see Figure 3.8). LVDT model DCTH300AG from the RDPE company is used with a measurement range of ± 7.5 mm and dimensions detailed in Figure 3.8-b. Data acquisition is done using an Agilent 34972A LXI Data Acquisition Switch Unit. Agilent VEE Pro 9.3 software is used to collect the

data in voltage format, at a data rate of 0.33Hz. To convert voltage data into mm, calibration is carried out five times before the start of each Scenario, and similar relationships between voltage and displacement in mm are achieved in all cases (see Figure 3.9):

$$y(mm) = -1.5605x(V) + 9.4236; R^2 = 1 \quad (3.12)$$

To calibrate the LVDT, the apparatus consisting of an adjustable micrometre and a hollow cylindrical opening is used (see Figure 3.8-a). Initially, the LVDT is placed in the cylindrical hole and is then moved downwards until the LVDT needle tip touches the micrometre. Displacements equal to 2mm are applied at each stage, using an adjustable micrometre with a 1-minute relaxation period, until the needle of the LVDT is completely compressed. Afterwards, the process is repeated in the reverse.

In addition to LVDT, an analogue dial gauge is also placed on the other side of the loading plate as a back-up for pile head movement readings (see Figure 3.2). It has a dial size of 75mm, a range of 0-50mm, a graduation of 0.01mm clockwise and a needle length of 55mm. A camera is used to capture dial gauge readings every 5 minutes, collecting readings during the entire 24 hours.

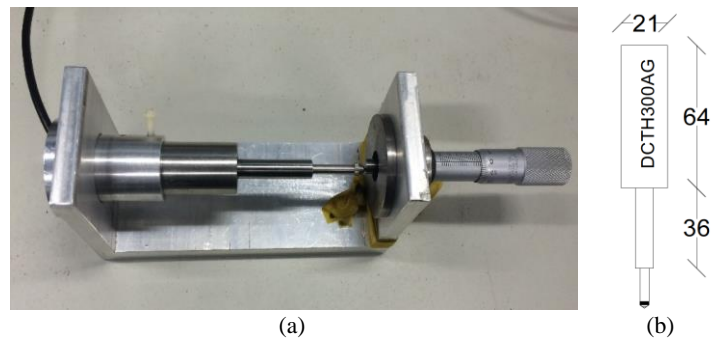


Figure 3-8. (a) LVDT calibration apparatus (b) LVDT dimensions

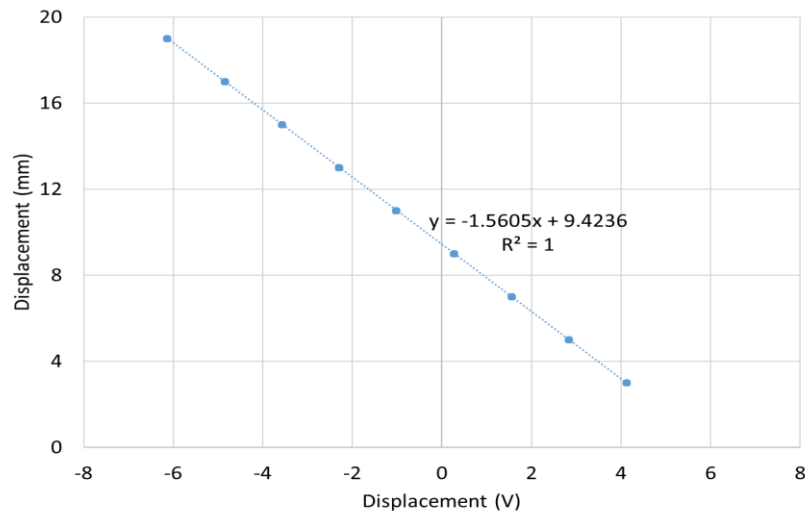


Figure 3-9. LVDT calibration

3.4.1.2 Container wall monitoring

In most laboratory studies on piles, the effect of temperature and changes in the strain of the model pile at boundaries are not usually monitored, and recommendations such as those given in Section 3.2.2 are used to justify the dimensioning of the boundaries. In this study, 2 FBG strain sensors, SC1 and SC2, and one thermocouple, TC3, are positioned on the container wall, with an additional thermocouple at the base of the container, TC2. This helps to assess and quantify the effect of changes in pile strain and temperature at the boundaries.

3.4.2 Monitoring using fibre optic sensors

3.4.2.1 Fibre optic sensors

The use of fibre optic sensors (FOS) in monitoring the health of geotechnical structures, such as foundations and tunnels, has increased significantly over the past decade (e.g. Kister et al., 2007; Klar et al., 2006, Li et al, 2009; Habel & Krebber, 2011; Weng et al., 2014). Optical fibres transmit signals in the form of light from one location to another within a glass or silica core, with low attenuation and high bandwidth, and are used widely in communication systems. The properties of light propagating through an optical fibre can be influenced by local environmental perturbations, such as temperature or strain. FOS exploit this sensitivity by transducing the environmental perturbation into changes in intensity, optical frequency, polarisation or phase of the lightwave (Anasri, 2007). The use of FOS, instead of conventional monitoring instruments such as strain gauges, offers several advantages including the small size, high sensitivity, large bandwidth and automated and fast data acquisition (Iten, 2011; Schwamb, 2010).

FOS are divided into two main categories: point-based and distributed measurement sensors. For the point-based FOS, a single point or multiple points are monitored, while in distributed FOS, environmental disturbances are monitored as a continuous function of length along the fibre. Typical strain resolution for distributed sensors is approximately $20\mu\epsilon$, compared to

approximately $1\mu\epsilon$ for point-based sensors (Schwamb, 2010). For the tests reported here, the magnitude of strain was anticipated to lie on the range of 0 to $500\mu\epsilon$ which is well within the measurement range of FBG sensor interrogation units. In this study, point-based optical fibres are chosen due to their higher spatial resolution and also due to the small strain values anticipated during the mechanical loading of the pile (see Figure 3.10).

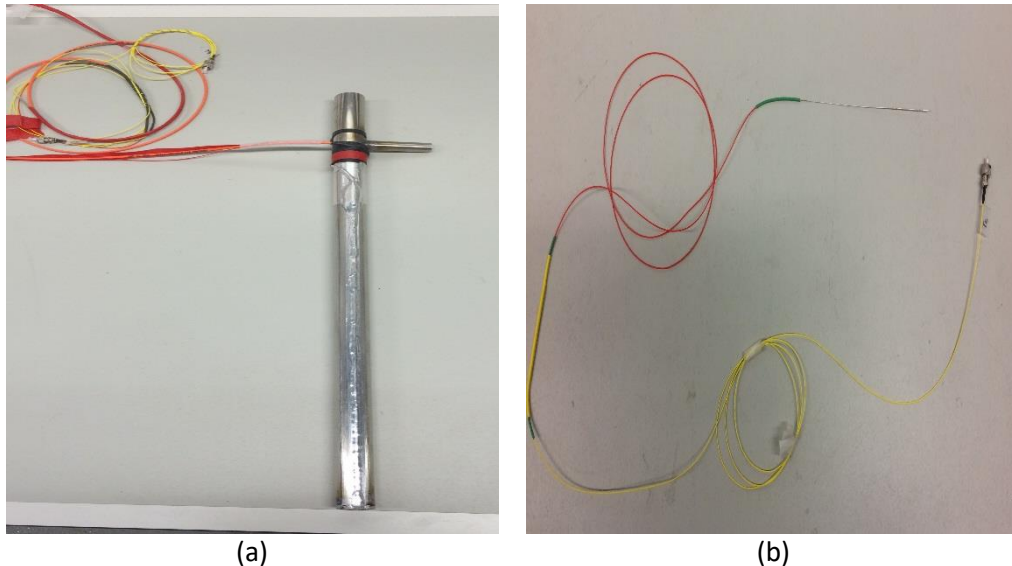


Figure 3-10. (a) FBG strain and temperature sensors mounted on the pile surface, (b) Temperature sensors for use in the sand

3.4.2.2 Fibre Bragg grating

The most commonly used FOS is the fibre Bragg grating. In this study, FBG sensors are used due to the following reasons:

- The sensor is a modified fibre, which means it can be of a similar strength to fibre (Doyle, 2003).
- FBGs measurement is based upon the wavelength of light reflected from the sensor, which is an absolute parameter and is hence traceable. Thus it is possible to make absolute measurements of strain and temperature.
- Most importantly, a number of FBG sensors can be multiplexed in a single length of optical fibre (Glisic & Inaudi, 2007). Commonly, WDM is employed where the FBGs are fabricated such that, under quiescent conditions, they each reflect a different wavelength. This is achieved by ensuring that each FBG has a unique period. A collection of FBGs can have arbitrary physical separation, ranging from overlapping to separations of km. Multiplexing FBGs is used in this research to allow for the measurement of temperature and strain at 5 locations along the pile surface and 4 points at each level in the sand bed (see Figures 3.2 & 3.3). The use of multiplexed FBG sensors eases the process of handling and installation sensors due to the decreased mass and volume of wires associated with

electrical sensors. It also eases the data acquisition process because there is no need for a dedicated channel for each sensor.

A typical optical fibre consists of three parts: core, cladding and a buffer jacket (see Figure 3.11). The diameter of the cladding is typically 125 μm . The buffer jacket, a polymer coating with a thickness of 100 μm , is present to provide mechanical protection and prevent the glass fibre from damage. To produce FBGs, intense, spatially modulated ultraviolet light is used to expose the fibre, producing periodic density alterations of the glass in the fibre core. For a given grating period, a specific wavelength of light, the Bragg wavelength λ_B is reflected, while all other wavelengths pass without any disturbance.

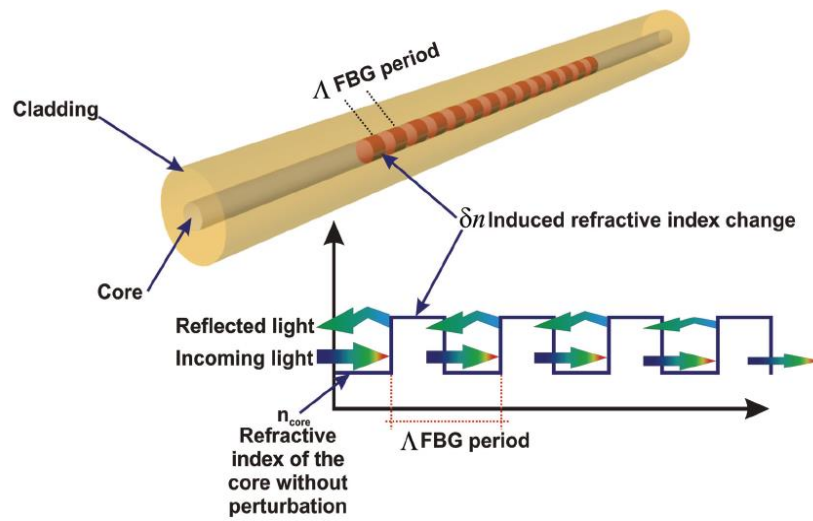


Figure 3-11. Refractive index change of a FBG (Correia, 2008) (Adopted from Zhao, 2001)

The wavelength corresponding to each FBG is dependent on the effective refractive index and grating period (Rao, 1997):

$$\lambda_B = 2n_{eff}\Lambda \quad (3.13)$$

Where,

λ_B : Bragg wavelength

n_{eff} : Effective refractive index

Λ : Grating period

The value of n_{eff} and Λ is equal to 1.482 (Othonos & Kalli, 1999) and 0.535 μm (Correia, 2008) respectively. Changes in temperature and strain will change the Bragg grating wavelength, because the grating periods are temperature and strain dependent, which results in changes in the spectrum of the reflected light (Rao, 1997; Othonos & Kalli, 1999):

$$\Delta\lambda_B = \lambda_B(1 - p_\alpha)\Delta\varepsilon + \lambda_B(\alpha + \xi)\Delta T \quad (3.14)$$

p_α : Photoelastic coefficient

α : Thermal expansion coefficient

ξ : Thermo-optic coefficient

The first and second part of the right side of Equation 3.14 show the shift in the wavelength due to strain and temperature variations, respectively. As shown in Equation 3.14, changes in wavelength due to temperature variations are dependent on two factors (Correia, 2008):

- A change of grating period, Λ , due to the thermal expansion of the fibre
- A change of refractive index, n_{eff} , due to the thermo-optic effect

For the silica optical fibre used in this study, the value of the thermal expansion coefficient is equal to $\alpha=0.55 \times 10^{-6} (\text{°C}^{-1})$. Additionally, the thermo-optic coefficient of a germanium-doped silica core fibre is equal to $\xi=8.6 \times 10^{-6} (\text{°C}^{-1})$ (Correia, 2008).

The strain sensitivity arises from a change during the grating period, and from the strain-optic effect; a strain dependent change in the refractive index. The photoelastic coefficient, p_α is 0.22. To utilise the multiplexing potential of FBGs, 5 FBGs with Bragg wavelengths spaced by approximately 5nm within a wavelength range of 1543nm to 1565nm are fabricated. A typical shift in the wavelength versus pile depth for FBGs located at different depths along the pile, caused by heating and cooling for S3T1, is shown in Figure 3.12. It is found that wavelengths shift between 0.818 to 0.860nm at the end of the heating period and then return to the original position at the end of cooling. Measurement of the temperature and strain sensitivities of the FBG sensors are described in Section 4.3.1.

In this study, the room temperature is kept constant during all tests, but FBG readings show that there are variations in the room temperature. Here, it becomes difficult to distinguish the effects caused by changes in the temperature or mechanical loading. Therefore, it is suggested by Farahi et al. (1990) that temperature compensation is required, and different methods are recommended by Rao (1997). In this study, a separate set of FBGs is used to measure the temperature in the same environment as the strain sensor. The wavelength shift caused by temperature variation is subtracted from total wavelength shift (Rao, 1997).

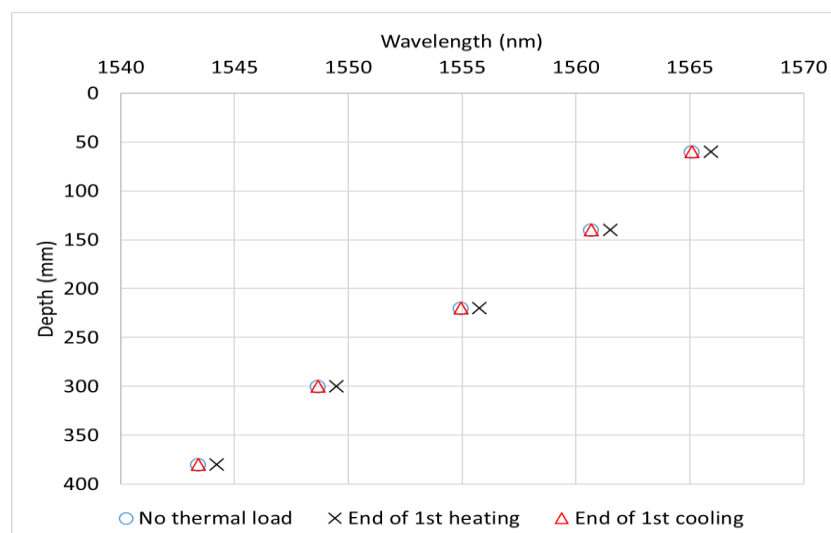


Figure 3-12. Bragg wavelength at different levels along the pile surface- Test S3T1

3.4.2.3 Protection and maintenance of FBGs

One of the main challenges of using FOS is installing them onto structural elements. Depending on the installation environment and the type of fibre, a specific protection measure must be applied. One of the most common protective measures is encapsulating the sensors in tubes. The fibre containing the selection of FBGs used to measure strain is directly attached to the pile surface using superglue and then covered with a layer of Araldite (see Figure 3.13-a). The Araldite is used to protect the FBGs from direct contact with sand or any other external contact. The fibre leads connecting the FBG array to the interrogator is placed in a loose plastic tube (see Figure 3.13-b). At the top of the pile, the fibre lead was attached by using an aluminium adhesive tape. This protects fibres from breakage due to bending (see Figure 3.13-c).

During the early stages of the tests, there was a breakage in the fibre lead, possibly due to bending, at the top of the pile. A replacement fibre was used with extra protection using a stiff plastic tube (see Figure 3.14a). When attaching the fibres to the interrogator, the best practice is to keep the fibres in their natural position, while avoiding applying any strain or sharp bends. Both temperature and strain fibres are covered in a single protective tube at the top of the pile for extra protection.

The optical fibres are attached to the interrogator using standard connectors (see Figure 3.15-b) and regular cleaning of the connectors is required to ensure that the ends of the fibres are not contaminated or scratched, as this would increase the attenuation at the connector. A cleaning instrument, as shown in Figure 3.14b, is used whereby the connector is pushed in the direction shown on the cleaner from right to left (see Figure 3.14C). The cleaning of connectors is conducted every 2 to 3 weeks to avoid any disturbance or light transfer through the fibres.

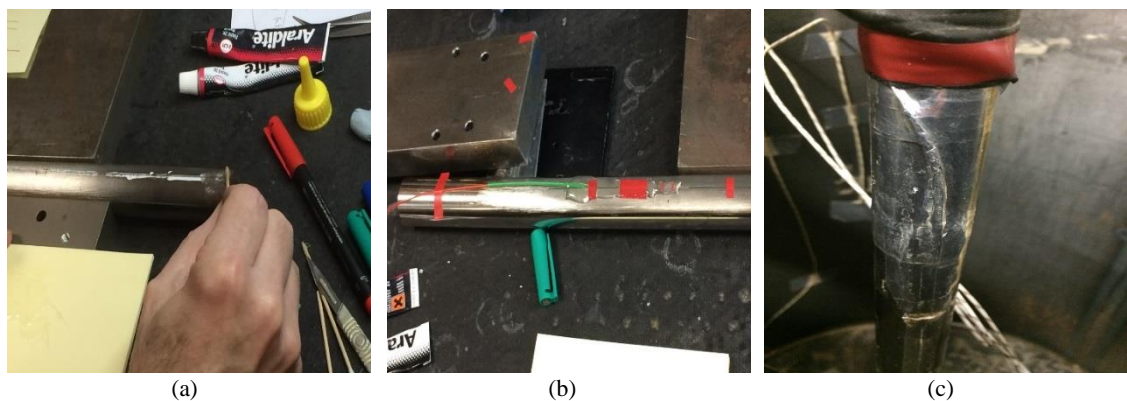


Figure 3-13. (a) FBG protection using Araldite epoxy adhesive, (b) Plastic tubes protection(c) Aluminium tape protection

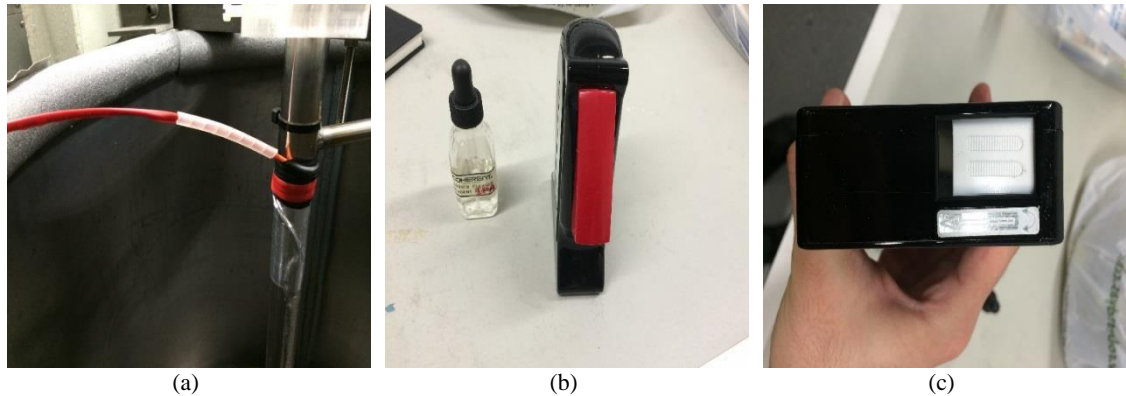


Figure 3-14. (a) Extra protection on the pile head, (b) Fibre optic connector cleaning instrument, (c) Opening of the fibre optic cleaner

3.4.2.4 Data acquisition of FBGs

Data acquisition is conducted using an interrogator provided by the Department of Engineering Photonics at Cranfield University. It consists of a tuneable laser (Tunics Plus) and an 8-channel interrogator (see Figure 3.15-a). One end of each fibre is attached to the pile surface or placed in the sand bed, and the other end of each fibre is connected to the specified channel on the interrogator unit. Each channel is designed for a specific fibre, where PS stands for pile strain sensor, PT is for pile temperature sensor and T1 to T5 are for soil bed temperature sensors (see Figure 3.15-b). The FBG interrogation system uses a tuneable laser as the optical source. The laser power is 2.0mw, and the wavelength is scanned over a range of 1520 to 1620nm at a rate of 100nm/s. The scan is repeated at a rate of 0.5Hz. The light reflected from each fibre is directed to a photodetector. As the laser scans through the spectrum, the voltage output from the detectors allows the reflection spectrum to be recorded. Knowledge of the time sweep of the laser wavelength allows the voltage time-series to be converted into a voltage – wavelength plot, from which the peak wavelength of each FBG in the optical fibre can be determined. The detectors are connected to a data acquisition card, and data is recorded on a PC using software written in LabVIEW. The data are then analysed using a built-in function in LabVIEW that identifies the peaks in the time-series of a single sweep of the laser by fitting a polynomial and differentiating. The wavelength resolution of the system is 1 pm, corresponding to temperature and strain resolutions of 0.1K and $1\mu\epsilon$.

A live feed on the PC screen is used to provide a view of the pile behaviour. All data is logged on the PC as an Excel file and at the end of the test, post-processing LabVIEW software is used to convert raw data into temperature and strain readings. Trial tests show that 1 minute is an acceptable frequency of data collection. A schematic view of the data acquisition process is provided in Figure 3.16.

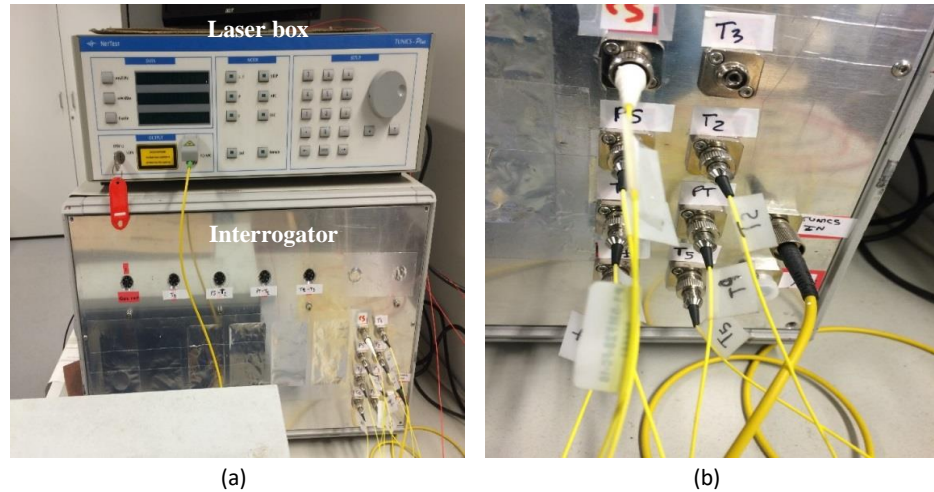


Figure 3-15. (a) Laser box and interrogator, (b) Interrogator channels

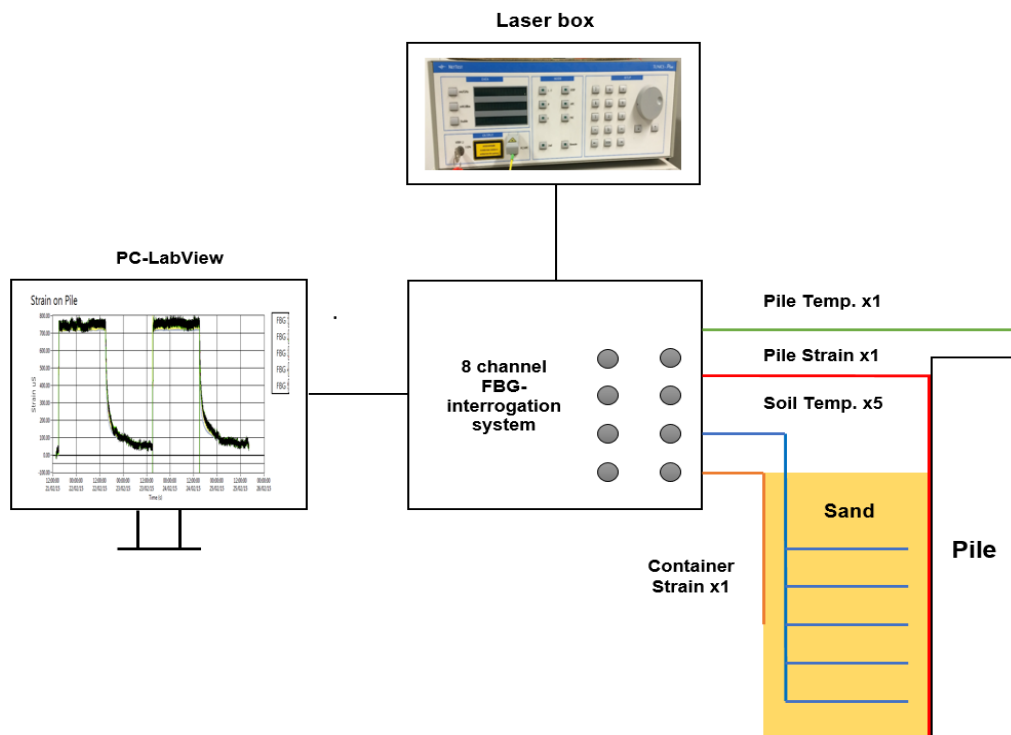


Figure 3-16. Schematic view of the data acquisition

3.5 Sand characteristics tests

3.5.1 Grain size distribution

A grain size distribution test is conducted using a dry sieving method according to BS 1377-2:1990:9.3 (British Standards Institution, 1990). It is found that the soil used in this study is a poorly graded uniform fine sand with a relatively small range of particle sizes, approximately between 0.1 and 0.3 mm, and a uniformity coefficient of 2.32 (see Figure 3.17). Sand with a grain size of between 0.06 and 0.2mm is categorised as fine graded sand (Atkinson, 2007). Effective grain size, D_{10} and D_{60} are equal to 0.086 and 0.2mm respectively. Data collected in this test is given in Appendix D.

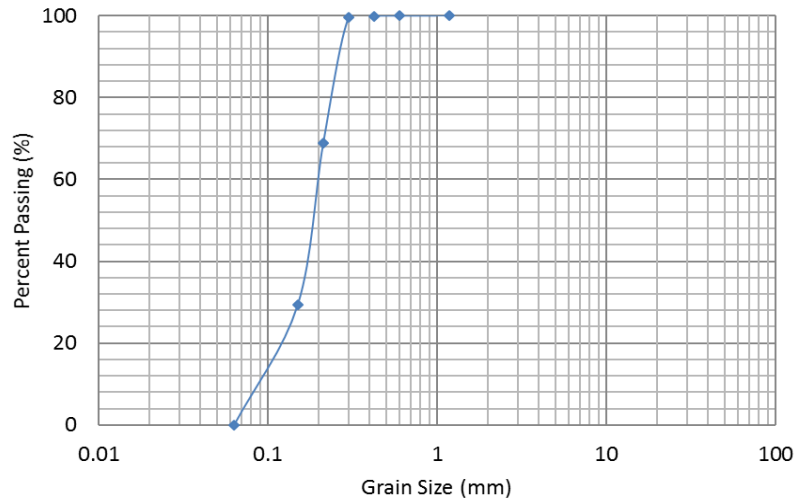


Figure 3-17. Sand grading curve

3.5.2 Specific gravity

To determine the specific gravity of sand, G_s , the small pycnometer method for particles finer than 2 mm is used in accordance with BS 1377-2:1990:8.3 (British Standards Institution, 1990). Five tests are carried out, and the average measured value is 2.64 gr/cm^3 . For sand that consists mainly or wholly of quartz, G_s is usually assumed as 2.65 gr/cm^3 , which is the density of quartz (Head, 2006). Data recorded for specific gravity measurements are provided in Appendix E.

3.5.3 Limiting densities

Maximum and minimum dry densities of sand are determined using vibrating hammer method according to BS 1377-4:1990 (British Standards Institution, 1990) for cohesionless soil; clauses 4.2 and 4.4 respectively. It is found that maximum and minimum densities are equal to 1.658 and 1.349 gr/cm^3 respectively, which are closely in line with 1.590 and 1.320 gr/cm^3 given by Kong and Zhang (2008) for Leighton Buzzard sand with D_{50} equal to 0.14mm, which is a finer sand to the sand used in this study with D_{50} of 0.18mm. Using minimum and maximum densities, the maximum and minimum void ratio is calculated at 0.957 and 0.592 respectively using Equations 3.15 and 3.16. Data for both tests are given in Appendix F.

$$e_{max} = \frac{G_s \cdot \gamma_w}{\gamma_{d,min}} - 1 \quad (3.15)$$

$$e_{min} = \frac{G_s \cdot \gamma_w}{\gamma_{d,max}} - 1 \quad (3.16)$$

3.5.4 Direct shear test

Shear strength of sand is measured using the direct shear box test method according to BS 1377: Part 7:1990:4 (British Standards Institution, 1990), using a small box of 60 x 60mm, suitable for soils with a maximum particle size of 4mm (Head and Epps, 2011). Maximum normal stress is usually chosen based on the magnitude of applied pressure on the soil in the test condition or in-

situ. Due to the use of dry sand in this study and the absence of surcharge pressure on the sand surface, the magnitude of applied stress at the base of the container from the sand self-weight is equal to 5.28kPa and 5.88kPa for Scenarios 3, 4 and 5 respectively. Four sets of vertical stresses equal to 25, 50, 75, 100kPa are applied to 4 specimens. The relation between the shear stress and horizontal displacement is shown in Figure 3.18. Using both peak and critical shear stresses for each test, a relationship between shear stress and normal stress is developed (see Figure 3.19). Using the slope of $\sigma - \tau$ in Figure 3.19, the peak and critical angle of friction are determined as approximately 35° and 27.8° respectively.

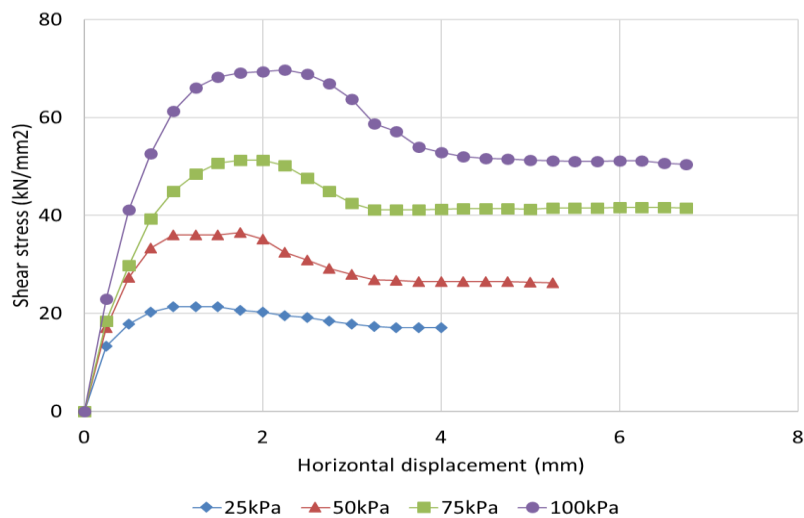


Figure 3-18. Shear stress vs. horizontal displacement- shear box test

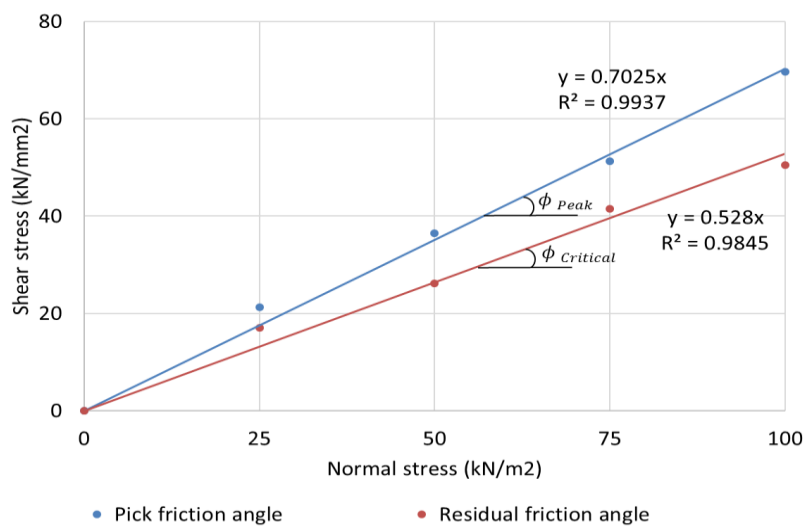


Figure 3-19. Shear stress vs. normal stress for peak and critical shear states

3.6 Test programme

Five series of experiments are carried out to investigate the behaviour of thermal piles under mechanical-only, thermal-only and thermo-mechanical loading. Tests are divided into 5 Scenarios based on the framework presented in Chapter 2 for Scenarios 1 to 4 and an additional Scenario 5 for tests on the base and shaft resisting piles. The test schedule with variables involved is presented in Table 3.6. As shown in Table 3.6, a labelling mechanism is used with a format of S#1TM#2, where:

- S: Scenario
- #1: Scenario number
- T: Thermal loading, if applicable
- M: Mechanical loading, if applicable
- #2: Test number within that category in the specified Scenario

For instance, S5TM2 stands for the test in Scenario 5 where both thermal and mechanical loadings are present, and it is the 2nd test in this Scenario. Test labels do not present the magnitude of mechanical loading or restraint condition on the pile (see Table 3.6) A summary of test conditions and procedures in each Scenario is presented below. Additionally, 4 tests are performed to determine the bearing capacity of the pile in Scenario 5, S5M1-S5M4, which are described in Section 5.2).

Table 3-6. Test Programme - Scenarios 1 to 5

Test no.	Temp. (°C)	Axial load (N)	Top restraint	Bottom restraint	Soil restraint
SCENARIO 1					
S1T1	50	0	Free	Free	No
SCENARIO 2					
S2TM1	50	30	Mechanical load	Standing	No
S2TM2	50	55	Mechanical load	Standing	No
S2TM3	50	75	Mechanical load	Standing	No
S2TM4	50	120	Mechanical load	Standing	No
S2TM5	50	160	Mechanical load	Standing	No
SCENARIO 3					
S3T1	50	0	Free	Free	Yes
S3T2	50	0	Free	Standing	Yes
SCENARIO 4					
S4TM1	50	30	Mechanical load	Free	Yes
S4TM2	50	55	Mechanical load	Free	Yes
S4TM3	50	75	Mechanical load	Free	Yes
S4TM4	50	120	Mechanical load	Free	Yes
S4TM5	50	160	Mechanical load	Free	Yes
S4TM6	50	75	Mechanical load	Standing	Yes
S4TM7	50	120	Mechanical load	Standing	Yes
S4TM8	50	160	Mechanical load	Standing	Yes
SCENARIO 5					
S5M1	22	300	Mechanical load	Sand deposit	Yes
S5M2	22	320	Mechanical load	Sand deposit	Yes
S5M3	22	320	Mechanical load	Sand deposit	Yes
S5M4	22	320	Mechanical load	Sand deposit	Yes
S5TM1	50	0	Free	Sand deposit	Yes
S5TM2	50	75	Mechanical load	Sand deposit	Yes
S5TM3	50	150	Mechanical load	Sand deposit	Yes
S5TM4	50	225	Mechanical load	Sand deposit	Yes

3.7 Test procedure

3.7.1 Scenario 1

The aim of Scenario 1 test is to understand the behaviour of a pile under thermal loading in the absence of soil and mechanical loading restraints. The magnitude of mechanical loading applied to the pile head in Scenarios 2 and 4 are equal to approximately 18.1, 33.3, 45.4, 72.7 and 97% of the ultimate capacity of the pile at 165N (see Table 3.6). A description of how ultimate shaft resistance is achieved is given in Section 4.2. In S1T1, top and bottom restraints do not exist, and the pile is held in position using a support shown in Figure 3.20-a. For S1T1, the following procedure is followed:

1. The pile is kept constant in the middle of the container using a pile support (see Figure 3.20-a). The triangular pile head support keeps the pile in place, but it is loose enough to allow the

pile to move upwards and downwards. To protect the sensors, two Latex membranes are cut into circular shapes and fitted to the bottom of the container (see Figure 3.21-a).

2. Inlet and outlet pipes are attached to the pile, and the loading frame is placed on top of the pile head. An LVDT and dial gauge are placed on the loading frame to record any possible head movement. The thermocouple is also attached to the pile surface.
3. To have a comparable situation with Scenarios 3 and 4, the pile is filled with water, without circulating the water to avoid possible effects on strain readings.
4. The laser box, LabVIEW software and LVDT software are started to run.
5. Then, the water circulator is turned on, and water is heated up to 50°C and is kept constant for 24 hours. Afterwards, it is left to cool for 24 hours to complete the 1st heating-cooling cycle.
6. The 2nd heating-cooling cycle is repeated similarly to the previous step.

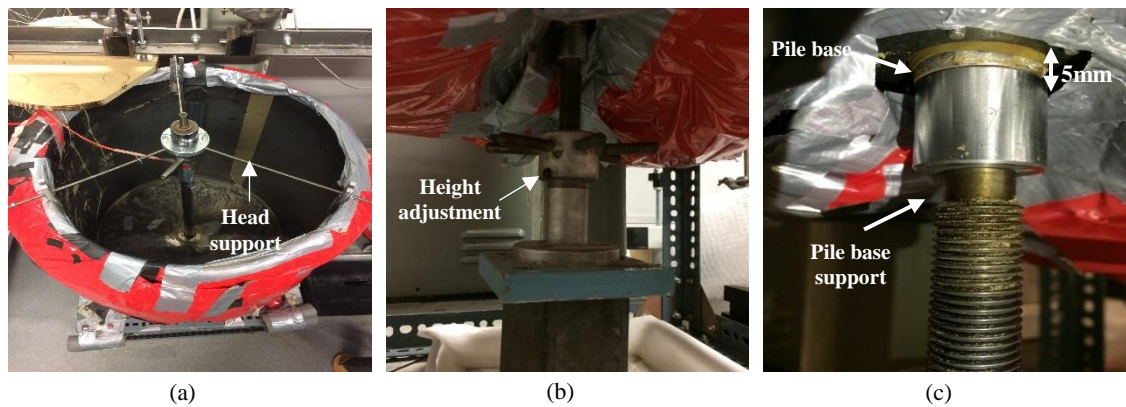


Figure 3-20. (a) Pile head support, (b) & (c) Pile base support

3.7.2 Scenario 2

Similar to the aim of Scenario 1, but instead of using thermal-only test, mechanical loading and a combination of mechanical and thermal loading is applied to the pile, yet without soil restraint. In S2TM1-S2TM5, the pile is restrained at the top by weights used as mechanical loading, while the bottom is restrained by a pile base support where the pile is standing. For S2TM1-S2TM5, the following procedure is followed:

1. Steps 1 to 4 for S1T1 in Scenario 1 is repeated. Additionally, base support is located at the bottom of the pile.
2. The first mechanical loading is applied to the pile head and a 10-minute relaxation period is considered, as no considerable movement is expected.
3. Mechanical loads are kept constant, and water temperature is increased from the room temperature to approximately 50°C and kept constant for 24 hours. It is then followed by a 24-hour cooling period, and the same procedure is repeated for the 2nd heating-cooling cycle.

4. In the end, mechanical loads are removed in the same order as loading and step 4 for S1T1 is repeated.

3.7.3 Scenario 3

The aim of Scenario 3 tests, S3T1 and S3T2, is to understand the pile behaviour in the sand during two heating-cooling cycles in the absence of mechanical loading. In S3T1, there is no restraint on the pile head and bottom, but in S3T2 the pile bottom is supported to determine the effect of end bearing on the strain profile. In Scenarios 3 to 5, sand with properties described in Section 3.5 is used to fill the container. The addition of soil induces lateral restraints to the pile, unlike in Scenarios 1 and 2. Additionally, in Scenarios 3 to 5, FBG sensors are positioned at different layers in the soil to monitor the temperature in the sand bed.

To have similar sand beds in Scenarios 3 and 4, a sand deposition method is developed to achieve the desired relative density for all tests. The available methods in the literature are: (1) raining method, (2) pouring the air-dried sand through the nozzle, (3) pluviating air-dried sand, (4) using tamping to compact the surface and vibrating table (Paik and Salgado, 2004; Yasufuku and Hyde, 1995). In this study, to avoid any possible damage to FBGs, the pile is initially placed in the container and then sand is poured around the pile using the procedure described below.

Initially, a trial test was performed to determine the state of the sand in the container. Sand was poured in the container layer by layer, and then a slight compaction was applied using a wooden tamper to level the sand surface. Using Equations 3.17 and 3.18, relative density is measured at 57.6% which categorises the sand bed as a medium-dense sample, $35% < D_r < 65%$ (Kaniraj, 1988).

Relative density can be calculated using void ratio values or density:

$$D_r = \frac{e_{max} - e}{e_{max} - e_{min}} \quad (3.17)$$

$$D_r = \frac{\rho_D - \rho_{D,min}}{\rho_{D,max} - \rho_{D,min}} \cdot \frac{\rho_{D,max}}{\rho_D} \quad (3.18)$$

Where, e_{max} and e_{min} are the maximum and minimum void ratios, they are measured based on the limiting densities found in Section 3.5.3. ρ_D , $\rho_{D,min}$ and $\rho_{D,max}$ are measured; minimum and maximum dry densities, respectively. Relative density of 57.6% is chosen as the target D_r and a sand deposition method described in the fourth step below is used to achieve it. Following the 10-step test procedure is followed for Scenario 3 tests:

1. 1st step similar to S1T1.
2. All three thermocouples, TC1-TC3, are attached to their surfaces.
3. An insulation jacket with properties described in Section 3.3.2 is used to cover the container wall and base.
4. Sand is poured into the container using the following procedure:

- a. A target relative density of 57.6% is chosen for medium-dense samples.
 - b. To achieve target D_r , the required dry density is equal to $1.51\text{gr}/\text{cm}^3$. The effective pile length embedded in the soil is set at 390mm. In order to achieve the dry density target, 114.3kg of sand is poured into the container with a final soil height of 390mm.
 - c. The soil mass of 114.3kg is divided into 15 batches of 7.2kg and one batch of 6.3kg.
 - d. Sand is poured into the container from the container edge at the height of 500mm. After pouring the sand at each layer, it is slightly compacted to level the surface.
 - e. Sand deposition is continued until it reaches the heights of 10, 90, 170, 250 and 330mm from the base of the container, where FOSs T1, T2, T3, T4 and T5 are installed. The approximate height of the soil was measured using a ruler tape attached to the container wall. This allows aligning the sensors in the soil with those on the pile surface. In the compaction process, care is taken to avoid damaging the sensors.
 - f. The installation of FOSs in the sand bed involves three steps. Initially, the fibre is laid on the sand, 5mm away from the pile surface (see Figure 3.22-a). Then, the fibre is taped to the container wall to fix the position of the fibre (see Figure 3.22-b). Then, the fibre in the sand needs to be adjusted. In the end, sand is slowly poured on the fibre without applying any compaction. The location of fibre needs to be checked at the end to make sure that it has not moved. Moreover, at the end of each test, a visual inspection of the sensors is done to ensure that it has not moved during the test and sand deposition (see Figure 3.22-c).
 - g. At the end of the sand pouring stage, the sand surface is levelled, and the height of the sample is measured with $\pm 2\text{mm}$ error, resulting in $\pm 2.45\%$ change in relative density.
 - h. The insulation jacket is used to cover the sand surface.
5. A water circulator is connected to the pile using inlet and outlet transparent PVC pipes with internal and external diameters of 12 and 15mm respectively (see Figure 3.21-b). They are covered with Climaflex insulation pipes with internal and external diameters of 13 and 15mm respectively, and a thermal conductivity value of $0.034\text{W}/\text{m}\cdot\text{k}$ (see Figure 3.21-c). Pipes are filled with water using a tap on the inlet pipe until full, with no air trapped in the tubes.
 6. The loading frame is placed on the pile head. The LVDT and dial gauge are placed at two sides of the loading plate, and both are levelled using a spirit.
 7. The laser box is switched on using the following procedure:
 - Switch it on and leave it until the initialising and referencing is finished.
 - Enable the power and set it at 2.0mw.
 - Enter the wavelength ranges from 1520-1620nm with 0 changes in the wavelength.
 - dt is set at 0.1s.

8. LabVIEW, Picologger and LVDT software are all turned on, and the pile base support is removed. The pile settlement due to the pile self-weight is recorded. The LVDT recording frequency is set as 3 seconds. Dial gauge readings are recorded at 5-minute intervals using a camera attached to the wall beam to provide an extra check on LVDT readings (see Figure 3.21-c).
9. The water circulator is turned on, and the temperature is increased from 22 to 50°C. It is a swift heating process, and no intermediate heating steps are involved. The water enters the steel pile from the top of the pile and it is then filled the entire pile. After filling up the pile, it is then moves outward from the pipe located at the pile head. This process is repeated for 24 hours. After 24 hours of heating, the water circulator temperature is returned to 22°C, and it is left to run for a further 24 hours. The same inlet-outlet of water flow happens during the cooling period. During the heating process, it takes a short time for the pile to reach to the target temperature while in the cooling period, it takes much longer. For the cooling period, the water circulator can only circulate the water and it cannot force the water to lower temperatures, In fact, the applied water circulator in this study is only capable of heating the water, in a forced process, while it cannot be used for the cooling purposes. Comparison between temperature recordings for the heating and cooling processes are given in Chapters 4 and 5.
10. After the first heating-cooling cycle, step 9 is repeated for the second cycle. At the end of each test, sand is removed layer by layer and then replaced for the next test.

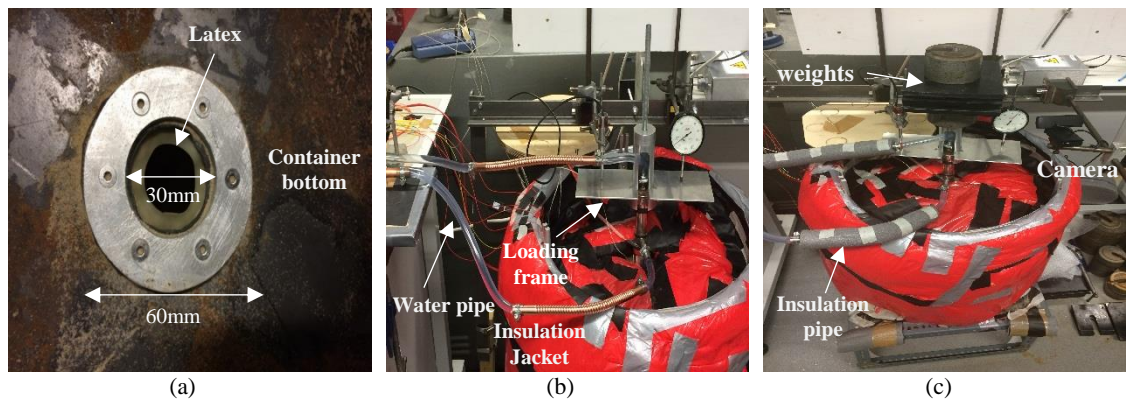


Figure 3-21. (a) Latex protection, (b) Scenario 3 test set-up, (c) Scenario 4 test set-up

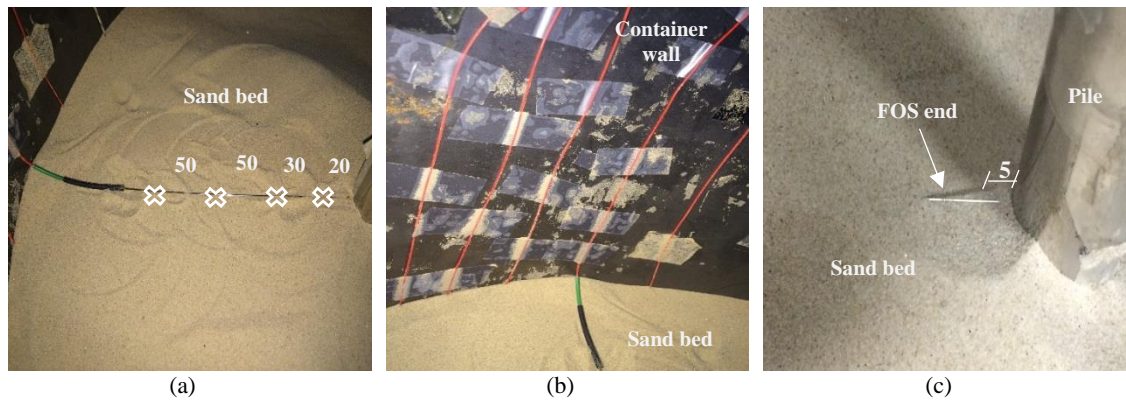


Figure 3-22. Installation of FOS in the sand bed, dimensions in mm

3.7.4 Scenario 4

In Scenario 4, in addition to the thermal loading applied in Scenario 3, mechanical loadings of 30, 55, 75, 120 and 160N are applied on the pile head. The aim is to understand the pile response under combined mechanical and thermal loadings. The pile head is held with weights used for mechanical loading, while the pile base is free to move in S4TM1-S4TM5 and supported by a pile base in S4TM6-S4TM8. A summary of the test procedure for the Scenario 4 test is given below:

1. Steps 1-8 are similar to Scenario 3. For S4TM1-S4TM5, the pile base is removed at the end of the 8th step, but for S4TM6-S4TM8 the pile base support is kept in position.
2. Mechanical loading is applied using 1, 2, and 5kg weights based on the target load with a relaxation period ranging from 10-45 minutes after each loading step (see Figure 3.21-c).
3. Step 9 is similar to the procedure described in Scenario 3. At the end of each test, weights are unloaded in the same order as loading and sand is removed layer by layer.

3.7.5 Scenario 5

In Scenario 5 the pile base sits on a 90mm sand bed, and the embedded pile length is equal to 350mm. Moreover, the distance between the top sensor and the soil surface is equal to 15mm compared to 60mm for Scenarios 3 & 4. The distance between FBG sensors are kept constant, and they are all shifted up to be placed at the same levels as those on the pile surface.

Mechanical loadings applied on the pile head in Scenario 5 are equal to 0, 75, 150 and 225N equal to 0, 25, 50 and 75% of the ultimate bearing capacity of the model pile (see Section 5.2). A summary of the test procedure for Scenario 5 test is given below:

1. Steps 2 and 3 in the Scenario 3 test procedure is repeated. There is no need to conduct step 1.
2. Sand is poured into the container with small differences with Scenarios 3 and 4:
 - a. A target relative density of $D_r = 57.6\%$ is chosen for medium-dense samples. The total soil weight is equal to 129kg and is used for a 440mm soil height.
 - b. The total mass is divided into 17 batches of 7.2kg and a final batch of 6.6kg.

- c. Step 4-d from Scenario 3 is repeated. Sand deposition is continued until it reached a height of 90mm where the pile base is placed upon it and kept constant using the pile support.
 - d. Similarly, the 4-e to the 4-h procedure is followed with one difference in that the location of sensors is 10, 90, 170, 250 and 330mm from the pile base and not the container base.
3. Steps 5 to 8 in the Scenario 3 test procedure is repeated.
4. For S5TM1, steps 9 and 10 from Scenario 3 are repeated. For S5TM2-S5TM4, before applying step 9, aforementioned mechanical loading is applied, followed by steps 9 and 10.

Chapter 4. Thermo-mechanical behaviour of shaft resisting pile

4.1 Introduction

This chapter presents the results of the laboratory tests that were performed to determine the effects of thermo-mechanical loading on the performance of a shaft resisting pile. The test procedures for each scenario are described in the previous chapter. The results presented in this chapter will also be used to assess the behaviour of a shaft and base resisting pile in Chapter 5. A shaft bearing capacity test is used to determine the ultimate capacity and, therefore, the required magnitude of mechanical loading for each test. This is followed by a thermal reference test to determine the thermal expansion coefficient of the pile, and to determine the temperature and strain sensitivities of FBGs on the pile. The test results for the shaft resisting piles are divided into scenarios 1 to 4, according to the framework given by the Thermal Pile Standard (GSHPA, 2012). This is followed by the presentation of the test results for Scenarios 1 and 2, where no soil is present, followed by the test results for Scenarios 3 and 4. Different aspects of the thermo-mechanical behaviour of thermal piles are investigated: observed thermo-elastic and thermo-plastic behaviours, variations in the DoF of the pile, induced axial loading due to cyclic temperature changes, pile head displacement, and variations in the mobilised friction along the pile length. The results are compared with the framework proposed by the Thermal Pile Standard (GSHPA, 2012) to assess the applicability of the framework for 1g model studies and, in particular, piles installed in dry sand.

4.2 Ultimate shaft resistance of model pile

To understand the effects of additional thermal loading on the load-bearing capacity of a model pile, its shaft resistance under mechanical loading needs to be determined. The magnitudes of mechanical loadings in Scenarios 1 to 4 are different percentages of the ultimate shaft resistance of the pile. The shaft resistance of the pile is determined using a similar test set-up as in Scenarios 3 and 4. There are different techniques outlined in the literature for estimating the shaft capacity of piles (see Appendix I). According to BS 8004:1986 (British Standards Institution, 1986), the shaft resistance is fully mobilised when the pile head settlement is equal to 1% of its diameter (0.28mm in this study), and a small increment in load will result in continuous displacement. In this study, the pile is loaded until the visual failure is achieved. An incremental loading procedure is followed: first, a 10N load is applied to the pile head; then, from 10N to 90N, loads are implemented in 20N increments at 10-minute intervals; and, from 90N upwards, loads are increased by 10N at each stage, until the visual failure is achieved. Three tests were carried out, and an average ultimate shaft capacity of 165N was found. The pile head displacement for one of the three tests is shown in Figure 4.1. From these results, it was decided that the magnitudes of

the mechanical loads that are to be applied to the pile are 0N, 30N, 55N, 75N, 120N and 160N, which are approximately 0%, 18%, 33%, 45%, 72% and 96% of the ultimate shaft capacity.

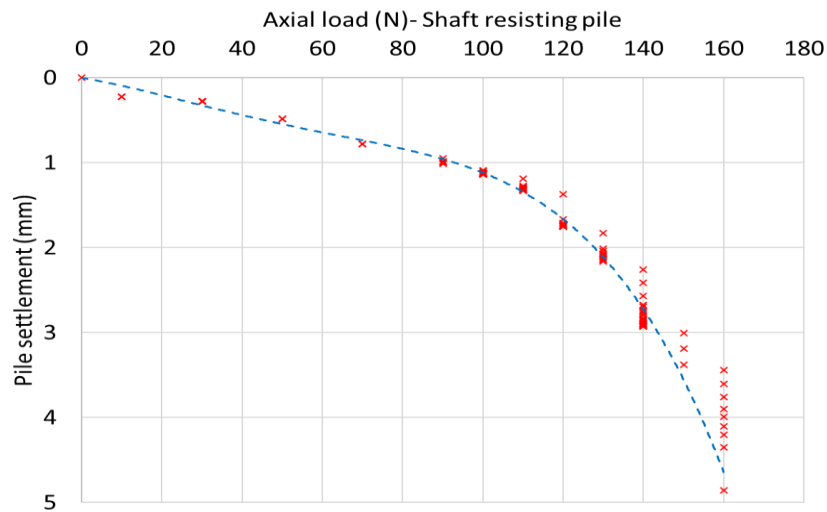


Figure 4-1. Load-Displacement curve for a shaft resistant pile

4.3 Scenario 1

The aim of the Scenario 1 test is to understand the pile's response when it is under no restraint from the pile head and surrounding soil. The thermal expansion coefficient of the model pile, and the temperature and strain sensitivities of FBGs located at five levels along the pile, are also measured. S1T1, a reference (or calibration) test, is performed at which the pile is held in the middle of an empty container, using a lateral support to allow the free expansion of the pile at both ends. In S1T1, the pile is heated up to 50°C, from an initial room temperature of 22°C, for 24 hours, and then returned to room temperature during the cooling period for another 24 hours. The same process is repeated in the second cycle. As mentioned in Chapter 3, two sets of optical fibres are used on the pile surface; one set measures the temperature, and the other set measures the temperature and strain. A brief description of the procedure used to determine the temperature and strain sensitivities of the FBGs is given below. This is followed by a description of the procedure used to determine the thermal expansion coefficient of the model pile.

4.3.1 Temperature and strain sensitivity of FBGs

- Step 1: The temperature of the temperature-only sensors – i.e. the FBGs that were not directly bonded to the pile surface but were in the loose tube – was calculated from the shift in the wavelengths by using Equations 4.1 to 4.5. The initial wavelength values of FBGs are chosen during the manufacturing of the multiplexed fibres, with an approximate 5nm increase in the initial wavelength values:

$$\lambda_{T_{i,1}} = 1544.19 + 0.011 * (T_{i,1} - 21.7) \quad (4.1)$$

$$\lambda_{T_{i,2}} = 1548.83 + 0.011 * (T_{i,2} - 21.7) \quad (4.2)$$

$$\lambda_{T_{i,3}} = 1554.90 + 0.011 * (T_{i,3} - 21.7) \quad (4.3)$$

$$\lambda_{T_{i,4}} = 1560.57 + 0.011 * (T_{i,4} - 21.7) \quad (4.4)$$

$$\lambda_{T_{i,5}} = 1564.49 + 0.011 * (T_{i,5} - 21.7) \quad (4.5)$$

In these equations, 1544.19nm, 1548.83nm, 1554.90nm, 1560.57nm and 1564.49nm are the initial wavelength values for TP1 to TP5 respectively, 0.011nm/°C is the temperature sensitivity of the loose tube, and 21.7°C is the initial pile temperature. $T_{i,j}$ is the temperature at time 'i' and level 'j' (°C), and $\lambda_{T_{i,j}}$ is the wavelength at time 'i' and level 'j' (nm).

- Step 2: To determine the temperature sensitivity of FBGs that are bonded to the pile surface, the wavelength values of the temperature and strain-measuring fibre are plotted against the temperature readings from temperature-only FBGs for all five FBGs: TP1–TP5 (see Figure 4.2). It is observed that the temperature sensitivity of FBGs that are bonded to the pile surface varies between 29.7pm/°C and 32.5pm/°C, with an average of 30.66pm/°C. This is 2.28 to 2.95 times greater than the theoretical value of bare fibre given by Rao (1997), which is 11pm/°C to 13pm/°C (see Table 4.1).

Table 4-1. Temperature sensitivity of FBGs

FBGs	Wavelength vs temperature (fitted)	Temperature sensitivity (pm/°C)
TP1	$\lambda = 0.0325T + 1542.7$	32.5
TP2	$\lambda = 0.0302T + 1548$	30.2
TP3	$\lambda = 0.0308T + 1554.3$	30.8
TP4	$\lambda = 0.0297T + 1560.1$	29.7
TP5	$\lambda = 0.0301T + 1564.4$	30.1

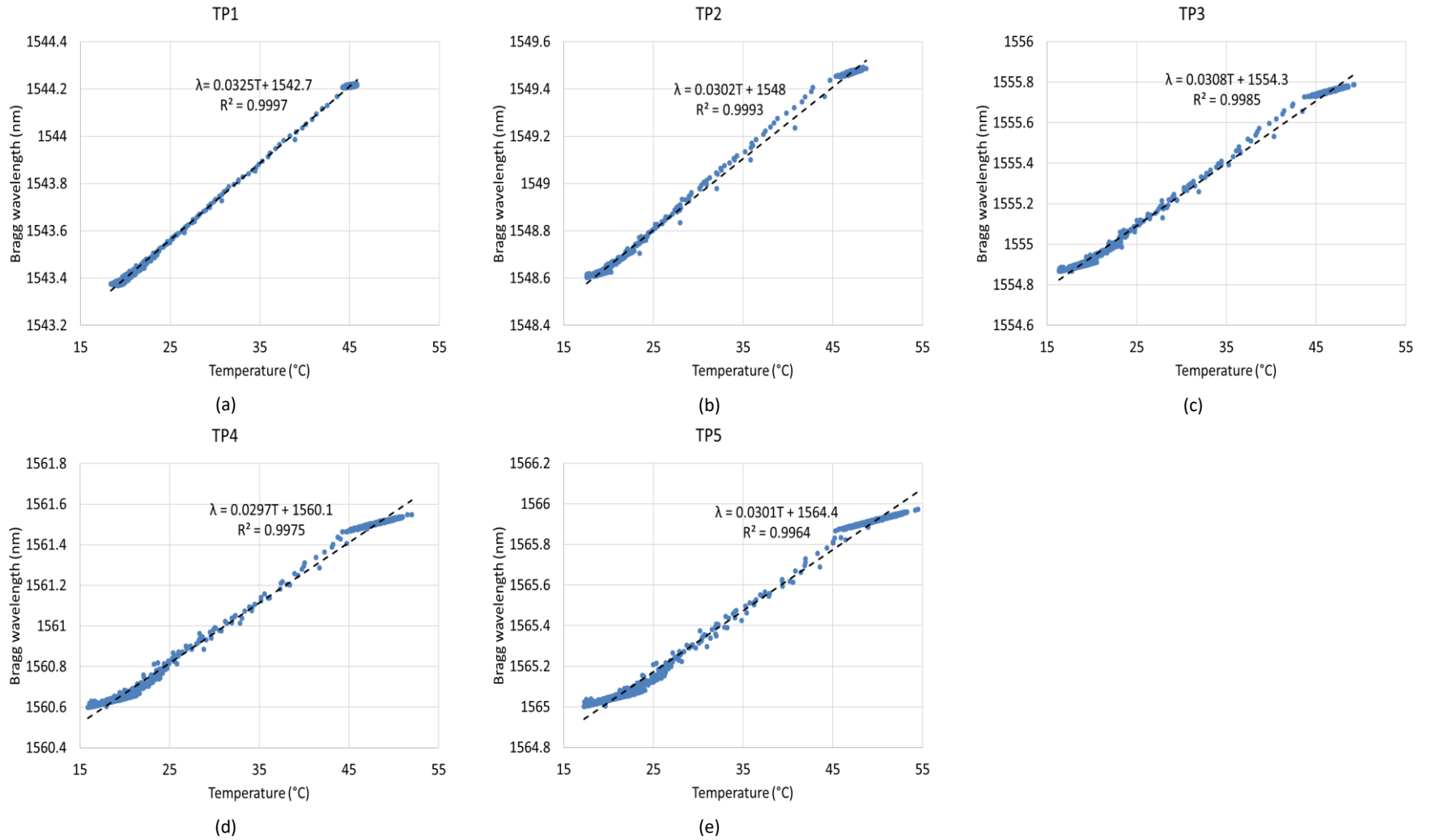


Figure 4-2. Variations in wavelengths with temperature – S1T1

- Step 3: In order to measure the strain sensitivity, the compensated shift in the wavelength has to be plotted against the compensated strain. As mentioned in Section 3.4.2.2, FBGs in the loose tube, which are attached onto the pile surface, are used to compensate the effects of temperature on the readings. Two sets of wavelengths are measured in each test: (1) the wavelength measured by the FBGs in the loose tube ($\Delta\lambda_{T,i}$) (see Figure 4.3-b); and (2) the wavelength measured by the FBGs that are bonded by epoxy resin onto the pile surface ($\Delta\lambda_{Total,i}$) (see Figure 4.3-a). Using Equation 4.6, which is given by Leung et al. (2013), the compensated strain can be obtained by subtracting the shift in the wavelength for the loose tube FBGs from the total shift in the wavelength for the FBGs that are bonded onto the pile surface. The shift in the wavelength for the FBGs that are bonded onto the pile surface is due to the expansion and contraction of the pile surface under mechanical and thermal loading, while the shift in the wavelength for the loose fibre is due to the variations of the ambient temperature (Mohamad, 2012).

$$\varepsilon_{SPi} = \left(\frac{1}{1 - p_\alpha} \right) \left(\frac{\Delta\lambda_{Total,i}}{\lambda_0} - \frac{\Delta\lambda_{T,i}}{\lambda_{T0}} \right) \quad (4.6)$$

Where:

$\Delta\lambda_{Total,i}$: The total uncompensated shift in the wavelength of surface-bonded FBGs

λ_0 : The initial wavelength of surface-bonded FBGs

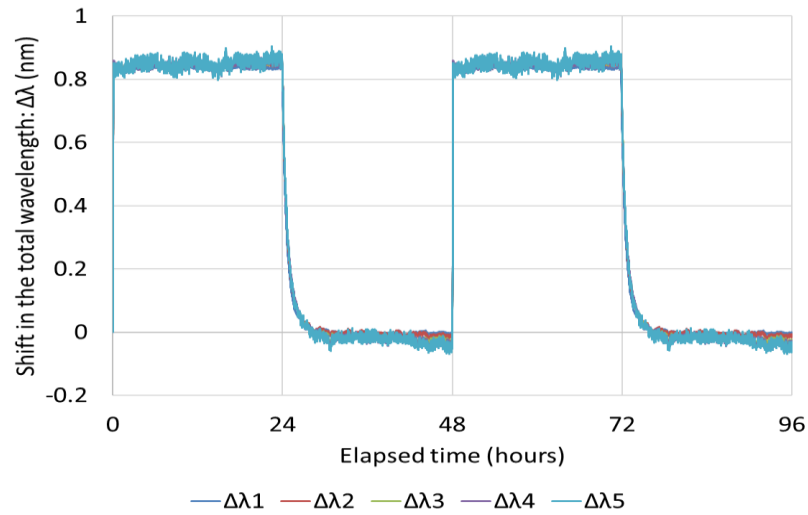
$\Delta\lambda_{T,i}$: The shift in the wavelength of FBGs in the loose tube, using Equations 4.1–4.5

λ_{T0} : The initial wavelength of temperature-measuring FBGs in the loose tube

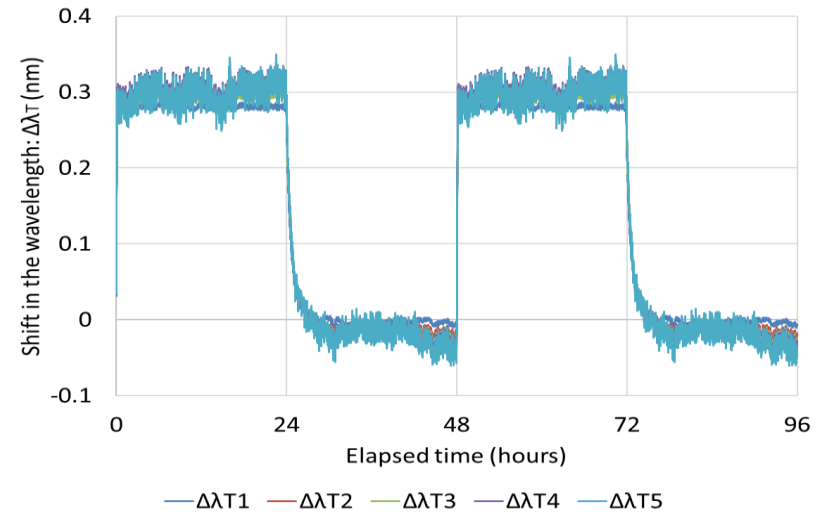
- Step 4: The compensated shift in the wavelength, $\Delta\lambda_{Total} - \Delta\lambda_T$, is plotted against the compensated strain, using Equation 4.6, to determine the strain sensitivity of FBGs (see Figure 4.4 and Table 4.2). Strain sensitivity varies between 0.001204nm/ $\mu\varepsilon$ and 0.001221nm/ $\mu\varepsilon$, which agrees with the 0.0012nm/ $\mu\varepsilon$ that is suggested by Rao (1997). This means that, to determine the compensated observed strain, the $\Delta\lambda_{Total} - \Delta\lambda_T$ at a specific time will be multiplied by 830.56 $\mu\varepsilon$ /nm, 827.81 $\mu\varepsilon$ /nm, 824.40 $\mu\varepsilon$ /nm, 821.69 $\mu\varepsilon$ /nm and 819 $\mu\varepsilon$ /nm, at the SP1 to SP5 levels respectively.

Table 4-2. Strain sensitivity of FBGs

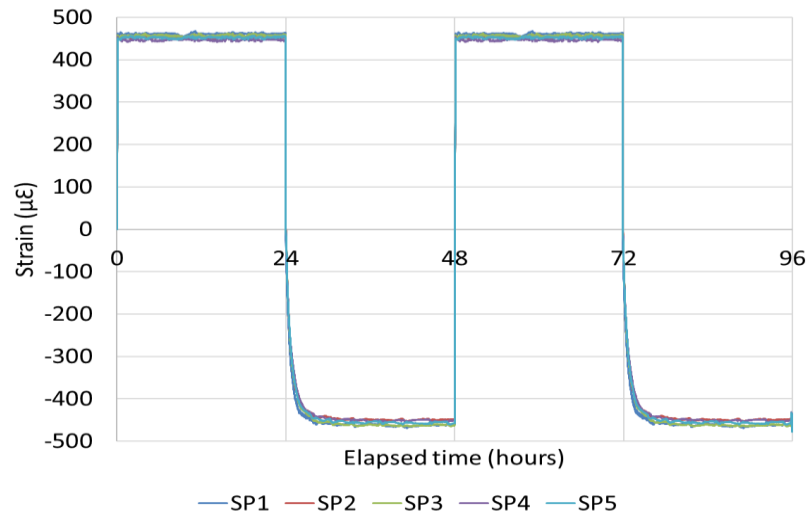
FBGs	Wavelength vs strain (fitted line – Figure 4.4)	Strain sensitivity ($\mu\varepsilon$ /nm)
SP1	$\Delta\lambda_1 = 0.001204\Delta\varepsilon_1$	830.56
SP2	$\Delta\lambda_2 = 0.001208\Delta\varepsilon_2$	827.81
SP3	$\Delta\lambda_3 = 0.001213\Delta\varepsilon_3$	824.40
SP4	$\Delta\lambda_4 = 0.001217\Delta\varepsilon_4$	821.69
SP5	$\Delta\lambda_5 = 0.001221\Delta\varepsilon_5$	819



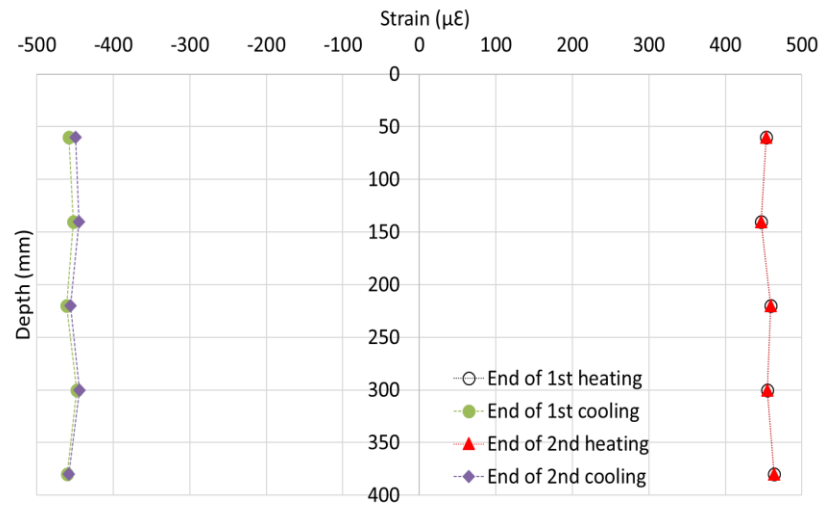
(a)



(b)



(c)



(d)

Figure 4-3. (a) Shift in total wavelength vs time, (b) shift in the wavelength of temperature FBGs during heating-cooling cycles, (c) compensated observed strain along the pile at different levels, (d) observed strain at various depths at the end of heating and cooling

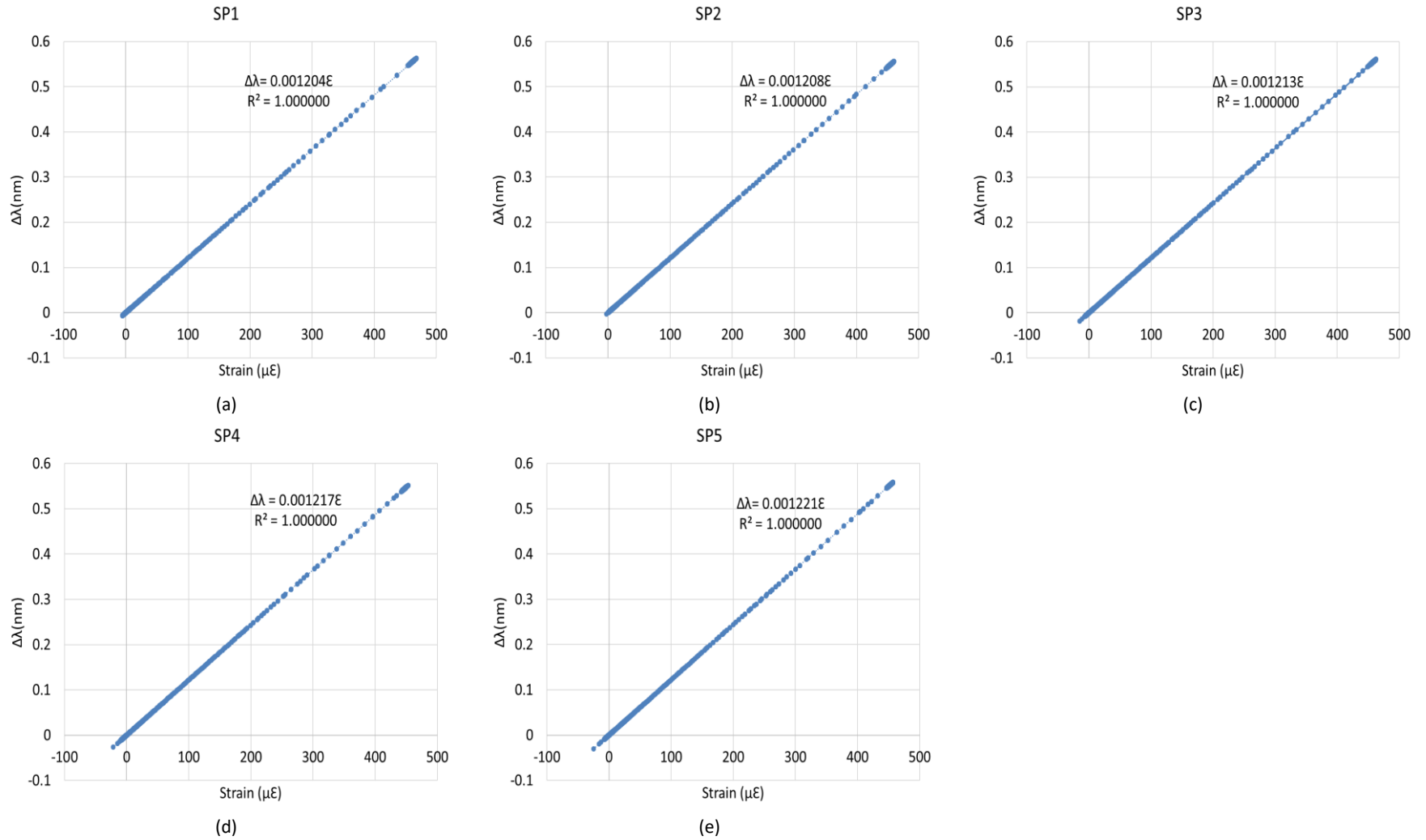


Figure 4-4. Variation in the wavelength with changes in the compensated strain – S1T1

4.3.2 Thermal expansion coefficient of the model pile

For a stainless steel pile, the recommended value of the thermal expansion coefficient is 16.0 (10^{-6} m/m.K), according to EN 1993-1-4:2006 (British Standards Institution, 2006). This is a conservative value, compared to the values given by manufacturers, which are in the range of 17–18.3 (10^{-6} m/m.K). In order to avoid any errors being caused by estimating the value of α , which can considerably affect the results, its value needs to be accurately measured. This procedure is followed to determine ΔT and α :

- Step 1: The total observed strain is a combination of strain caused by mechanical and thermal loading (see Equation 4.7). In S1T1, the total strain is equal to the strain caused by thermal loading, due to the absence of mechanical loading (see Equation 4.8). The thermal strain is a function of the changes in the pile temperature and the thermal expansion coefficient of the pile material:

$$\epsilon_{Total} = \epsilon_{Mechanical} + \epsilon_{Thermal} \quad (4.7)$$

$$\epsilon_{Total} = \epsilon_{Thermal} = \alpha \cdot \Delta T \quad (4.8)$$

- Step 2: Compensated observed thermal strain at each level is determined by multiplying the strain sensitivity values given in Table 4.2 by a shift in the compensated wavelength. The strain profiles gained during the two heating-cooling cycles, and at the end of two heating and cooling periods against the pile depth for S1T1, are shown in Figures 4.3-c and 4.3-d. The thermo-elastic behaviour of the model pile is noted where the magnitudes of the thermal strain at the ends of both cycles are the same. According to Equation 4.8, ΔT needs to be determined first, and then the α value is achieved by dividing observed strain over ΔT .
- Step 3: As shown in Figures 4.5-a and 4.5-b, the values from the temperature-only sensors show a considerable amount of noise. This is partly due to the use of looser FBGs for temperature-only FBGs. While this has an adverse effect on the analysis, a one-degree variation results in an increment of approximately $15\mu\epsilon$ – $18\mu\epsilon$, which is up to 4% of the maximum observed strain, depending on the magnitude of the thermal expansion. This will be described in the next section. Hence, an alternative method is needed, and it needs to involve the application of the relationships between wavelength and temperature, as shown in Figure 4.2 and Table 4.1. The pile temperature at each point, and the temperature changes along the pile surface, can be calculated using Equations 4.9 and 4.10 respectively:

$$T_i = 21.7 + \Delta\lambda / \text{Temperature sensitivity values at each level} \quad (4.9)$$

$$\Delta T = \Delta\lambda / \text{Temperature sensitivity values at each level} \quad (4.10)$$

Where:

T_i : Temperature at a specific time

$\Delta\lambda$: Total uncompensated shift in the wavelength

The absolute temperature and temperature change profiles for S1T1, which use Equations 4.9 and 4.10, are shown in Figures 4.5-a and 4.5-b. The maximum and minimum temperature values are 51.74°C and 19.45°C, both at the SP5 level. Moreover, the highest and lowest ΔT values are +30.04°C and -30.04°C respectively, showing symmetry in the temperature changes. Comparing this with the first method, the maximum and minimum ΔT values during the heating and cooling processes are 31.77°C and -31.23°C.

- Step 4: The thermal expansion coefficient at each level is calculated by dividing the observed strain over ΔT (see Table 4.3). The maximum and minimum thermal expansion coefficients are 17.98 and 15.79 (10^{-6} m/m.K) respectively. The variation of the α value along the pile surface, at the end of the heating and cooling periods, is shown in Figure 4.5-c, where the maximum and minimum values are given at the SP1 and SP4 levels respectively. The differences could be due to the non-uniform distribution of the epoxy resin coatings on the FBG sensors. The values found in Table 4.3 will be used to determine the free-state strain in the other experiments in Scenarios 2 to 5, using Equation 4.8.

Table 4-3. Variations in the coefficient of thermal expansion during heating-cooling cycles (10^{-6} m/m. K)

	α_1	α_2	α_3	α_4	α_5
First heating	17.94	16.26	16.74	15.83	16.25
First cooling	17.98	16.06	16.70	15.79	16.19
Average	17.96	16.16	16.72	15.81	16.22

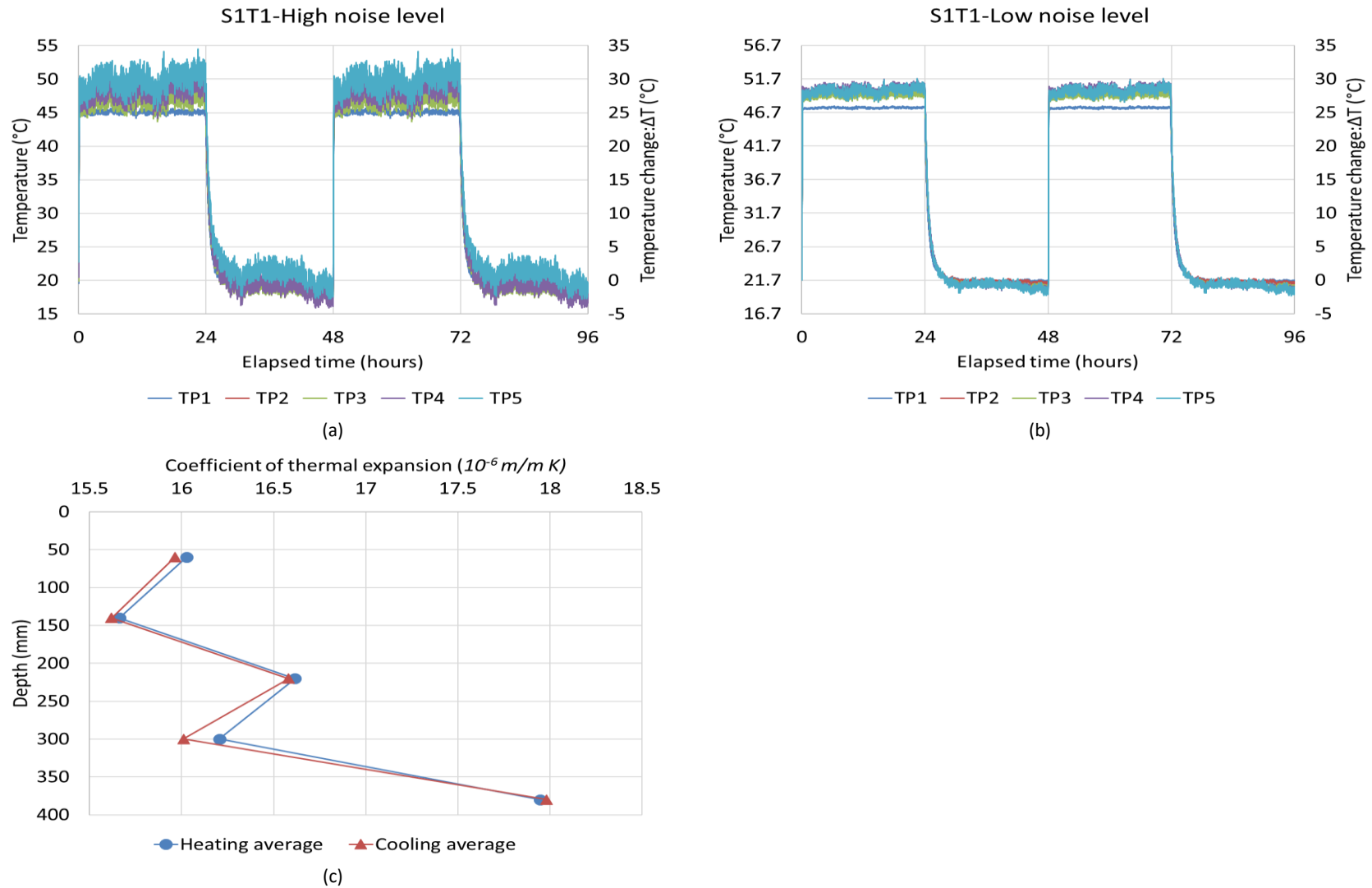


Figure 4-5. (a and b) Absolute temperature and temperature changes along the pile for high and low levels of noise in the data, (c) variations in the coefficient of thermal expansion along the pile – S1T1

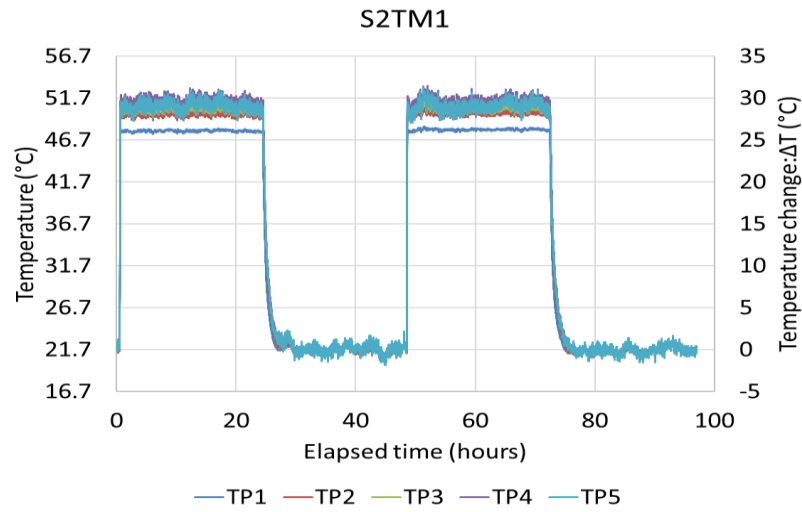
4.4 Scenario 2

The aim of the Scenario 2 tests is to determine the effect of thermo-mechanical loading on the performance of the model pile in the absence of soil. According to Equation 4.7, the total compensated strain is the combination of the strains caused by mechanical and thermal loading. By replacing Equations 4.7 and 4.8 with Equation 3.14, the following equation is achieved, in order to determine the strain caused by mechanical loading:

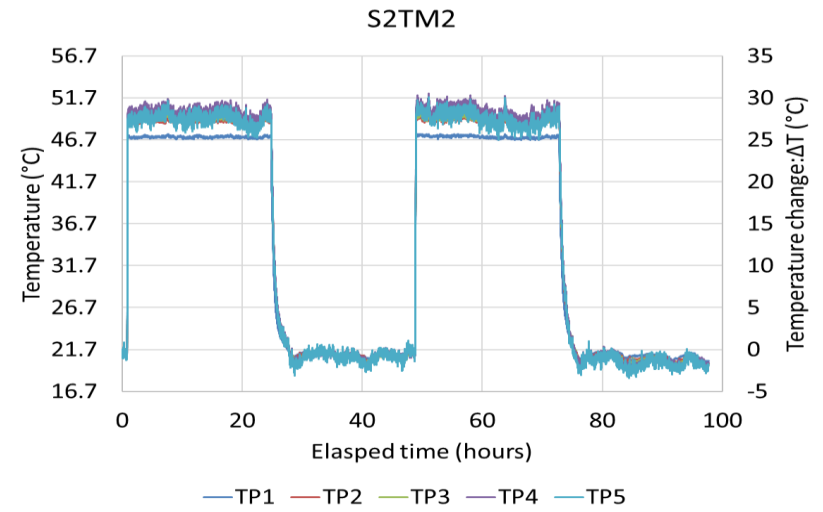
$$\varepsilon_M = \frac{1}{1 - p_\alpha} \cdot \frac{\Delta\lambda}{\lambda_0} - \Delta T \cdot \left(\alpha + \frac{\xi + \alpha_{glass}}{1 - p_\alpha} \right) \quad (4.11)$$

The coefficient values are given in Section 3.4.2.2. It is seen that:

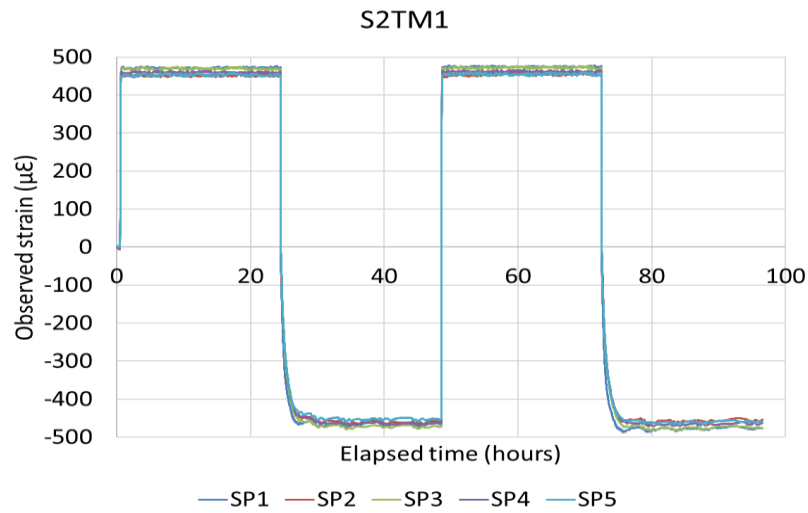
- Using Equation 4.11, the maximum mechanical strain captured by FBGs is equal to $1.41\mu\varepsilon$, $2.35\mu\varepsilon$, $3.31\mu\varepsilon$, $4.67\mu\varepsilon$ and $5.82\mu\varepsilon$, for S2TM1 to S2TM5 respectively. The maximum mechanical strain is 1.38% of the maximum strain that is observed during thermal loading in S1T1.
- The pile target temperature was 50°C , but fluctuations are seen, which is mainly due to the exposure of the pile to the room temperature. In the Scenario 2 tests, the average pile temperature during each heating period fluctuated between 47.48°C and 52.09°C . In all of the tests, the temperature returns to its original position, or to a lower temperature (see Figures 4.6-a and 4.6-b). Due to the similarities between the temperature and strain profiles that are seen in S2TM1–S2TM5, only the S2TM1 and S2TM2 figures are presented in Figure 4.6, and S2TM3–S2TM5 profiles are given in Appendix G.
- The observed strain profiles for the S2TM1 and S2TM2 tests are presented in Figures 4.6-c and 4.6-d. The thermo-elastic behaviour of the model pile is seen where an approximate $1.6\mu\varepsilon$ difference, which is negligible, exists between the first and second heating periods.



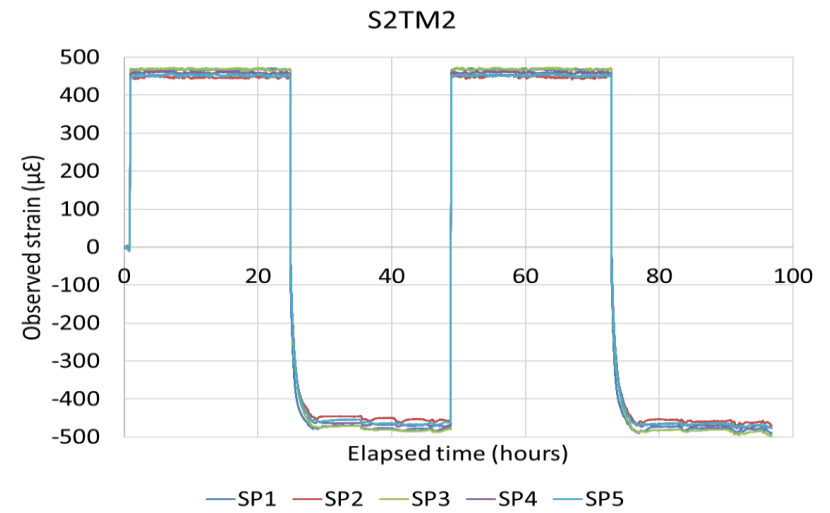
(a)



(b)



(c)



(d)

Figure 4-6. (a and b) Temperature distribution along the pile, (c and d) observed strain along the pile – Scenario 2

4.5 Scenario 3

4.5.1 Pile temperature profiles

This scenario focuses on the behaviour of the pile under thermal loading, when sand surrounds the pile. In this section, the results of the S3T1 and S3T2 tests, where the model pile undergoes two cyclic heating and cooling periods, are presented. In S3T1, the top and bottom of the pile are free to move, and the pile is held in place using surrounding sand to assess the pure shaft resistance of the pile. In S3T2, the pile base is placed onto a base support to avoid the pile from moving downward, in order to understand the effect of end restraint on the pile response. In both tests, the pile is heated up to approximately 50°C for 24 hours and allowed to recover to room temperature. This procedure is repeated for two cycles. The changes in the pile temperature during the entire test period, and the changes in the soil temperature at the end of each cycle, are presented in Figure 4.7. The following observations are made:

- The average pile temperatures during the first and second heating periods for S3T1 are 48.54°C and 48.47°C respectively. Despite the symmetry of the pile temperatures during the two heating periods, the values are lower than 50°C. This is improved in S3T2, where the average pile temperatures are 49.80°C and 49.32°C, during the first and second heating periods respectively.
- In S3T1, the maximum and minimum temperatures are 51.06°C and 20.56°C, which are both noted at the TP5 level. This means that the maximum temperature is 2.5°C higher than the average temperature. The maximum changes in temperature during the heating and cooling periods are $\Delta T_{max,heating} = 29.36^\circ\text{C}$ and $\Delta T_{max,cooling} = -28.85^\circ\text{C}$, as recorded at the TP5 level, which are higher than the initially expected $\Delta T = 28^\circ\text{C}$.
- In both tests, the maximum and minimum temperature profiles are recorded at the TP5 and TP1 levels respectively. This shows that the pile temperature decreases with depth.
- For the FBGs placed in the sand, the minimum temperature increase occurs at the SP1 level, during both heating periods (see Figures 4.7-c and 4.7-d). In the cooling periods, a similar trend is seen, but with a lower rate of heat dissipation than heat propagation. After 24 hours of cooling, the sensor that is located at a depth of 300mm experiences the maximum temperature recovery, at approximately -17°C. This is approximately 3°C less than the temperature increase that was seen at that level in the heating period. This shows that soil cools at a slower rate than it heats – in this case, 15% lower. Also, the maximum and minimum changes in temperature occur within the sensors that are located 34mm and 164mm away from the pile centre respectively. Relatively similar observation is made for Scenarios 4 and 5 with minor differences in the temperature values for FBGs in each test. Investigating the heat transfer in soil is not within the scope of this project but soil temperature profiles for Scenarios 3 to 5 are provided in Appendix J for the reference of future works in this area.

- Less of a change in temperature is observed during the second heating and cooling periods, due to the residual heat from the first heating period providing the sand bed with a higher initial temperature at the start of the second period.

4.5.2 Strain profiles

4.5.2.1 Observed strain

The strain distribution during the two heating-cooling cycles for the Scenario 3 tests is shown in Figures 4.8-a and 4.8-b). It is noted that:

- In S3T1, the maximum strain values during the first heating and cooling periods are at the SP3 level, at the mid-depth of the pile, while the maximum strain during the second cooling period is at SP5. In S3T2, the maximum strain during all four periods is at the SP3 level. Conversely, the maximum ΔT for both tests occurs at the TP5 level.
- The strain profiles in both tests did not completely return to their original positions after each heating period. In S3T1, the differences between the maximum and minimum strain, for the first and second cycles, are $17.65\mu\epsilon$ and $20.56\mu\epsilon$ respectively. In S3T2, these values rise to $20.69\mu\epsilon$ and $27.59\mu\epsilon$. The difference is partly because of the presence of sand around the pile, which traps the heat from the pile surface and does not allow the pile to completely return to its original position.
- Higher strain values are observed for S3T2 at all five levels, during both the heating and cooling periods, due to higher temperature changes in S3T2 (from 0.43°C to 2.31°C) than in S3T1.
- Linear strain profiles are observed in both tests, particularly during the heating periods (see Figures 4.8-a and 4.8-b). They show consistent levels of restraint that are caused by the soil or, in other words, similar levels of friction between the pile surface and sand.

4.5.2.2 Restrained strain

The restrained strain profiles for the Scenario 3 tests are shown in Figures 4.8-c and 4.8-d). It is noted that:

- The maximum restrained strains in S3T1 and S3T2 are equal to $10.25\mu\epsilon$ and $10.24\mu\epsilon$ respectively. In S3T1, the maximum restrained strain occurs at the end of the second heating period, while the maximum restraint is noted at the end of the second cooling period for S3T2.
- In S3T1, the minimum restraint is applied at the end of the first and second cooling periods, while greater restraint is noted during both heating periods. This means that, for a pile embedded in the sand with no support at the top or bottom, it is more difficult to expand than contract.
- In S3T1, the maximum restraints are applied at the SP4 and SP5 levels, while the minimum restrained strain is noted at the SP1 and SP2 levels. As the effect of the base support in S3T2

is apparent, a more non-linear profile is noted. At the end of the second cooling period, where the maximum restraint is applied at the top of the pile, the restrained profile reduces towards the bottom of the pile, with a sudden increase at the SP1 level.

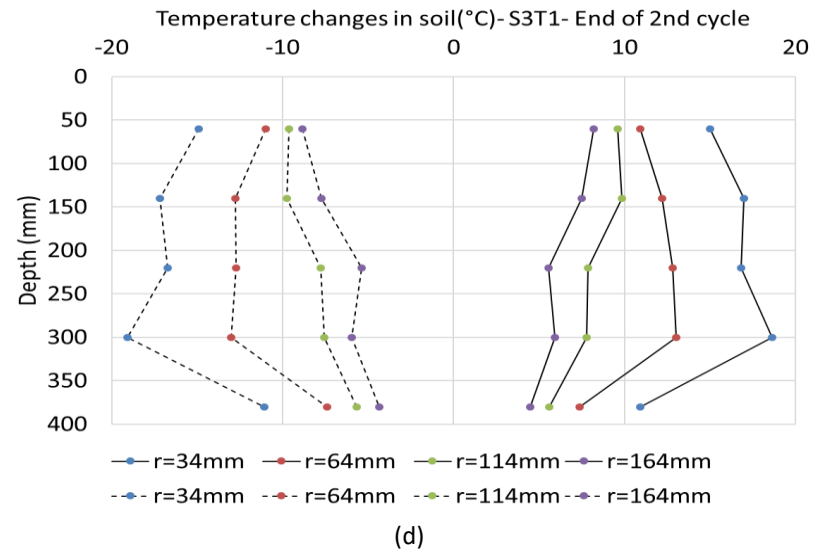
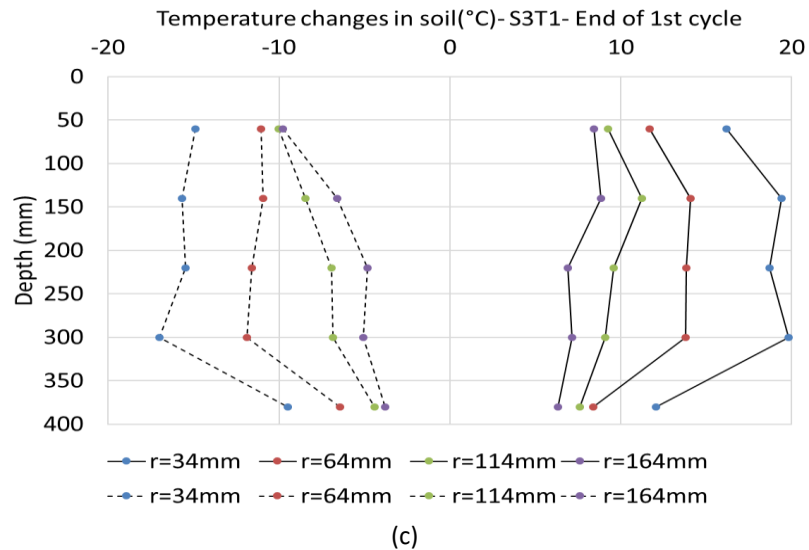
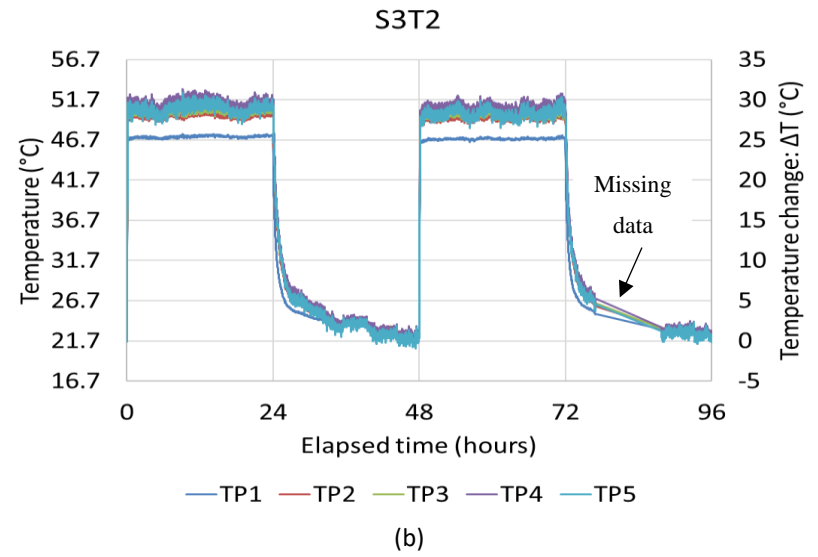
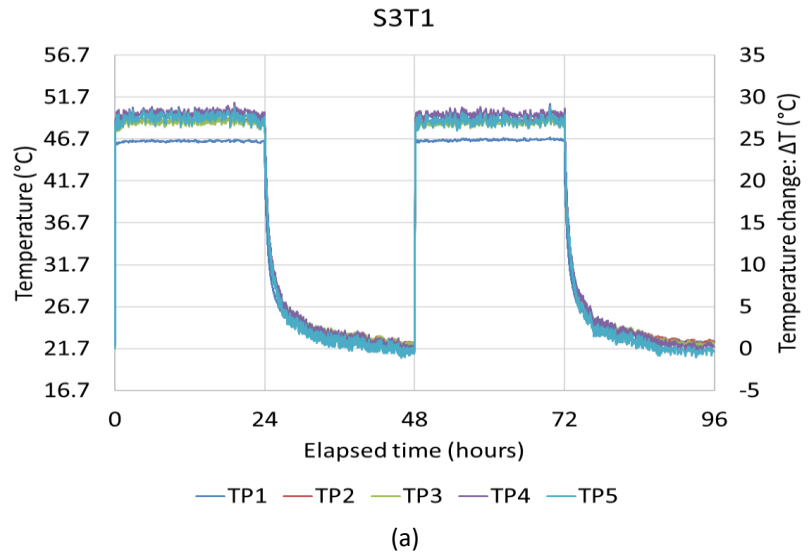


Figure 4-7. Temperature distribution: (a and b) along the pile surface, (c and d) in the soil

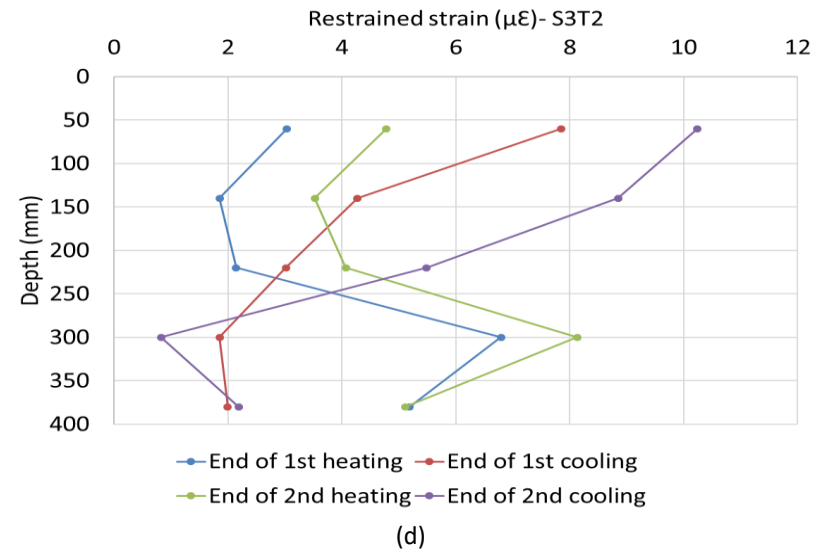
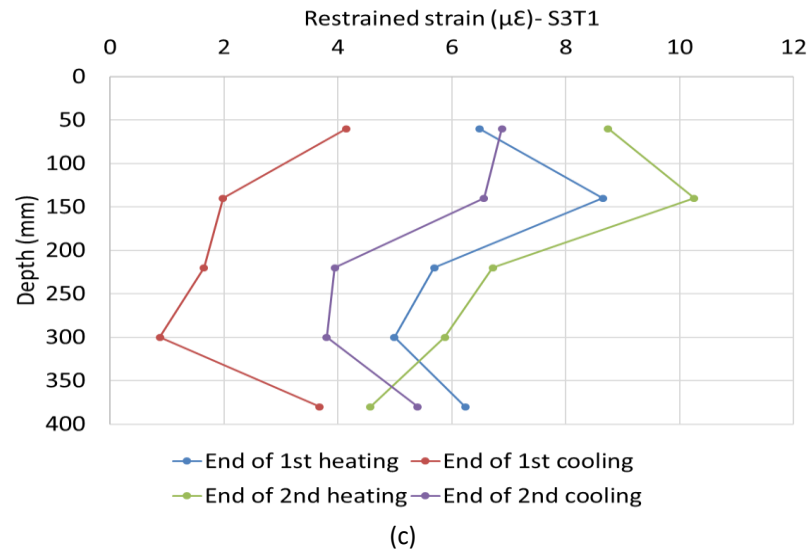
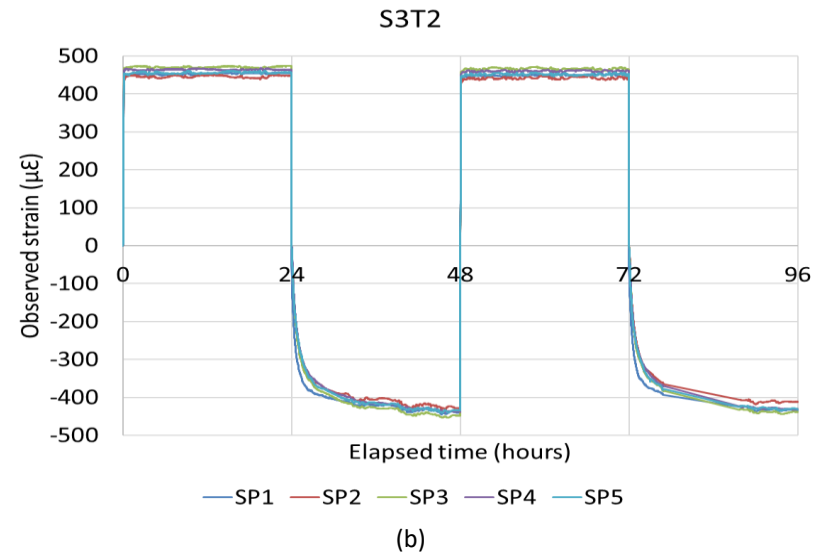
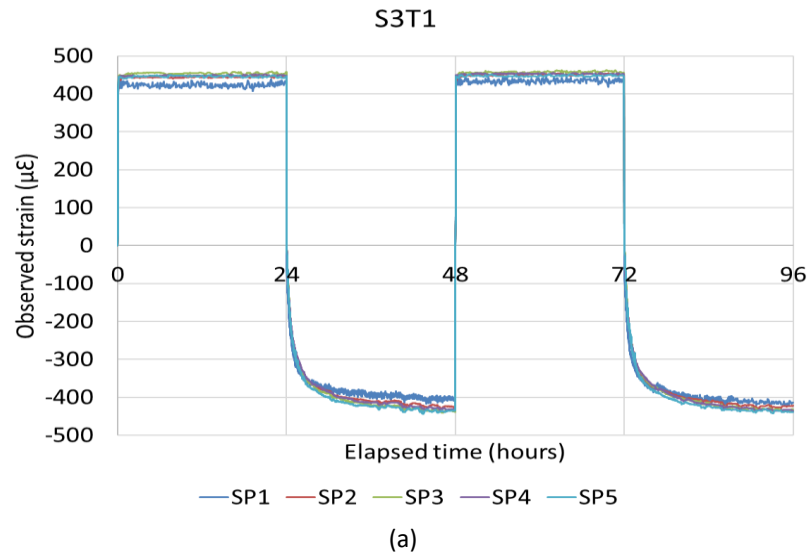


Figure 4-8. (a and b) Observed strain, (c and d) restrained strain at the end of each heating-cooling period – Scenario 3

4.5.3 Degree of freedom

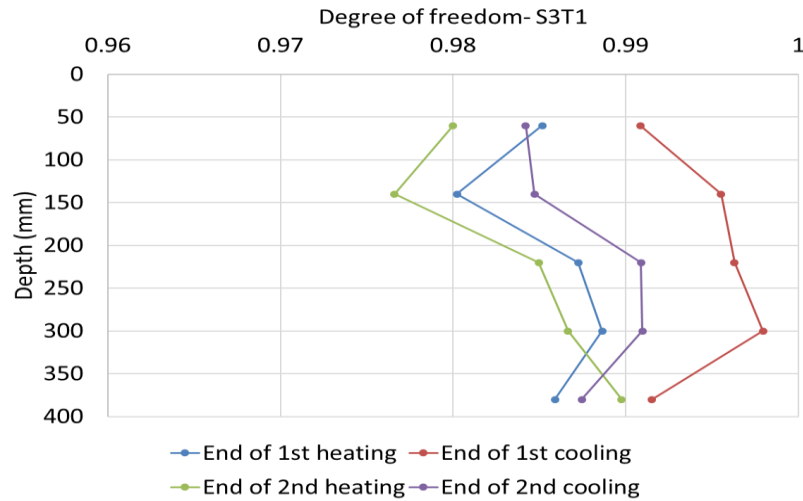
The term 'degree of freedom' is introduced in Section 2.2. For the Scenario 3 tests, DoF represents the level of restraint that is caused by sand. The variations of the DoF noted along the pile length during Scenario 3 tests are shown in Figures 4.9-a and 4.9-b. It is observed that:

- In S3T1, similar with the restrained strain profile, the minimum DoF is noted at the end of the first heating period, while the maximum restraint is applied during the first cooling period. After the initial settlement caused by the first cooling period, higher DoF values are seen during the subsequent heating-cooling cycle. For both heating periods, the null point is at the SP4 level – 140m below the sand's surface. The location of the maximum DoF changes along the pile, during each heating or cooling period. This means that the null point shifts due to the thermal loading, and there is not a constant location for the entire test.
- Despite small differences in the DoF's value in the Scenario 3 tests, the values change between 0.975 and 1.0 in both tests, which shows that the level of restraint caused by sand is low. A higher level of restraint is expected in the Scenario 4 tests, due to the existence of mechanical loading on the pile head.

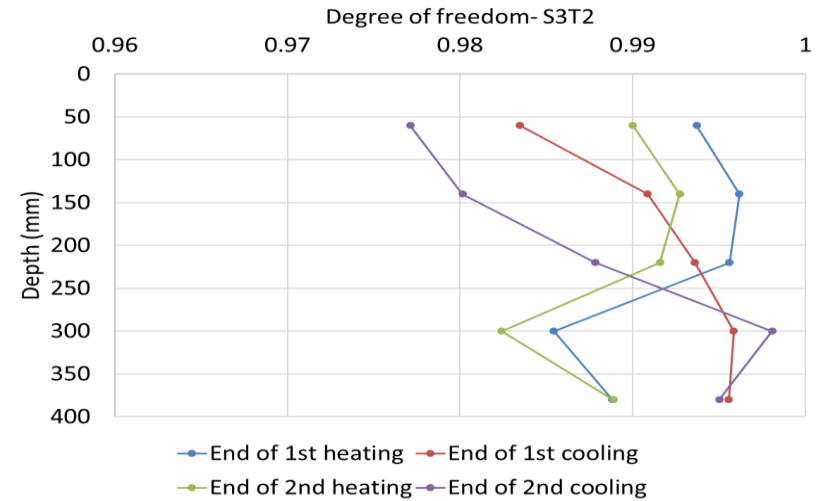
4.5.4 Thermally induced axial force and stress in the pile

Induced axial force, and axial stress caused by restrained strain, are shown in Figures 4.9-c and 4.9-d. The following observations are made:

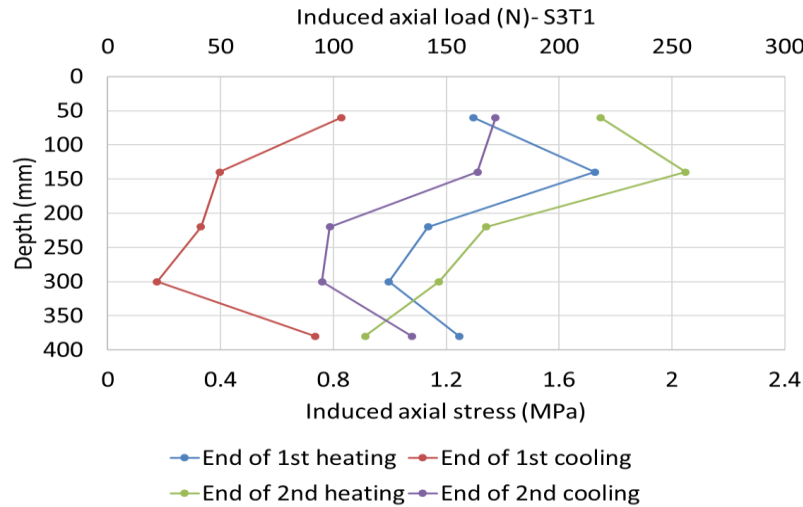
- The location of the maximum induced load and stress in each test is similar to those of restrained strain and DoF in both tests. It seems that, despite the low level of restraint, a considerable axial load is applied onto the pile. The maximum induced axial load in S3T1 and S3T2 is equal to 256N, which is 1.6 times greater than the ultimate load carried by the pile head for the shaft resisting pile.
- The maximum induced stress is equal to 2.05MPa for both tests, which is only 3.26% of the allowable compressive stress for the stainless steel model pile. According to BS 8004:1986 (British Standards Institution, 1986), the maximum allowable induced stress has to be less than 30% of the yield stress of stainless steel (210MPa), which is equal to 63MPa.
- The ratio of induced stress per degree of temperature change has been considered a design parameter for thermal piles. The maximum ratios of 74kPa/°C and -74kPa/°C are noted during the heating and cooling periods. The values range from 104kPa/°C to 329kPa/°C for in-situ installations, as reported in Table 2.4.
- In S3T1, the heating process induces thermal loading in the pile, which is partially recovered during the subsequent cooling periods. Greater recovery is seen during the first cooling period, compared with the second cooling period. The opposite behaviour is seen in S3T2, where the heating process acts as the recovery for the induced axial loads during the cooling periods.



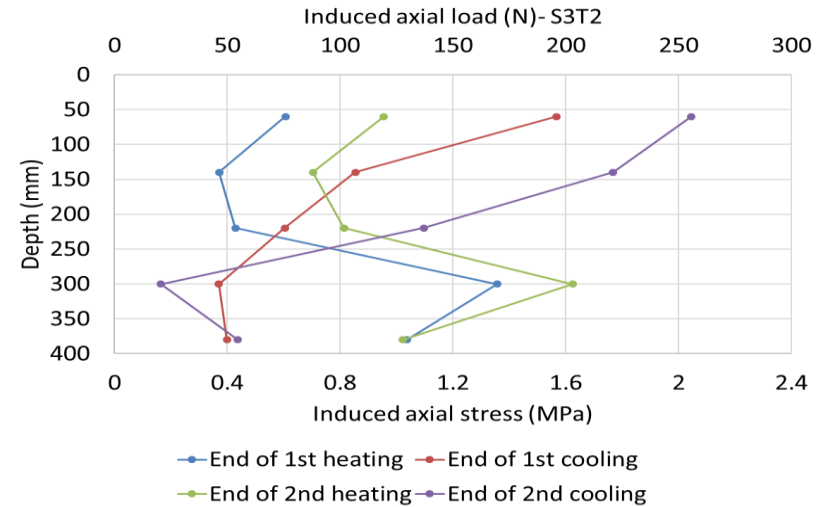
(a)



(b)



(c)



(d)

Figure 4-9. (a and b) Variation of DoF, (c and d) induced axial load and stress – Scenario 3

4.5.5 Pile head displacement

The pile head displacements under the two heating-cooling cycles for the Scenario 3 tests are shown in Figures 4.10-a and 4.10-b. The following observations are made:

- In both experiments, the pile heaves and settles in the two heating and cooling cycles. In S3T1, the pile does not return to its original position after the heating and cooling cycles. A residual settlement of 0.136mm, or 4.85% of the maximum allowable settlement (2.8mm), is observed. Taking into account the 0.1mm pile settlement under its self-weight, the overall settlement is only 0.036mm, which is within the range of measurement resolution.
- In S3T1, the maximum pile head displacement is noted during the first cooling period, and is 0.24mm. This is 1.17 times greater than the result of the second cooling period. This also accounts for approximately 70% of the cumulative pile settlement (0.115mm) after the two heating-cooling cycles. In the second heating period, 79% of the pile settlement from the first cooling period is recovered.
- In S3T1, the residual settlement after the two heating-cooling cycles is 0.136mm, which is equivalent to the pile head displacement caused by 40N of mechanical loading.
- In S3T2, where the pile is restrained at the bottom of the pile, the upward movement at the end of the first heating period is approximately 1.5 times greater than in S3T1. The pile is restrained at the bottom but is free to expand from the pile head. Due to the presence of the sand, the entire downward movement of the pile is not converted to the upward movement; otherwise, the ratio of the pile's upward movement in S3T2 would be two times greater than in S3T1. During the first cooling period, the pile settles but does not return to its original position, and small residual heave remains in the pile at the end of the period. Similar behaviour is noted during the second heating-cooling cycle.

4.5.6 Mobilised friction at the soil–pile interface

Soil resists the movement of the pile, whether upward or downward, under thermal loading, and this results in the mobilisation of friction at the soil–pile interface. The pile length is divided into four zones: Zone 1 is the area between SP1 and SP2, Zone 2 is the area between SP2 and SP3, Zone 3 is the area between SP3 and SP4, and Zone 4 is the area between SP4 and SP5. Equation 2.9 is used to determine the mobilised friction at each zone. The mobilised friction that is noted at the zones at the end of each heating and cooling period is shown in Figures 4.10-c and 4.10-d.

- In S3T1, the maximum mobilised friction (9.11kPa) is noted at the end of the second heating period in Zone 1, at the bottom of the pile. In S3T2, the maximum mobilised friction (-20.66kPa) is seen at the end of the first heating period. Negative skin friction is observed due to the resistance towards the pile's upward movement.
- In both tests, it seems that the mobilised friction noted at the end of each period can be a positive or negative magnitude. In S3T1, most of the mobilised friction is positive.

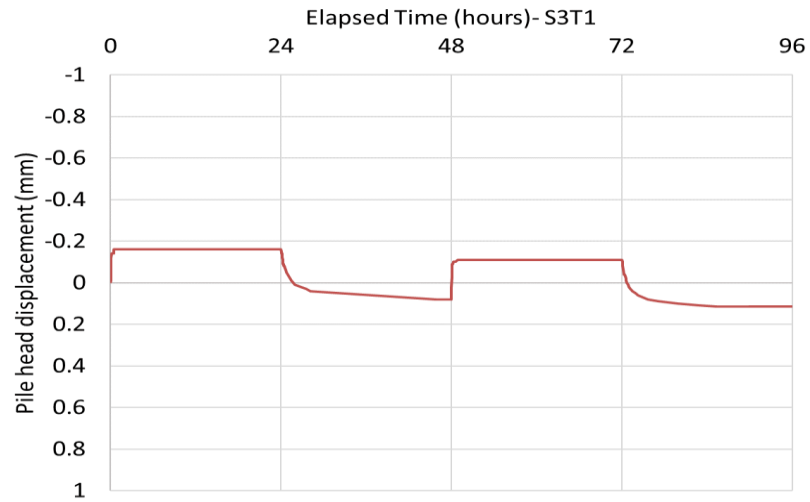
- In S3T1, at Zone 1, the maximum amount of positive friction is mobilised at the end of the second heating period, while at Zone 4, the maximum amount of negative friction is mobilised at the end of first heating period, so as to resist pile upward movement. In S3T2, the maximum amount of positive friction is mobilised at the end of the second cooling period, in Zone 1. The maximum amount of negative friction is mobilised at Zone 2, at the end of second heating period.

4.5.7 Comparison with the framework

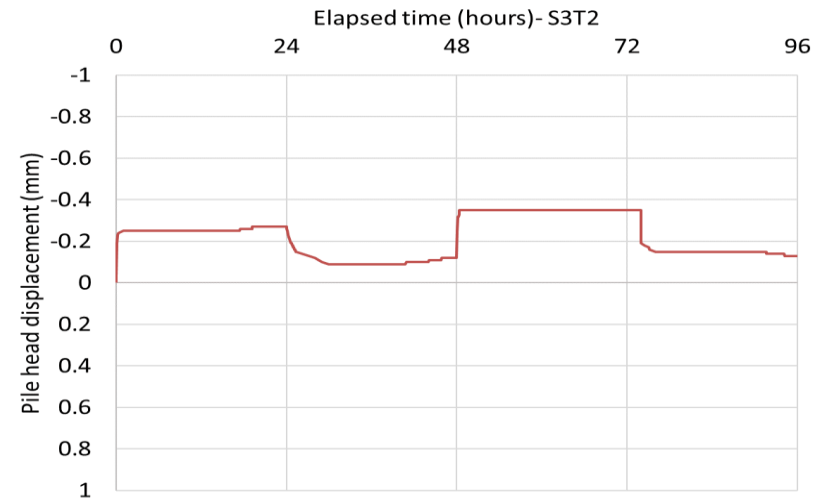
According to the framework, the maximum restrained strain in S3T1 is expected to be at mid-depth, with values of zero at both ends. The same profile, with a negative sign, will be noted during the cooling period (see Scenario 3A in Table 2.3). Using the restrained strain profile for S3T1, given in Figure 4.8-c, it seems that the restrained strain increases from the SP5 to SP4 level, and then decreased towards the pile bottom. While the null point is expected to occur at mid-depth for both cooling and heating periods, it is noted at the SP4 level during both heating periods, and at the SP5 level during both cooling periods. It seems that, during the heating periods, the restrained strain profiles follow the trend that was suggested by the Thermal Pile Standard (GSHPA, 2012), with a shift in the location of the maximum restraint. The reverse of this behaviour is noted in S3T2, where a continuous reduction of restrained strain is noted during the cooling periods, while the maximum restrained strain is noted at the SP2 level during the cooling periods. The differences in the restrained profiles of the framework and the Scenario 3 profiles can be explained as follows:

- Differences in the levels of relative density and homogeneity in the samples affect the location of the null point and the magnitude of restrained strain. The relative density of the sand bed that is used in this study is approximately 57%, whereas a denser soil or different soil material, such as clay, would result in higher magnitudes of restrained strain.
- The temperature difference between the pile head and the pile bottom is observed, and a lower temperature is usually recorded at the pile bottom. Despite the differences in the absolute temperature readings, relatively similar ΔT values are achieved. The perfect linear strain profiles that are given by the framework are the result of having perfect temperature distribution along the pile, as well as homogenous soil.

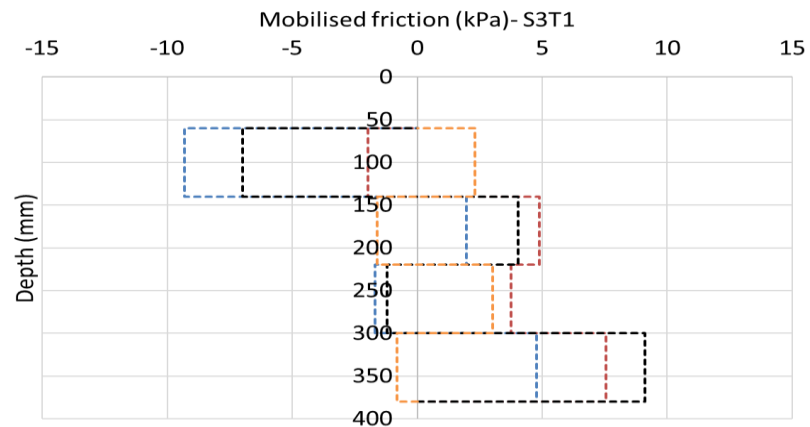
According to the framework, the mobilised friction is expected to have an equal magnitude along the pile, with different signs at the top and bottom halves. Using Figure 4.10-c, it seems that the mobilised friction at Zone 4 is similar to that of the framework. Other zones shift into the positive region, which is also similar to the framework. The only difference is the location in which the shift in the signs happens: the top third in S3T1 and the bottom third in S3T2. Additionally, shifts to the positive and negative regions are observed in S3T1 and S3T2, while the proposed framework is only divided into two regions: positive and negative.



(a)

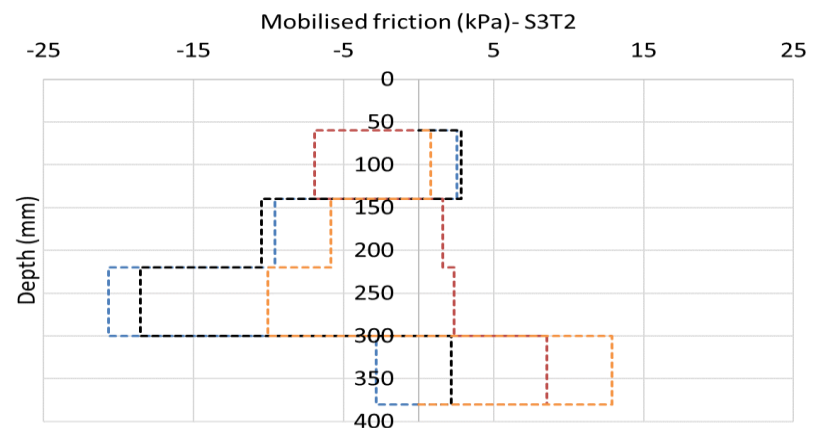


(b)



--- End of 1st heating - - - End of 1st cooling
 - - - End of 2nd heating - - - End of 2nd cooling

(c)



--- End of 1st heating - - - End of 1st cooling
 - - - End of 2nd heating - - - End of 2nd cooling

(d)

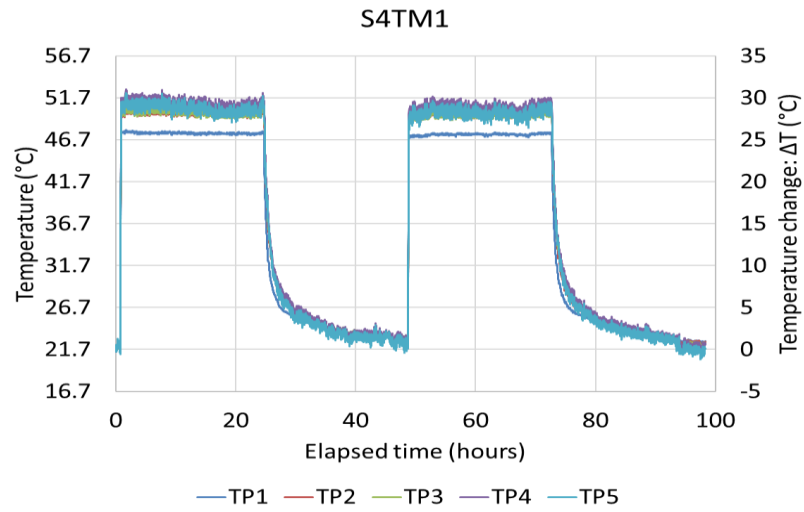
Figure 4-10. (a and b) Pile head displacement, (c and d) mobilised friction at the end of each heating-cooling period – Scenario 3

4.6 Scenario 4

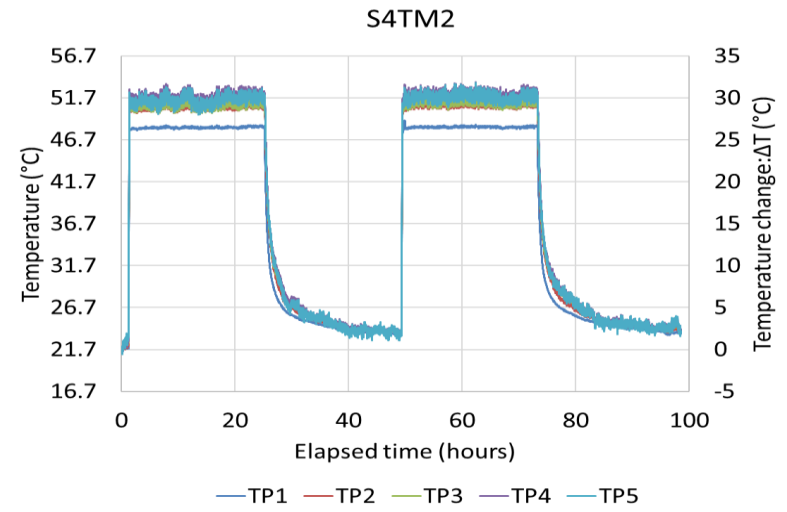
4.6.1 Pile temperature profiles

The temperature distribution along the pile surface for the Scenario 4 tests is shown in Figure 4.11. In all of the Scenario 4 tests, mechanical loading is first applied onto the pile head at room temperature, and then the pile is heated to 50°C for 24 hours, followed by 24-hour cooling period to allow it to return to room temperature. This is followed by a second heating and cooling process, for the same period of 24 hours. In order to gain a better understanding of the changes in the pile strain, the temperature changes that occur throughout the entire test period are shown in Figure 4.11.

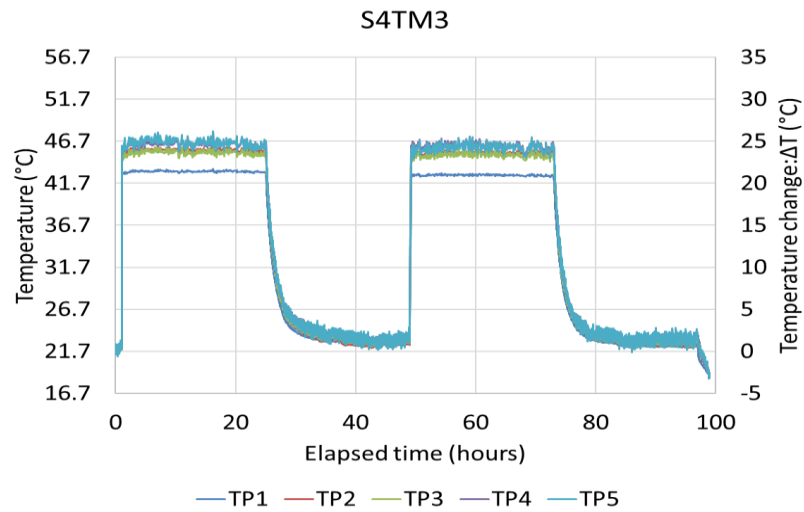
- For all of the Scenario 4 tests, the maximum and minimum temperatures are consistently recorded at the TP5 and TP1 levels respectively, during both the heating and cooling periods.
- The maximum ΔT values during the heating periods of all the Scenario 4 tests vary, and range from 25.25°C to 31.80°C. The exception is S4TM3, which recorded the lowest readings of the entire test, with a maximum ΔT of between 21.68°C and 26.19°C. The main reason for the lower temperature in S4TM3 was a partial blockage in the pipe that transfers the water, which was discovered at the end of the test. It had no effect on the other tests.
- An approximate reversibility of the temperature profile is noted throughout all of the Scenario 4 tests, with small differences (up to 0.79°C) within the maximum temperature increments during the heating periods. This value increases to 0.94°C for the cooling periods of all of the tests.
- External parameters, such as end bearing conditions and the magnitude of mechanical loadings, have not affected the temperature profile and the distribution of temperature along the pile. Due to the software crashing, the temperature during the second heating period in S4TM8 is not recorded between 57.3 hours and 66.3 hours (see Figure 4.11-h).



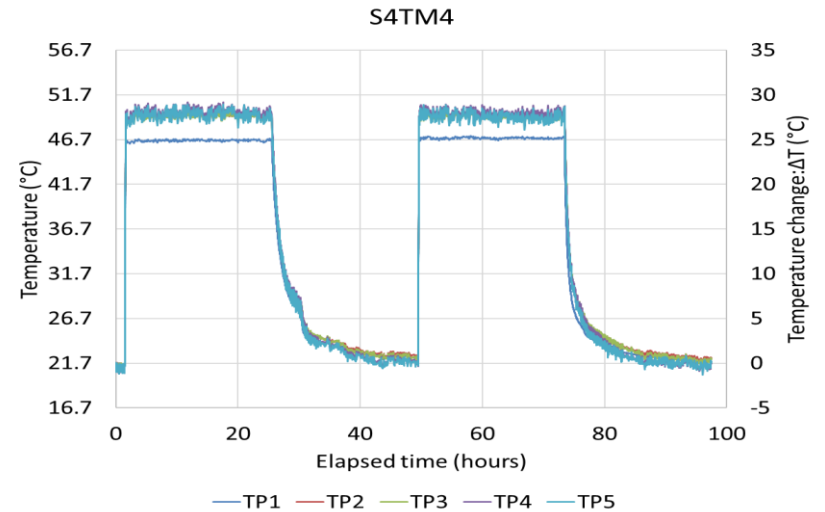
(a)



(b)



(c)



(d)

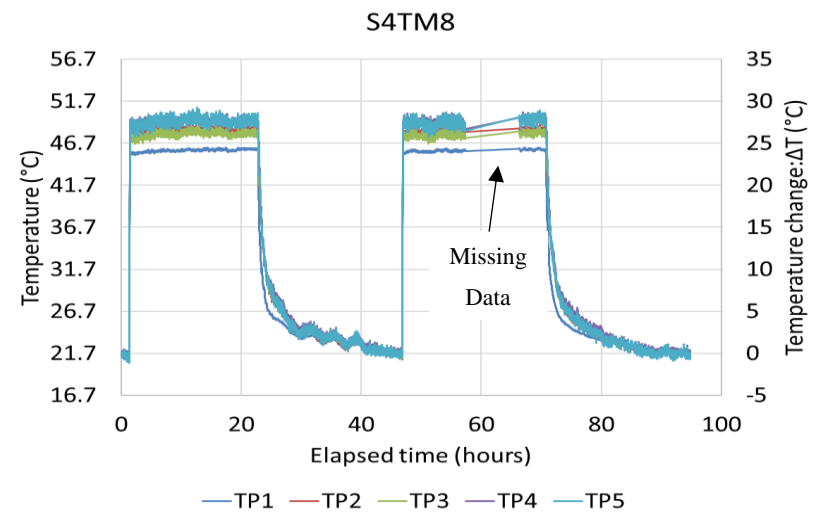
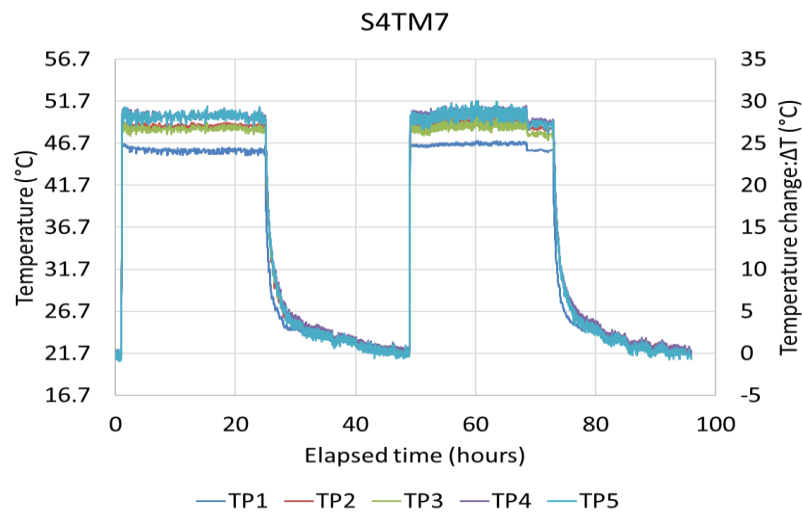
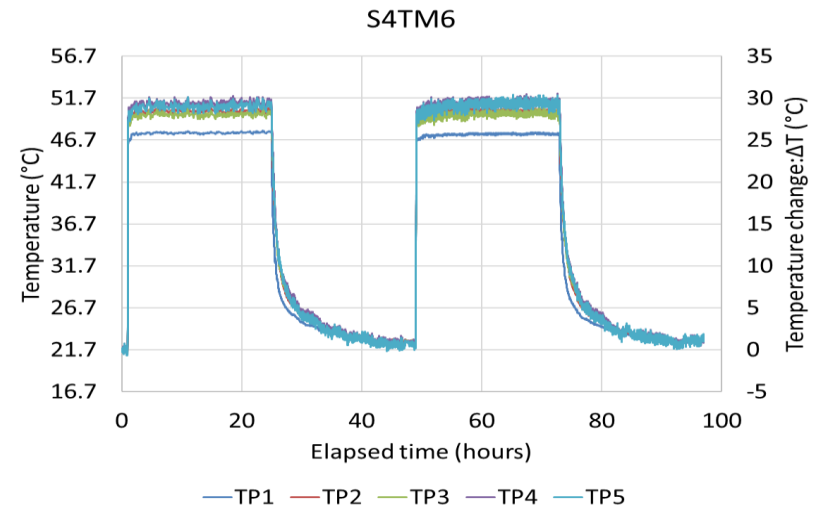
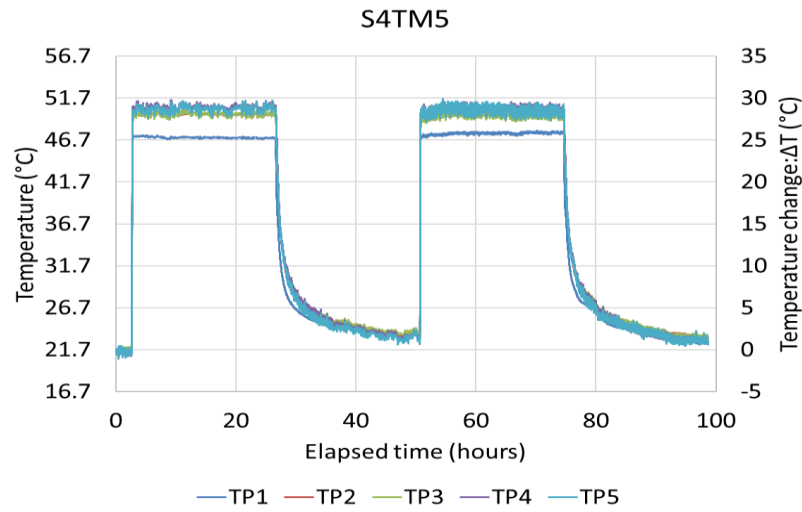


Figure 4-11. Temperature distribution and temperature changes along the pile surface – Scenario 4

4.6.2 Strain profiles

4.6.2.1 Observed strain

Three series of Scenario 4 strain profiles are shown in this section. Firstly, the profiles of observed strains along the pile under mechanical loading are presented (see Figure 4.12). In each figure, the axial strain and load distribution are both presented, and show a linear relationship between axial strain and load. To determine the mechanical strain, the procedure described in Section 4.3.2 is used. For a shaft resisting pile, it is expected that the maximum load will be carried at the pile head, with the dissipation of the load occurring towards the bottom of the pile, and zero loads at the pile toe.

- The expected load distribution profile is noted in all tests, with differences in its shape depending on the magnitude of the mechanical loading. In S4TM1, the maximum strain is $1.13\mu\epsilon$, under 30N of mechanical loading, while the minimum strain ($0.04\mu\epsilon$) is observed close to the pile toe, at the SP1 level. It should be noted that SP5 is located 60mm below the sand's surface, and that part of the load will have been shed by the sand in this area; this has not been recorded. Moreover, SP1 is located 15mm above the pile bottom, and no strain should be seen at the pile toe. A similar trend is seen at S4TM2 and S4TM3, where the maximum axial loads are lower than the applied mechanical loads of 55N and 75N, due to the positioning of the sensors on the pile surface.
- In S4TM4, where higher magnitudes of pile head displacement are observed than in S4TM1–S4TM3, the load transfer profile is slightly different. An increase in the strain is noted between the SP5 and the SP4 levels, which could be due to the resistance of the soil due to the pile downward movement. In S4TM5, where the maximum settlement occurs, some irregularities are also seen, despite the general load transfer profile being as expected. The maximum mechanical strain at S4TM5 is $4.87\mu\epsilon$, which is equivalent to 121.5N.

From S4TM6 to S4TM8, where the pile is placed on a base support, the axial load at the SP1 level, which is close to the pile toe, does not get close to zero. This seems to be a function of the magnitude of the mechanical load on the pile head. In S4TM6, S4TM7 and S4TM8, the maximum axial loads at the SP1 level are 5.4N, 26.6N and 35.01N respectively, which is mainly due to the pile base support. The observed strain distribution along the pile surface, during the entire test period for the Scenario 4 tests, is shown in Figure 4.13. It is noted that:

- Differences are observed between the strain values at the end of each heating period, and the subsequent cooling periods. The differences range from $-9.27\mu\epsilon$ to $+49.32\mu\epsilon$, but most of this is due to the differences in the temperatures, which are between -1.18°C and 2.83°C . Assuming the pile has complete freedom to expand and contract, the maximum observed strain (due to temperature differences) is determined, and subtracted from the initial differences in the strain values, as mentioned above. This has resulted in the difference

between the strain values of $-5.43\mu\epsilon$ to $+10.95\mu\epsilon$. This is approximately 2.2% of the maximum observed strain in the Scenario 4 tests.

- The maximum observed strain in all of the Scenario 4 tests is equal to $480.7\mu\epsilon$, and is noted during the first heating period of S4TM2. The maximum strain with a negative sign during a cooling period is $-460.64\mu\epsilon$, and is recorded during the first cooling period in S4TM6.
- In S4TM1–S4TM5, the maximum strain values are mostly seen at the SP3 level, during both of the heating periods. Similarly, the location of the maximum observed strain during both cooling periods is either at the SP3 or the SP5 levels. In S4TM6–S4TM8, the location of the maximum observed strain shifts to the SP5 level.

The observed strain profiles along the pile length, that occur at the end of each heating-cooling period during the Scenario 4 tests, are shown in Figure 4.14.

- At the end of the first heating period, the maximum observed strain is noted at S4TM4, whereas the minimum observed strain is noted at S4TM8, where the maximum restraint is applied onto the pile from both the top and the bottom. A relatively linear profile is noted across all of the tests, with an increase in the strain values at the SP3 level. A similar trend is also seen in the other three heating and cooling periods.
- By comparing S4TM6, S4TM7 and S4TM8, it seems that higher magnitudes of mechanical loading have resulted in lower observed strains.
- At the end of the second heating period, the differences between the strain profiles increase across all of the tests, and at all five levels, and this is where the effect of the magnitude of mechanical loading on the observed strain has become clearer. At the end of the second cooling period, where the maximum observed strain occurs at S4TM4, the order of the maximum observed strain is completely overhauled. This means that the considerable settlements noted in S4TM4 and S4TM5 have changed the response in the second cycle, and resulted in lower observed strain.
- Effect of temperature changes on the container wall is investigated using two FBGs attached on the container wall to monitor the strain caused by thermal loading (SC1 and SC2). It is observed that in Scenarios 3 to 5, minor changes happen on strain-measuring FBGs which is negligible compared to the observed strain of the pile. Moreover, it shows that the container is large enough to avoid any possible effects on the test results.

4.6.2.2 *Restrained strain*

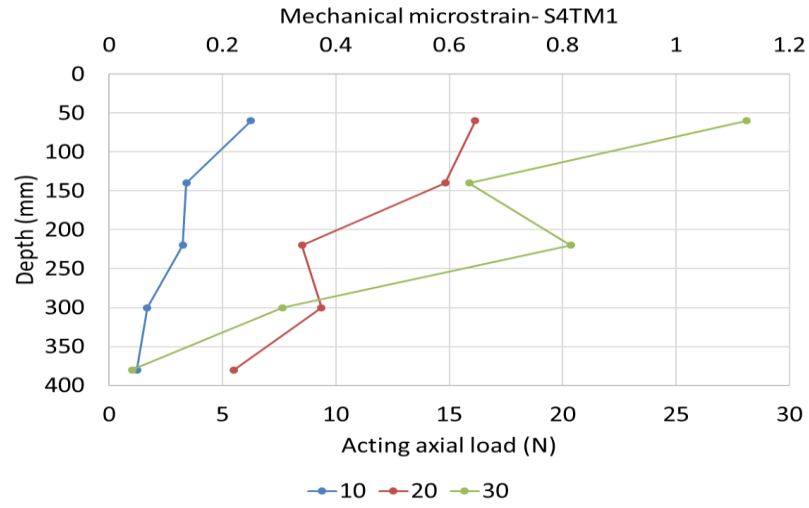
The restrained strain profiles noted at the end of each heating and cooling period are compared in Figure 4.15. It is observed that:

- At the end of the first heating period (see Figure 4.15-a):

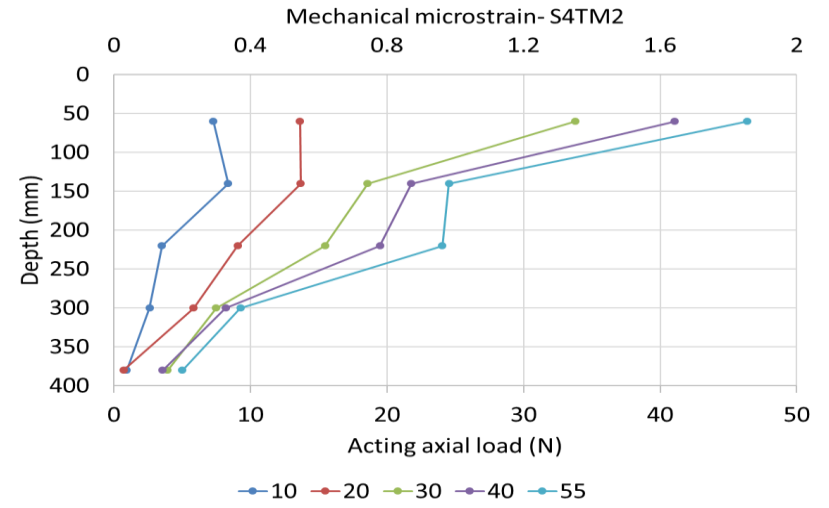
- The maximum restrained strain is equal to $10.3\mu\epsilon$, which is recorded at the SP5 level in S4TM2. This is approximately 2.14% of the maximum observed strain of the same test. The minimum restrained strain is $0.05\mu\epsilon$, which is recorded at the SP5 level in S4TM5.
- In S4TM1 and S4TM2, where the mechanical loading is 30N and 55N respectively, the maximum restrained strain values are recorded at the SP4 and SP5 levels. With an increase in the magnitude of the mechanical loading, the maximum restrained strain in S4TM3 and S4TM4 is noted at the SP3 level. In S4TM5, the maximum restrained strain is noted at the SP2 level. This means that, with an increase in the magnitude of the mechanical loading, and a subsequent increase in the pile head settlement, the location at which the maximum restriction occurs along the pile moves downward, towards the pile mid-depth and bottom.
- The maximum restrained strain at the pile bottom is seen in S4TM7 and S4TM8, where the pile is placed onto the base support. This shows that the base support is able to restrict the pile's downward expansion. The maximum restrained strain in S4TM8 is also noted at the SP1 level, close to the base support.
- For a specific magnitude of mechanical loading, which is above the working load, the maximum restrained strain for a pile with a free base is noted at the mid-depth, while for a pile with a base support, the maximum restrained strain reduces towards the bottom.
- At the end of first cooling period (see Figure 4.15-b):
 - The maximum restrained strain is $-9.89\mu\epsilon$, which is slightly lower than the maximum restrained strain noted at the end of the first heating period. The maximum restrained strain at the pile head is noted in S4TM1. In S4TM1 and S4TM2, the restrained strain is reduced from the pile head towards the pile toe. In S4TM3–S4TM5, the strain profiles change, and the maximum restrained strain happens at SP2, SP3 and SP4. This shows that, due to the small levels of restraint caused by sand, the location of the maximum restrained strain changes depending on the magnitude of displacement before heating and cooling.
- At the end of second heating period:
 - The maximum restrained strain is $10.38\mu\epsilon$, which is observed at the SP4 level in S4TM7, while the minimum restrained strain is $0.48\mu\epsilon$, which is recorded at the SP1 level in S4TM1.
 - The maximum restrained strain for S4TM1–S5TM5 is seen at the SP4, SP5, SP2, SP3 and SP1 levels respectively, showing how the maximum restrained strain varies with a change in the magnitude of the pile settlement. With an increase in the magnitude

of the mechanical loading, more downward movement take place, and the location of the maximum restrained strain shifts towards the bottom half of the pile.

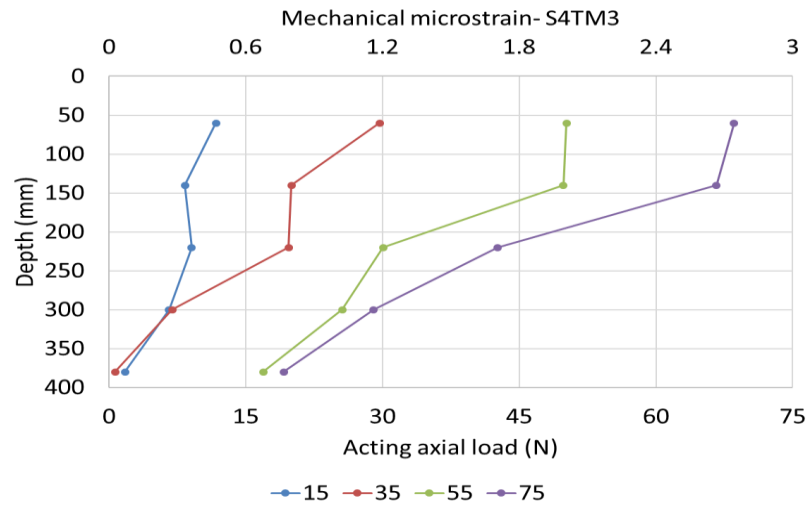
- In S4TM6–S4TM7, the maximum restrained strain is noted at the SP5 and SP4 levels respectively. Just like the end of the first heating period, the location of the maximum restrained strain in S4TM8 is noted at the SP1 level, showing the effectiveness of the pile base support for dealing with higher magnitudes of mechanical loading.
- At the end of second cooling period:
 - Differences exist between the restrained strain profiles, when compared with those of the first cooling period. The maximum restrained strain is $-11.43\mu\epsilon$, and is noted in S4TM4. In S4TM1, a linear decrease in the strain values is noted while, in S4TM2 and S4TM3, a linear increase is noted along the pile, with a sudden decrease at the SP2 level. In S4TM4, a decrease is noted towards the pile bottom, with a sudden increase at SP2. In S5TM5, a linear increase towards the pile bottom is noted. In S4TM6–S4TM8, the less restrained strain is observed at the pile bottom, unlike during the first cooling period.



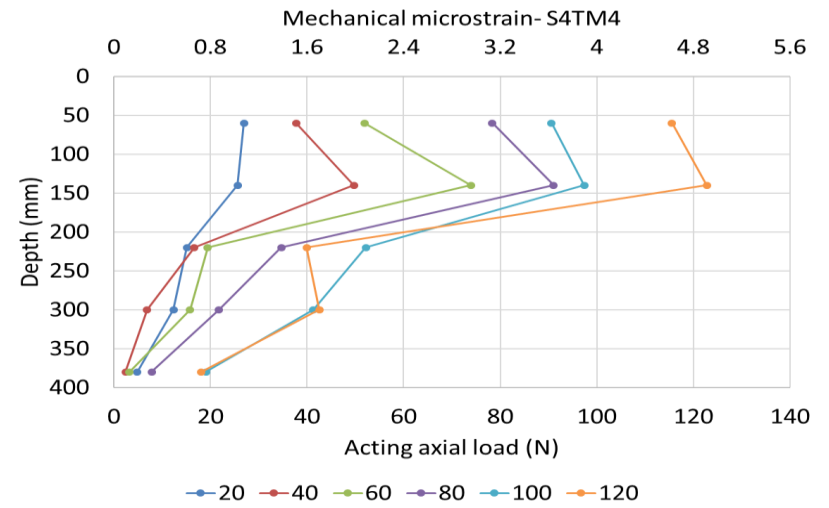
(a)



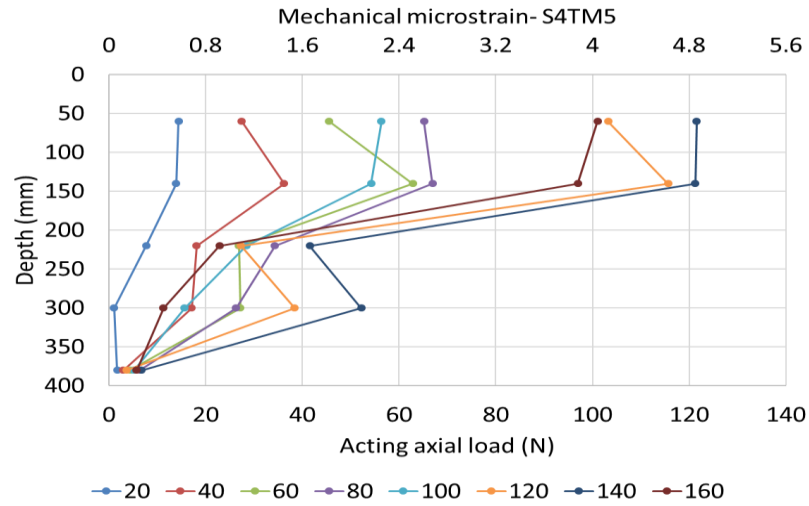
(b)



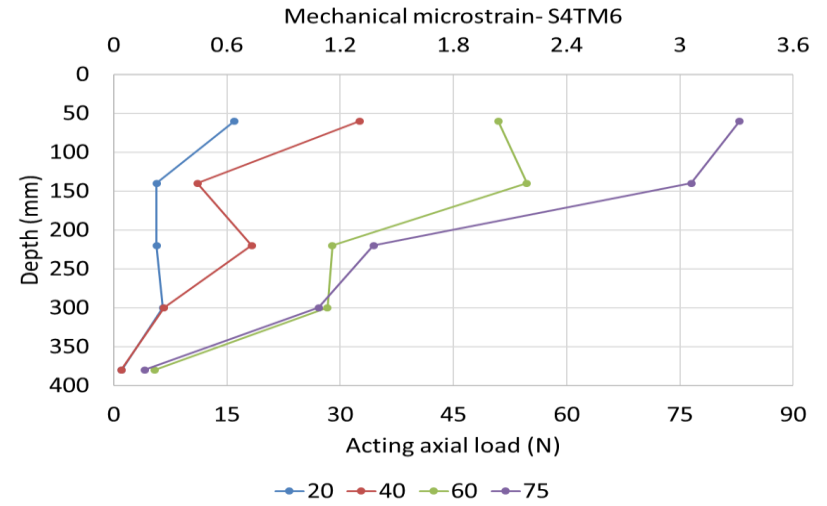
(c)



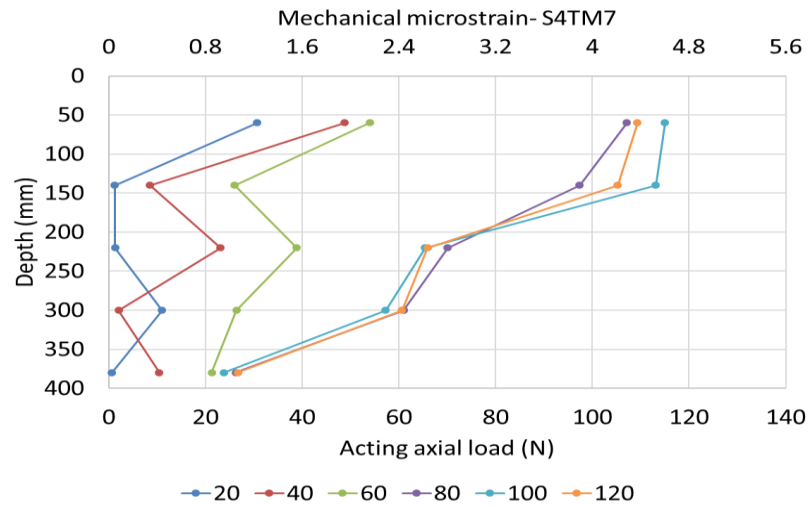
(d)



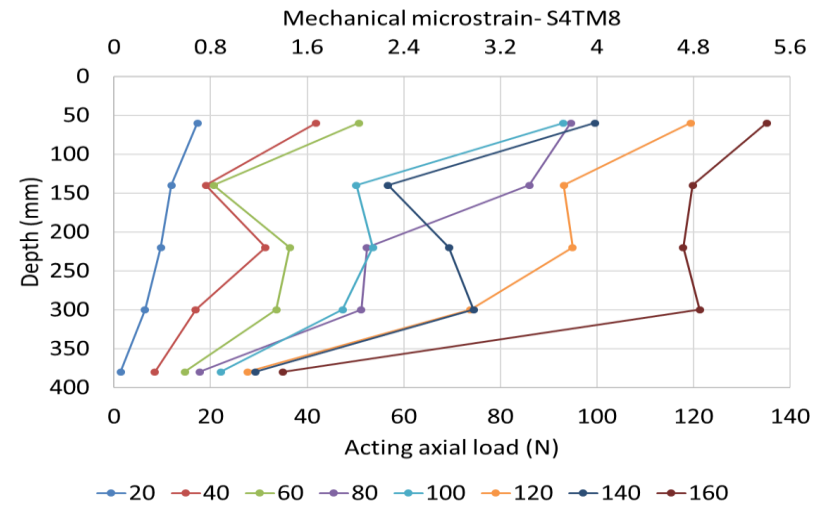
(e)



(f)

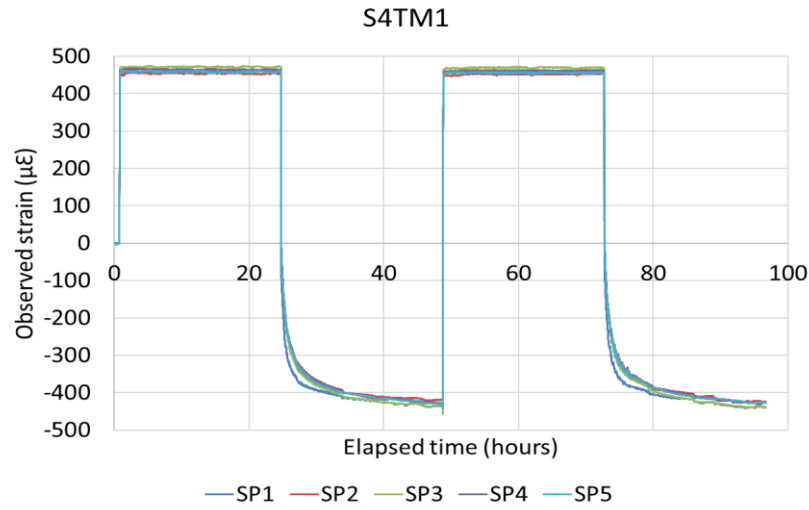


(g)

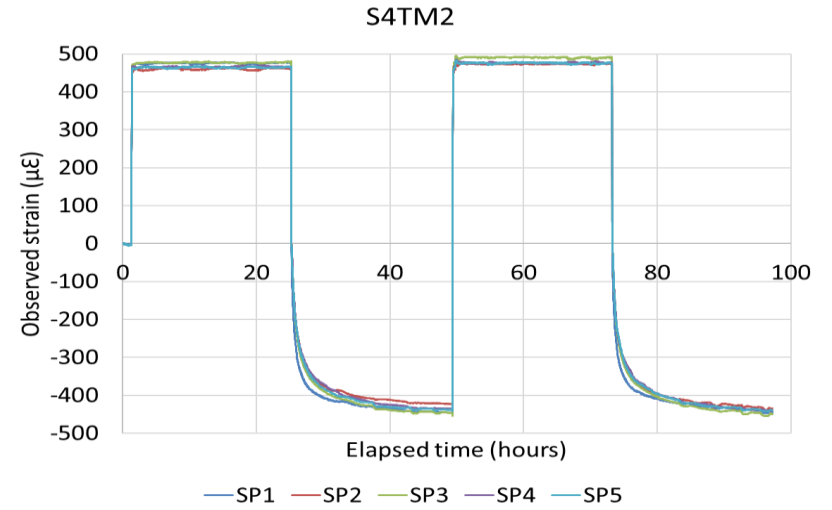


(h)

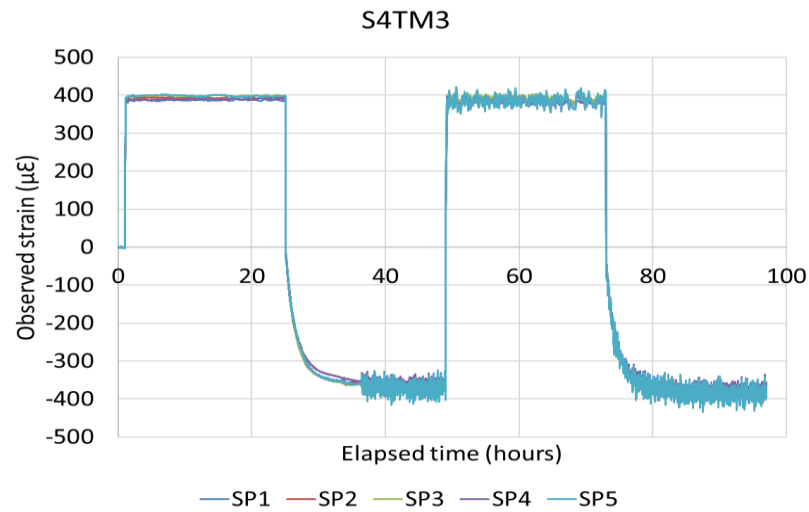
Figure 4-12. Observed mechanical strain and acting axial load along the pile – Scenario 4



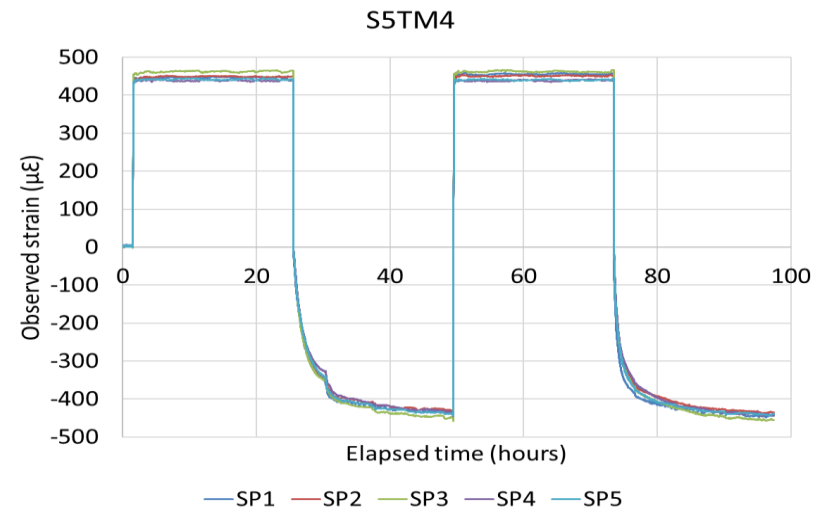
(a)



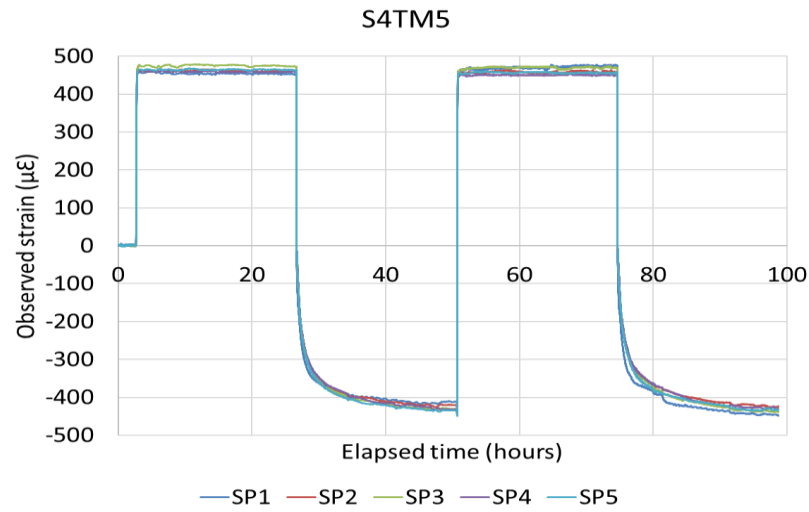
(b)



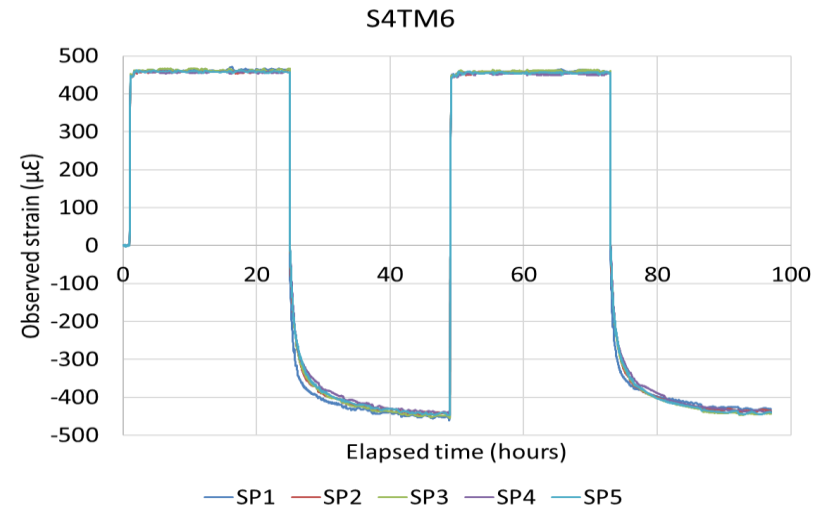
(c)



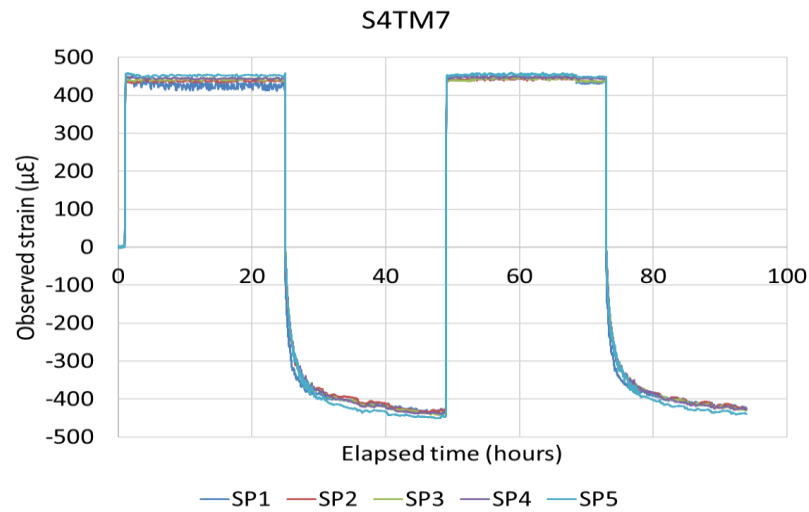
(d)



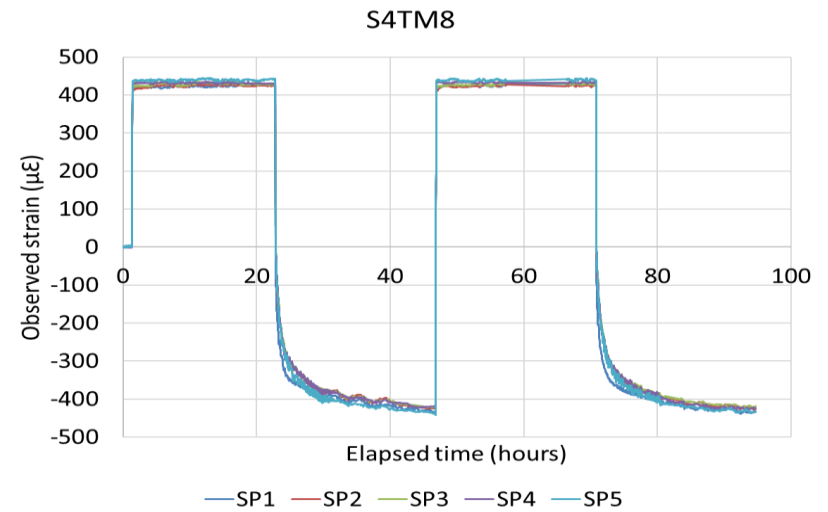
(e)



(f)



(g)



(h)

Figure 4-13. Observed strain during two heating-cooling cycles – Scenario 4

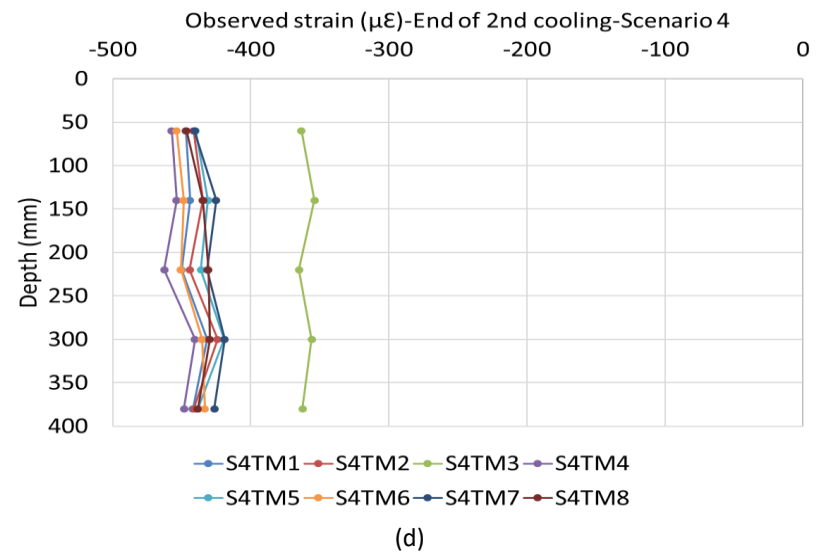
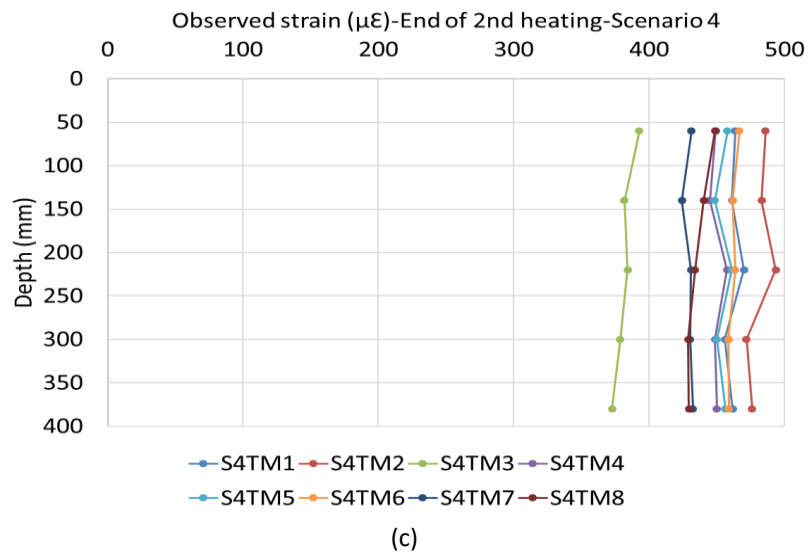
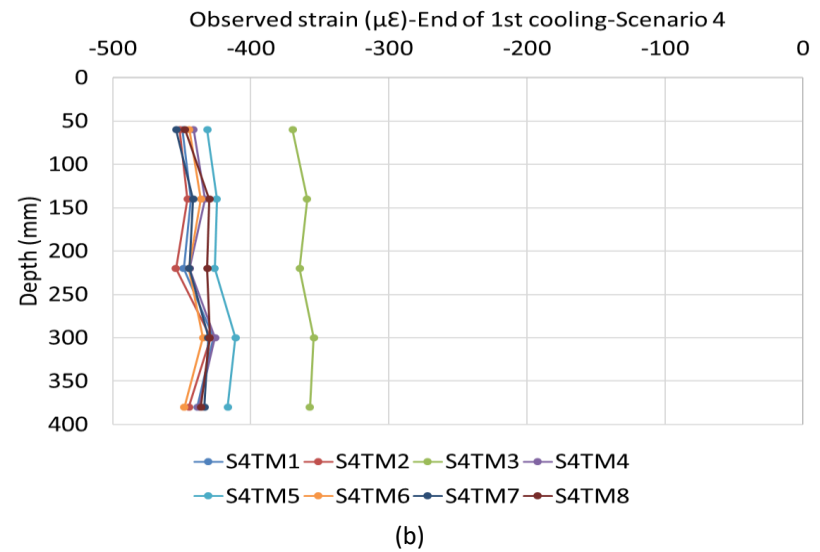
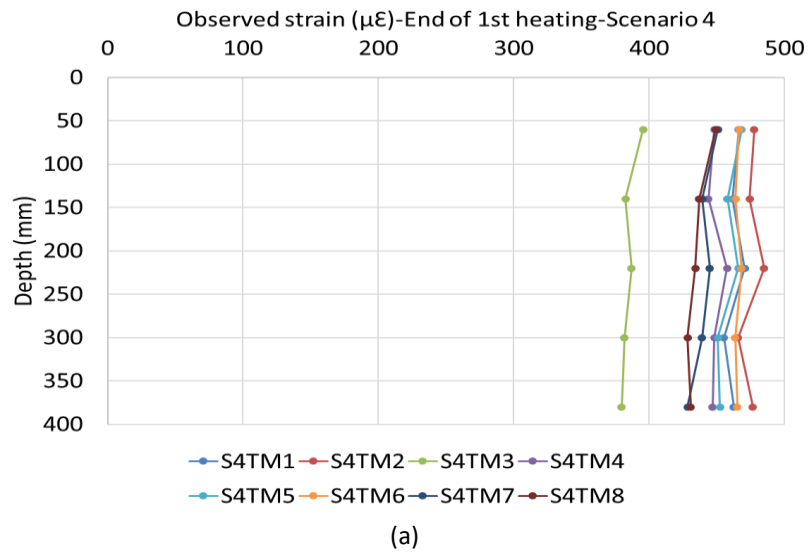
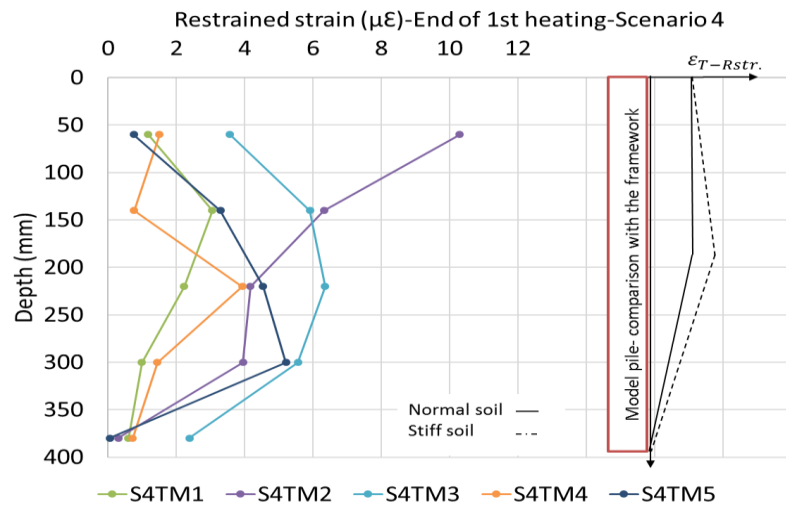
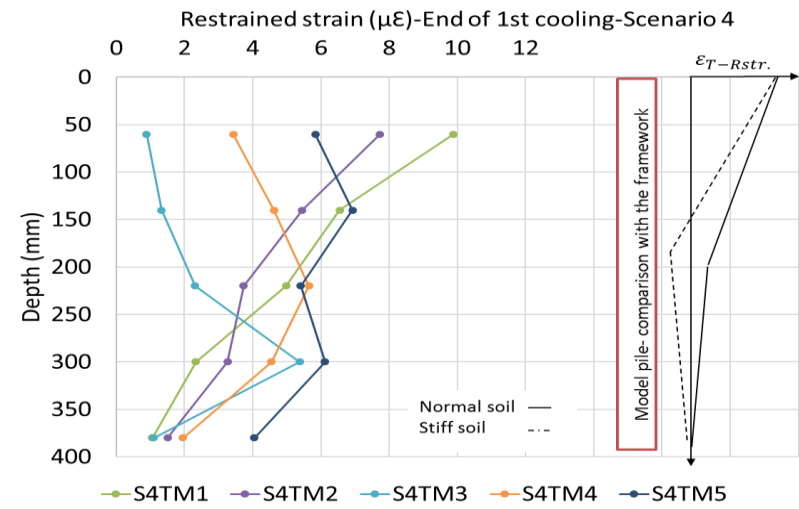


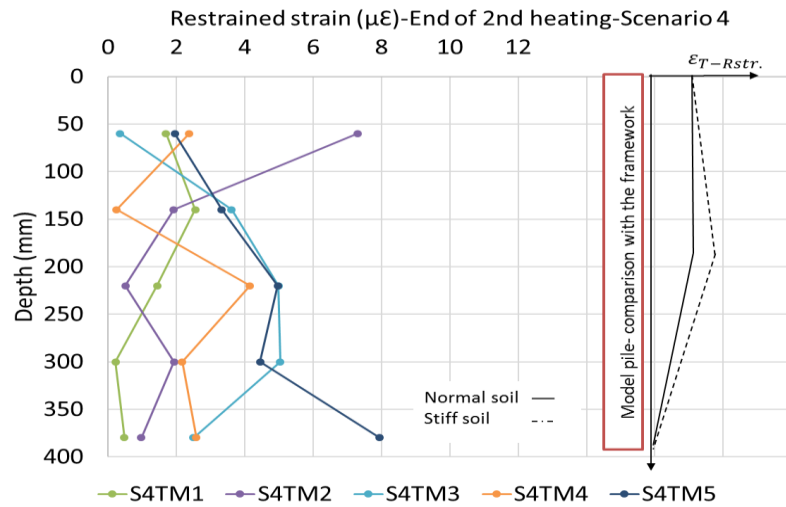
Figure 4-14. Observed strain at the end of each heating-cooling period – Scenario 4



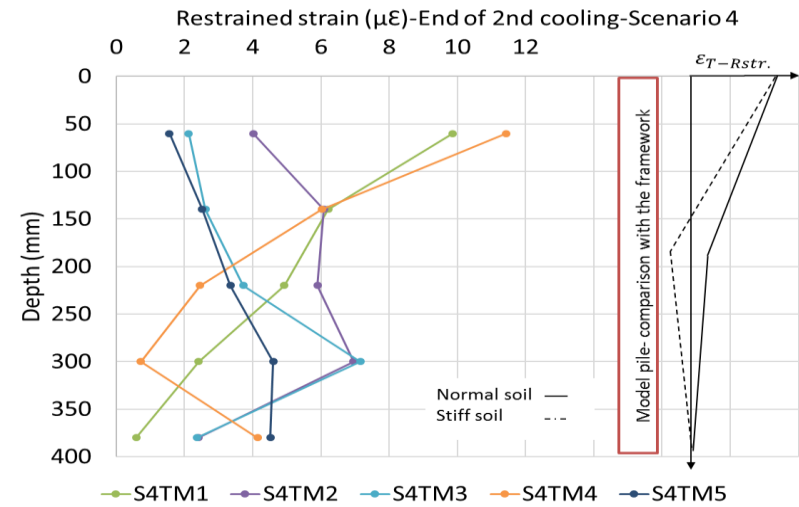
(a)



(b)



(c)



(d)

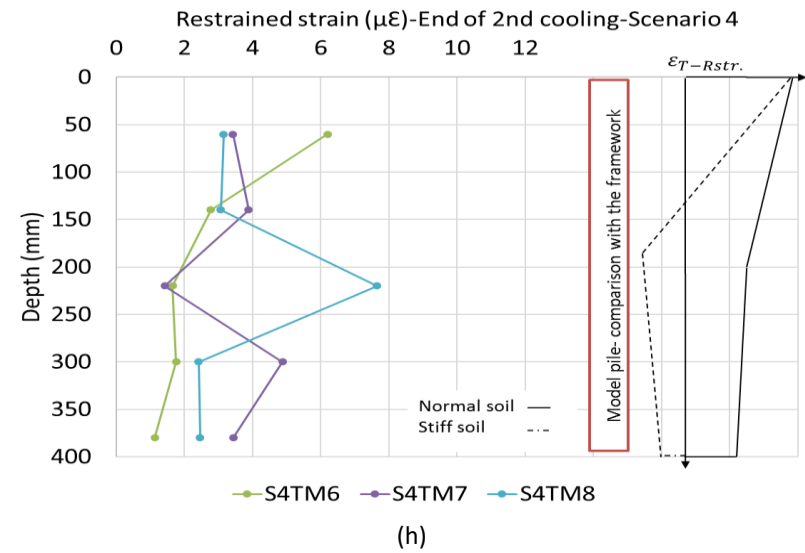
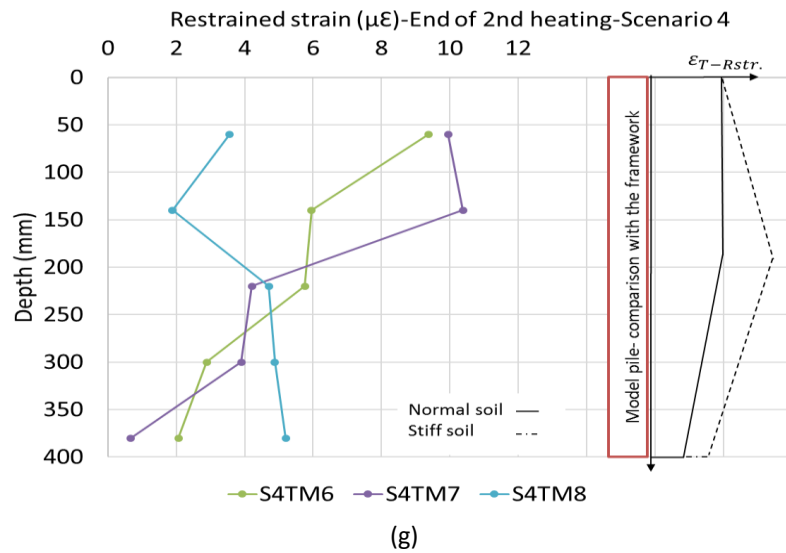
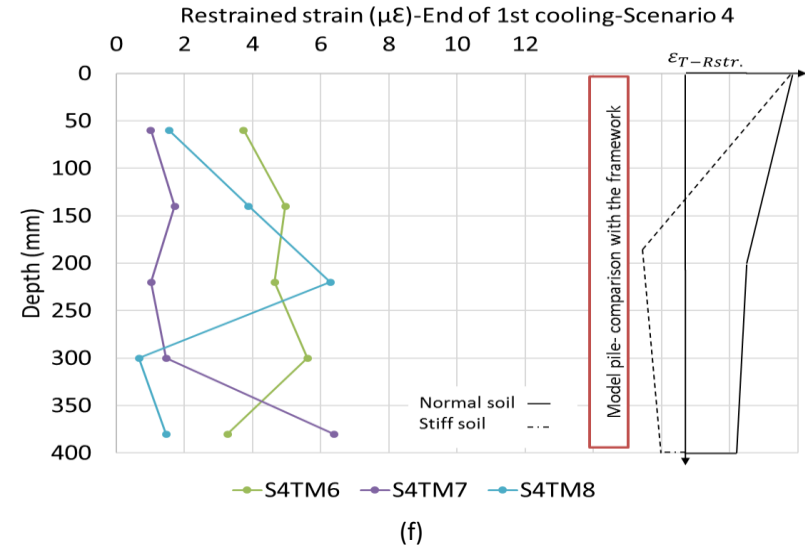
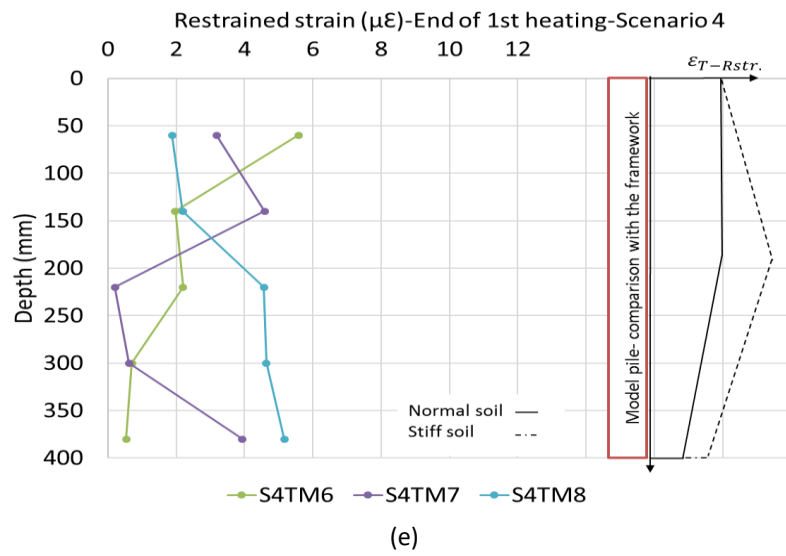
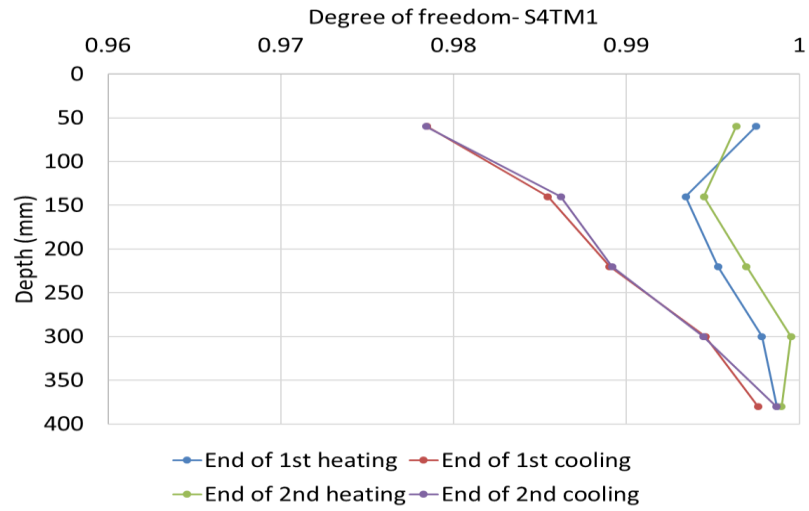


Figure 4-15. Restrained strain at the end of each heating-cooling period – (a) to (d): S4TM1-S4TM5; (e) to (f): S4TM6-S4TM8

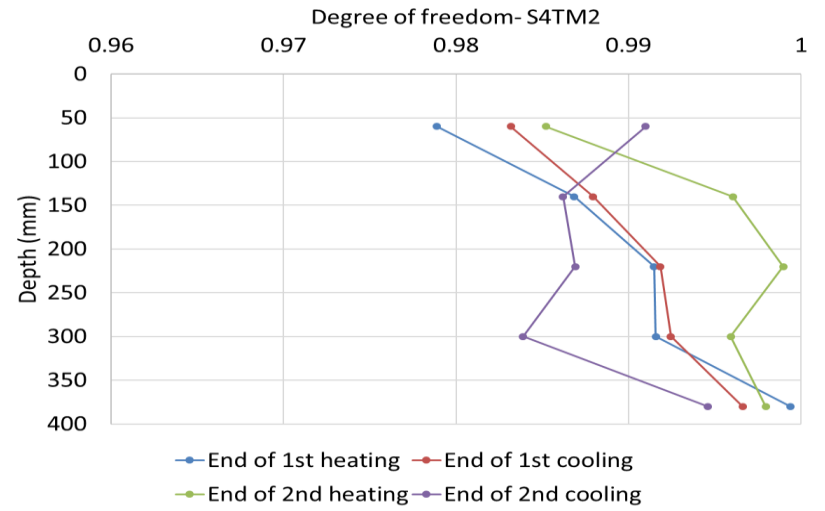
4.6.3 Degree of freedom

The changes in the DoF along the pile, at the end of each heating and cooling period during the Scenario 4 tests, are shown in Figure 4.16. A summary of the findings is presented below:

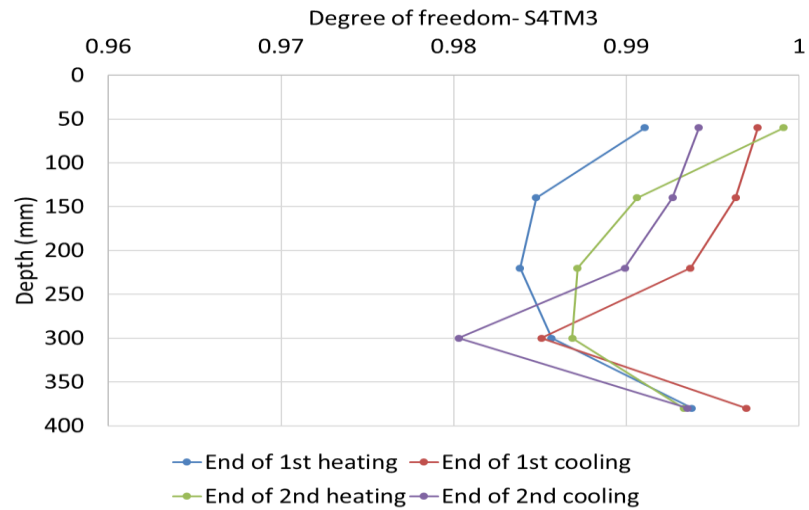
- In S4TM1, where a mechanical loading of 30N is applied to the pile head, the lowest DoF value is noted at the end of the first cooling period, followed by the second cooling period. The maximum DoF is noted at the end of the second heating period, followed by the first heating period. This means that there is a greater level of restraint for the pile during the cooling periods than during the heating periods. This is mainly due to the low magnitude of the mechanical load, which has not been able to provide sufficient restraint for the pile upward movement. In S4TM2, the maximum and minimum restraint at the pile head occurs at the end of the first and second heating periods respectively.
- In S4TM1–S4TM3, the maximum restrained strain is noted at the end of the second cooling period. The shape of the profiles changes considerably for the minimum DoF at the SP3 level during the heating period, and at the SP2 level during the cooling periods. This shows the shift in the location of the minimum DoF at each period and highlights that it would be inappropriate to consider a constant null point during the entire test period.
- In S4TM4, where a mechanical loading of 120N is applied to the pile head, the maximum restraint is applied at the pile head at the end of the second cooling period. This is followed by the restraint at the mid-depth, at the end of the first cooling period. In S4TM5, where a considerable settlement is experienced before thermal loading, the minimum DoF is seen at the end of the first cooling period.
- Different behaviour is noted in S4TM6–S4TM8 than in S4TM1–S4TM5, mainly due to the restraint that exists at the pile bottom. In S4TM6 and S4TM7, the minimum DoF is noted at the end of the second heating period. In S4TM8, the minimum DoF is noted at the SP3 level during the second cooling period. This is the only test where the minimum DoF is seen at the mid-depth, with an increase towards both ends.
- Regarding magnitude, the change in the DoF is between 0.975 and 1.0, which means a minor restraint caused by the sand and mechanical loads applied onto the pile head.



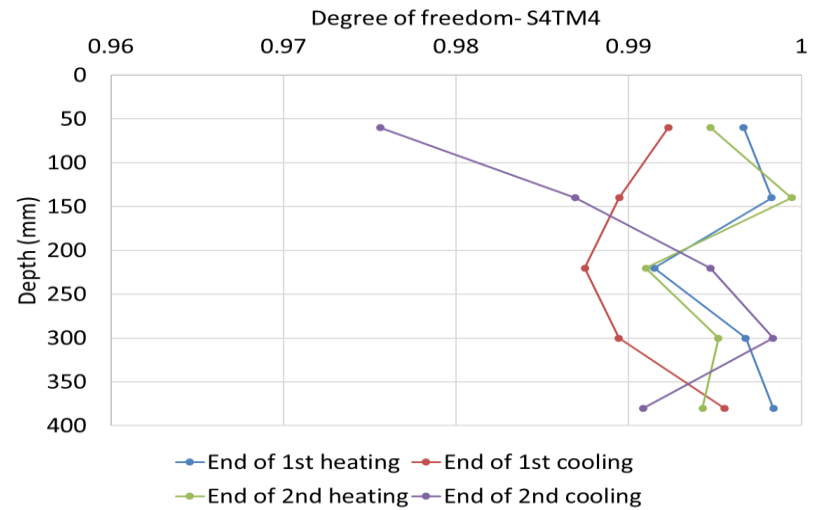
(a)



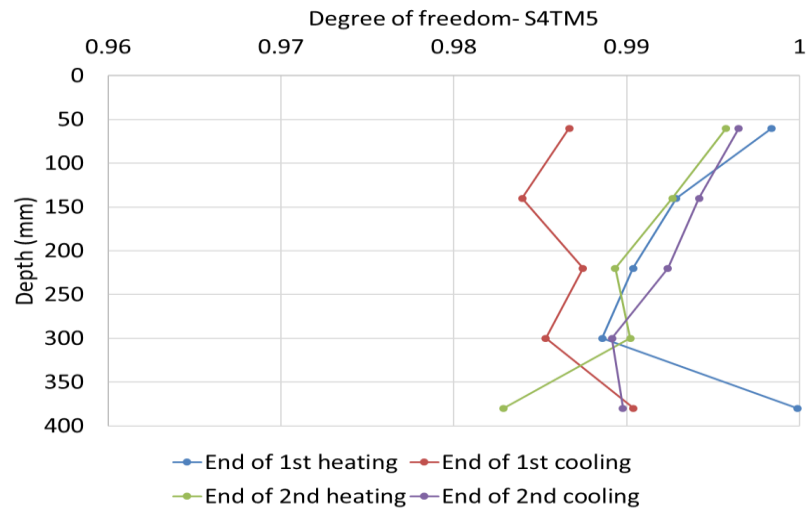
(b)



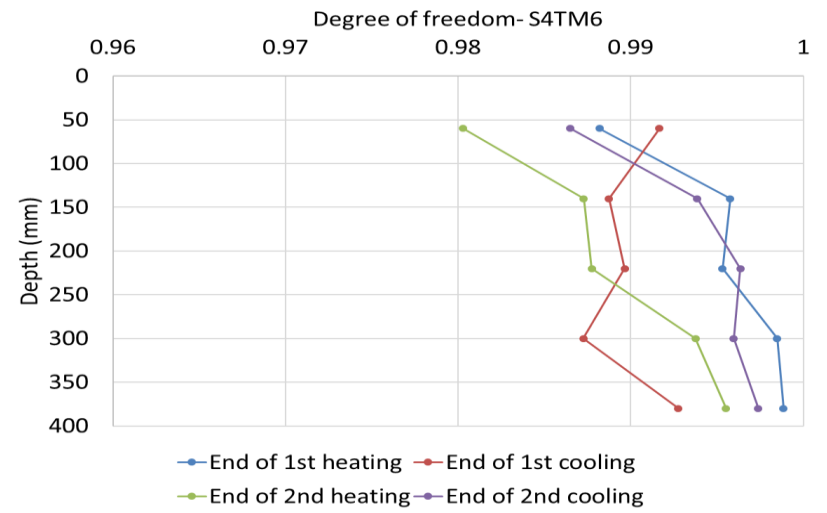
(c)



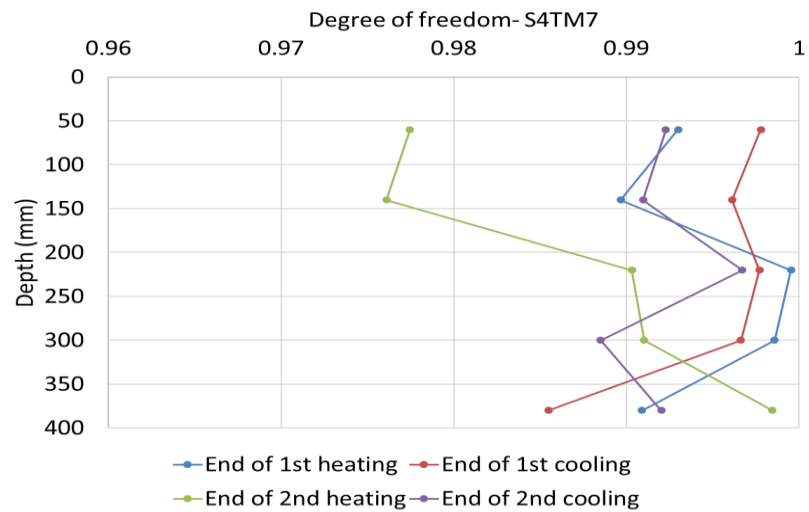
(d)



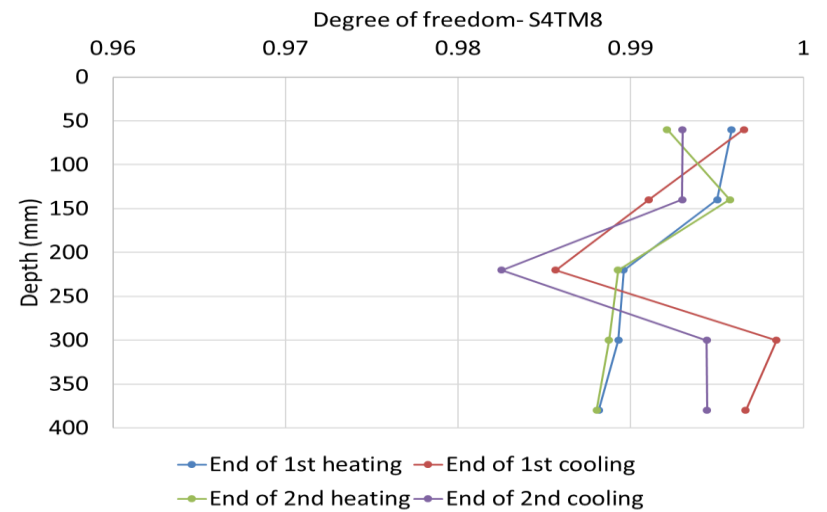
(e)



(f)



(g)



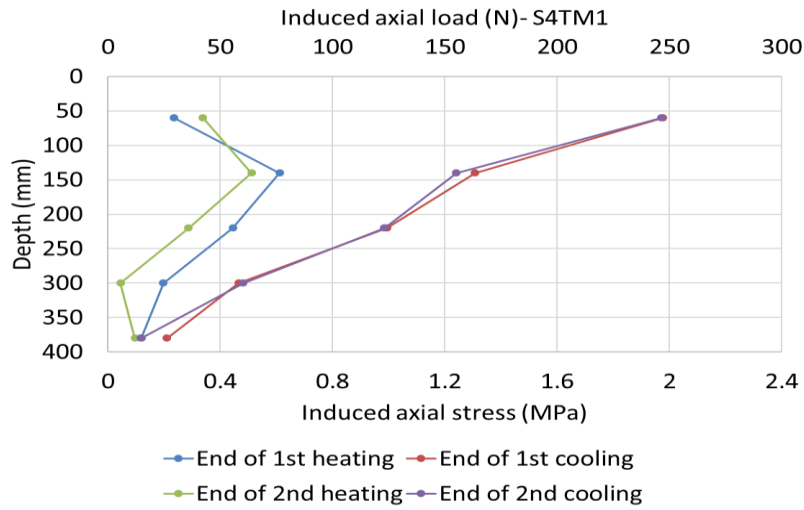
(h)

Figure 4-16. Variation of DoF along the pile length – Scenario 4

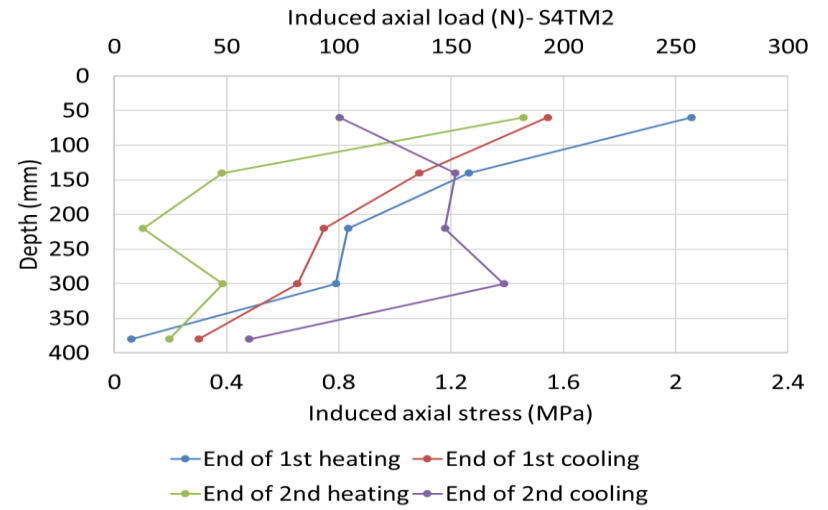
4.6.4 Thermally induced axial force and stress in the pile

Due to the restraint caused by the surrounding soil and the mechanical load on the pile head, axial force and stress are induced in the pile. Due to the linear, elastic relationship between $\epsilon_{Rstr.}$ and the induced force and stress for the stainless steel model pile, scaled profiles are noted (see Figure 4.17).

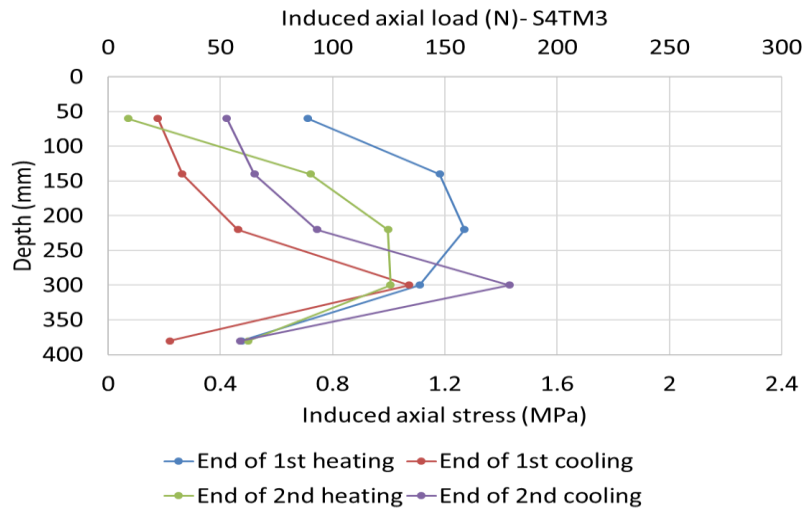
- In S4TM1, the maximum induced load at the end of the first heating period is 76.3N. This is then increased to 246N at the end of the first cooling period. This is followed by a recovery during the heating period, and lowered to 63N, with another increase to 246N occurring at the end of the second cooling period. It seems that the induced loads during the cooling periods are not completely recovered during the subsequent heating periods. Similarly, greater magnitudes of induced loads are observed during the cooling periods than the heating periods in S4TM4–S4TM6. The reverse of this is seen in S4TM7 and S4TM8. This means that, with restraint at both ends, additional induced loads that are caused by heating are recovered during the cooling period. This is mainly due to the pile's inability to expand.
- Unlike the mechanical loading case, where the pile at the SP1 level carries the minimum load, in thermal loading, a considerable load of up to 198N is supported at the SP1 level, due to the distributed heat transfer along the pile surface. This is more apparent in the tests S4TM6–S4TM8, which use supports at the bottom of the pile.
- The maximum induced axial load of 285N occurred at the end of the second cooling period in S4TM4. This is 1.72 times greater than the ultimate load-bearing capacity of the shaft, as determined in Section 4.2. The maximum induced stress is 2.29MPa, which is only 3.63% of the allowable stress for the stainless steel model pile, according to BS 8004:1986 (British Standards Institution, 1986).



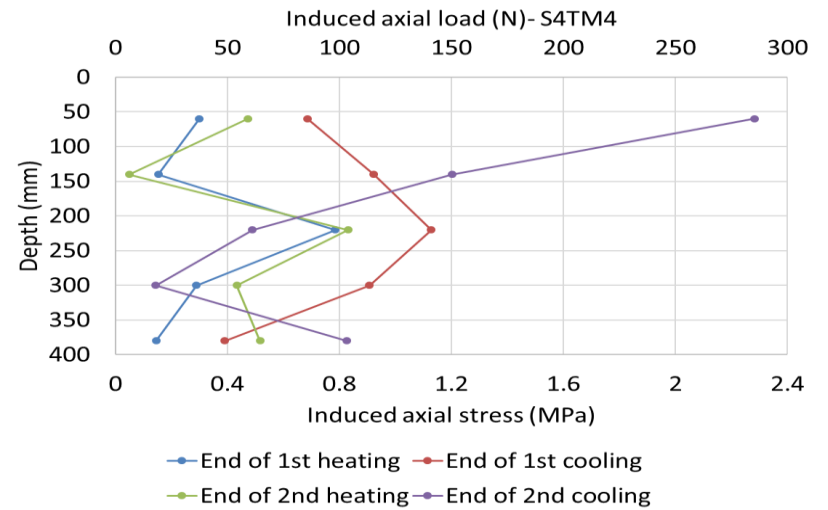
(a)



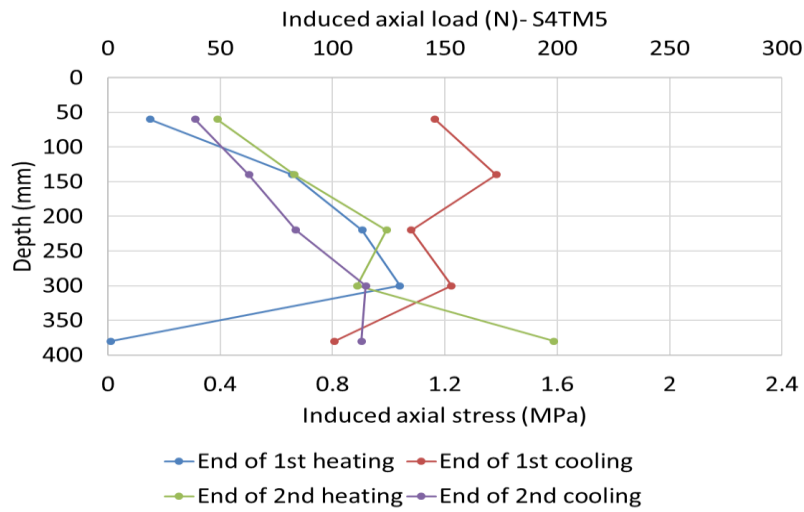
(b)



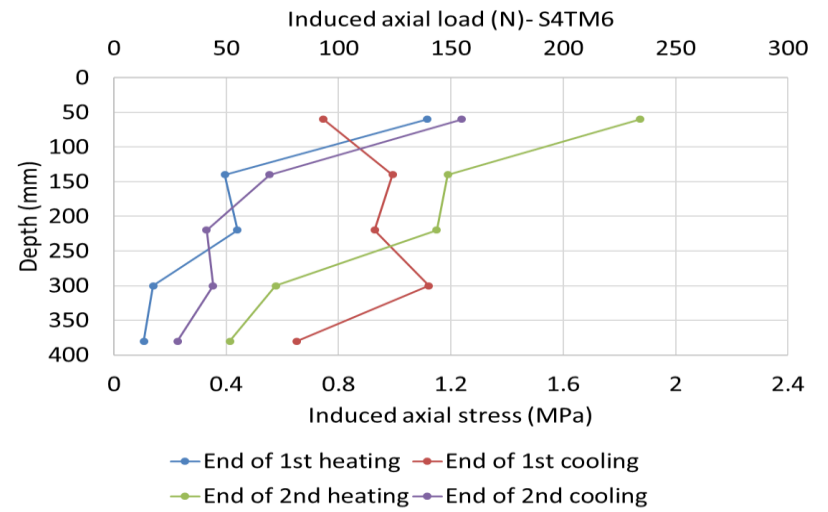
(c)



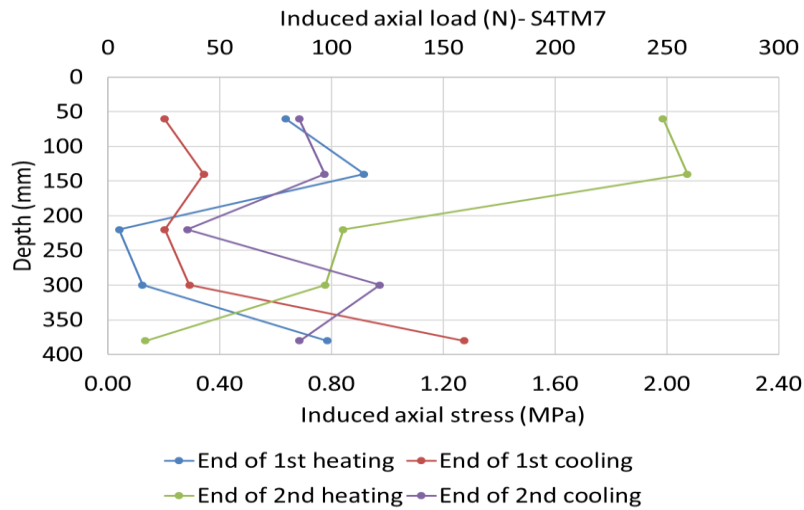
(d)



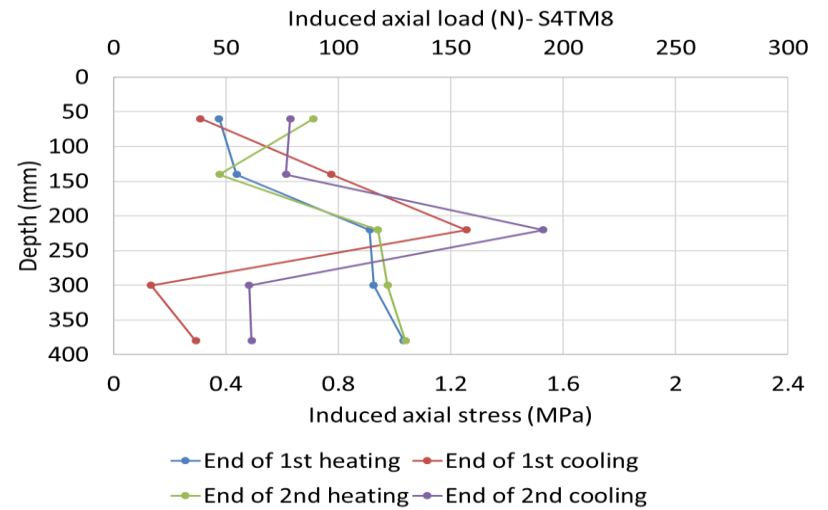
(e)



(f)



(g)



(h)

Figure 4-17. Induced thermal force in the pile – Scenario 4

4.6.5 Pile head displacement

The changes in pile head settlement for the Scenario 4 tests are shown in Figure 4.18. In a similar way to the Scenario 3 pile head displacement figures, the pile first settles under the mechanical loading. After applying the heating load, the pile heaves and then settles during the cooling period. The same procedure is repeated in the second cycle. At the end of heating-cooling cycles, the pile head is unloaded in the same order, with 10–20N being removed at each step, as with the initial mechanical loading. This results in a partial recovery of the cumulative pile settlement. The following observations are made:

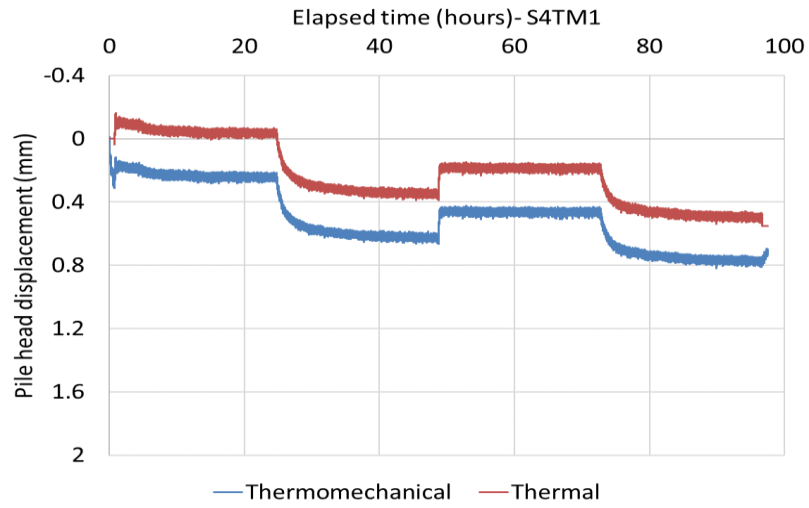
- In the tests S4TM1 to S4TM3, where the amount of mechanical loading is less than 50% of the ultimate shaft resistance of the pile, the maximum pile head displacement is noted during the first cooling period. In the second cooling period, the accumulated pile head settlement is increased, but the larger proportion is achieved during the first cooling period.
- For the shaft resistant pile used in Scenarios 3 and 4, a larger settlement during the first cooling period means that, during the first cooling, considerable friction is lost between the pile surface and the soil. For higher loads, it seems that the pile slips and is unable to get back to its previous position after the second heating. This is discussed further in Chapter 6.
- Different behaviours are noted between S4TM1–S4TM3 and S4TM4–S4TM5, in the heaving–settlement process. In the first three tests, where the mechanical load is below 50% of the ultimate shaft capacity, settlement in the first cooling period is the greatest, and lowers during the second cooling period, despite an overall increase in the cumulative settlement. In S4TM4, the pile undergoes a considerable settlement of 0.554mm but, after five hours of continuous settlement, the pile has reaches a steady-state. A small heave is also seen during the second heating period but, at the start of the second cooling period, the pile starts to settle continuously until failure.
- In S4TM5, the initial mechanical loading is approximately 97% of the ultimate capacity, but heating has caused a small recovery in the settlement. With the start of the first cooling period, a significant settlement of approximately 5.5mm occurs and, with the start of the second heating period, it stops the pile from further settlement, and keeps it in that position. With the start of the second cooling period, a further settlement is observed, and failure happens again.
- According to Figures 4.18-a to 4.18-e, under all mechanical loadings, the cooling period acts as a trigger for the pile settlement, and adds to the initial settlement that is caused by the mechanical loading, while the heating period recovers the small amount of settlement for the shaft resistant pile. With an increase in the mechanical loading to more than 50% of the ultimate capacity of the pile, the first cooling cycle considerably reduces the friction between the pile and soil, and the second cooling period results in complete pile failure. This is due to

the loss of the friction between the pile and soil, and not being able to return to its original position, as described in Chapter 6.

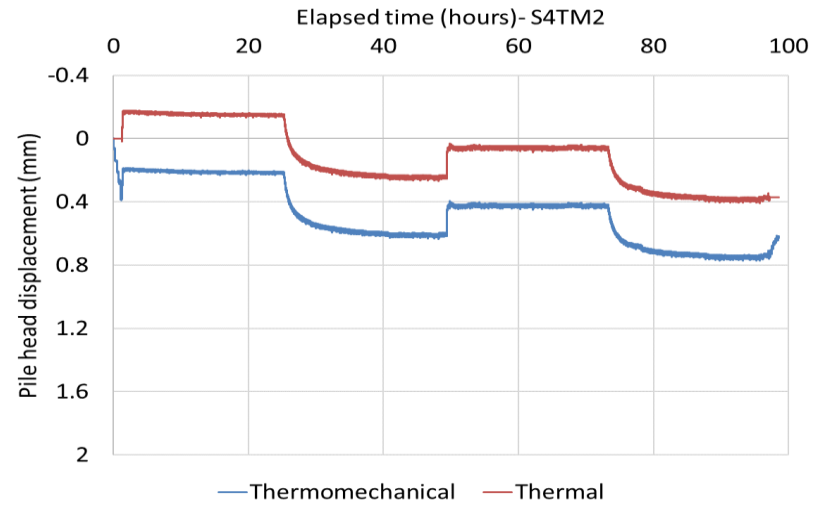
- The average pile head settlement under mechanical loading (0N to 160N) is calculated to simulate the magnitude of the increase in the settlement due to the cooling periods, to an equivalent increase in the mechanical loading. Unlike the results of Scenario 5 (see Chapter 5), the pile head settlement more than doubles in the tests S4TM1 to S4TM5, after the thermal cycles. This means that the cumulative settlements noted in S4TM1–S4TM3 reach close to the equivalent pile head settlement under 120N–130N mechanical-only loading (see Table 4.4). The factor of safety, the ratios of the applied mechanical loads over the ultimate shaft capacity (165N), are reduced from 5.5, 3.0 and 2.2 to less than 1.28 for all three tests, causing failure in S4TM4 and S4TM5.
- Similar to S3T2, the larger settlement in the S4TM7 and S4TM8 tests is noted in the second cooling period, and the larger heaving in the first heating period. The bottom support seems to push the pile up and, instead of releasing the pile strain in both directions, releases it from the pile head, despite being partially restrained at the pile head.
- In S4TM6, similar behaviour as in S4TM1–S4TM3 is noted, with less pile head displacement due to the existence of the bottom support.
- In all of the tests, the pile head settlement under its self-weight is measured at 0.1mm, which is considerable, and justifies part of the thermo-plastic behaviour of the pile without any mechanical loading on the pile head.

Table 4-4. Changes in pile head settlement under heating and cooling cycles – Scenario 4 tests

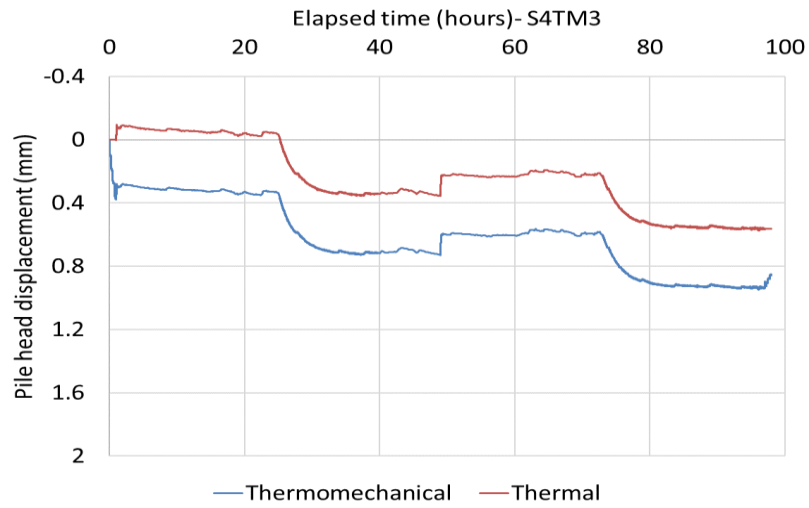
Test	Mechanical load (N)	Settlement – mechanical (mm)	Settlement – thermo-mechanical (mm)	Thermo-mechanical/mechanical
S4TM1	30	0.31	0.815	2.63
S4TM2	55	0.389	0.772	1.98
S4TM3	75	0.377	0.948	2.51
S4TM4	120	0.713	Failure	N/A
S4TM5	160	1.899	Failure	N/A



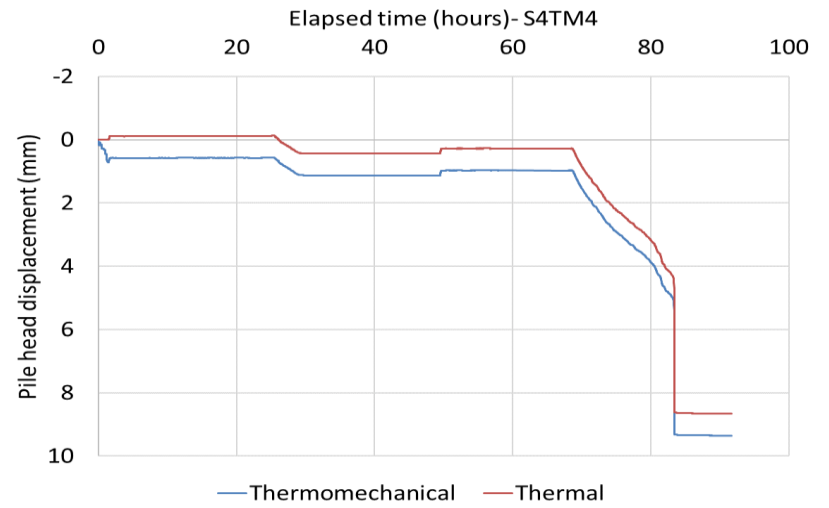
(a)



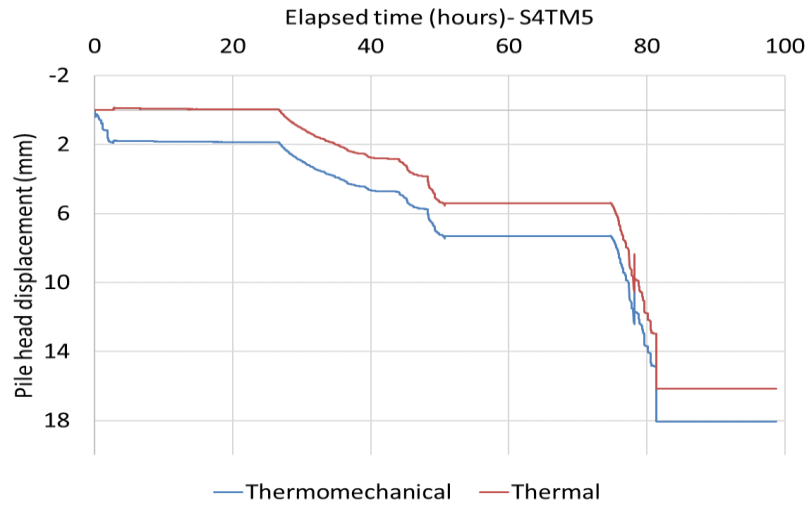
(b)



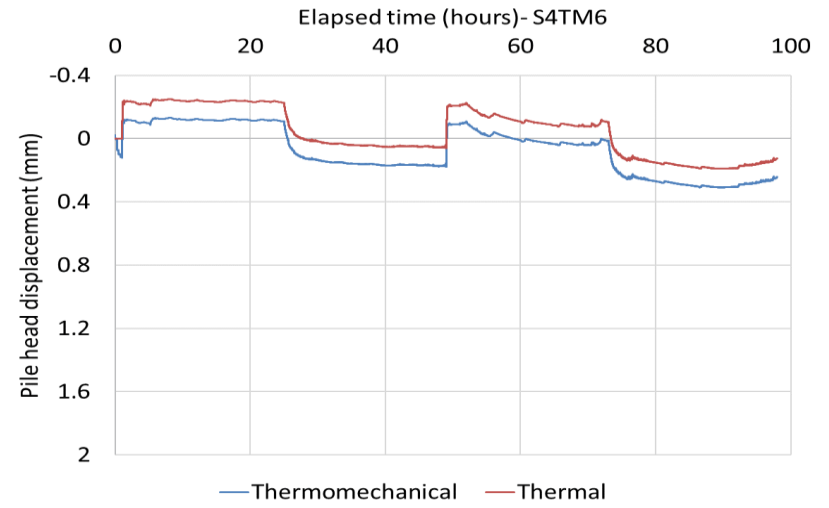
(c)



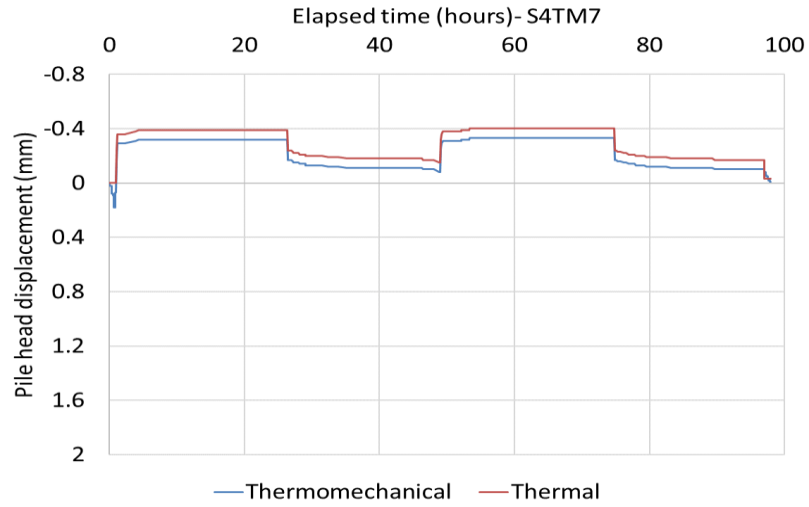
(d)



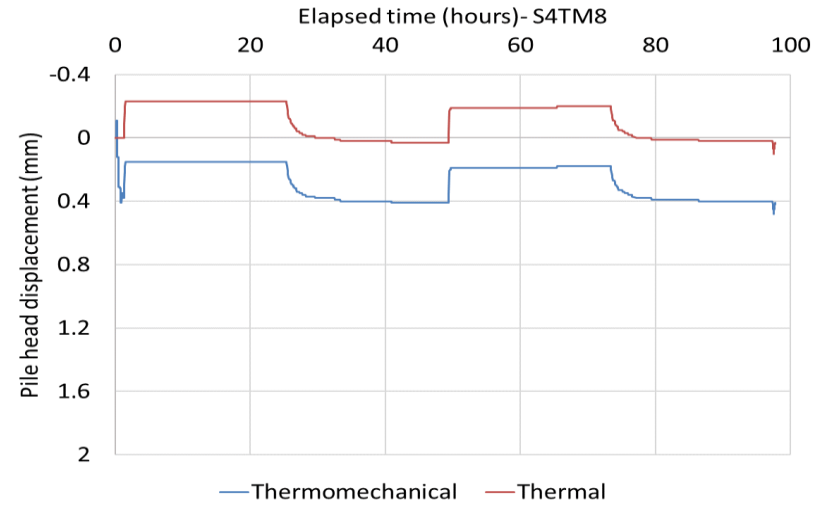
(e)



(f)



(g)



(h)

Figure 4-18. Pile head displacement vs time – Scenario 4

4.6.6 Mobilised friction at the soil–pile interface

In a similar way to Scenario 3, the pile is divided into four zones, and the same calculation procedure is adopted for each. The mobilised shaft friction under mechanical loading is presented in Figure 4.19. It is noted that:

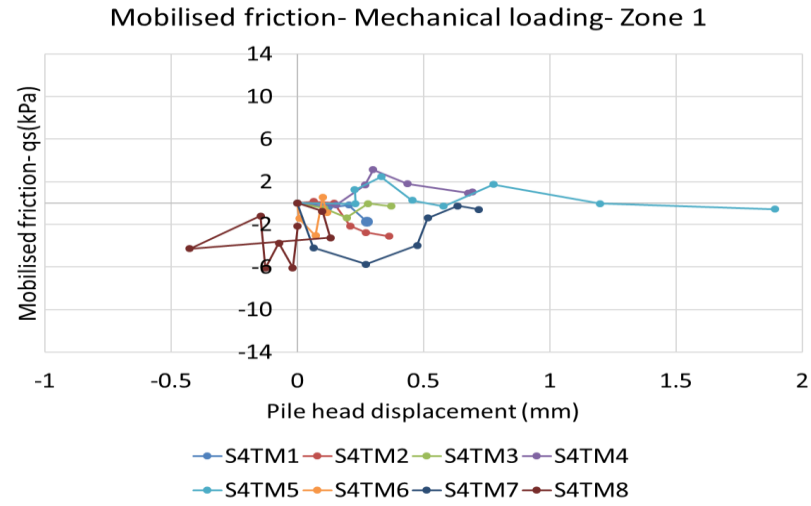
- In S4TM1 to S4TM5, an increase in the magnitude of the mechanical loading results in an increase in the magnitude of the mobilised shaft friction, due to the increase in the magnitude of the pile displacement. The maximum mobilised friction is seen in S4TM4 and S4TM5 at 3.13kPa and 2.47kPa respectively. In S4TM6–S4TM8, irregular behaviour is noted, with continuous increases and a decrease in the mobilised friction due to the base support.
- In all four zones, a low magnitude of mobilised friction is noted for mechanical loads of 30N, 55N and 75N. The mobilised friction is then increased in S4TM4, with a further, considerable increase occurring in S4TM5. This result shows that tests with higher settlements have higher levels of mobilised friction.

The changes in the mobilised shaft friction of the pile head displacement, during the entire mechanical and thermal loading for four zones in S4TM1, is shown in Figure 4.20. This figure is used to describe a sample of the behaviours noted during the entire test; similar profiles for the other seven tests are provided in Appendix H. It is noted that:

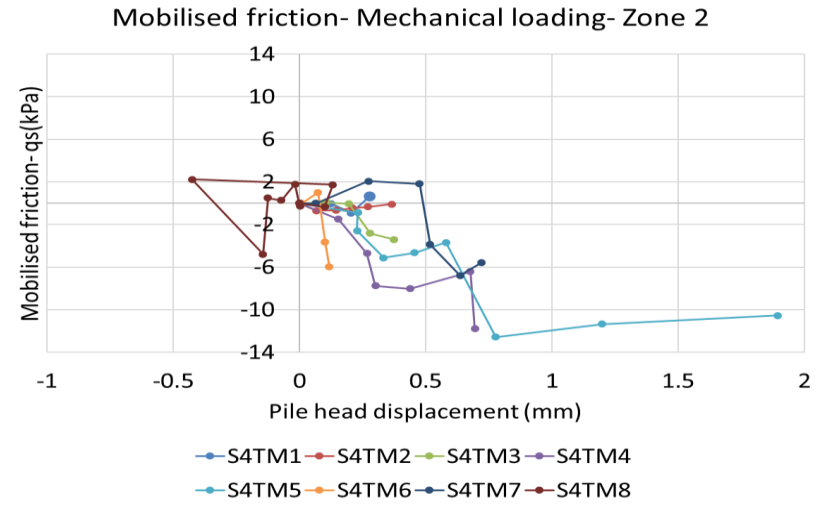
- In Zone 1, the mobilised friction increases from -1.74kPa to -7.12kPa at the end of first heating period (see Figure 4.20-a). This is then lowered to +3.5kPa at the end of the first cooling period. This is then followed by an increase to -9.4kPa at the end of the second heating period, with another drop in mobilised friction to +1.59kPa at the end of the second cooling period. This means that the friction is mobilised to a higher level than the mechanical loading values, and the cooling period acts as a relief to the mobilised friction. The increase in the mobilised friction during the heating period is due to pile expansion and the increase in the contact between the pile and soil surface, while the reverse of this process happens in the cooling periods. This is in line with the observations of Mimouni (2014).
- In Zone 2, a minor change in the mobilised friction is noted after the first heating period, and then the friction is mobilised up to -2.89kPa at the end of the first cooling period. It is then returned to 0.15kPa at the end of the second heating period, and increased to approximately the same level as that noted at the end of the first cooling period. The observed behaviour in Zone 2 is the reverse of the process in Zone 1, which is mainly due to the low magnitudes of mobilised friction seen in this zone.
- Zone 3 uses a similar procedure to Zone 1, in which the mobilised friction is increased during the heating periods, and then recovered during the subsequent cooling periods. Similar behaviour is noted in the first cycle of thermal loading in Zone 4.

The mobilised friction profiles at the end of the mechanical loading, and at the end of each heating-cooling period along the four zones of the pile, are shown in Figure 4.21.

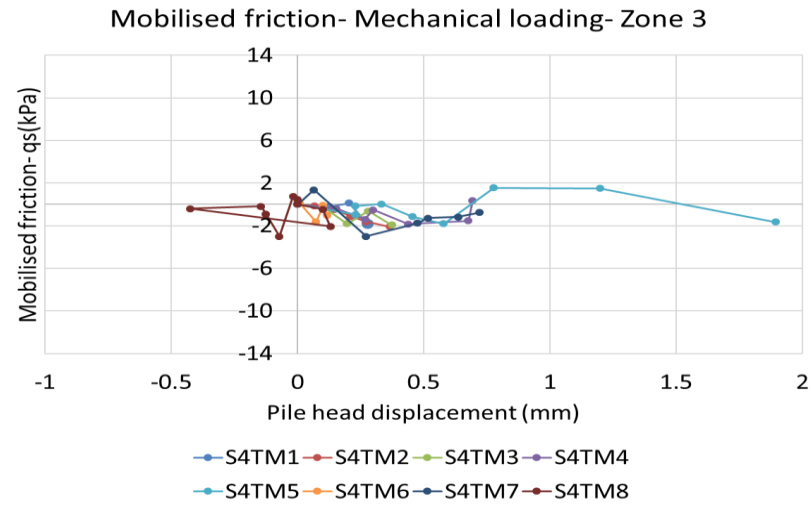
- In S4TM1, the maximum mobilised friction is noted during the first and second heating periods, with all values lower than 10kPa, which is lower than the 10.53kPa noted under the mechanical loading of 160N in S4TM5.
- In S4TM2, the largest magnitudes of mobilised friction are seen at the end of the second heating and cooling periods in the positive region, with values up to 17.47kPa. This is larger than the 10.53kPa limit caused by 160N of mechanical loading. It shows the significant impact of thermal loading on the mobilisation of the shaft along the pile.
- Similarly, in six other tests, the magnitude of the mobilised friction at the end of the heating-cooling periods surpasses the maximum mobilised friction under the maximum mechanical loading of 160N. This is justified by Figure 4.18-e, where it is shown that heating has stopped the pile from achieving further settlement and expansion of the contact surface between the pile and sand. The irregular decreases and increases in the mobilised friction during the cooling periods can be justified in a different way. A decrease in the mobilised friction could be due to the contraction of the pile and the sand, and the possible reduction in the contact level between the pile and the sand, while an increase could be explained by the irregular movement of the sand at the soil–pile vicinity, resulting in areas with higher and lower densities than the original state. This will be further discussed in Chapter 6.



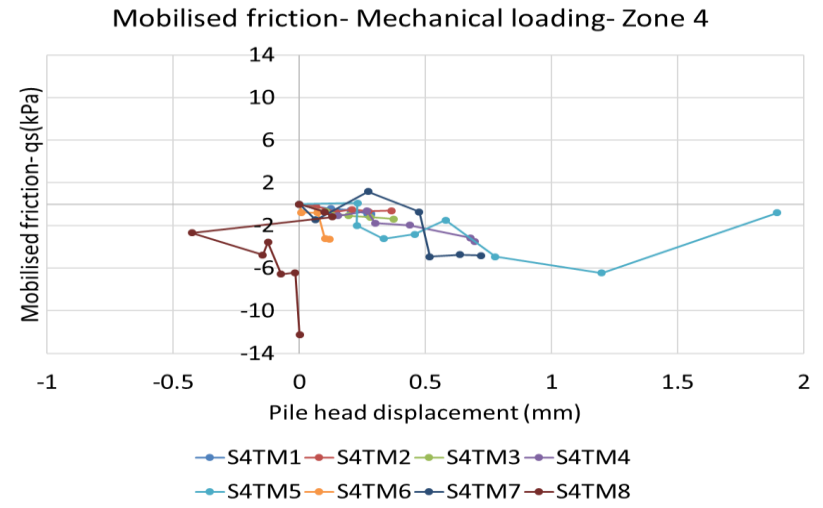
(a)



(b)

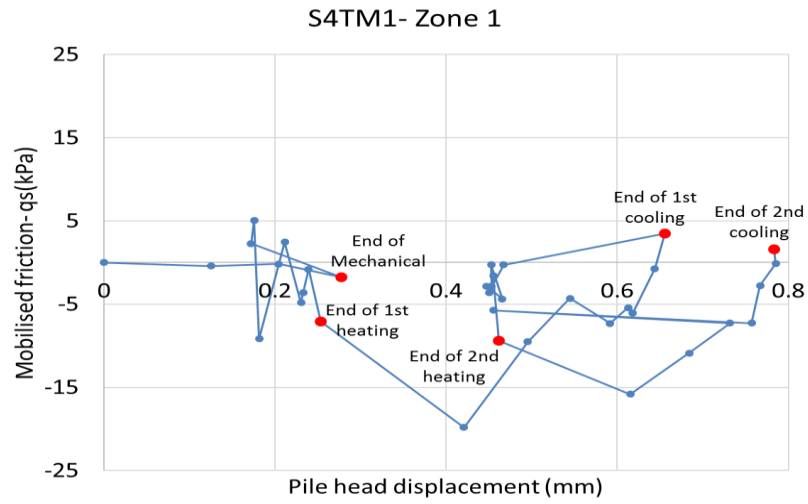


(c)

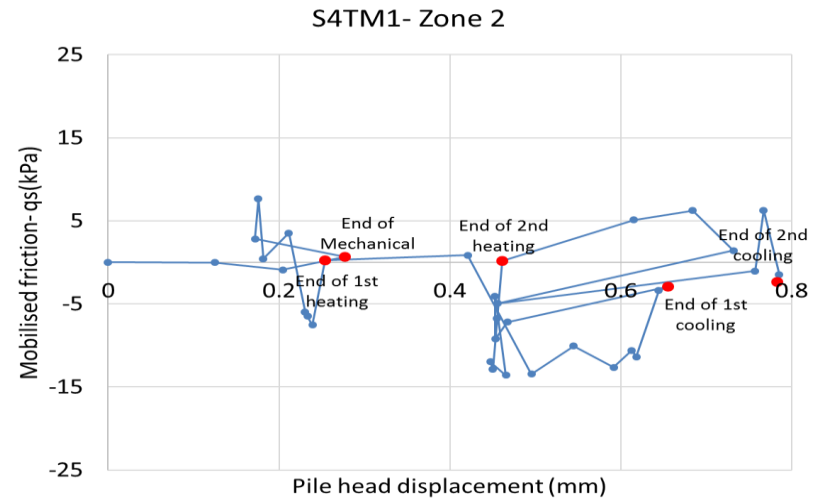


(d)

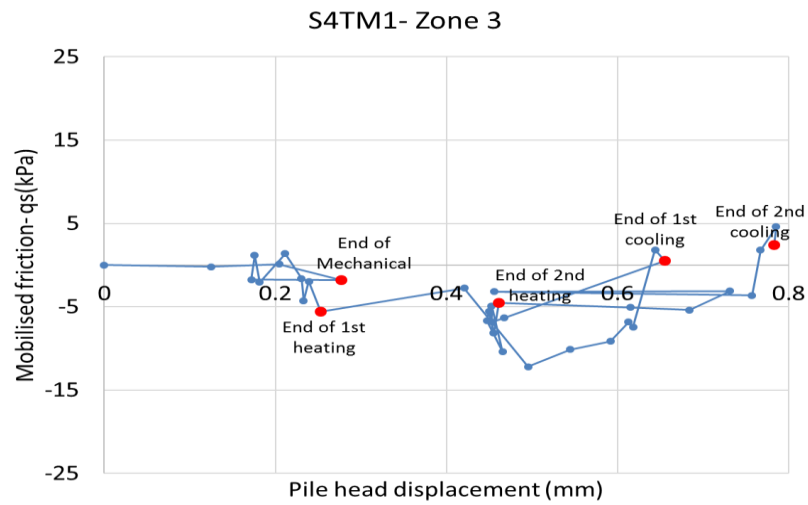
Figure 4-19. Mobilised shaft friction under mechanical loading in four zones along the pile – Scenario 4



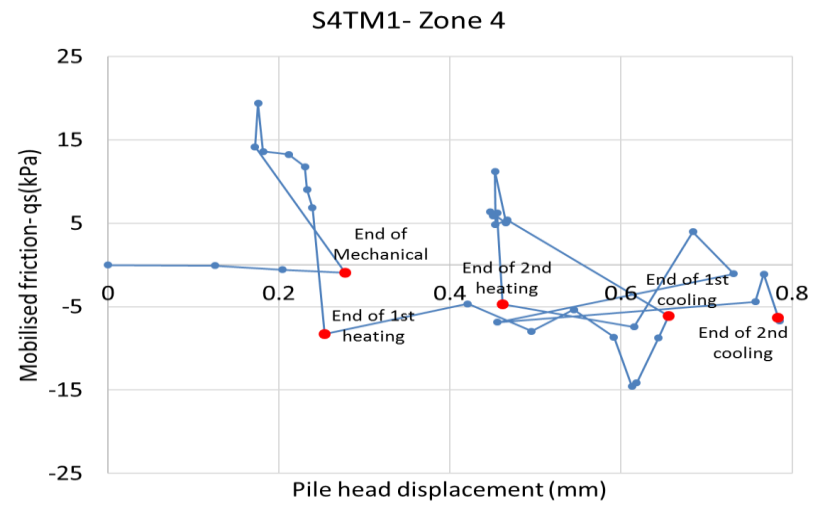
(a)



(b)

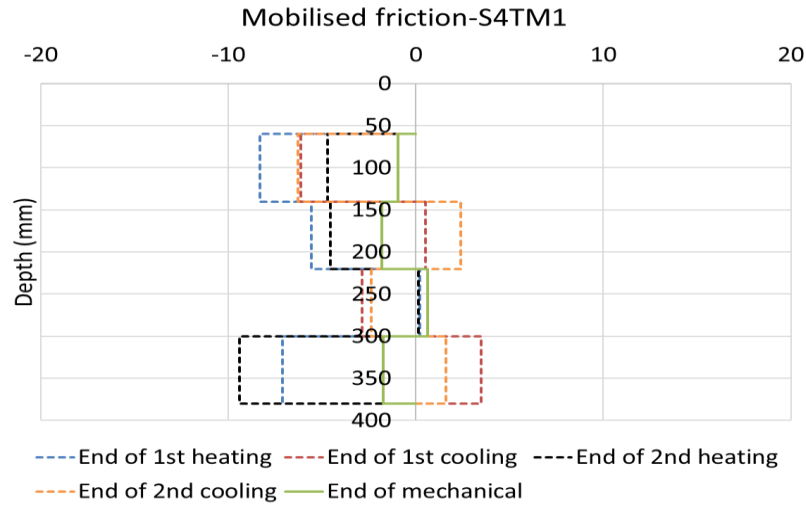


(c)

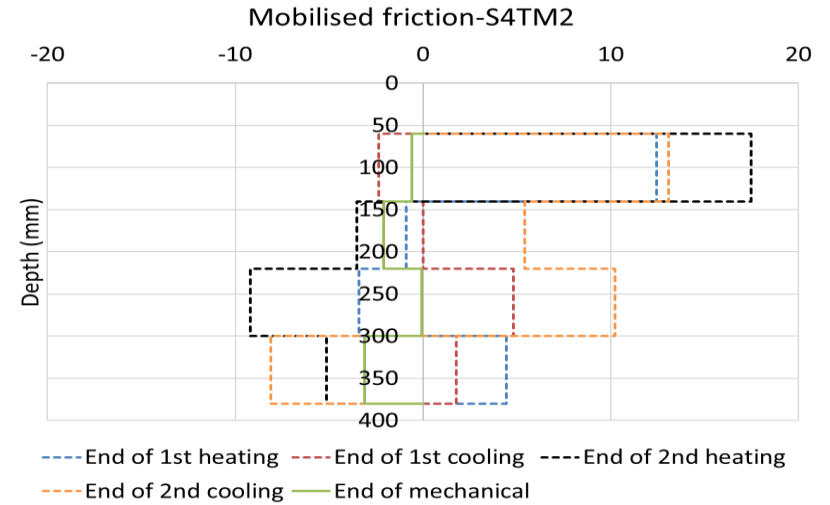


(d)

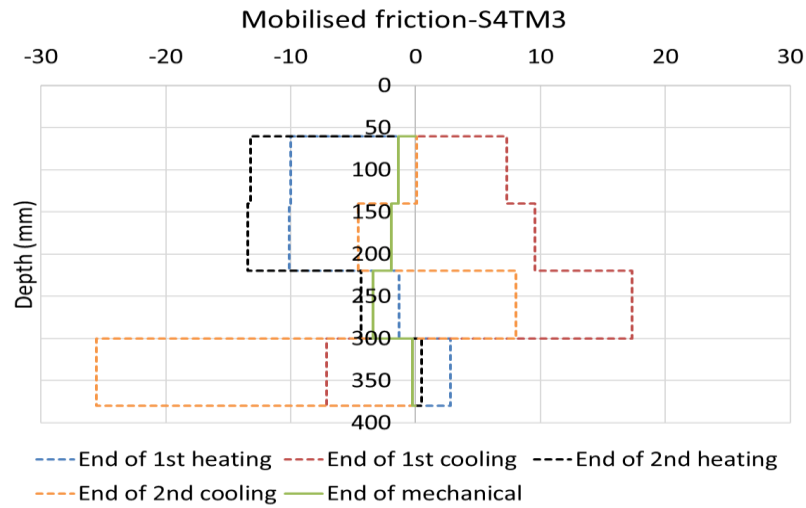
Figure 4-20. Mobilised shaft friction vs pile head displacement – Scenario 4 – S4TM1



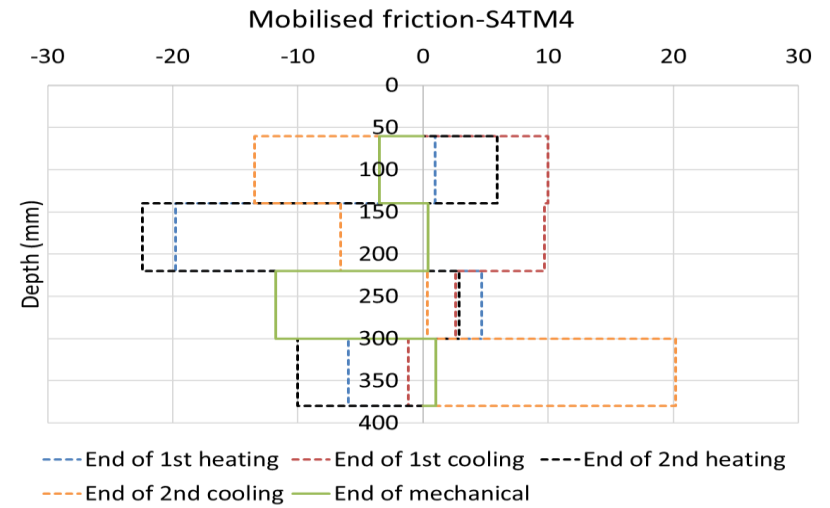
(a)



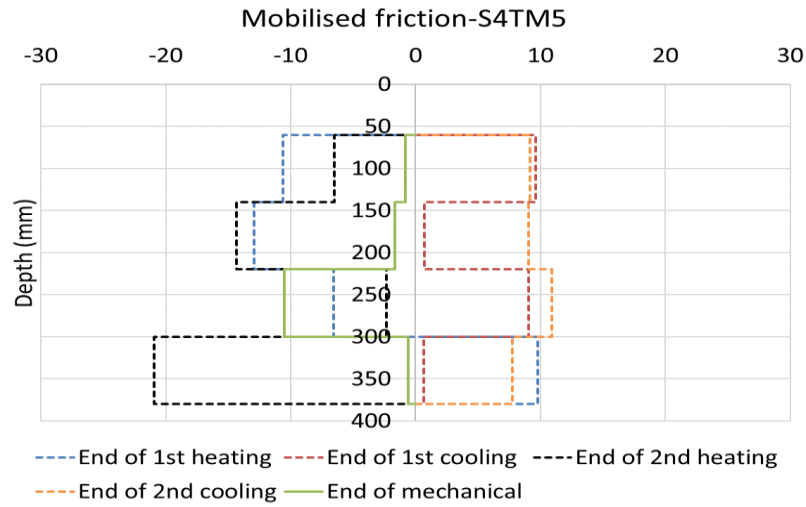
(b)



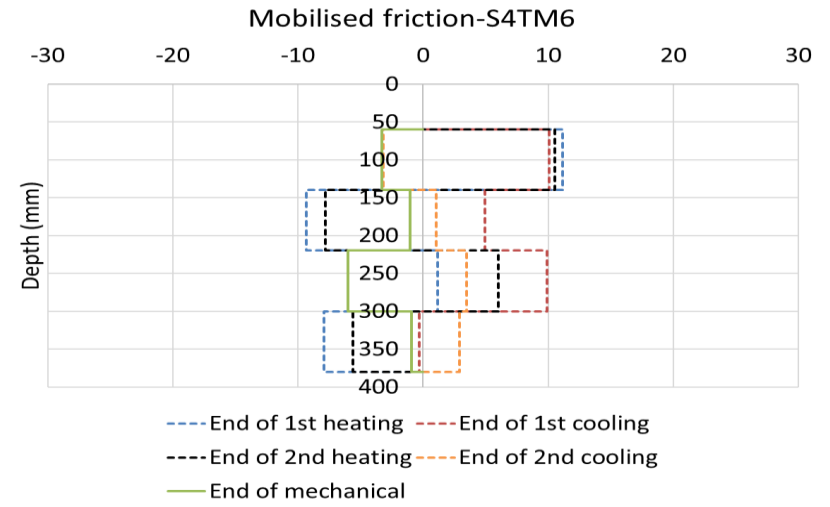
(c)



(d)



(e)



(f)

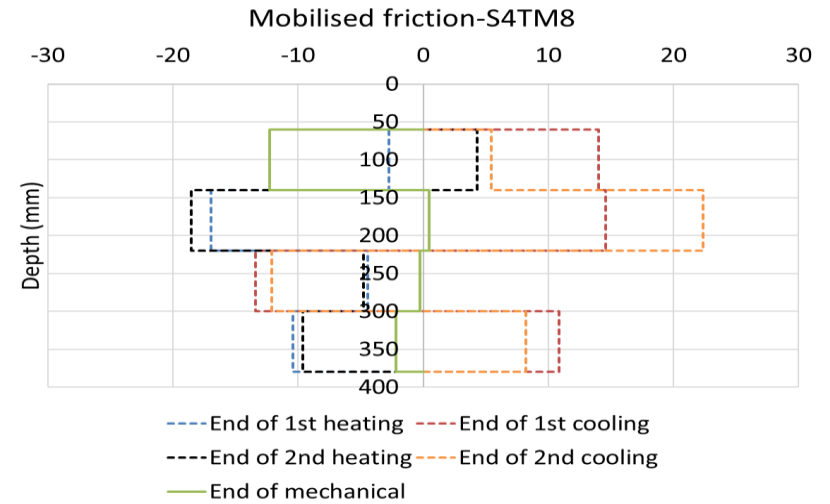
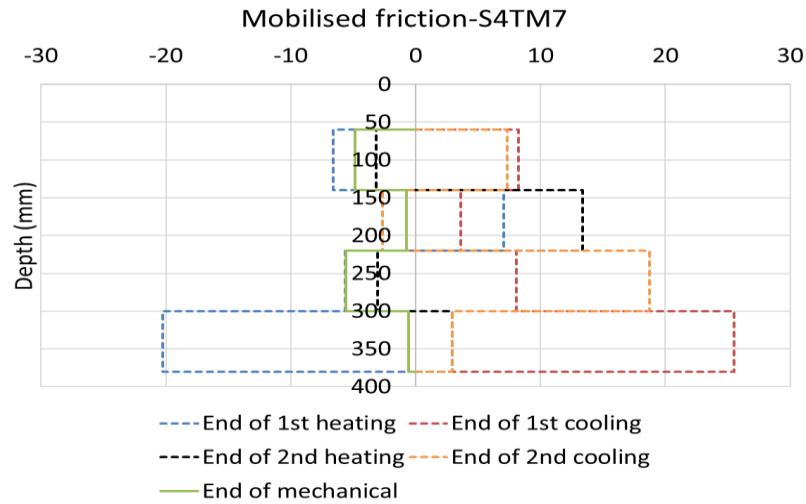


Figure 4-21. Mobilised friction along the pile at the end of each heating and cooling period – Scenario 4

4.6.7 Comparison with the framework

According to the framework given by the Thermal Pile Standard (GSHPA, 2012), the maximum restrained strain for a shaft resisting pile, with no restraint at the pile bottom and with mechanical loading on the pile head, is expected to occur at the top half of the pile, and then increase towards the pile bottom during the heating period (see Scenario 4A in Table 2.3). Using the restrained profiles from the Scenario 4 tests, given in Figure 4.15, it is noted that, in S4TM1–S4TM2, the maximum restrained strain occurs at the top half of the pile, with a linear decrease towards the pile bottom. In S4TM3–S4TM5, the maximum restrained strain is seen at the mid-depth, which is the extreme case proposed by the framework. In S4TM6–S4TM8, due to the base support, the more restrained strain is seen at the pile bottom, compared to other tests that are in agreement with the framework, where the restraint is increased in the presence of base support. For the cooling period, the framework suggests that a sudden reduction in the restrained strain at the bottom half of the pile will occur. The overall response of the tests S4TM1–S4TM5 is the reduction of the restrained strain towards the pile bottom. A lower magnitude of mobilised friction is expected at the top half of the pile during the heating period, with the reverse occurring during the cooling period (see Scenario 4A in Table 2.3). Using Figure 4.21, it is hard to distinguish a trend for all of the figures, as some tests show the same behaviours and other tests show the opposite behaviours. The main difference is a result of the assumptions made by the proposed framework, which is discussed in Chapter 6. For the shaft resisting pile with considerable pile head settlement under mechanical loading, the change in friction between the sand and the pile can change the response, as discussed in Chapter 6.

Chapter 5. Thermo-mechanical behaviour of shaft and base resisting pile

5.1 Introduction

In this chapter, the results of experiments performed on the shaft and base resisting pile are presented. The shaft and base resisting pile is a better representation of piles installed in the field, where the shaft partially carries the pile load and the pile base carries the rest. Initially, the load resistant capacity of the pile is determined using four experiments: S5M1–S5M4. In Scenario 5, one experiment under thermal loading, S5TM1, and three thermo-mechanical tests, S5TM2–S5TM4, are conducted. The aim of the Scenario 5 tests is to investigate the model pile response under thermal and thermo-mechanical loading. In the end, a comparison with the proposed framework by Bourne-Webb et al. (2013) is given.

5.2 Shaft and base resistant capacity – Scenario 5

The bearing capacity of the shaft and base resistant pile is determined using the Scenario 5 test set-up without temperature-monitoring FBGs in the sand bed (see Figure 3.3). For shaft and base resistant piles, failure occurs when the pile head settlement is equal to 10% of the pile diameter (i.e. 2.8mm for this laboratory model). An appropriate distance between the pile bottom and container base must be selected to determine the pile capacity and also to choose the appropriate axial mechanical loading for Scenario 5 tests. In the literature, the H/D ratio is used for this purpose, where D is the pile diameter and H is the distance between the pile bottom and container base. Different H/D values are used in the literature: 15.7 (Li et al., 2012), 12.5 (Yavari et al., 2014; Kalantidou et al., 2012) and 1.5 (El Naggar & Wei, 2000). The minimum sand height required to cover all the sensors with a 15mm margin to allow insulation on the top and bottom is 350mm. Four mechanical tests, S5M1–S5M4, are carried out to investigate the effects of changes in the bottom distance from 65mm to 130mm and in the embedded pile length from 285mm to 350mm (H/D ratios between 2.32 and 4.64) (see Table 5.1). The relative density of the sand bed is determined as 57.64% in all four tests. The pile is loaded in 20N increments until failure. Up to 120N, smaller settlements are observed and less time is needed to reach a steady condition (10 minutes). From 120N onwards, each load is kept on the pile head for 15 minutes to allow the pile to settle completely under higher magnitudes of mechanical loading.

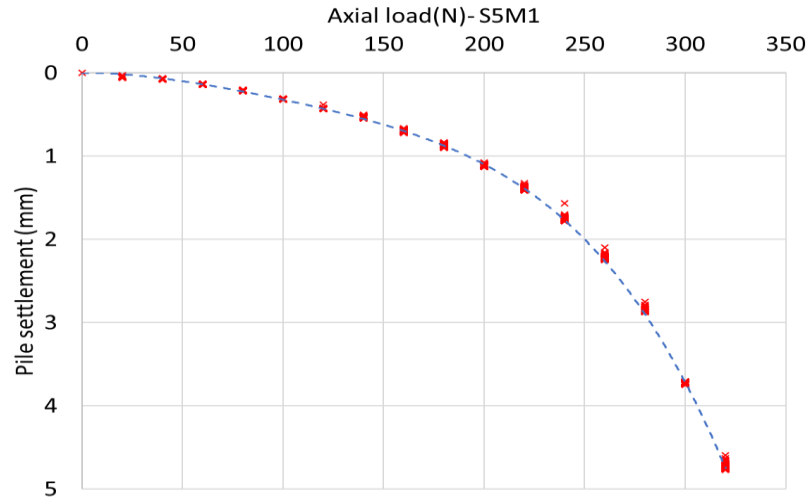
- The pile effective length is kept constant in S5M1 and S5M2 at 285mm, while the bottom distances are chosen as 65mm and 130mm respectively. It is found that the ultimate capacity is increased by 20N (approximately 6.5%) when the pile bottom distance is doubled. This could be mainly due to the existence of a stiff sand base beneath the pile with a relative density

of approximately 57%. Increase in the sand deposit beneath the pile seems to increase the stiffness at the pile bottom, resulting in a small increase (6.5%) in pile bearing capacity.

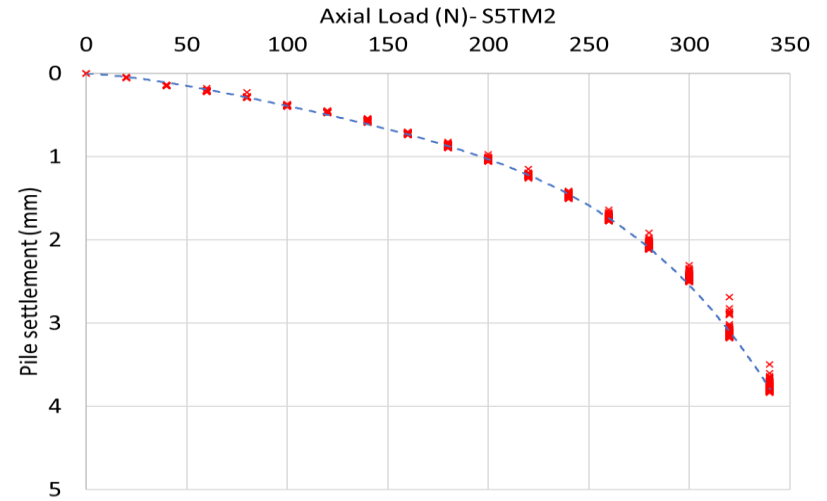
- H is kept constant in S5M2 and S5M3 while the embedded pile lengths are selected as 285mm and 310mm respectively. It is found that a 25mm increase in the embedded pile length while the pile bottom distance remains constant does not change the ultimate load-bearing capacity of the model pile.
- A comparison is made between S5M4 (with a pile effective length and a bottom distance of 350mm and 90mm) and S5M1–S5M3 with various pile effective length and bottom distances. It is found that, for this margin of changes, the value of the bearing capacity remains constant. The shape of the load-displacement diagrams in Figure 5.1 is similar except for S5M1, where the ultimate capacity is 20N less than S5M2–S5M4.
- Using Table 5.1 and Figure 5.1, the distance between the pile bottom and the container base, H , is chosen as 90mm. This results in a H/D ratio of 3.21 with an ultimate bearing capacity of 320N.
- Based on the determined ultimate bearing capacity (320N), applied loads in the Scenario 5 thermo-mechanical tests are chosen as 0.00%, 31.25%, 46.87% and 70.31% of the ultimate capacity of the pile equal to 0N, 100N, 150N and 225N respectively. Mechanical loading equal to 100N represents the working load on the pile head with an overall safety factor of 3.2 when the ultimate shaft and base resistance of the pile is 320N.

Table 5-1. Comparison between various test layouts in Scenario 5

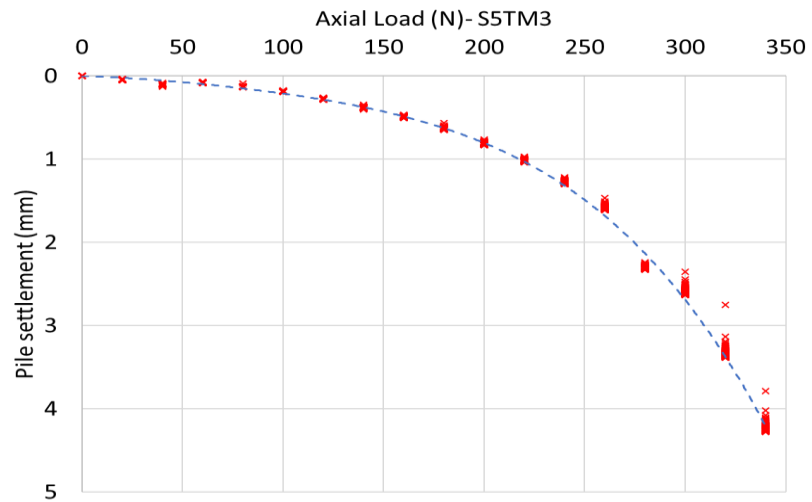
	S5M1	S5M2	S5M3	S5M4
Pile effective length (mm)	285	285	310	350
Bottom distance (mm)	65	130	130	90
Ultimate axial load (N)	300	320	320	320
H/D	2.32	4.64	4.64	3.21



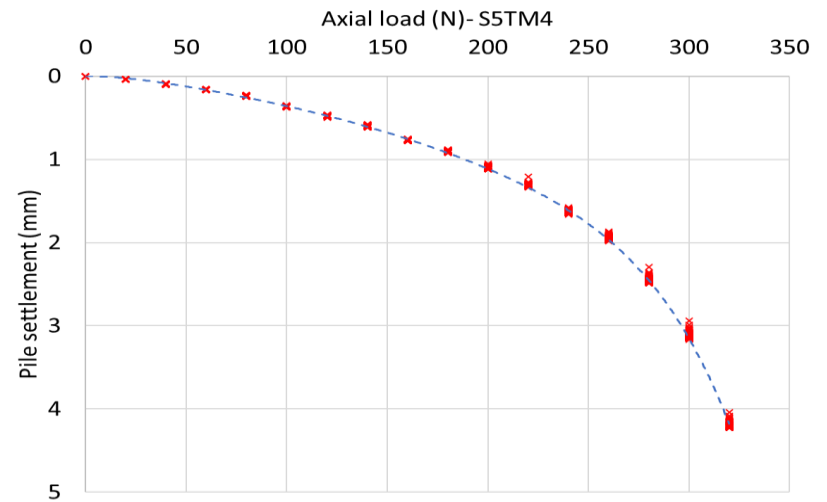
(a)



(b)



(c)



(d)

Figure 5-1. Load-displacement curve: S5M1-S5M4

5.3 Pile temperature profiles

Both absolute temperature and temperature change profiles along the pile surface during the entire test period are shown in Figure 5.2. Moreover, changes in the temperature at the end of each heating and cooling period along the pile at five depths are shown in Figure 5.3. The temperature data shown in Figure 5.2 is determined using Equations 4.9 and 4.10 given in Section 4.3.2. It is seen that:

- Similar to Scenarios 3 and 4, despite adjusting the water circulator at 50°C, temperatures higher and lower than 50°C are also recorded (see Figure 5.2). Average pile temperature during each heating period in S5TM1 to S5TM4 ranges between 47.48°C and 51.12°C (see Table 5.2).
- In all Scenario 5 tests, unlike Scenarios 3 and 4, the bottom of the pile is placed on the sand and it is not exposed to the ambient air. Despite no exposure of the bottom sensor to the ambient air, the minimum temperature is consistently recorded at SP1 level.
- The maximum temperature is recorded by TP5 in all tests. This shows that the sand surface has been well insulated in all tests. Moreover, it shows that the pile temperature is mainly related to the closeness of the sensor to the heating source and higher water flow rate.
- The difference between the maximum ΔT during heating and cooling periods ranges between 0.73°C and 2.38°C. It means that the pile temperature does not return to the original position, which is mainly due to the presence of sand around the pile.
- ΔT values at the end of each heating or cooling period at five depths along the pile are given in Figure 5.3. A linear temperature profile is seen in all four tests for both heating and cooling modes. Moreover, the maximum and minimum temperatures are recorded at the SP5 and SP1 levels respectively. An approximate symmetry is also seen for all four tests with slightly higher temperature changes (0.73–2.38°C) observed during heating periods.

Table 5-2. Temperature readings for Scenario 5 tests (°C)

	Avg. pile temp. first heating	Avg. pile temp. second heating	Min pile temp.	Max pile temp.	Max ΔT : TP1	Max ΔT : TP2	Max ΔT : TP3	Max ΔT : TP4	Max ΔT : TP5
S5TM1	48.99	50.23	19.43	53.07	27.04	29.60	29.81	31.37	31.27
S5TM2	51.12	50.78	20.23	54.24	27.56	30.12	30.78	32.54	32.53
S5TM3	48.23	47.48	19.68	50.55	27.24	29.52	30.03	31.44	31.15
S5TM4	49.54	49.42	19.72	53.06	26.60	29.16	29.09	30.60	31.36

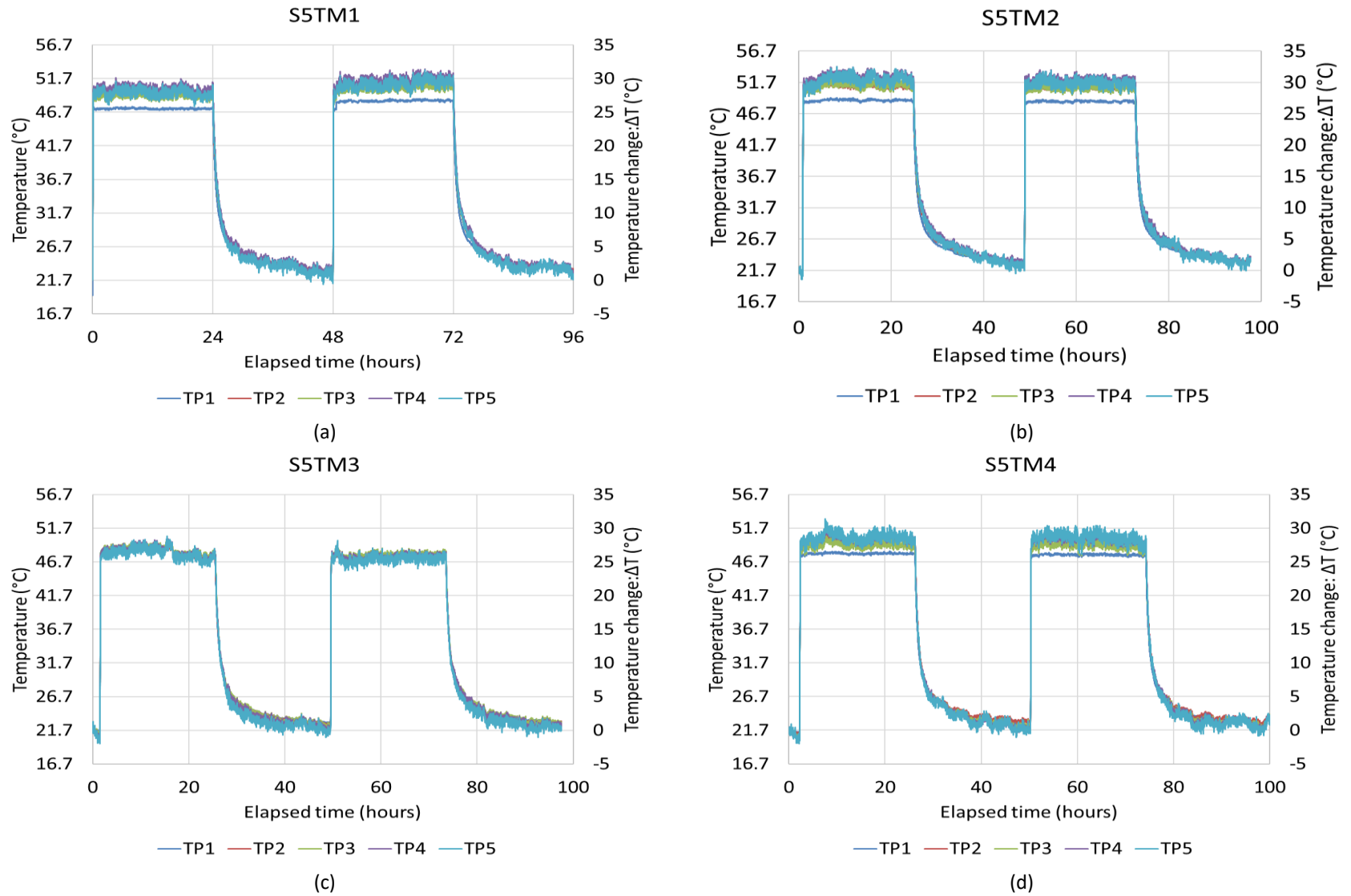


Figure 5-2. Temperature distribution along the pile surface – Scenario 5

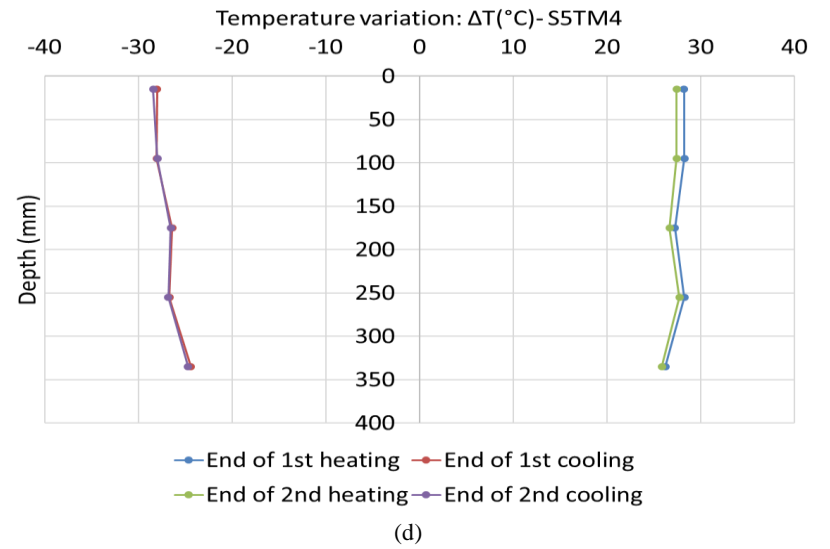
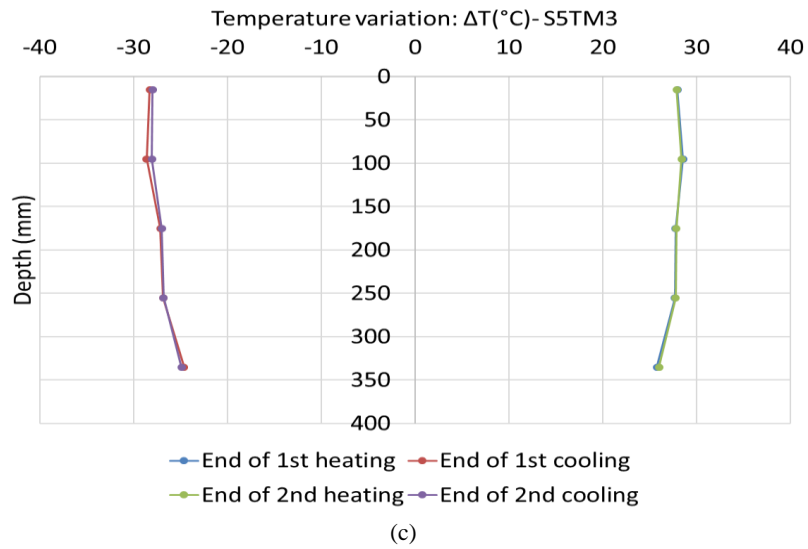
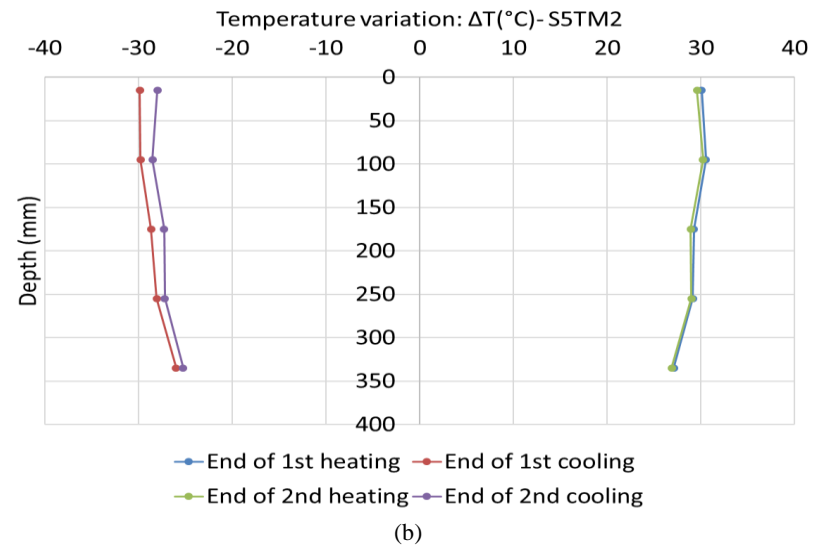
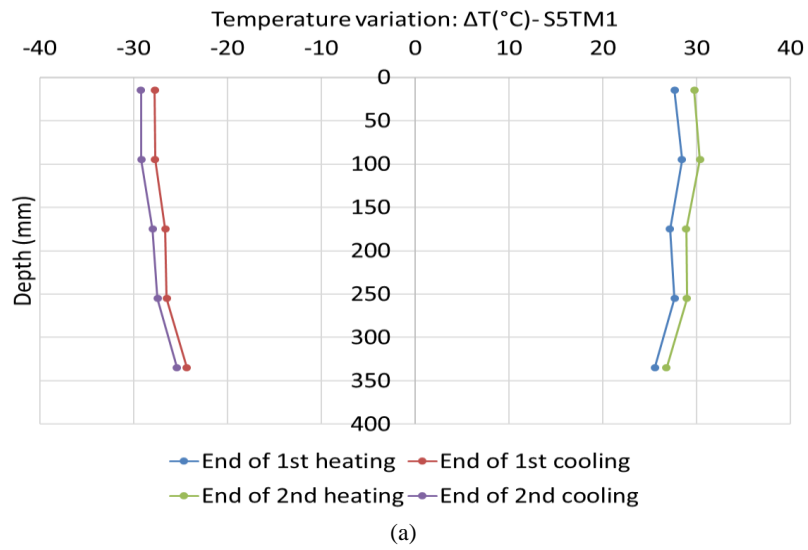


Figure 5-3. Changes in temperature along the pile surface – Scenario 5

5.4 Strain profiles

5.4.1 Observed strain

Initially, the mechanical strains for S5TM2–S5TM4 are determined using Equation 4.11 and are presented along with the axial load along the pile (see Figure 5.4). It is seen that:

- The observed strain increases with an increase in the magnitude of mechanical loading.
- The maximum and minimum strains are observed at the pile head and at the bottom. Due to the elastic behaviour of the stainless steel model pile, the same trend is applied for the distribution of the axial load along the pile.
- The magnitude of strain at the bottom of the pile $0.03\mu\epsilon$ in S5TM3, while it increases up to $1.07\mu\epsilon$ under 225N of mechanical loading in S5TM4. The maximum mechanical strain is observed at 225N and is equal to $9.93\mu\epsilon$ at SP4 level with a minor difference with strain at SP5 at $9.91\mu\epsilon$.
- In S5TM2–S5TM4, the maximum strain caused by mechanical loading, $9.93\mu\epsilon$, is approximately 2.1% of the maximum observed thermal strain.

Observed strain profiles under thermo-mechanical loading during the two heating-cooling cycles are presented in Figure 5.5. The following observations are made:

- The observed strain ϵ_{obs} is rapidly increased to the maximum ϵ_{obs} values and remains relatively constant until the end of the heating period (see Figure 5.5). An increase of 0.01% to 1.73% in the ϵ_{obs} is seen after 24 hours of heating compared to the observed strain at the end of the first hour of heating, which shows a negligible effect of time on the observed strain during the heating process. Unlike heating, increase in the observed strain at the end of 24 hours of cooling compared to the end of the first hour of cooling ranges between 62% and 92%, which shows the importance of longer-term tests for the cooling period.
- In S5TM1, despite having no mechanical loading on the pile head, perfect thermo-elastic behaviour is not seen in the strain profile, with an average residual strain (i.e. the difference between the maximum strain in the heating and cooling periods) of $26.22\mu\epsilon$ and $32.12\mu\epsilon$ for the first and second cycles (see Table 5.3). However, when the effect of temperature differences is included in the analysis, it is seen that up to $19.82\mu\epsilon$ is due to differences in temperature values.
- In S5TM2, an increase is seen in the observed thermal strain compared to S5TM1, which is mainly due to the slightly higher temperature changes recorded by FBGs. In S5TM3, a drop in the observed strain is seen in the middle of the first heating period, which is due to the unexpected temperature drop in the pile caused by sudden water blockage in the pipe. In S5TM4, despite having similar ΔT as S5TM3, lower strain values are captured. This could be due to a larger restraint caused by 225N mechanical loading on the pile head.

- The locations of the maximum and minimum observed strains for two heating-cooling cycles are shown in Table 5.4. Maximum observed strain is mainly seen at the SP1 level for both heating and cooling cycles. When the minimum ΔT is experienced at the SP1 level at the bottom of the pile, the least restraint is shown at the SP1 level.

The observed strain at five depths at the end of each heating-cooling period is shown in Figure 5.6.

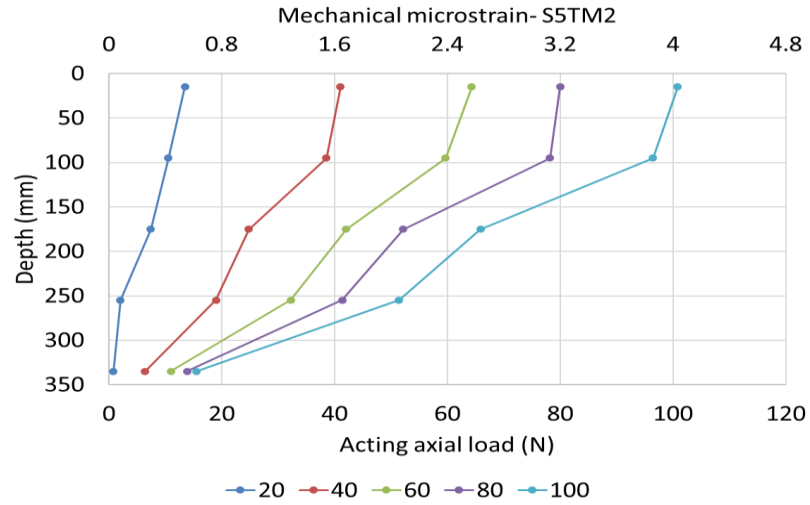
- The lowest strain values are consistently recorded by S5TM4 at the end of both heating and cooling periods. This demonstrates the effect of the magnitude of mechanical loading as a pile head restraint on the strain readings.
- The location of the maximum observed strain changes during heating and cooling periods, possibly due to pile heave and settlement as well as shifts in the state of the sand–pile friction level.
- The maximum observed strain is recorded by S5TM1 and S5TM2, where there is more freedom to move compared with the other two tests.

Table 5-3. Difference between maximum heating and cooling strain values – Scenario 5

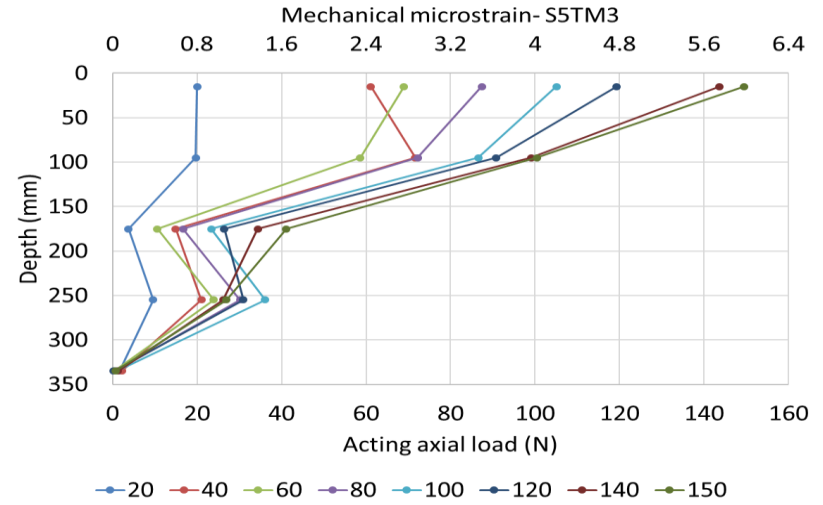
Test	Cycle no.	SP1	SP2	SP3	SP4	SP5	Average
S5TM1	1	25.87	29.99	21.12	31.36	22.74	26.22
	2	27.40	43.69	28.87	35.37	25.27	32.12
S5TM2	1	12.55	18.77	13.89	16.09	17.81	15.82
	2	27.45	32.24	34.07	31.16	31.20	31.22
S5TM3	1	38.63	23.35	22.59	6.53	5.67	19.35
	2	18.51	17.90	16.12	0.39	-1.58	10.27
S5TM4	1	23.67	25.46	19.63	5.79	7.15	16.34
	2	20.8	24.45	12.95	6.26	-0.52	12.79

Table 5-4. Location of maximum strain value along the pile surface – Scenario 5

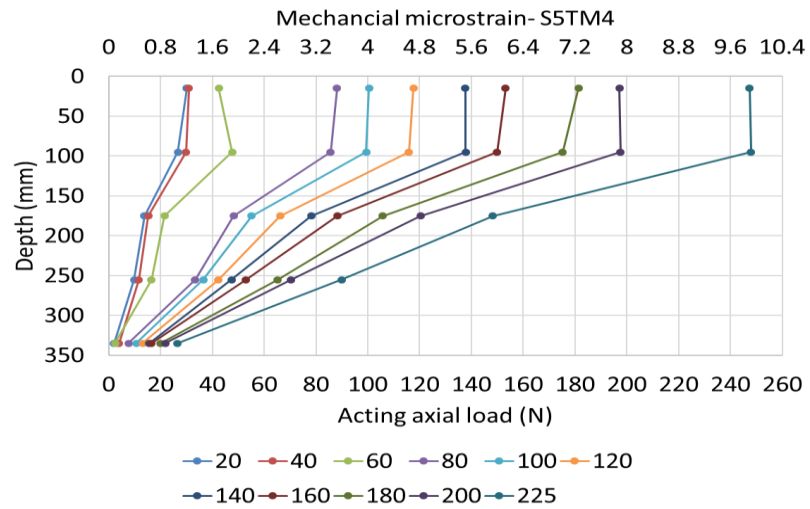
Test	First heating	First cooling	Second heating	Second cooling
S5TM1	SP1	SP3	SP1	SP1
S5TM2	SP3	SP1	SP1	SP1
S5TM3	SP1	SP3	SP1	SP1
S5TM4	SP1	SP1	SP1	SP1



(a)

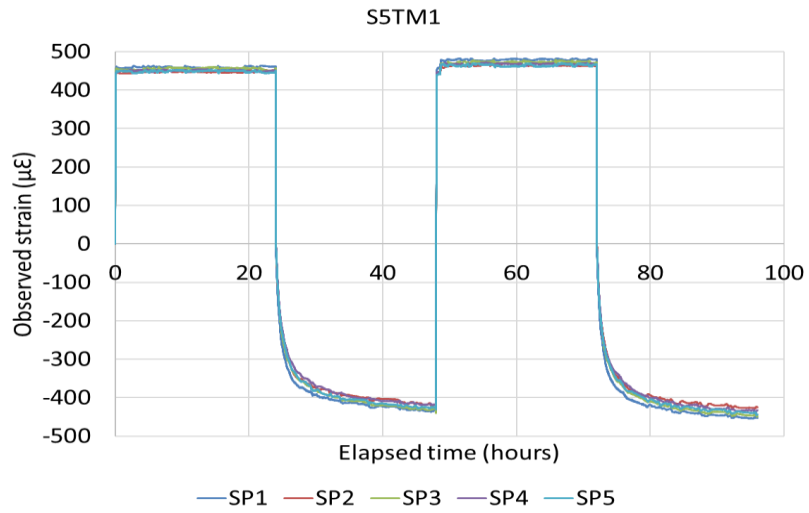


(b)

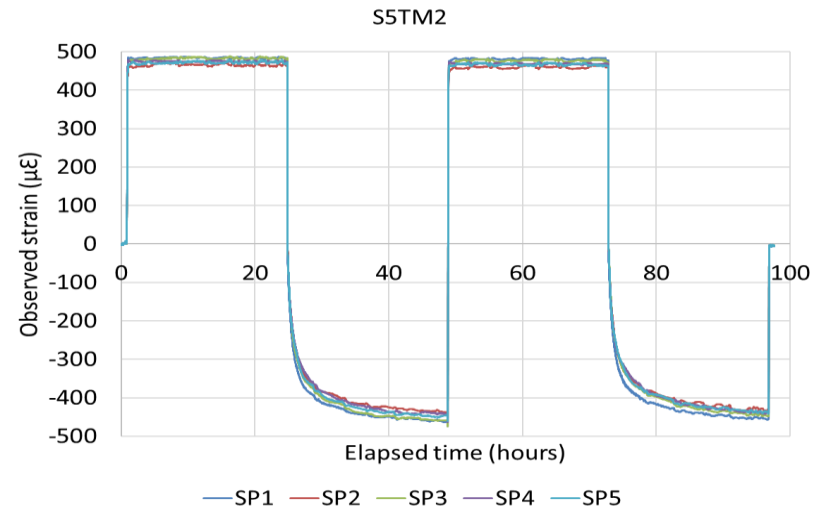


(c)

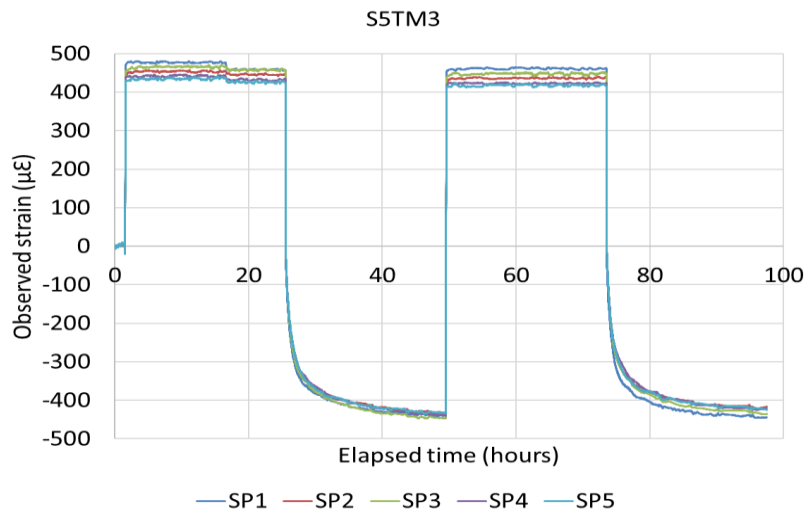
Figure 5-4. Observed mechanical strain and acting axial load along the pile before thermal loading– Scenario 5



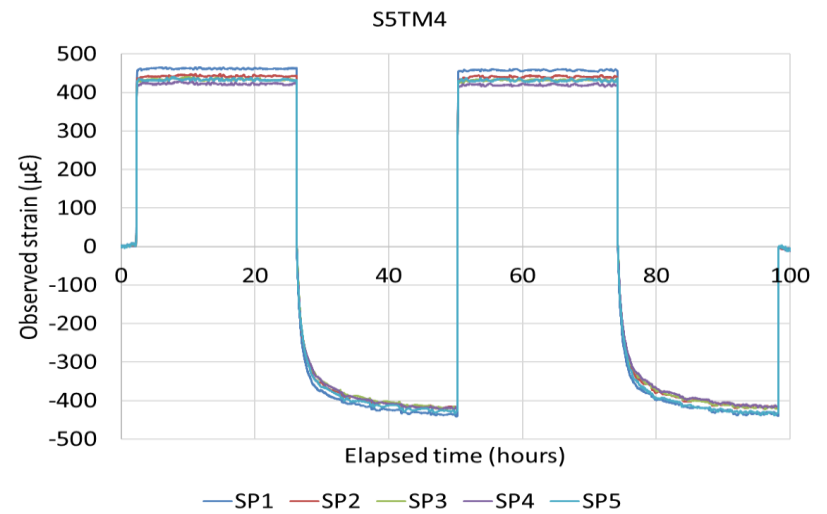
(a)



(b)

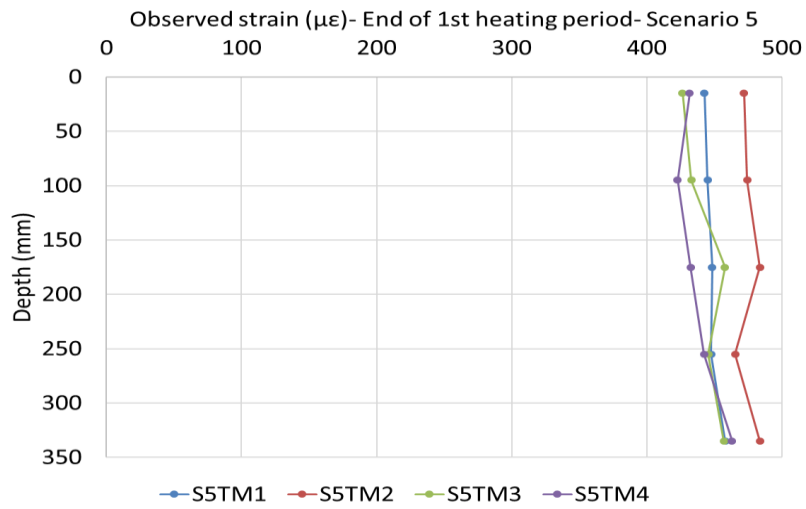


(c)

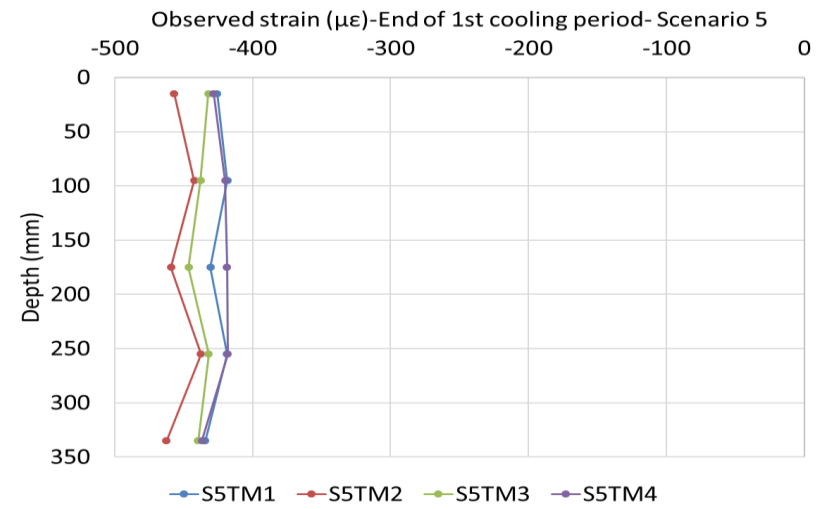


(d)

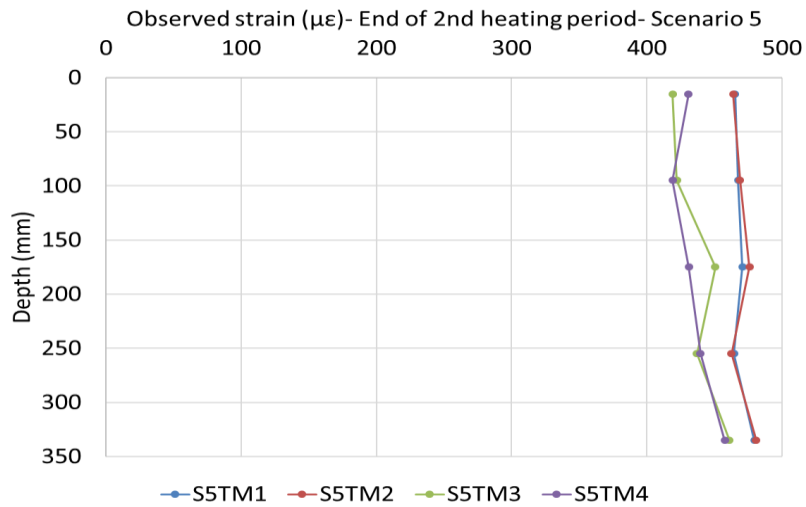
Figure 5-5. Observed thermal strain during the entire test period – Scenario 5



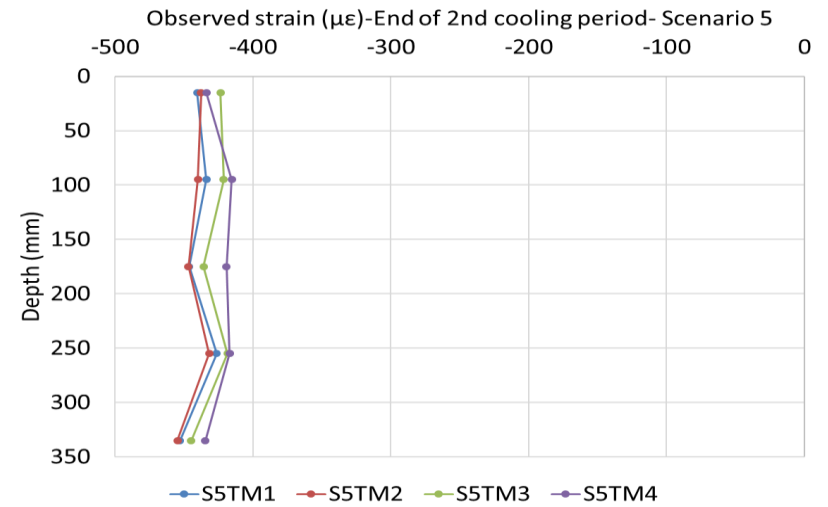
(a)



(b)



(c)



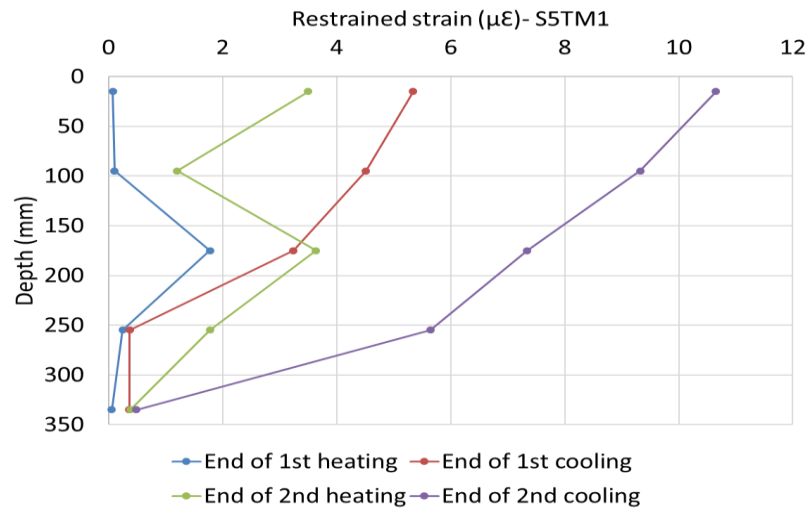
(d)

Figure 5-6. Observed thermal strain along the pile – Scenario

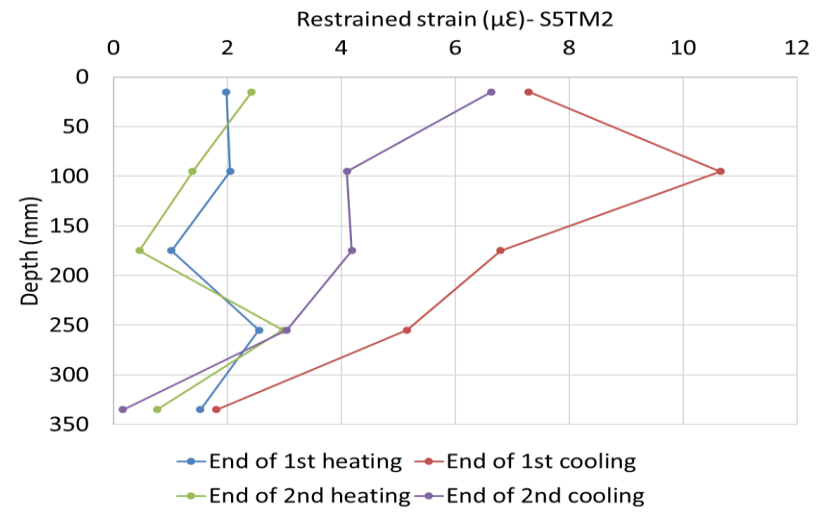
5.4.2 Restrained strain

Restrained strain profiles for Scenario 5 tests are shown in Figure 5.7. Comparison between restrained strain profiles achieved from FBG readings and the expected restrained strain profiles according to the proposed framework is given in Figure 5.18.

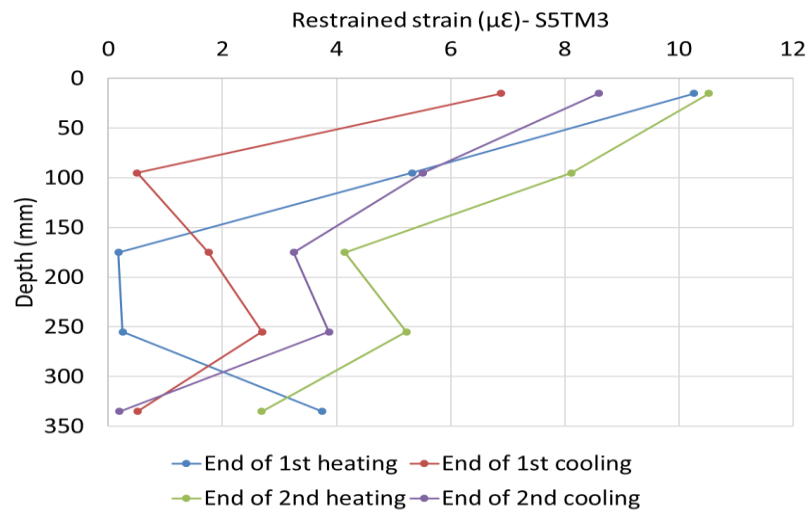
- The restrained strain at the end of each heating and cooling period for S5TM1–S5TM4 is shown in Figure 5.7. In S5TM1, the maximum restrained strain is seen at the end of the second and first cooling periods and the minimum restrained strain is seen at the end of the first heating period. A similar trend is seen in S5TM2, where more restrained strain is seen during cooling periods compared to heating periods. This procedure is reversed from S5TM3 onwards, where maximum restrained strain is seen at the end of the second and first heating periods. It shows that, until 100N, the effect of the pile head restraint caused by mechanical loading is minimal and is unable to restrict the pile from moving upward. From 150N onwards, where mechanical loading that is higher than the working load is applied on the pile head, the maximum restraint is caused by the weights on the pile head and not the soil (see Figure 5.7).
- In S5TM1–S5TM3, the maximum restrained strain is observed at the pile head; this lowers towards the pile bottom with sudden increases along the pile. In S5TM4, a different pattern is seen where the maximum restrained strain during all four periods occurs at the mid-depth of the pile. Despite having maximum mechanical loading on the pile head compared to other Scenario 5 tests, the location of the maximum restrained strain shifts from the pile head to the mid-depth of the pile.
- At the end of 1st heating period, it is seen that the maximum and minimum restrained strains are recorded at S5TM4 and S5TM1 respectively, where maximum and minimum mechanical loads are applied to the pile head. This procedure can be extended to the second heating period with a small difference in which the maximum restrained strain is seen for S5TM3. This trend is not followed during cooling periods.
- The restrained strain seen at the end of the first cooling period is 33%, and is 25.38% lower than the restrained strain seen at the end of the first heating period in S5TM3 and S5TM4 respectively. It shows a relief in the restraint during the cooling period. This could be due to the partial loss of soil–pile interaction after the initial pile heave and the subsequent settlement.
- The maximum restrained strain is seen at the end of the first heating period for S5TM4 and is equal to $11.62\mu\epsilon$. It is approximately $1.71\mu\epsilon$ higher than the magnitude of the maximum strain caused by mechanical loading of 225N in S5TM4.



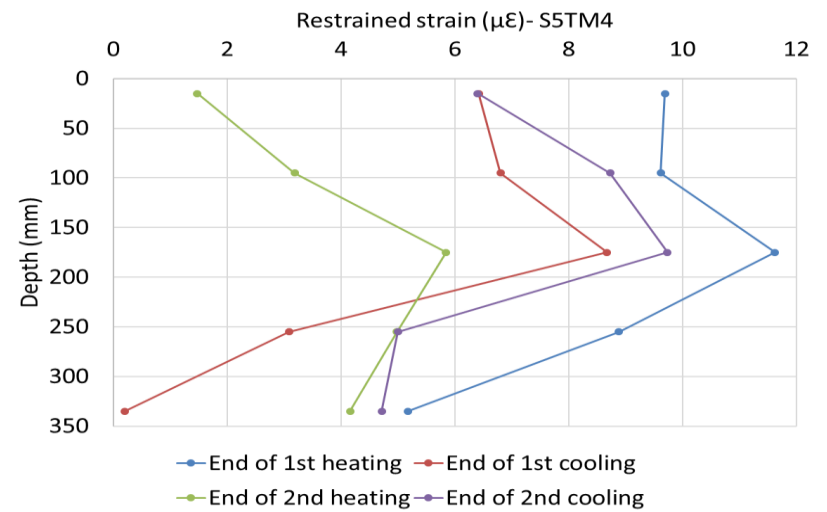
(a)



(b)



(c)



(d)

Figure 5-7. Restrained thermal strain along the pile – Scenario 5

5.5 Degree of freedom

Variations in the DoF at the end of each heating or cooling period along the pile surface for all Scenario 5 tests are shown in Figure 5.8. The following observations are made:

- In S5TM1–S5TM3, the maximum pile restraint occurs at the SP5 level but, in S5TM4, the maximum restraint is seen at the SP3 level at the mid-depth. In fact, the null point is seen at the mid-depth of the pile where the maximum restraint exists.
- At the end of the first heating period, the maximum restraint is seen for S5TM4, where the maximum load (equal to 225N) is applied to the pile head. The minimum DoF is observed during cooling periods in S5TM1 and S5TM2, while in S5TM3 and S5TM4, the minimum DoF is seen during heating periods. This shows the impact of the magnitude of mechanical loading on the restriction opposed by the pile's upward movement. The effect of mechanical loading on the pile head is more obvious in the S5TM3 and S5TM4 tests, where the pile has more restraint for heaving due to the existence of higher magnitudes of mechanical loading.
- Although differences exist for the DoF values in all tests, the range of variation of the DoF is limited between 0.97 and 1.0. This means that the restriction opposed by the surrounding soil and the mechanical load on the pile head is rather limited.

5.6 Thermally induced axial force and stress in the pile

The distribution of axial force along the pile under mechanical loading before applying any thermal loading is presented in Figure 5.4, along with the strain profiles. For a long pile embedded in the soil with mechanical loading on the pile head, it is expected that the maximum and minimum loads will be observed at the pile head and the tip respectively (Oh et al., 2000). This trend is seen for S5TM2–S5TM4 under different mechanical loadings (see Figure 5.4). It is seen that an increase in the magnitude of mechanical loading results in an increase in the axial load along the pile. Dissipation of the load towards the bottom of the pile is seen in all tests. Part of the load is expected to be carried by the base, and that is why non-zero loads up to 26N, equal to 8.1% of the ultimate pile capacity, are seen at the SP1 level located 15mm away from the pile base. From SP4 to SP3, a considerable reduction of 29.5% to 81.8% of axial load is observed. The ratio of combined axial load carried by SP4 and SP5 over the combined load carried by SP1 to SP3 ranges between 1.45 and 3.92. Comparing the load transfer profile with the mechanical loading test shown by Laloui et al. (2003), a more linear reduction of the load from the pile head towards the pile bottom is seen in this study. This is mainly due to the use of a single homogenous soil profile in this study, whereas a combined soil profile with different friction levels between the soil and the pile is used by Laloui et al. (2003).

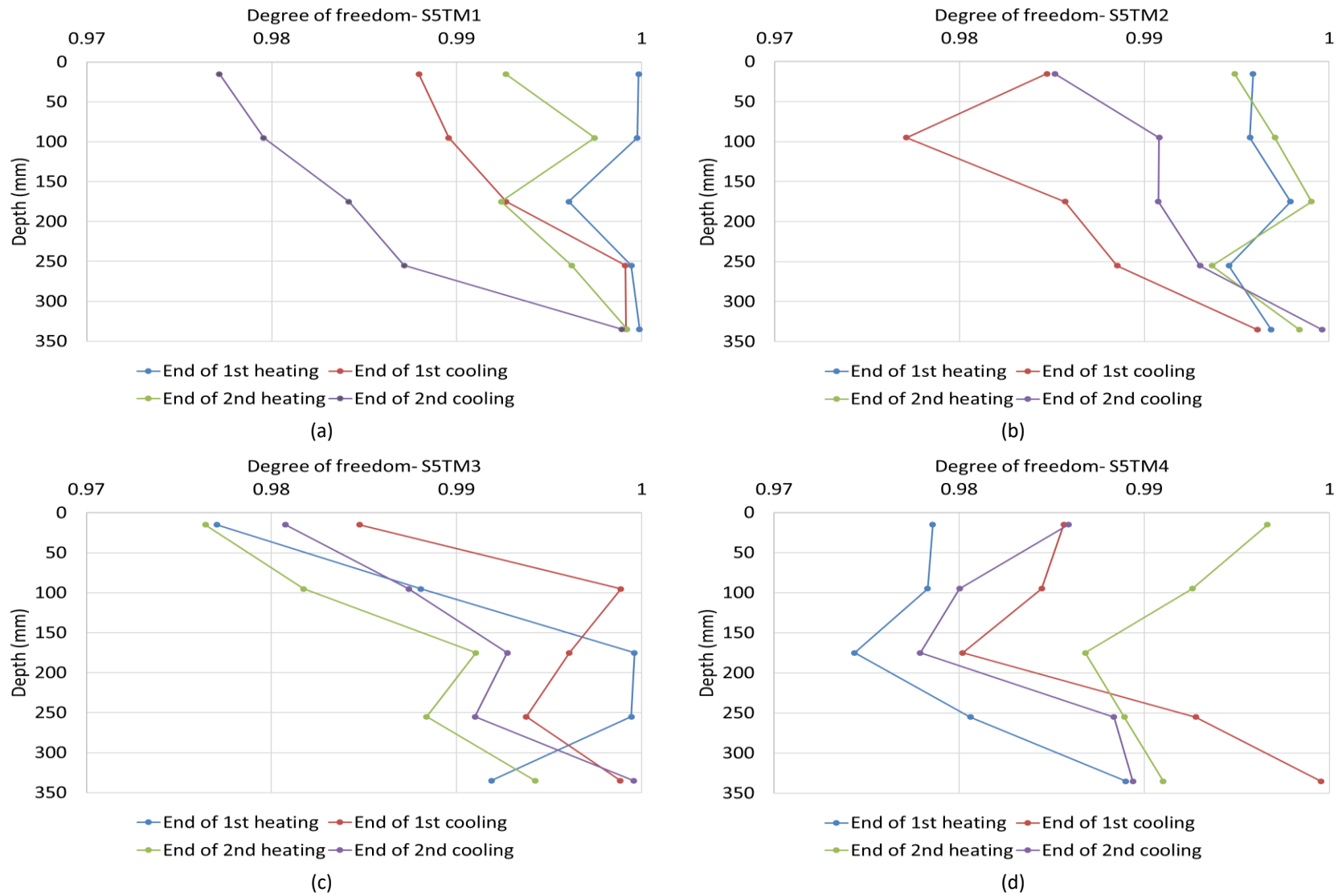


Figure 5-8. Variation of the DoF along the pile length – Scenario 5

Induced axial load and stress under thermal and thermo-mechanical loading is presented in Figures 5.9 and 5.10 respectively. In Figure 5.10, the ultimate load-bearing capacity of the shaft and base resisting pile is also given with a dashed line.

- In S5TM1, maximum and minimum induced loads are observed at the end of the second cooling and first heating periods respectively (see Figure 5.9-a). The maximum axial induced load in S5TM1 is 265N, which is 82% of the ultimate load-bearing capacity of the pile. In S5TM1, it is seen that induced load is increased during the cooling period and one-third of the maximum induced load during the cooling period is recovered in the subsequent heating period.
- In S5TM2, the magnitude of maximum induced load in the first cooling period is 4.16 times higher than in the first heating period (see Figure 5.10-b). This ratio is reduced to 2.22 in the second heating-cooling cycle. This means that the heating periods work as recovery for the excessive induced load during cooling periods. The maximum induced load in S5TM2 is seen at the end of the first cooling period, which is approximately 2.65 times the applied mechanical load in S5TM2 and 82% of the ultimate bearing capacity of the pile.
- In S5TM3, unlike S5TM1 and S5TM2, a larger magnitude of axial load (up to 262N) is induced on the pile during heating periods (see Figure 5.10-c). It shows that, due to the greater magnitude of mechanical loading on the pile head (46% of the ultimate bearing capacity of the pile), more restraint is applied on the pile's upward movement. The maximum induced thermal load is 1.74 times larger than the applied mechanical load of 150N.
- In S5TM4, considerable induced load (up to 290N) is seen during both heating and cooling periods, with the location of the maximum induced load shifting towards the mid-depth of the pile (see Figure 5.10-d). The maximum induced axial load is 1.16 times the applied mechanical load in S5TM4 and is equal to approximately 90% of the ultimate pile capacity.
- A similar trend is seen for the induced stress due to the linear relationship between induced load and stress (see Figure 5.10). The maximum induced stress is seen at the end of the first heating period of S5TM4, and is equal to 2.32MPa. Maximum induced stress is only 3.69% of the maximum admissible compressive stress for a stainless steel pile at 63MPa.
- The rate of change in the average induced axial stress per degree increase in temperature is a useful tool for thermal pile designers. The maximum average induced stress due to a one-degree decrease/increase in temperature during the cooling/heating period is approximately 72.90kPa/°C, 71.47kPa/°C, 75.54kPa/°C and 85.27kPa/°C for S5TM1 to S5TM4 respectively. The values given in the literature fall between 100 and 330kPa/°C (see Table 2.4). The difference in the rate of change is mainly due to the lower level of restraint caused by the surrounding soil and the magnitude of the mechanical and thermal loadings.

- Induced axial load along the pile under combined thermo-mechanical loading is shown in Figure 5.10. In S5TM2, it is seen that the maximum induced load due to combined thermo-mechanical loading is lower than the ultimate load-bearing capacity of the pile except at the end of the first cooling period, where a 40N additional load is seen (see Figure 5.10-a). In S5TM3, the maximum total axial load is 412N, which is 1.28 times larger than the ultimate pile capacity. The limit is only exceeded at the pile head; the rest of the pile is seen to be below the limit, particularly the bottom half of the pile. This ratio is increased to 1.52 in S5TM4, where the axial load at the top half of the pile exceeds the 320N limit.
- It can be seen in Figure 5.4 that the pile toe under mechanical loading carries the least load along the pile (between 0.3N and 26.62N). This means that, in the design of conventional piles, the load applied on the pile toe is usually neglected. In contrast, it is seen that the pile toe carries 1.3N to 129.24N in S5TM1–S5TM4. This means that the maximum induced load on the pile toe under thermal loading is 4.85 times larger than the load carried by the pile toe under mechanical loading. Moreover, the maximum induced load on the pile toe in S5TM4 is equal to 40% of the ultimate load-bearing capacity of the pile.

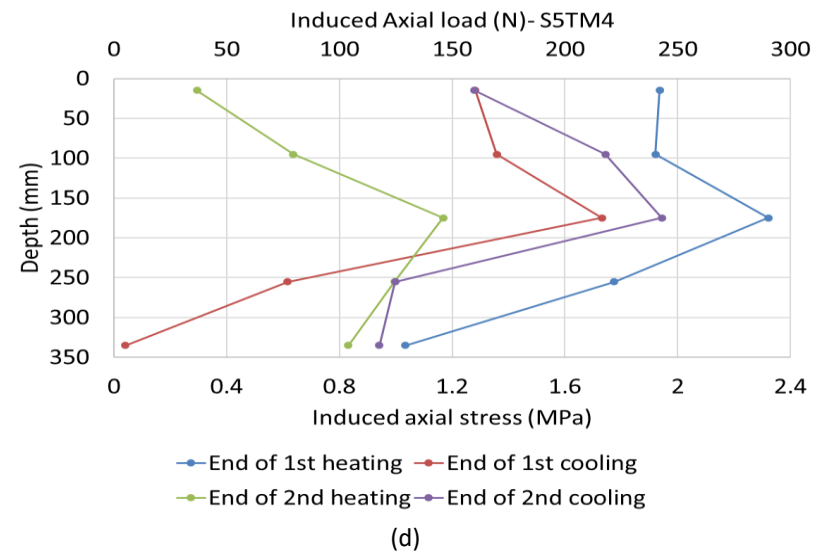
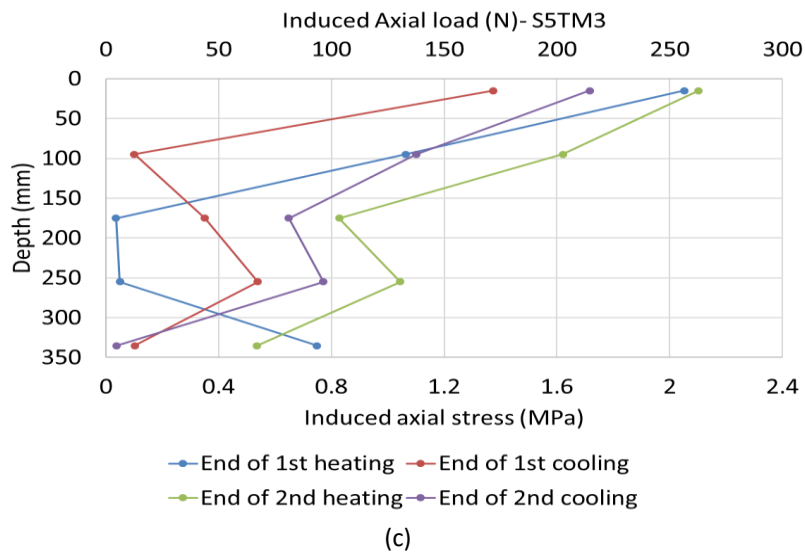
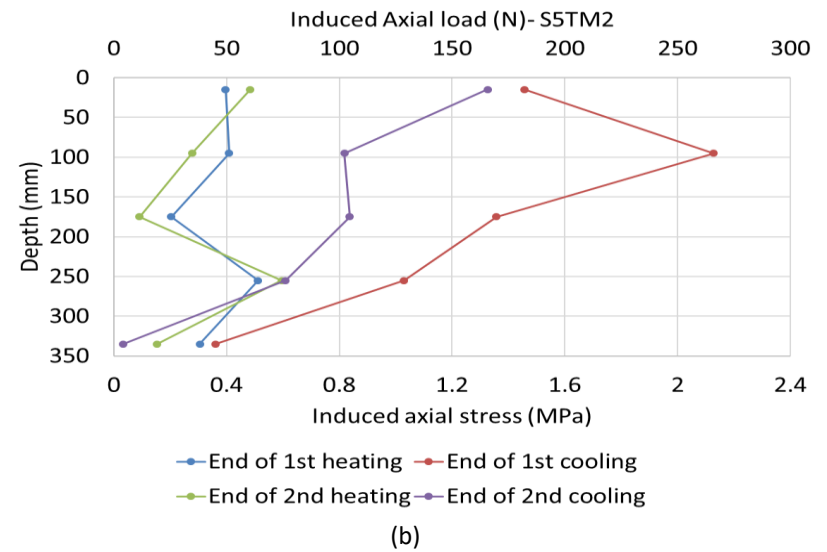
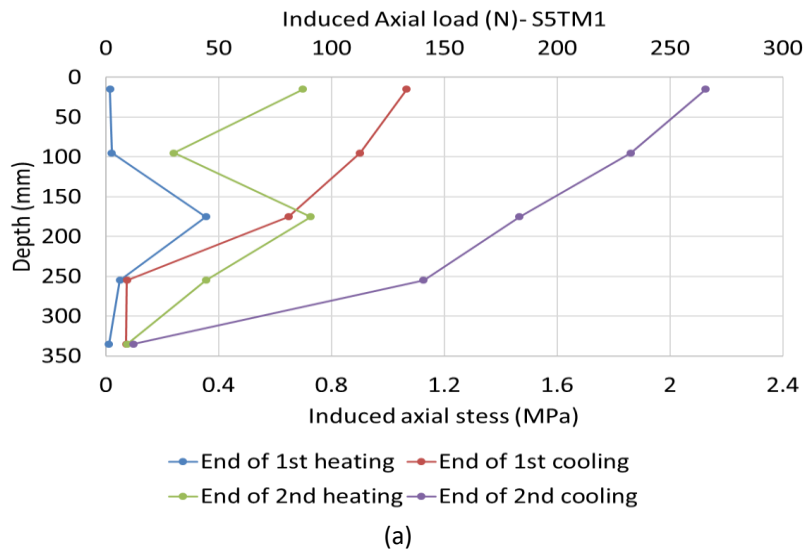
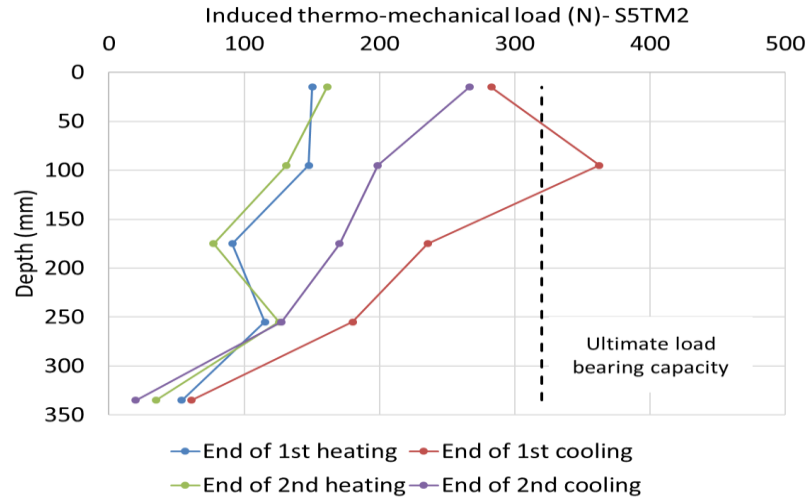
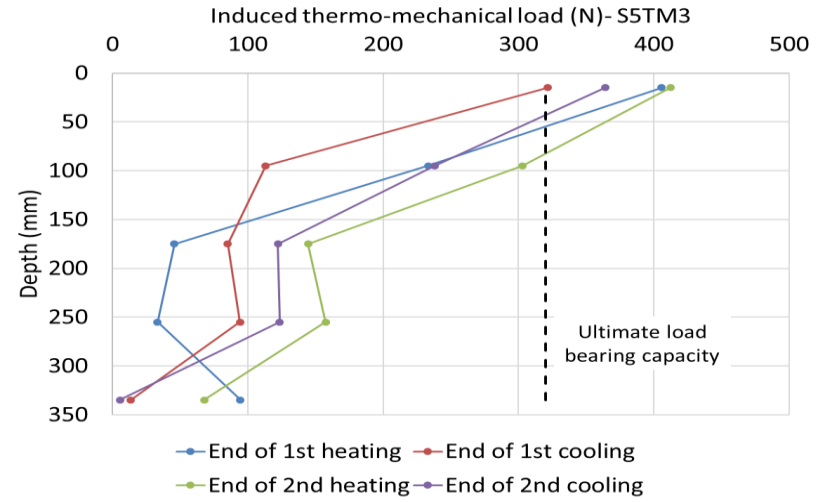


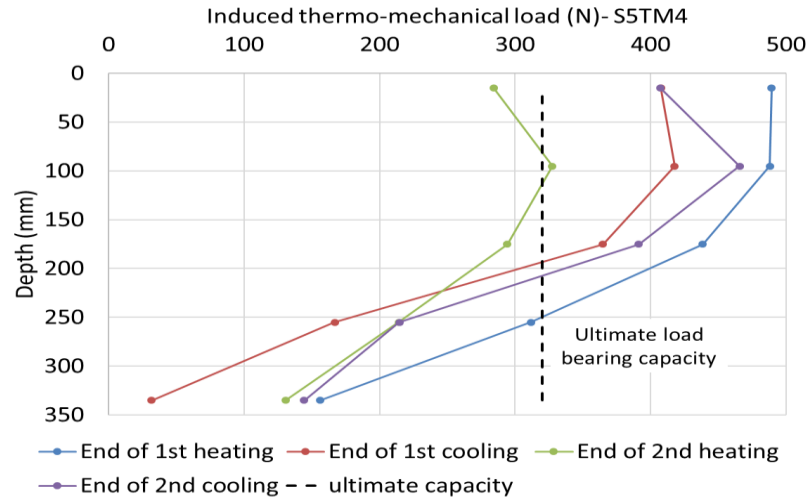
Figure 5-9. Induced thermal load and stress in the pile – Scenario 5



(a)



(b)



(c)

Figure 5-10. Axial load along the pile under both mechanical and thermal loading – Scenario 5

5.7 Pile head displacement

Changes in the pile head displacement for Scenario 5 tests are shown in Figure 5.11. The following observations are made:

- The maximum ratio of the pile settlement over pile heave in S5TM1 to S5TM4 is equal to 1.31, 2.22, 2.43 and 3.1 respectively. It shows that, with an increase in the magnitude of mechanical loading, the ratio is increased due to the larger settlement and additional restraint caused for the pile's upward movement.
- The maximum pile head displacement, heave or settlement are seen during the first cooling period in all four tests. The ratio of the settlement in the first cooling period over second cooling period is equal to 1.1, 1.27, 1.13 and 1.69 for S5TM1 to S5TM4 respectively. The share of the settlement at the end of the first cooling period from the cumulative settlement is approximately 75.0%, 96.0%, 90.5% and 80.1% for S5TM1 to S5TM4 respectively.
- To understand the effect of thermal loading on pile displacement, the settlement at the end of mechanical loading is subtracted from the total pile displacement. It is seen that the settlement caused by two heating-cooling cycles is approximately 81%, 79% and 27% of the settlement caused by mechanical loading for S5TM2 to S5TM4 respectively (see Table 5.5). This means that, for the model pile under a working load of 100N with a safety factor of 3.2, two heating-cooling cycles induce an additional 81% settlement compared to the original settlement caused by mechanical loading.
- The irreversible settlement is seen in S5TM1 to S5TM4, where the pile has not returned to the original position after each cycle. The recoveries of 88.30%, 85.24%, 77.70% and 47.47% of pile settlement at the end of the first cooling period are observed in the second heating period.
- At the end of the S5TM2–S5TM4 tests, the pile is unloaded in the same manner as the loading procedure and it is seen that only 0.42, 0.34 and 0.42 of the entire settlement are recovered for S5TM2 to S5TM4 respectively.
- The ratio of maximum pile head settlement over the maximum allowable settlement (10% of the pile diameter equal to 2.8mm) is equal to 0.04, 0.24, 0.4 and 0.59 for S5TM1 to S5TM4 respectively.
- Using the load-displacement data given in Figure 5.1, the magnitude of settlement at the end of two heating-cooling cycles for S5TM1 is equivalent to the pile head settlement under mechanical loading of approximately 30N to 40N. In S5TM2, S5TM3 and S5TM4, the pile head settlement after the respective mechanical loadings of 100N, 150N and 225N and two heating-cooling cycles is approximately equal to the pile head settlement under 150N, 200N and 250N of the respective mechanical loading situations. This means

that, for a model pile under mechanical loadings of up to 50% of the ultimate capacity, the addition of two heating-cooling cycles up to 50°C has resulted in an additional settlement equivalent to that of an additional 50N mechanical loading (see Table 5.5).

Table 5-5. Changes in pile head settlement under heating and cooling cycles – Scenario 5 tests

Test	Mechanical load (N)	Settlement – mechanical (mm)	Settlement – thermo-mechanical (mm)	Settlement – thermal (mm)	Thermo-mechanical/mechanical
S5TM1	0	0	0.115	0.115	-
S5TM2	100	0.352	0.639	0.287	1.81
S5TM3	150	0.638	1.146	0.508	1.79
S5TM4	225	1.278	1.632	0.354	1.27

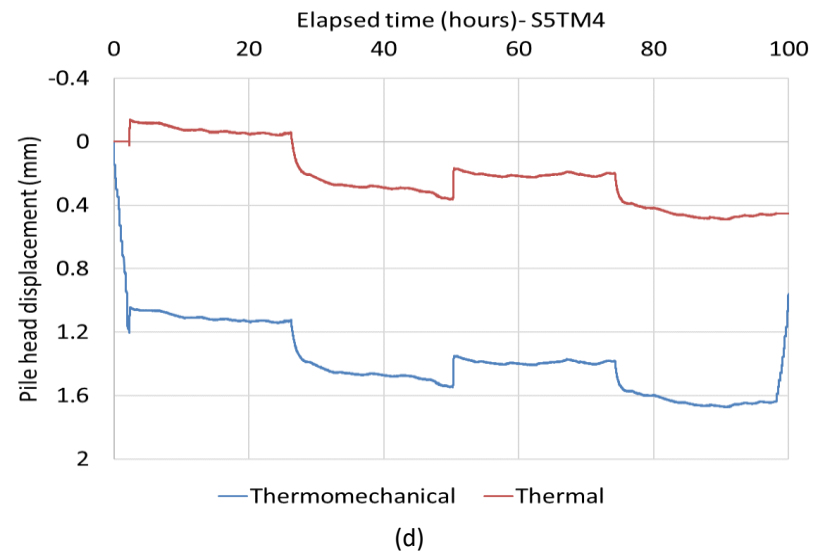
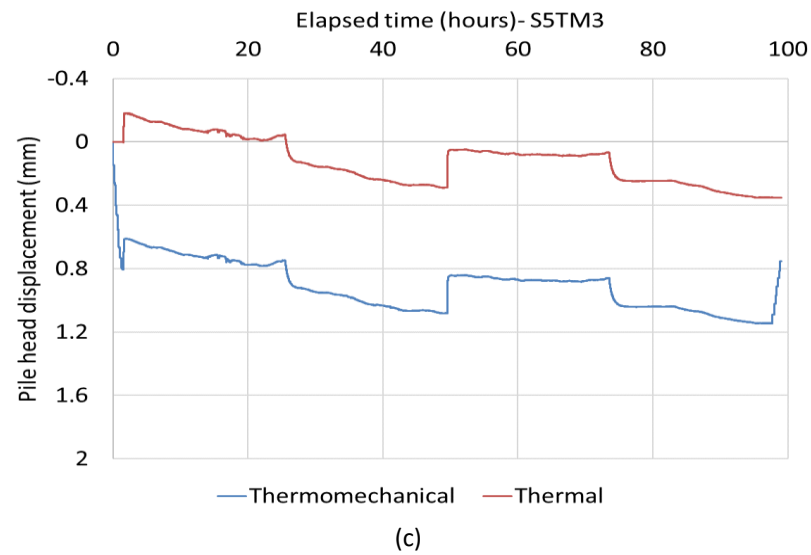
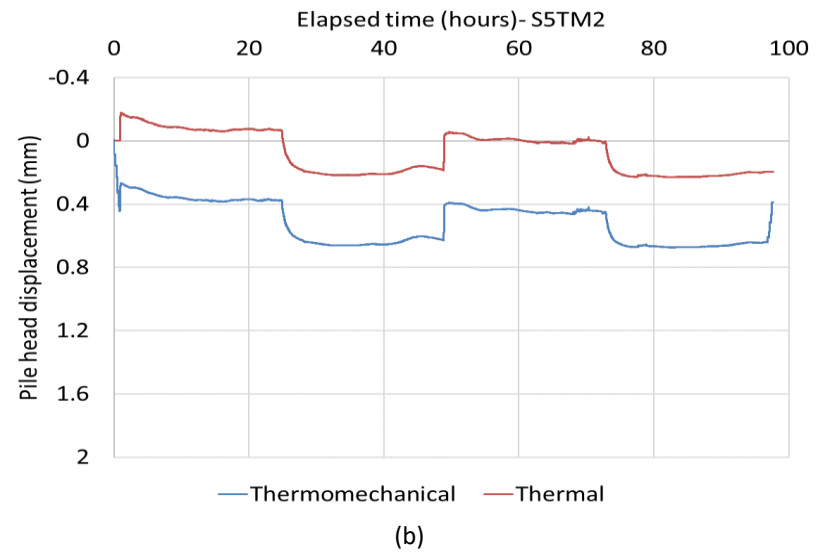
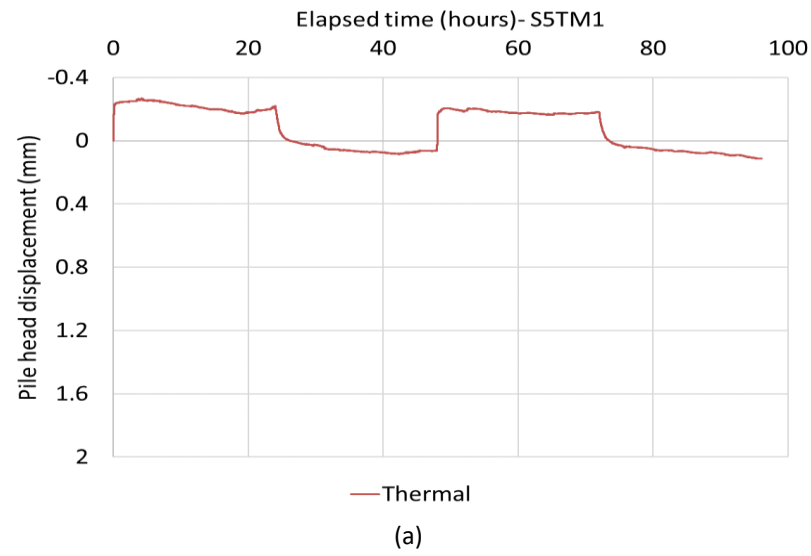


Figure 5-11. Pile head displacement – Scenario 5

5.8 Mobilised friction at the soil–pile interface

Mobilised friction along the pile length under mechanical and thermo-mechanical loading is determined using Equation 2.9. The numerator consists of a constant value of pile stiffness (i.e. $EA=24.96\text{MN}$ for the stainless steel model pile) and $\Delta\varepsilon$ is the difference in the strain value at the top and the bottom of each zone as described in Section 4.5.6. It is also an indicator of loss or gain of the axial load at the soil–pile interface in each zone. Similar to the procedure described in Scenarios 3 and 4, the pile is divided into four zones. The following results are obtained:

- Initially, the mobilised friction under mechanical loading vs pile head displacement is plotted in Figures 5.12-a to 5.12-c. In S5TM2, the maximum and minimum mobilised frictions are seen in Zones 1 and 4 at the bottom and top of the pile respectively (see Figure 5.12-a). In S5TM3 and S5TM4, with an increase in the magnitude of mechanical loading, the location of the maximum mobilised friction is shifted to Zone 3. The maximum mobilised friction is seen at the end of S5TM4 and is equal to 14.15kPa for an approximately 1.18mm pile settlement.
- Changes in the mobilised friction along the pile depth at the end of the mechanical loading procedure are also plotted in Figures 5.12-d to 5.12-f. In S5TM2, the maximum mobilised friction is seen in Zones 1 and 3, while in S5TM3, more friction is mobilised at the top half of the pile compared to the pile bottom. In S5TM4, an even distribution is seen in the bottom half of the pile with more resistance observed in Zone 3.
- Mobilised friction under thermo-mechanical loading for the entire test period is plotted for S5TM1–S5TM4 (see Figures 5.13 to 5.16). Mobilised frictions at the end of the 1st, 2nd, 4th, 8th, 12th, 16th, 20th and 24th hour of heating and cooling are presented. In S5TM1, the mobilised friction is increased at the end of the first heating period and it is then decreased during the cooling period in Zone 1 (see Figure 5.13). In the second cycle, friction is mobilised during both heating and cooling periods. In Zones 2 to 4, mobilised friction at the end of the first and second heating periods and then at the end of the first and second cooling periods are close to each other. This shows that, despite changes in the mobilised friction during the test, an approximate symmetry is seen in the response. The maximum positive mobilised friction is seen at the end of the second heating period in Zone 1 and is equal to 10.87kPa, which is 76.81% of the maximum mobilised friction under 225N of mechanical loading.
- In S5TM2, the initial mechanical loading has resulted in a maximum mobilised friction of 5.09kPa in Zone 1 (see Figure 5.14). This is then increased under the heating load to up to 11.7kPa at the end of the first heating period in Zone 1 and then the friction is decreased to nearly zero at the end of the first cooling period in Zone 1. It is then increased again up to 5.4kPa and then reduced to -3.3kPa during the cooling period. For Zone 1 in S5TM2, it can

be concluded that heating and cooling have resulted in an increase and decrease in the mobilised friction respectively.

- In S5TM2, mostly negative friction is seen in Zone 2, with maximum mobilised friction seen at the end of the first cooling period and is equal to -9.56kPa. Mobilised friction due to heating and cooling exceeds the mobilised friction due to mechanical loading in this test. This could be mainly due to the large thermal expansion coefficient of the stainless steel pile, high thermal expansion of the sand and the increase in the level of contact between soil and pile due to heating. During cooling periods, there is no guarantee that the sand particles will return to their original position due to possible dilations and possible increase in the interlocking of soil particles (this is discussed in Chapter 6). The results suggest that, for each zone, different behaviour can be seen.
- In S5TM3, the maximum mobilised friction under mechanical loading reaches 9.2kPa in Zone 3 (see Figure 5.15). It is then increased to 16.67kPa at the end of the first heating period. It is recovered during the cooling period to reach the negative friction of -5.72kPa. There is then a significant jump towards the end of the second heating period and then a reduction of mobilised friction to -8.45kPa at the end of the second cooling period. It is seen again in the zone where maximum mobilised friction happens under mechanical loading: an increase and decrease in the temperature results in an increase and decrease of mobilised friction.
- In the other three zones in S5TM3, irregularity is seen in the changes in mobilised friction, where positive and negative friction is seen during both heating and cooling periods. The maximum positive and negative frictions are equal to 18.68kPa and -17.11kPa respectively and are seen at the end of the first heating and first cooling periods.
- The maximum mobilised friction under mechanical loading in S5TM4 is seen at Zone 3, where mobilised friction up to 14.15kPa is achieved (see Figure 5.16). Decrease in the mobilised friction is seen at the end of the first heating period. This could be due to the restraint faced by the pile due to the mechanical loading, which has made it difficult for the pile to heave and less movement has resulted in less mobilised friction. It then increases to 5.12kPa at the end of the first cooling period, where larger pile settlements are seen compared to initial pile heave. The same procedure with smaller magnitudes is repeated in the second heating-cooling cycle. The maximum mobilised friction due to the heating and cooling process remains below the ultimate mobilised friction in Zone 3. A similar observation is made for Zone 1.
- A comparison between mobilised friction at the end of each heating and cooling period along the pile length is given in Figure 5.17. For S5TM1, the positive and negative skin frictions are seen during the heating and cooling periods respectively. In the absence of mechanical loading, the maximum positive mobilised friction is seen in Zone 1 at the end of the second

heating period, and it is not recovered during the subsequent cooling period. In S5TM2, it is seen that the maximum positive mobilised frictions during both heating periods are higher than the maximum mobilised friction due to initial mechanical loading. A similar observation is made in S5TM3. In S5TM4, the presence of 225N mechanical loading on the pile head results in a mixed response along the pile, where both higher and lower than maximum mobilised friction under mechanical loading are observed due to thermal loading.

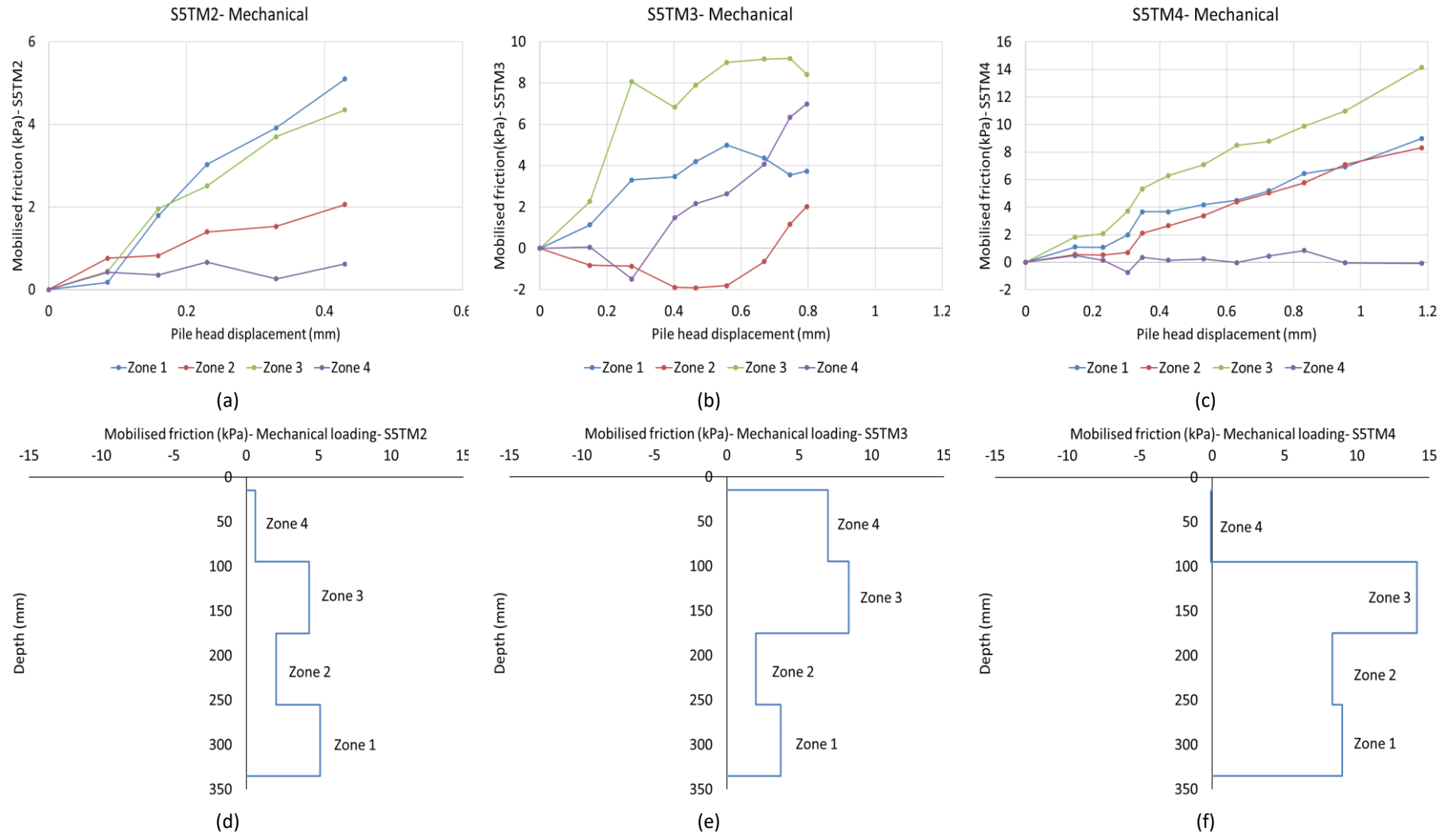
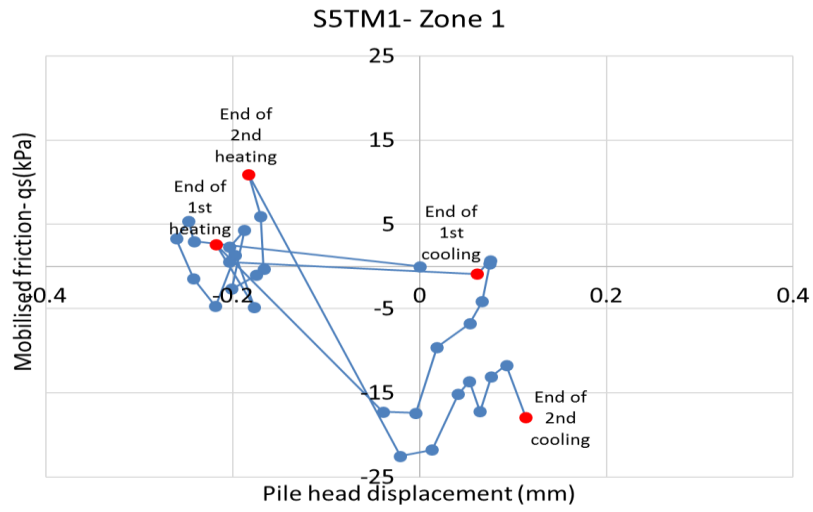
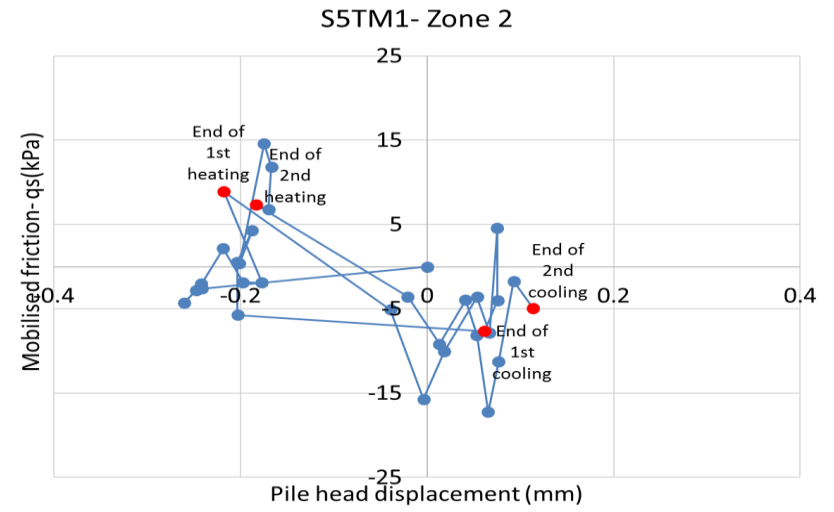


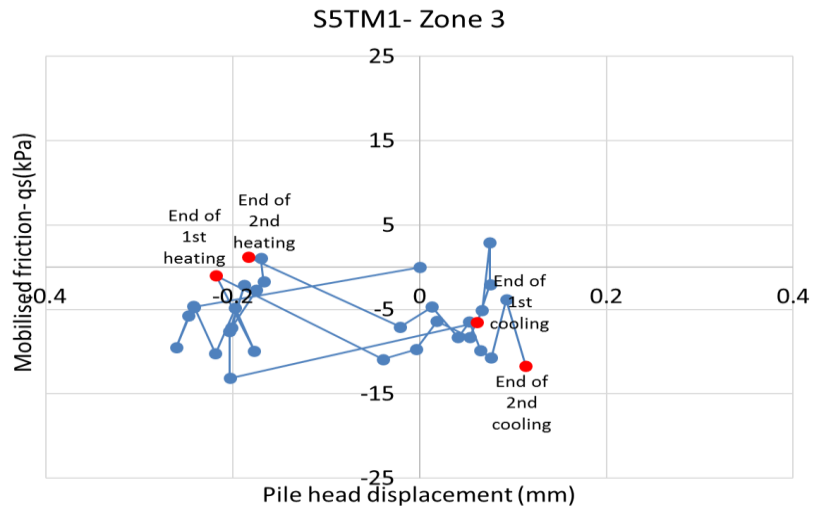
Figure 5-12. Mobilised friction along the pile at the end of mechanical loading – Scenario 5



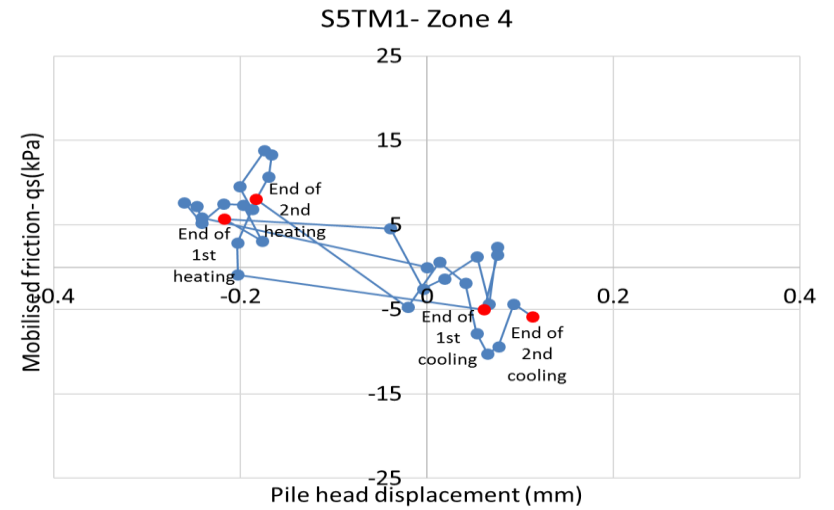
(a)



(b)

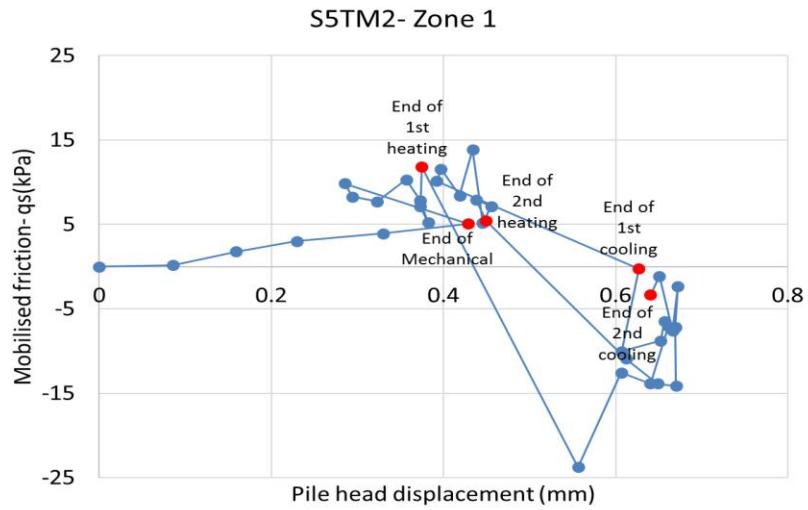


(c)

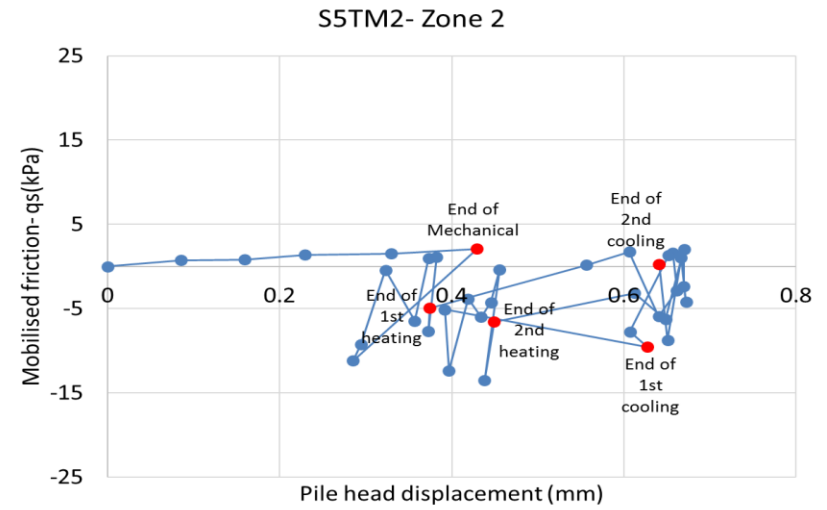


(d)

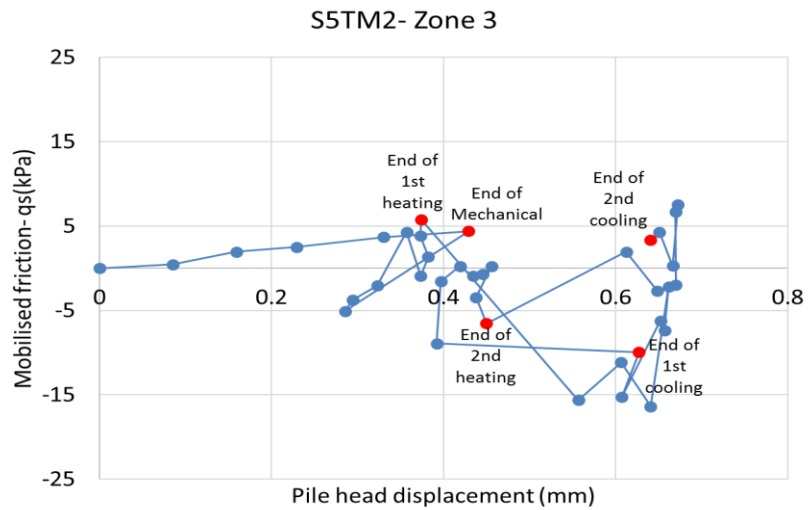
Figure 5-13. Mobilised shaft friction vs pile head displacement – Scenario 5 – S5TM1



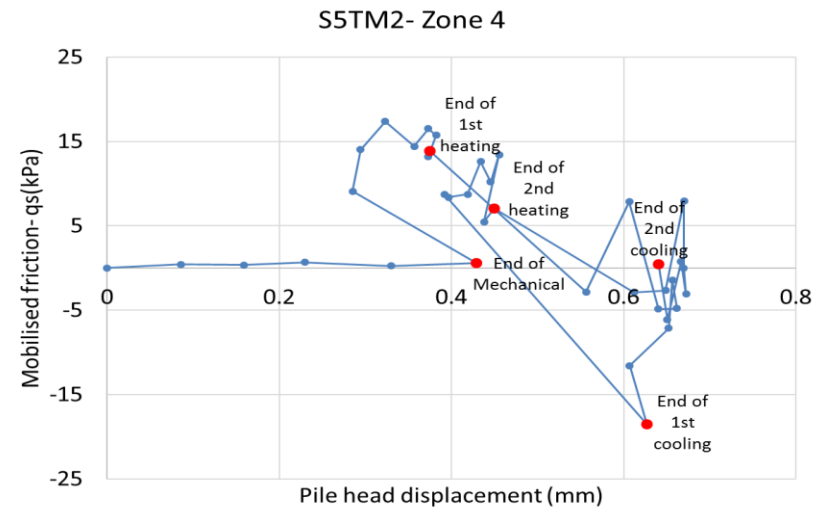
(a)



(b)

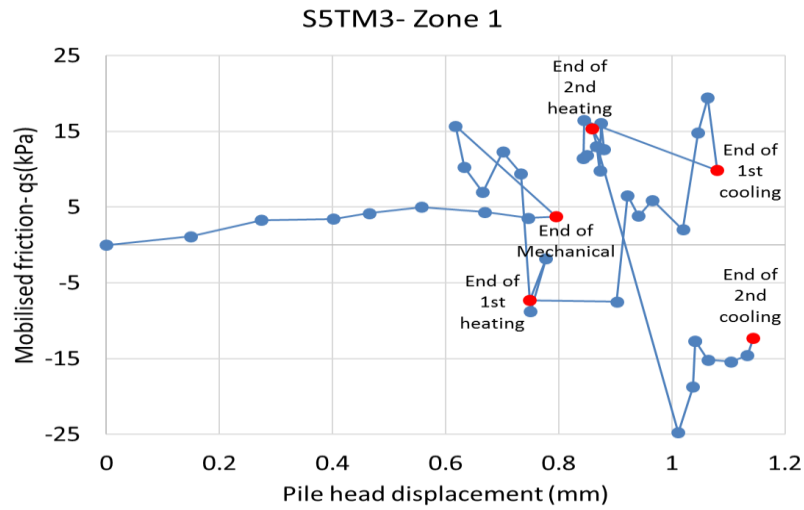


(c)

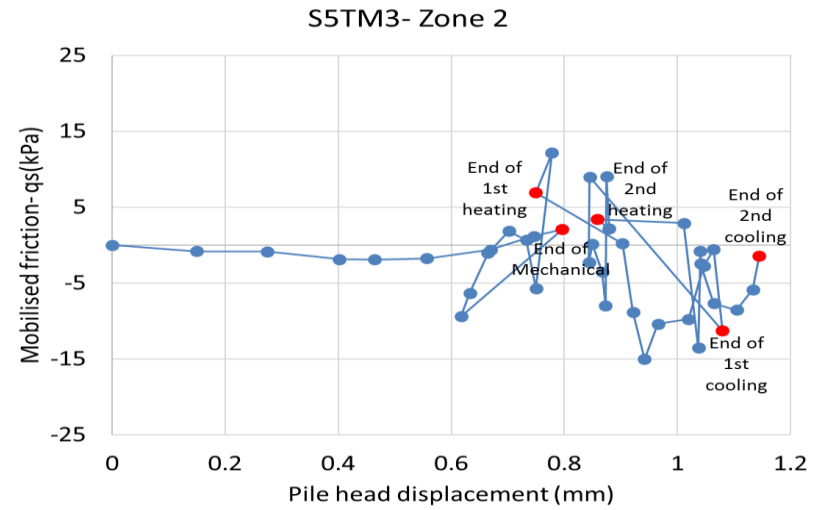


(d)

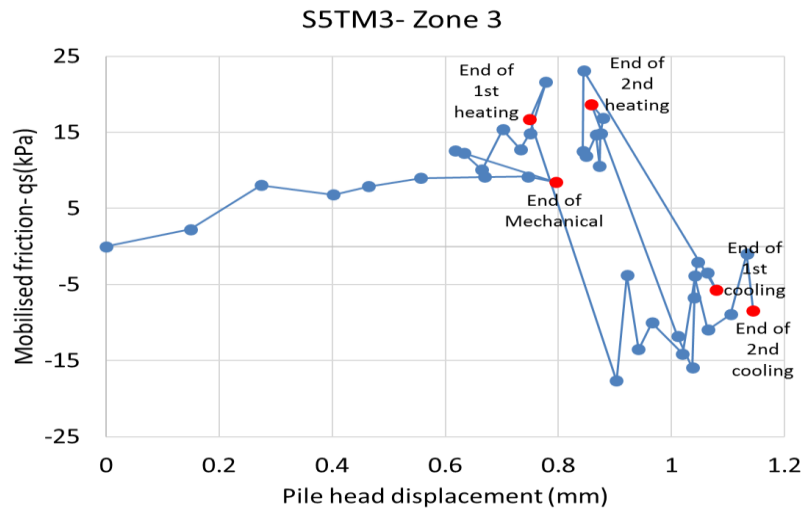
Figure 5-14. Mobilised shaft friction vs pile head displacement – Scenario 5 – S5TM2



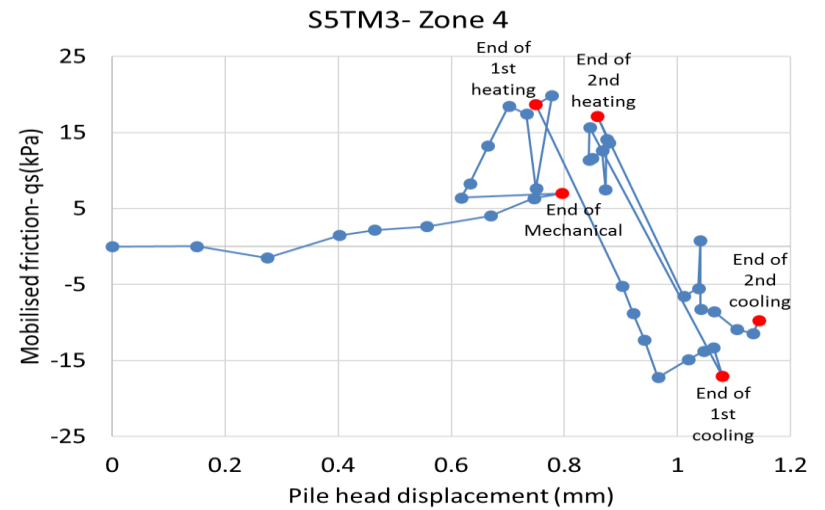
(a)



(b)

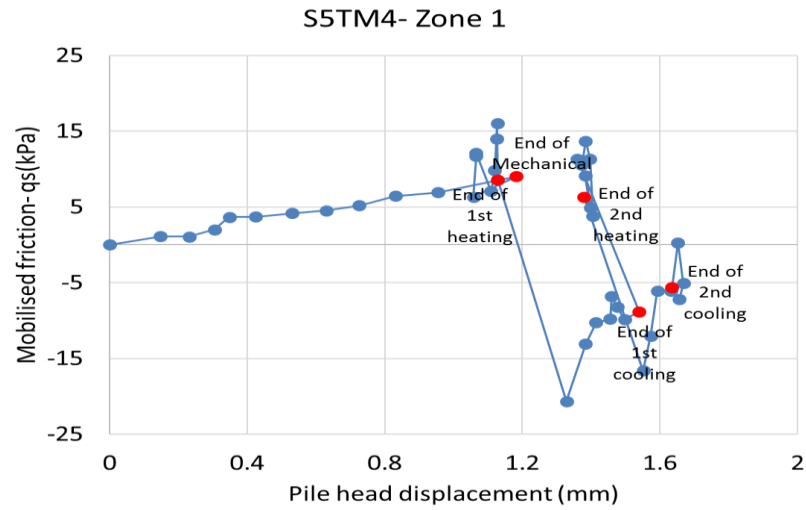


(c)

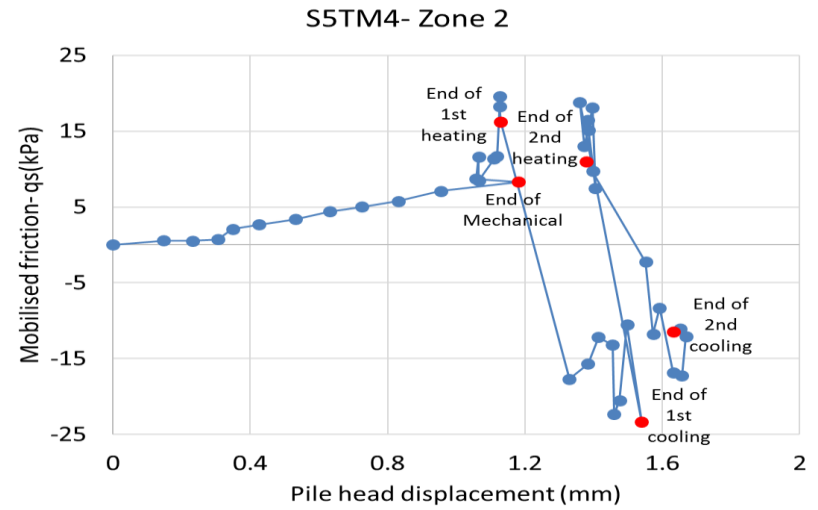


(d)

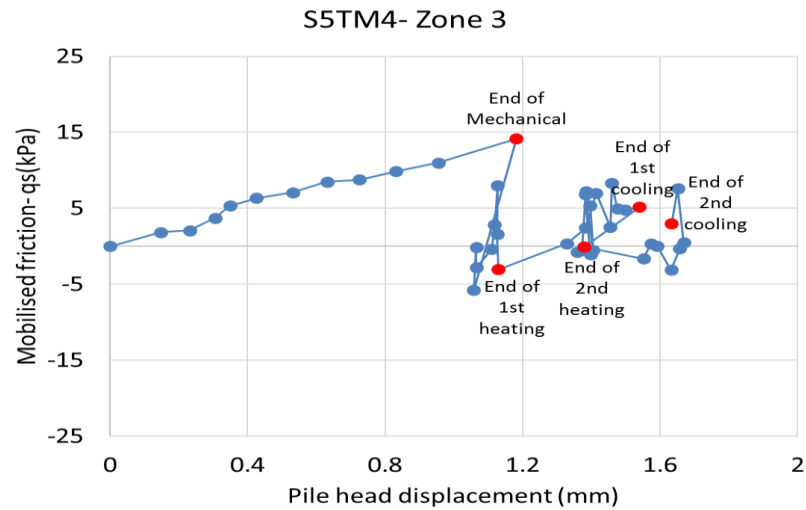
Figure 5-15. Mobilised shaft friction vs pile head displacement – Scenario 5 – S5TM3



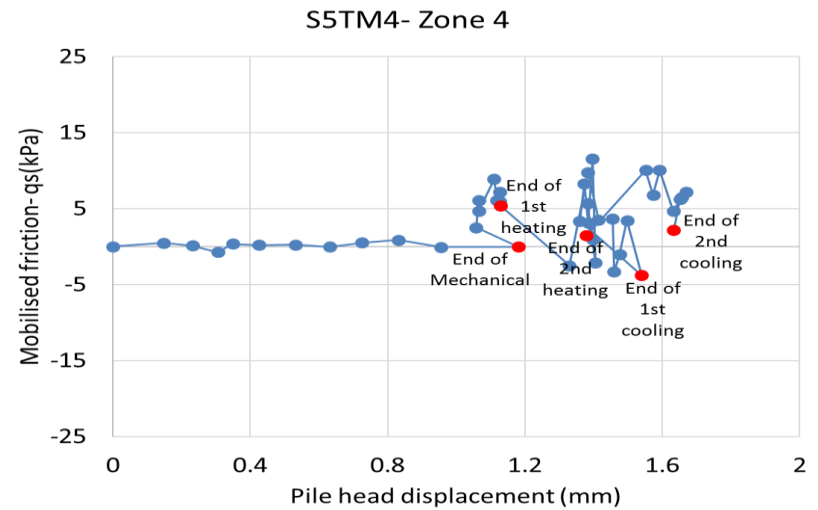
(a)



(b)

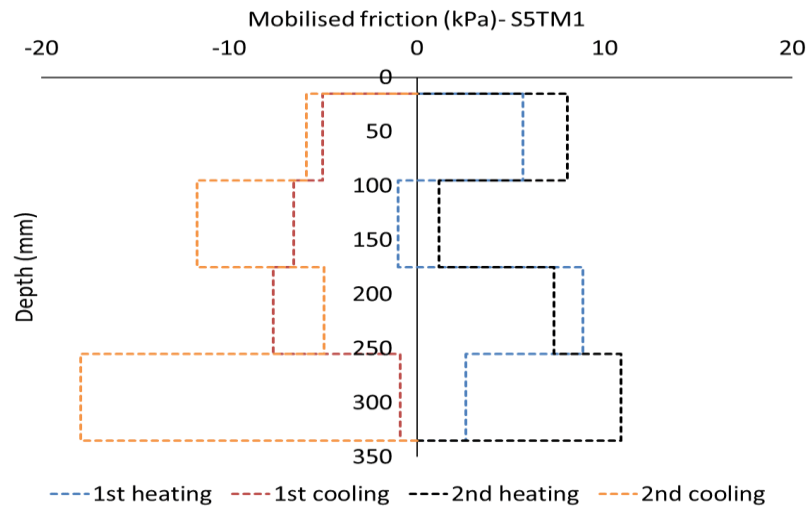


(c)

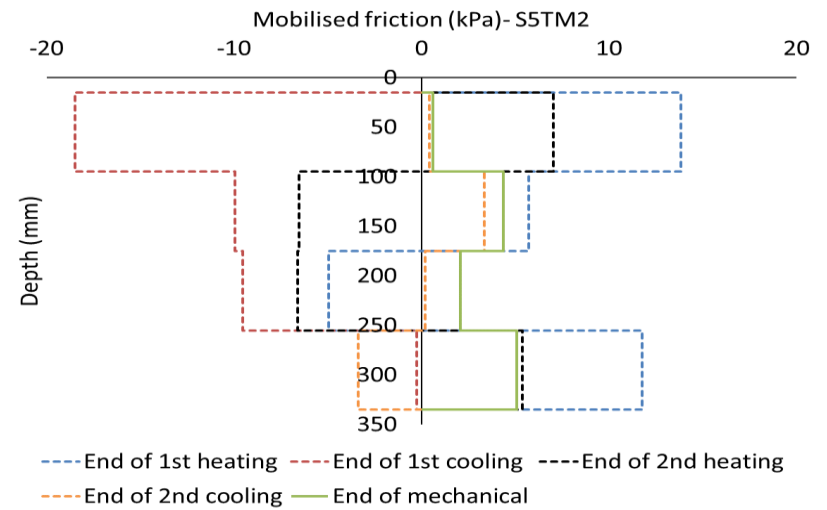


(d)

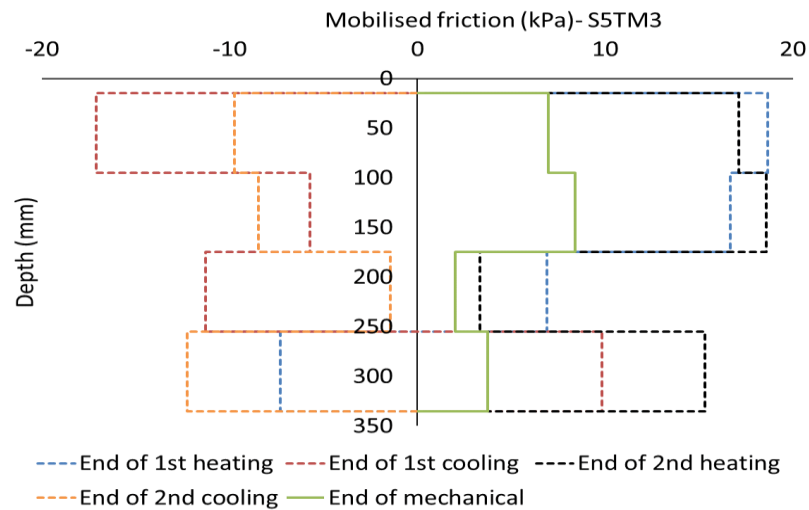
Figure 5-16. Mobilised shaft friction vs pile head displacement – Scenario 5 – S5TM4



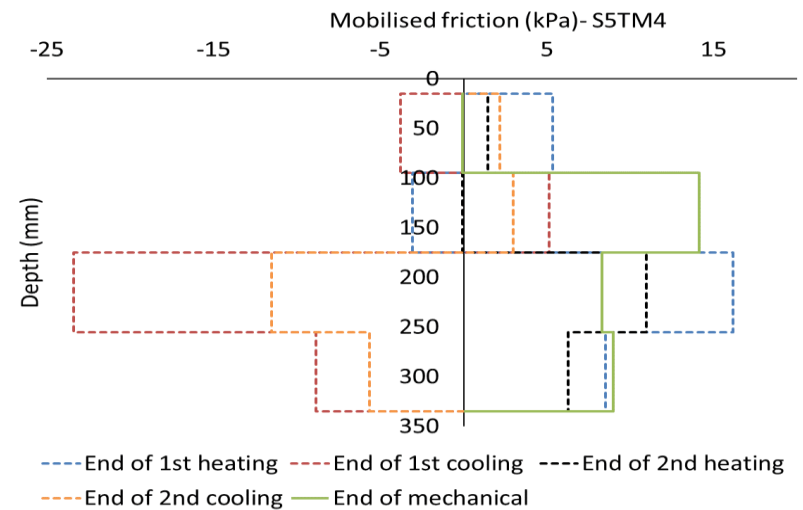
(a)



(b)



(c)



(d)

Figure 5-17. Mobilised friction along the pile at the end of each heating and cooling period – Scenario 5

5.9 Comparison with the framework

As mentioned earlier, the proposed framework has considered the perfect free and restrained conditions whereas, in this study, an intermediate level of restraint exists. Figures taken from Bourne-Webb et al. (2013) (i.e. Figures 5.18 and 5.19) relate to the condition where the pile is under mechanical loading and the base is free to move. The pile bottom in Scenario 5 is partially restrained by the sand layer below the pile. Moreover, in the proposed framework, the location of the null point is assumed to be in the middle of the pile, whereas in Scenario 5 tests, it is found that the location of the null point differs for each test and can also shift after the first heating-cooling cycle. The following comparisons are made:

- A comparison between restrained strain profiles at the end of each period is shown in Figure 5.18. According to the framework, the maximum restrained strain is expected to be seen at the pile head and the minimum restrained strain at the pile bottom. In this case, due to the existence of sand beneath the pile, the restrained strain is also expected to be seen below the pile. In S5TM4 (where the maximum restrained strain is observed), the profile follows the extreme case given by the framework, where maximum restrained strain occurs at the mid-depth of the pile and is then reduced towards the pile bottom where a certain level of restrained strain exists due to the soil beneath the pile. It shows a good agreement between the framework and the profile achieved from maximum restrained strain at the end of the first heating period. A similar observation is made during the second heating period (see Figure 5.18-c).
- For the cooling period, the restrained strain is expected to be lower towards the pile bottom and is expected to be close to zero at the pile bottom. At the end of the first cooling period, S5TM1 shows the same trend but, in other three tests, there is a sudden change at the SP4 level but they follow the same trend as the proposed profile in other levels. More similarity is seen during the second cooling period except for S5TM4, where maximum restraint happens at the mid-depth (see Figure 5.18-d). This difference could be due to the possible compression of the soil at the pile base due to the higher magnitude of mechanical loads in S5TM4 (see Chapter 6). In general, it seems that the restrained strain profiles for both heating and cooling periods follow the trend given by the proposed framework with a few distortions. Due to the elasticity of the stainless steel pile, the comparison could be extended to induced load and stress in the pile.
- A comparison between mobilised friction profiles at the end of the first heating period within the framework is shown in Figure 5.19-a. The null point is assumed to be at the mid-depth of the pile, and the upper part is expected to experience lower mobilised friction. This is with the assumption that the bottom of the pile is free. For this model, the magnitude of mobilised friction will be determined based on the level of restraint caused by the soil beneath the pile

and the mechanical loading at the pile head. In S5TM1, smaller mobilised friction is seen at the top half of the pile and larger mobilised friction is seen at the pile bottom, which is in line with the proposed framework. A similar observation is made for S5TM1 at the end of the second heating period. In S5TM2, a higher magnitude of mobilised friction is seen at the pile top and bottom (where maximum restraints exist) and less friction is mobilised in Zones 2 and 3. In S5TM3, opposite behaviour is seen, whereas in S5TM4, the profile is in agreement with the proposed framework.

- At the end of the first cooling period, a reversed profile is expected to be seen. Larger magnitudes of mobilised friction are seen at the pile top and smaller magnitudes of mobilised friction at the pile bottom, which is similar to the estimated behaviour by the framework. This procedure is not followed at the end of the second cooling period.

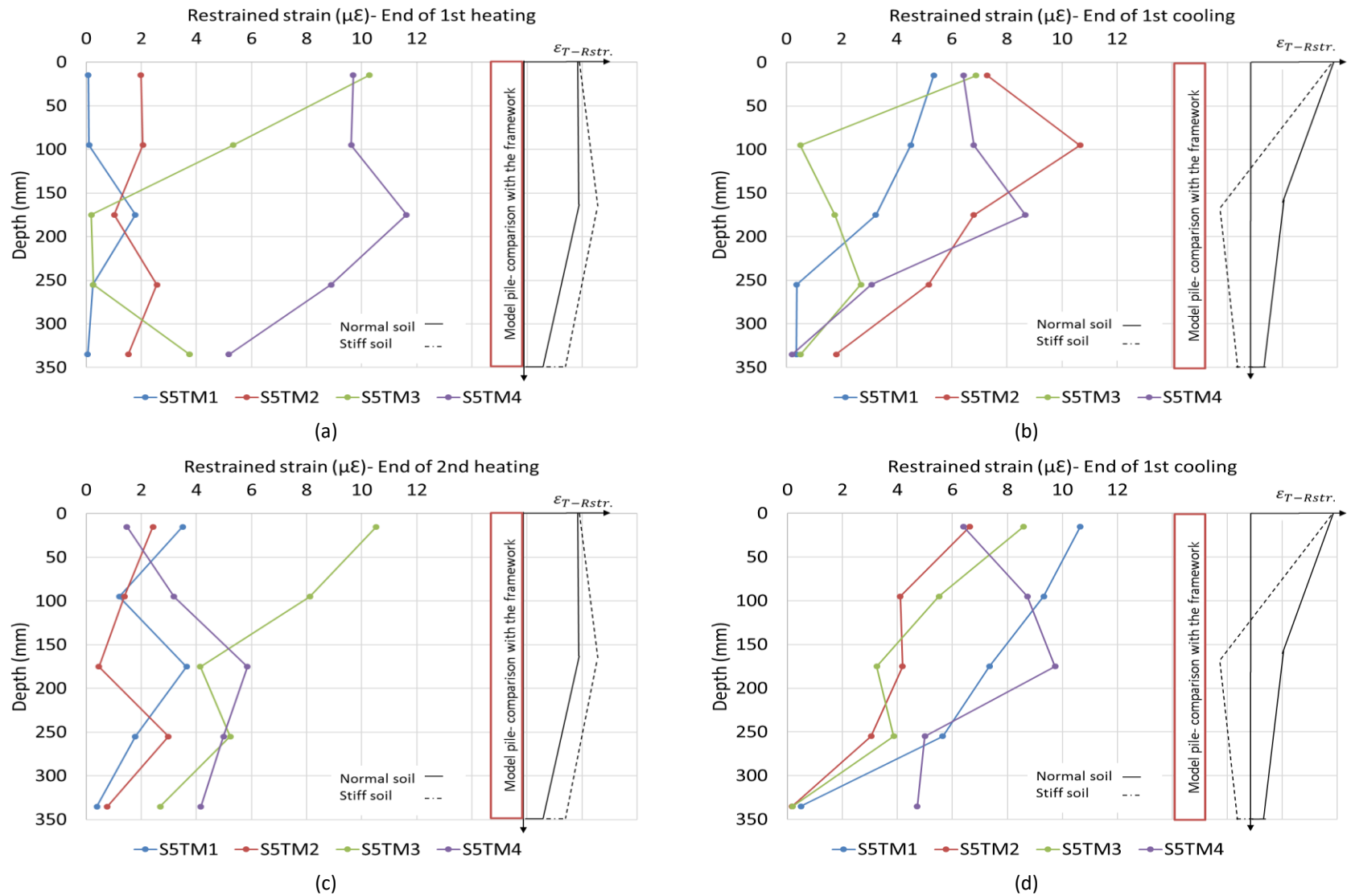


Figure 5-18. Comparison of restrained strain along the pile surface between Scenario 5 tests and the proposed framework

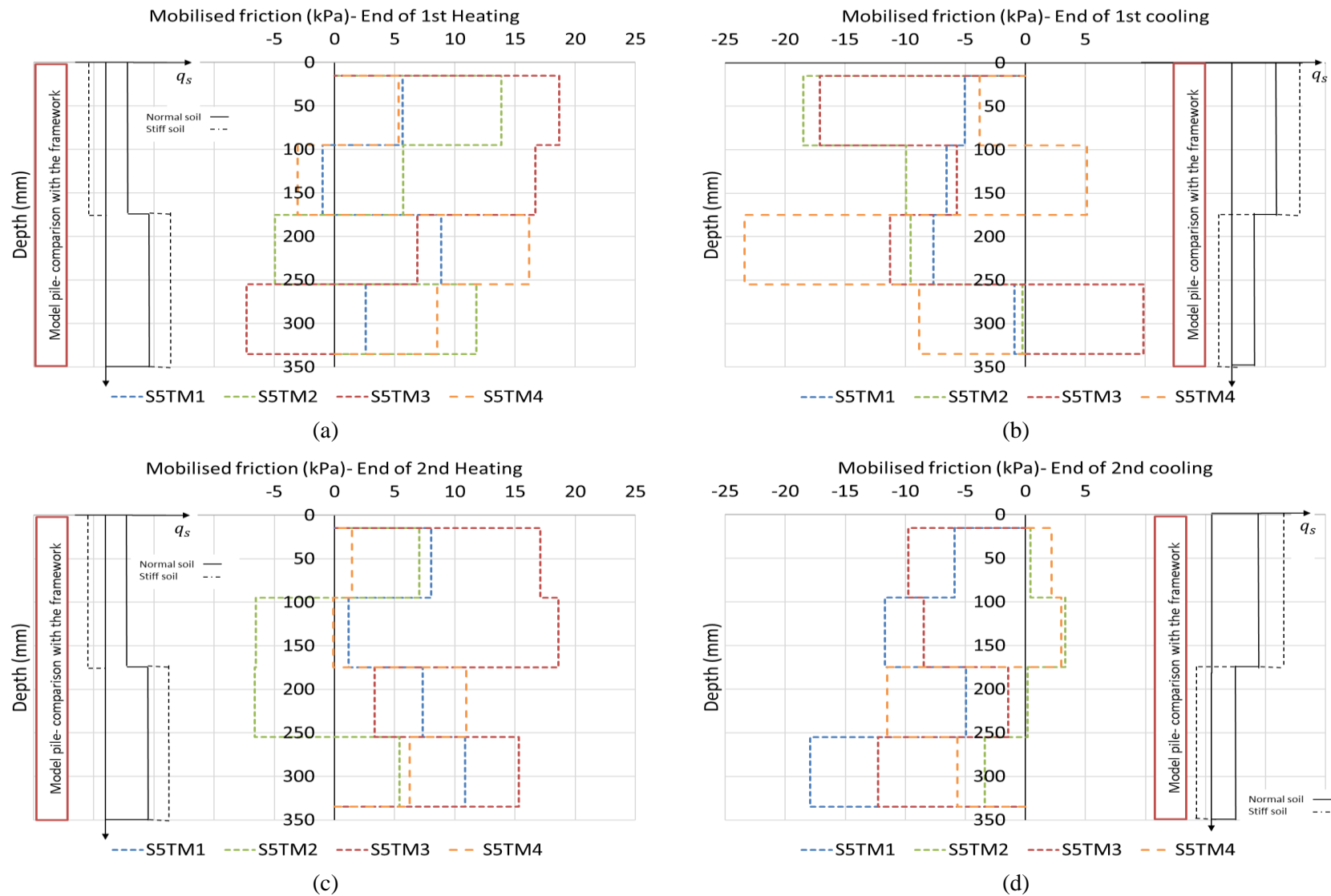


Figure 5-19. Comparison of mobilised shaft friction along the pile surface between Scenario 5 tests and the proposed framework

Chapter 6. Discussion on the laboratory results

6.1 Ultimate load-bearing capacity of the model pile

It is seen that the ultimate capacity of the shaft resisting pile is 165N, while the ultimate capacity of the shaft and base resisting pile is 320N. Parameters involved in determining the capacity of the shaft resisting pile include horizontal earth pressure (K), area of the shaft surface in contact with the soil (A_s), the effective overburden pressure (p_o) and the friction angle between the soil and pile wall (δ):

$$Q_s = A_s K p_o \tan \delta \quad (6.1)$$

For the shaft and base resisting pile, the effective pile length is 40mm less than the shaft resisting pile, but it is observed in Section 5.2 that a small decrease/increase in the pile's embedded length has up to 20N of an effect on the shaft bearing capacity. For the shaft and base resisting pile, the load is carried by both the shaft and the base. The embedded pile length in the shaft and base resisting pile is reduced by 10.25% compared to the shaft resisting pile, but the ultimate load-bearing capacity of the pile is doubled. Looking at the theoretical bearing capacity of the pile base, Kulhawy et al. (1983) state that the load carried by the pile base is a function of the pile base's cross-section area (A_b), bearing capacity (N_q) and mean normal ground effective stress at the pile base level (σ'_{v0}):

$$Q_b = A_b \cdot N_q \quad (6.2)$$

The value of N_q is estimated using the relationship developed by Berezantsev et al. (1961), which is a relationship between the drained angle of the shearing resistance of the soil at the pile base (ϕ') and the penetration depth of the pile. A modified version which includes both Berezantsev et al. and Brinch Hansen versions is presented by Tomlinson and Woodward, 2008). In this study, the ratio of the pile's embedded length over the pile's diameter is equal to 12.5, which results in a higher value for the bearing capacity factor.

Another part of the analysis for the shaft and base resisting pile is to determine an appropriate distance between the pile base and the container base as it can affect the bearing capacity of the pile. In order to determine the required distance between the pile base and container base, the ratio of the distance between the pile bottom and the container base over the pile diameter (H/D) is determined by trying various H values. As shown in Table 5.1, it is found that the difference between the ultimate capacity of the pile with H/D between 2.32 and 4.64 is only 20N. This means that, when the distance between the pile bottom and container base is doubled, the capacity

increases by only 6.7%. In the literature, a range of H/D values is used: 15.74 (Li et al., 2012), 12.5 (Yavari et al., 2014; Kalantidou et al., 2012), and 1.5 (El Naggar and Wei, 2000). This shows that the H/D values used in the literature lie within a large range of 1.5 to 15.74. This is mainly due to the differences in the type of soil used, the embedded pile length and the type of pile placement in the soil (i.e. displacement or no displacement).

Small variation of data in Figures 4.1 and 5.1 for both types of piles is seen. Similarly, it is reported by Kalantidou et al. (2012) that small variations of data for the load-displacement figures are achieved for a model pile embedded in sand (see Section 2.4.2 for apparatus details). It is stated by Kalantidou et al. (2012) that the loading mechanism is the main reason for variations observed for the load-displacement figures as each loading step works as a sudden shock to the pile. In this study, a similar loading mechanism to the one adopted by Kalantidou et al. (2012) is used, where the pile is loaded using weights applied on the pile head in incremental steps of 10–20N (which is similar to the procedure used in the construction of a thermal pile in the field). It is stated by Kalantidou et al. (2012) that this type of loading mechanism can work as a sudden shock on the pile head, but alternative loading mechanisms – such as continuous loading using a water tank or hydraulic jack – have to be tested in the same set-up to be able to make a definitive conclusion about them.

6.2 Pile temperature profiles

Changes in the pile temperature at the end of the first heating and cooling periods for Scenarios 3 to 5 are shown in Figure 6.1. It is seen that the maximum temperature change is recorded either at TP5 or TP4, and the minimum temperature change is recorded at TP1. This is mainly due to the lower rate of water flow at the bottom of the pile, using a long model pile, and the inefficiency of the water circulator. A similar observation regarding a temperature drop along the pile length is reported by Ghasemi-Fare and Basu (2013) using a 2D finite difference model, and Gao et al. (2008) for in-situ installations. The assumption of a constant heat flow along the entire pile surface results in error in the analysis of heat transfer along the pile (Ghasemi-Fare and Basu, 2013; Batini et al., 2015; Yu et al., 2015) and this study also shows that temperature does not remain constant along the pile surface.

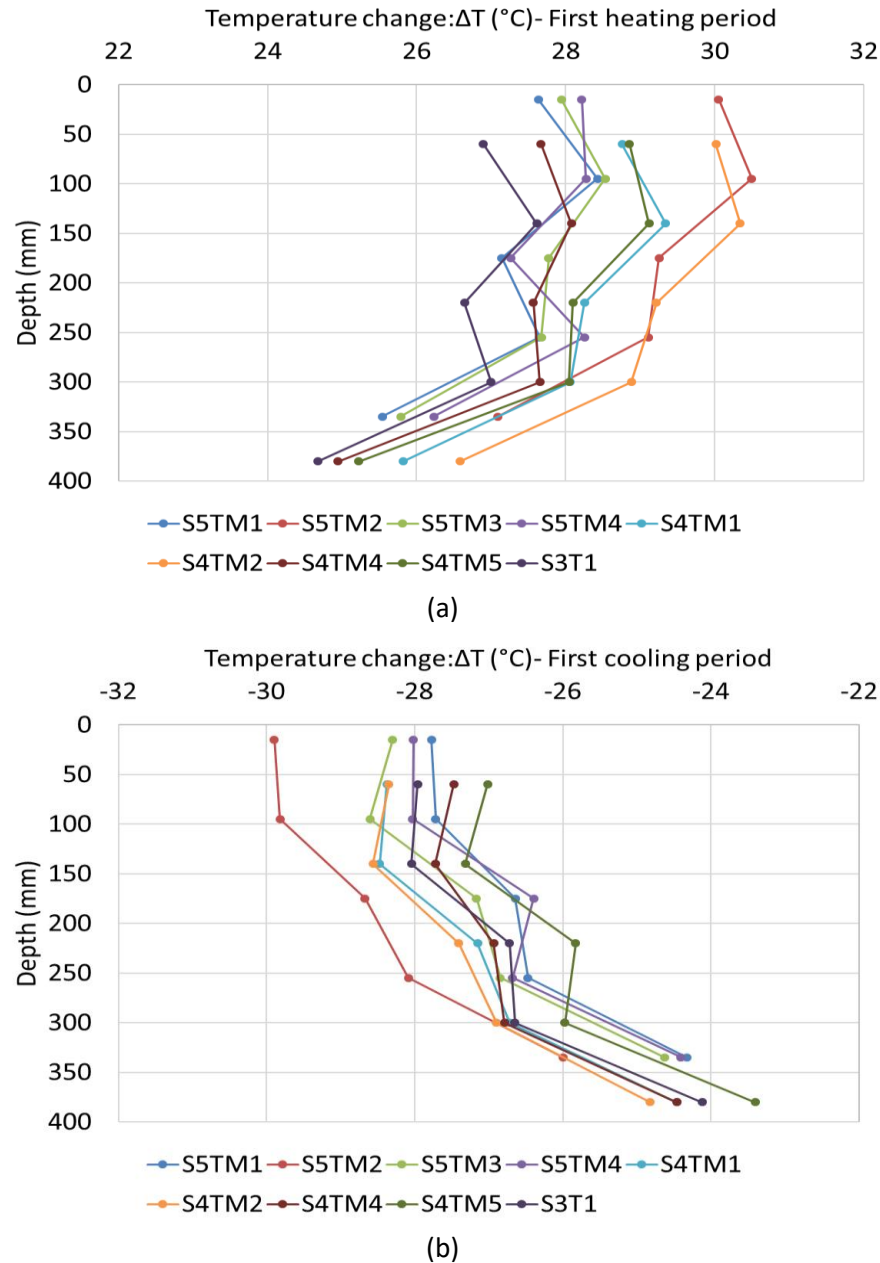


Figure 6-1. Temperature changes along the pile surface at the end of the: (a) first heating period and (b) first cooling period – Scenarios 3 to 5

In the Scenario 2 tests, it is seen that the temperature returns to the initial level after cooling while in Scenarios 3 to 5, the temperature does not return to the original position. In Figure 6.1, it is seen that, in Scenarios 3 to 5, higher ΔT values are observed during the heating period compared to during the cooling period. This means that, after one heating-cooling cycle, the initial temperature at the start of the second heating period is higher. Higher temperature for the heat source means a higher coefficient of performance for a thermal pile system. Similar findings are reported by Kramer et al. (2014), where a thermal pile is described as a system that is chargeable during summer, with the charge used in the winter. It also shows the benefits of using a thermal pile system in a two-mode format (both heating and cooling). Temperature variations along the

pile is more apparent in in-situ installations due to the heat loss caused by the surrounding air, low levels of insulation and constant variations in temperature, as reported by Laloui et al. (2006) and Bourne-Webb et al. (2009).

In all the tests, the pile temperature reaches a relatively stable condition after about 15 minutes of the heating period, while this process takes up to 20 hours during the cooling period. This means that, in order to understand pile behaviour, continuous monitoring – particularly in the cooling phase – is required until a steady state is achieved. The time required for a pile to reach a stable condition during the heating period is mainly dependent on the thermal properties of the pile's material, soil's thermal conductivity, method of applying temperature increments (quickly or step by step), the magnitude of the target temperature and the heat transfer process involving the carrying fluid, pipes and the pile surface. For the cooling period, thermal conductivity of the surrounding soil can considerably affect the time it takes to reach the steady state.

One of the main advantages of a thermal pile system is the stable temperature below a 5m depth in the ground (Preene and Powrie, 2009). Lower temperatures have been recorded by Bourne-Webb et al. (2009) at the top 5m of the pile; this is mainly due to variations in the ambient temperature. In this study, unlike the above-mentioned in-situ observations, due to the high level of insulation applied on the sand's surface, a negligible fluctuation of temperature is observed at the SP5 level during the heating periods, which is the closest sensor to the pile surface. This shows that boundaries can be better controlled in laboratory studies compared to in-situ installations.

In this study, temperature changes of approximately $\pm 28^{\circ}\text{C}$ to 32°C are seen during the heating and cooling periods, which are within the high range of temperature variations expected for thermal piles (between -1°C to $+38^{\circ}\text{C}$) (Amatya et al., 2008). A comparison between the temperature changes in several studies carried out in the literature is shown in Table 6.1. For a two-mode operating thermal pile system, due to the seasonal variations in temperature, it is unlikely that the pile temperature will exceed the maximum value of 38°C given by Amatya et al. (2008). However, for a single-mode operating thermal pile – particularly for the cooling mode, where heat is constantly injected into the ground – the soil and pile temperatures can exceed the values given by Amatya et al. (2008). This can also be considered a critical assessment of thermal piles under thermal loading.

Table 6-1. Comparison between changes in the pile temperature for previous studies

Reference	ΔT ($^{\circ}\text{C}$)	Reference	ΔT ($^{\circ}\text{C}$)	Reference	ΔT ($^{\circ}\text{C}$)
Sutman et al. (2015)	-6.0 to +8.8	Murphy and McCartney (2012)	-5.0 to +14.0	Goode et al. (2014)	+7 and +12 and +18
Murphy et al. (2014)	+18 to +19	Laloui et al. (2003;2006)	T1: +20.9 T7: +18.0	Wang et al. (2011), Kramer and Basu (2014)	+20
Amis et al. (2008), Bourne-Webb et al. (2009)	Free: +29.4 Restrained: -19 to +10	Wang et al. (2013)	0 to +25	Tang et al. (2013), Kalantidou et al. (2012)	± 25
Ng et al. (2015)	+15 and +30	Wang et al. (2012)	+20 and 40	McCartney and Rosenberg (2011)	+29 and +41

6.3 Strain profiles

6.3.1 Observed strain

Strain and temperature data is collected in the form of wavelengths. It is then converted into absolute temperature and strain readings using temperature and strain sensitivity coefficients respectively. It is found that the temperature sensitivity of FBGs is between 29.7pm/ $^{\circ}\text{C}$ to 32.5pm/ $^{\circ}\text{C}$ with an average of 30.66pm/ $^{\circ}\text{C}$, which is approximately 2.5 times larger than the theoretical value of 11pm/ $^{\circ}\text{C}$ to 13pm/ $^{\circ}\text{C}$ given by Rao (1997) for a bare FBG with a wavelength of 1550nm. A similar observation has been made by Ren et al. (2004), where a temperature sensitivity of 30.73pm/ $^{\circ}\text{C}$ is observed for FBGs attached to stainless steel pipes and covered with epoxy resin (similar to the material used in this study to cover FBGs). It shows the effect of the host material and the covering/adhesive material on the temperature sensitivity of FBGs. It is also shown by Mishra et al. (2016) that the temperature sensitivity of a coated FBG is much higher than of a bare FBG. In addition to the above-mentioned parameters, temperature sensitivity is also seen as a function of wavelength, where temperature sensitivities of 6.8pm/ $^{\circ}\text{C}$ and 10pm/ $^{\circ}\text{C}$ are expected to be seen for a bare fibre with wavelengths of 830nm and 1300nm respectively (Rao, 1997). This means that there is no constant temperature sensitivity value for FBGs, and the sensitivity value depends on the host body and the wavelength used to write the FBGs.

Strain sensitivity of FBGs varies between 0.001204nm/ μE and 0.001221nm/ μE , which is in close agreement with the 0.0012nm/ μE suggested by Rao (1997) for the wavelength of 1550nm. Using strain sensitivity values, a temperature-compensated shift in the wavelength is multiplied by coefficients of 830.56 $\mu\text{E}/\text{nm}$, 827.81 $\mu\text{E}/\text{nm}$, 824.40 $\mu\text{E}/\text{nm}$, 821.69 $\mu\text{E}/\text{nm}$ and 819.00 $\mu\text{E}/\text{nm}$ at the

SP1 to SP5 levels respectively. It is seen that, with an approximately 5nm difference between FBGs' wavelengths at each level, a difference of up to 1.4% exists between strain sensitivities at SP1 and SP5. Similar to the temperature sensitivity coefficients, the strain sensitivity coefficient is also a function of the wavelength whereas, for lower wavelength values such as 830nm and 1300nm, the value of the strain sensitivity for a bare fibre is equal to $0.64\text{pm}/\mu\text{E}$ and $1.0\text{pm}/\mu\text{E}$ respectively (Rao, 1997). A uniaxial tensile test was performed by Lee et al. (2004) on a steel rod and it is seen that, for the wavelength of 1548.94nm, the strain sensitivity of $0.00127\text{nm}/\mu\text{E}$ is achieved (which is in close agreement with the strain sensitivities found in this study). This minor difference between strain sensitivities could also be due to the differences in the material of host body. Additionally, it is stated by Kouroussis et al. (2016) that differences in the interrogation system can also result in different strain sensitivity values.

Using the reference test S1T1, it is found that the thermal expansion coefficient of the stainless steel model pile varies between 15.79 and 17.89 ($10^{-6}\text{m}/\text{m.K}$). This means that assuming a constant value for the thermal expansion coefficient can result in considerable error in the readings. Due to the high thermal expansion coefficient of stainless steel piles, a 1°C change in temperature would cause $15.79\mu\text{E}$ to $17.89\mu\text{E}$ observed strain, which is nearly 3.75% of the maximum observed strain under thermal loading. For a stainless steel pile, the value of the thermal expansion coefficient is considered as $16.0 (10^{-6} \text{ m}/\text{m.K})$ by EN 1993-1-4:2006 (British Standards Institution, 2006), which seems to be a conservative value compared to the values given by steel manufacturers (in the range of $17.0\text{--}18.3 (10^{-6} \text{ m}/\text{m.K})$). If the recommended α value by EN 1993-1-4:2006 (British Standards Institution, 2006) is used in the analysis, a 30°C increase in temperature results in an error in determining the observed strain values in the range of $-6.3\mu\text{E}$ to $56.7\mu\text{E}$. The thermal expansion coefficient value is determined in a few studies, such as Goode et al. (2014), using the free-state condition. In other studies, such as Murphy and McCartney (2012) and Sutman et al. (2015), a constant thermal expansion coefficient is assumed along the pile length without measuring it for a specific concrete mix. It is unlikely to achieve a perfectly homogenous concrete pile, which means the assumption of a constant thermal expansion value along the pile should be avoided. Such an assumption can result in either an underprediction or an overprediction of the free-state strain, which can lead to considerable errors in the analysis.

Using FBGs, the strain caused by mechanical loading is determined in Scenarios 2, 4 and 5. In Scenario 2 tests, it is seen that the maximum strain caused by mechanical loading is only 1.33% of the maximum strain caused by thermal loading. This ratio is increased to 2.1% for Scenario 5 tests. Due to the small magnitude of strain developed under mechanical loading compared to thermal loading, it is crucial to use accurate thermo-optic and thermal expansion coefficients in Equation 4.11. Additionally, the small ratio of mechanical strain to thermal strain magnifies the importance of temperature compensation, as recommended by Farahi et al. (1990).

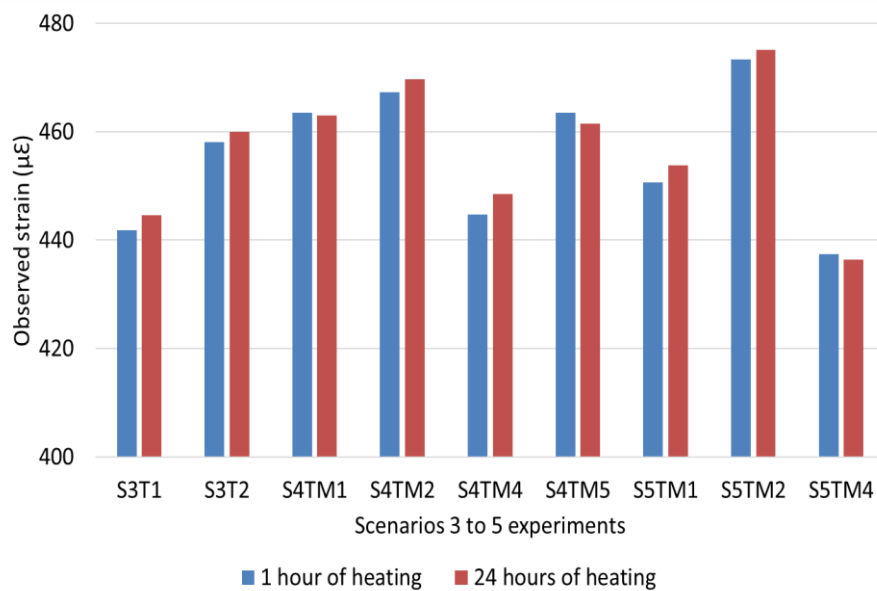
Relatively uniform strain profiles are seen along the pile surface for Scenarios 3, 4 and 5 tests. More similarity is observed among the strain profiles during the heating period compared to the observed strain profiles during the cooling period. This shows that, even without automated sampling methods – such as the raining method, the air-dried sand nozzle, pluviating air-dried sand, and the vibrating table (Paik and Salgado, 2004; Yasufuku and Hyde, 1995) – a relatively homogenous sample can be achieved by following the repeatable method described in Section 3.7.3. This results in a relatively similar friction level at the soil–pile surface at each sample that leads to a relatively uniform strain profiles. The non-uniform strain profile has been recorded by Laloui et al. (2006) and Bourne-Webb et al. (2009) during heating, where a significant difference is seen between the observed strains at different levels compared to the small differences in the strain profiles in this study. In both Laloui et al. (2006) and Bourne-Webb et al. (2009), a compound soil profile exists (see Table 2.4). This results in variations in the friction level along the pile, and it is observed that stiffer soil layers result in greater restraint levels and a higher magnitude of friction at the soil–pile interface.

Unlike Scenario 2 tests, the expected load transfer mechanism under mechanical loading is seen for Scenarios 4 and 5 tests, where the maximum strain is observed at the pile head and is then reduced towards the pile bottom. This shows the applicability of FBGs for capturing small magnitudes of mechanical strain. A uniaxial tension test is performed by Oh et al. (2000) on a steel bar with a diameter and length of 3mm and 50mm respectively. The static load test on a model pile made of steel (with a diameter and length of 30mm and 500mm) is carried out by Lee et al. (2004). When comparing load transfer profiles achieved in Scenarios 4 and 5 with Oh et al. (2000) and Lee et al. (2004) where FBGs are used, it is observed that a similar trend is achieved with maximum and minimum loads occurring at the pile head and toe respectively.

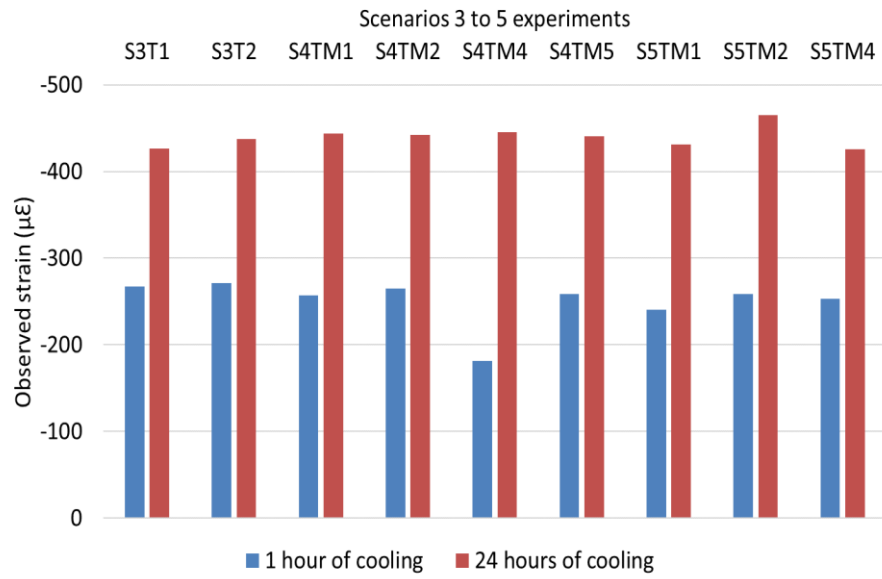
Imperfect thermo-elastic strain profiles are seen for all Scenario 4 tests, which could be mainly due to the pile temperature not returning to its original position. This means that a small magnitude of heat is kept inside the soil after each cycle. In S5TM1, in the absence of mechanical loading, perfect thermo-elastic behaviour for the model pile is not observed. This is partially due to the heat absorbed by the sand as a low-grade insulator, which does not allow the pile's heat to dissipate. Additionally, changes in the water flow rate and velocity can result in variations in the temperature. A similar observation is made for S5TM2 to S5TM4. If the minor differences observed in S5TM1 are ignored, the threshold for thermo-elastic behaviour – where strain values before and after the heating cycles are equal – can be considered as 100N, which is 31% of the ultimate pile capacity for the shaft and base resisting pile (or a safety factor of 3.22 if the load is limited to this value). For the shaft resisting pile, this threshold is reduced to 18% (30N), which results in a considerable safety factor of 5.5. For the shaft and base resisting pile, it is found by Kalantidou et al. (2012) that thermo-elastic behaviour is up to 40% of the ultimate pile capacity,

while this threshold is reported as 30% by Yavari et al. (2014). For the shaft and base resisting pile, difference between the threshold found in this study and findings in the literature can be mainly due to the differences in the magnitude of thermal loading.

The effect of the heating and cooling durations on the observed strain is investigated by comparing the observed strain values achieved at the end of the 1st and 24th hour of the heating and cooling periods (see Figure 6.2). For the cooling periods, the value of the observed strain at the end of the 24th hour of cooling is 59.51% (S3T1) to 145.66% (S4TM4) higher than the observed strain value seen at the end of the 1st hour of cooling. This shows the importance of time on the observed strain during the cooling process (see Figure 6.2-b). Unlike the cooling period, minor increases up to 0.84% are seen for the observed strain values for the 1st and 24th hour of heating (see Figure 6.2-a). This is mainly due to the quick increase in temperature in the model pile during the heating period. The stainless steel pile used in this study has a low specific heat capacity, approximately 0.5J/g-°C, compared to other materials (such as water, which has a specific heat capacity of 4.179J/g-°C). This means that it only takes 0.5J of heat to raise 1g of stainless steel by 1°C. Additionally, the heating procedure used in this study is a quick heating process, where the pile is heated up from room temperature to approximately 50°C in less than 10 minutes. The use of water inside the pile also results in a uniform and quick distribution of heat along the pile.



(a)



(b)
Figure 6-2. Comparison between the 1st and 24th hour of thermal loading: (a) heating and (b) cooling

6.3.2 Restrained strain

Restrained strain is determined for Scenarios 3 to 5 for three types of restraints: pile base support, mechanical load on the pile head, and the surrounding sand. The restrained strain is determined by subtracting the observed strain from the free-state strain. In order to correctly determine the free-state strain in each test, thermal expansion coefficients at each level along the pile are determined – between 17.98 and 15.79 (10^{-6} m/m.K) – and the values are multiplied by ΔT in each test at the end of each heating or cooling period.

In S3T1, the maximum restrained strain is seen at the SP4 and SP5 levels. In terms of the heating and cooling periods, the maximum restrained strain is seen at the end of the second heating period and the minimum restrained strain is seen during the cooling periods. This means that, in the absence of end restraints, more restriction is applied from the surrounding sand to the pile during expansion rather than contraction. In S3T2, an irregular response is seen where, during both cooling periods, more restraint is seen at the top half of the pile and, during both heating periods, more restraint is seen at the bottom half of the pile. This could be justified by considering the pile base support, which resists pile expansion.

In Scenario 4 tests, for mechanical loading up to 33% of the ultimate capacity (S4TM1 and S4TM2), the maximum restraint towards pile expansion during the first heating period is seen at the SP4 and SP5 levels. This is similar to the observation made regarding the heating periods in S3T1. When mechanical loading on the pile head is increased to 45.45% and 72.72% of the ultimate pile capacity, the maximum restrained strain is seen at the mid-depth of the pile. With a further increase to 160N (i.e. 97% of the ultimate pile capacity), the location of the maximum restrained strain moves to the SP2 level. The downward shift in the location of the maximum

restrained strain is mainly due to the larger displacements that occur under larger initial mechanical loading. An increase in the restrained strain at the SP1 level in S4TM7 and S4TM8 is the result of the pile base support that restricts the pile's downward movement. When comparing the effects of the operation mode (heating or cooling) for S4TM1–S4TM5, more restraint is seen during the cooling periods compared to the heating periods. This is mainly due to the free pile toe that can expand with no restrictions and the larger magnitudes of pile settlement under initial mechanical loading. The addition of base support in S4TM6 and S4TM7 results in higher magnitudes of restrained strain in the heating periods compared to the cooling periods.

For Scenario 5 tests, the maximum restrained strain is observed at the pile head for tests with mechanical loadings from 0% to 47% of the ultimate capacity. When mechanical loading is increased to 70% of the ultimate capacity, the maximum restrained strain is observed at the mid-depth of the pile. This means that the location of the maximum restrained strain is dependent on the magnitude of mechanical loading on the pile head. Moreover, a larger degree of restraint is applied on the pile in S5TM4 due to the larger mechanical load on the pile head. In Scenario 5 tests, the maximum restrained strain for S5TM1 and S5TM2 is seen during cooling periods, while the maximum restrained strain in S5TM3 and S5TM4 is seen during heating periods. This means that, for the shaft and base resisting pile with up to 31% of the ultimate capacity, the mechanical loading on the pile head cannot cause considerable restraint during the heating process. When the magnitude of mechanical loading is increased to 46% of the ultimate pile capacity, the effect of the pile head restraint during heating is better observed. Thus, for the shaft and base resistant model pile used in Scenario 5 tests, the applied mechanical load on the pile head needs to be at least 46% of the ultimate pile capacity to provide a sufficient level of restraint to avoid the free upward movement of the pile.

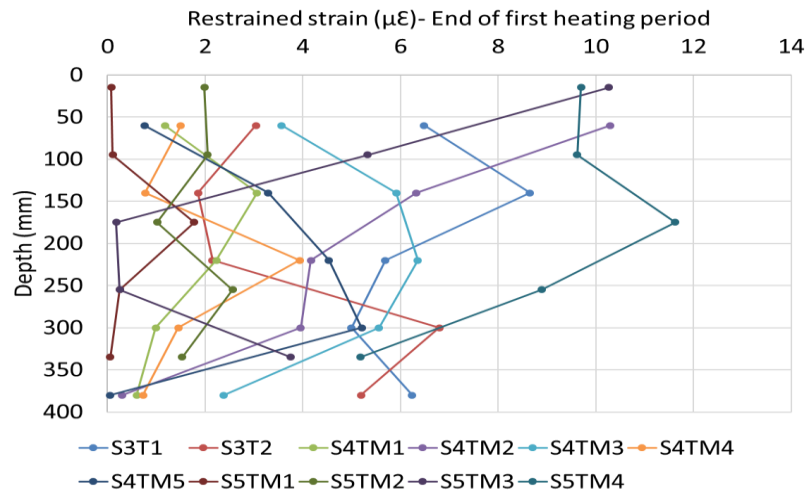
A comparison between the restrained strain profiles at the end of each heating and cooling period for Scenarios 3 to 5 are given in Figure 6.3. In Scenario 5, similar to Scenarios 3 and 4, the location of the maximum restrained strain is initially at the SP5 level and it is then shifted towards the SP3 and SP2 levels with an increase in the magnitude of mechanical loading (see Figure 6.3).

Using Figure 6.3, it is seen that, for all three scenarios, small magnitudes of restrained strain are observed, with the maximum restrained strain equal to $11.62\mu\epsilon$ in S5TM4 (which is only 2.5% of the maximum observed strain in S5TM4). Similarly, a low level of restrained strain has been observed by Goode et al. (2014) and Rotta Loria et al. (2015) for a model pile embedded in sand. In the centrifuge study done by Stewart and McCartney (2014) in unsaturated silt, the restrained strain is more depth dependent. In this centrifuge study, the maximum strain (close to the free-state strain) is seen at the pile surface and, with an increase in the pile depth, the magnitude of

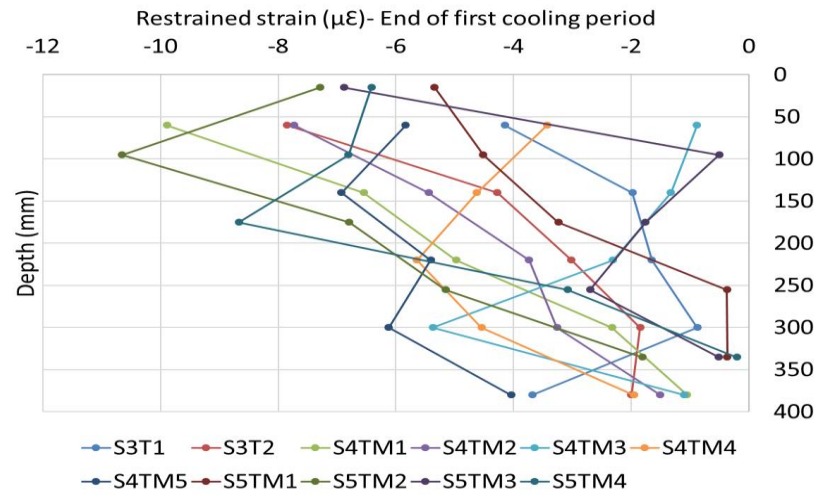
observed strain is reduced, resulting in an increase in the restrained strain and, consequently, induced thermal load and stress.

In the model pile used in this study, no overburden pressure is applied on the sand. Decreasing the void ratio by preparing a denser sand sample (with $D_r=57\%$ and mechanical loads of up to 70% of the ultimate capacity) does not provide considerable restraint to the pile. On the other hand, the roughness of the pile surface can be considered as another reason for the low level of restraint caused by the surrounding soil. A smooth pile surface is used in this study compared to the roughened concrete surfaces used in the in-situ studies by Bourne-Webb et al. (2009) and Laloui et al. (2006). The effect of the pile surface's roughness on the pile response at the soil–pile interface has been studied by Sadrekarimi et al. (2009). A shaft resisting model pile with a diameter and length of 42.5mm and 750mm is used in that study, and sandpaper with various grit sizes is used to simulate the smooth to rough surface condition for the model pile. Similar to the model pile used in this study, the non-displacement pile installation method is used, where the pile is initially placed in the container and then the container is filled with sand. It is found by Sadrekarimi et al. (2009) that, with an increase in the level of surface roughness, the interlocking effect between the pile and sand is increased. This means that the roughened surface provides extra resistance for the pile's downward movement, resulting in an increase in pile shaft capacity. More resistance from the shaft towards the downward movement means an increase in the magnitude of the restrained strain. Due to the presence of a smooth pile surface, the reverse holds true for Scenarios 3 to 5, resulting in a low level of soil–pile interlocking at the soil–pile interface and, consequently, smaller restrained strain values.

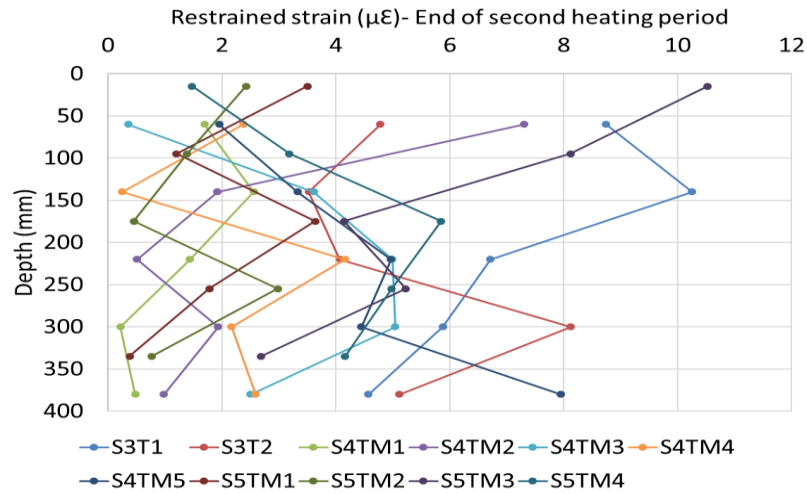
It is seen that a decrease in the sandpaper grit number (i.e. an increase in the average abrasive particle size) from 1000 to 40 results in an increase in the unit shaft resistance and, consequently, an increase in the level of resistance caused by sand. In Scenarios 3 to 5, fine sand is used with $D_{50} = 0.18mm$, which categorises the sand used in this study as fine sand. It is also stated by Sadrekarimi et al. (2009) that an increase in the interlocking power between the pile and the sand results in an increase in the lateral earth pressure and interface friction angle. This is mainly due to an increase in the sand's tendency to dilate when in contact with a roughened pile surface. The findings by Sadrekarimi et al. (2009) can also be used to justify the considerable difference observed in the load-bearing capacities of two type of piles used in this study. Similar observations regarding the effect of the pile surface's roughness on the bearing capacity of the pile and lateral earth pressure is made by Tehrani et al. (2016) with a relatively similar test set-up as Sadrekarimi et al. (2009).



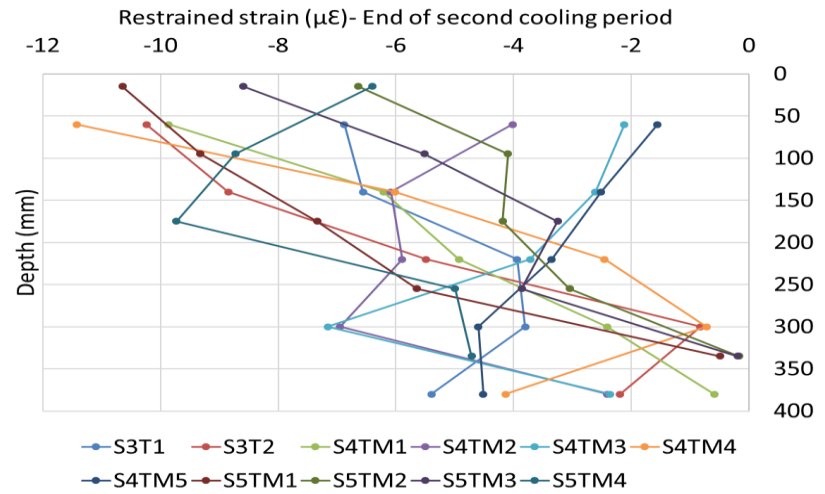
(a)



(b)



(c)



(d)

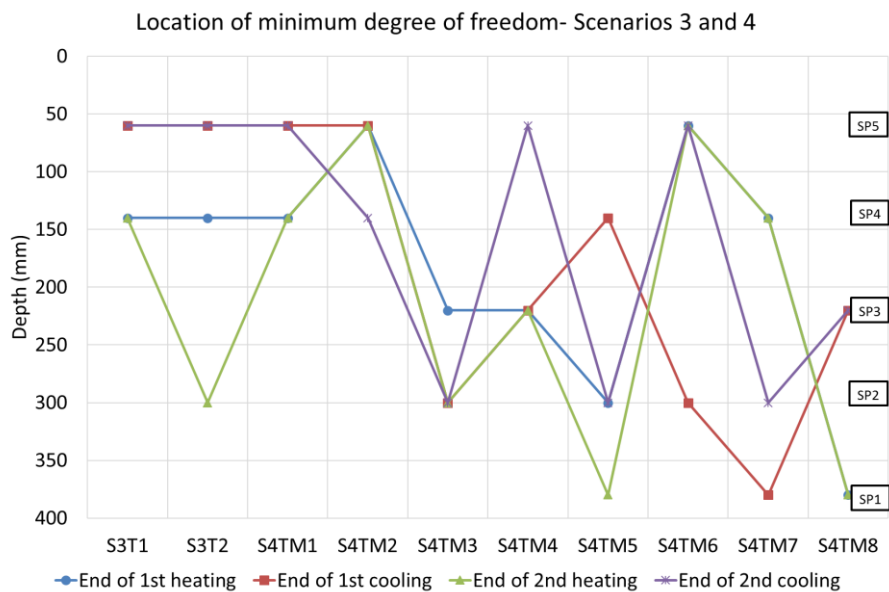
Figure 6-3. Comparison between restrained strain profiles at the end of each heating and cooling period – Scenarios 3 to 5

6.4 Degree of freedom

DoF is the common term used to quantify the restrained strain caused by the surrounding soil, structural weight and the base support. The value of the DoF ranges between 0.97 and 1 in all the tests of Scenarios 3 to 5. It shows that the amount of restraint opposed by the sand bed and mechanical loading is rather limited. In the finite element model developed by Rotta Loria et al. (2015), the average value of the DoF along the pile length is equal to 0.91, 0.94 and 0.96 for three temperature variations of 7°C, 12°C and 18°C respectively for piles embedded in dry sand with $D_r = 60\%$ (similar to this study). This is unlike findings by Mimouni and Laloui (2015), which state that, for the free-head condition, the DoF decreases from 0.82 at the pile head to 0.14 at the 0.85 of the pile depth, followed by an increase to 0.72 at the pile base. Similarly, in the numerical study done by Knellwolf et al. (2011), it is seen that, for the free-head condition, the DoF is reduced from 0.82 at the pile head to 0.14 at a depth of 24m and it is then increased to 0.72 at the pile base. Many of the smaller values of the DoF seen in Mimouni and Laloui (2015) and Knellwolf et al. (2011) are mainly due to the use of a roughened pile surface, stiffer soil and a stiffer base compared to the laboratory model. It is also stated by Bourne-Webb et al. (2013) that the value of the DoF is mainly dependent on the soil's resistance to expansion and contraction at that specific point.

The location of the minimum DoF (the maximum level of restraint) along the pile surface at the end of each heating and cooling period for Scenarios 3 to 5 is given in Figure 6.4. At the end of the first heating period, it is seen that the minimum DoF is located at the SP4 level for S3T1, S3T2 and S4TM1. With an increase in the magnitude of mechanical loading on the pile, the location where the minimum DoF is observed shifts towards SP2 (i.e. the lower half of the pile). At the end of the first cooling period, the location of the minimum DoF is consistently observed at the SP5 level for S3T1, S3T2, S4TM1 and S4TM2, with the mechanical load on the pile head being up to 33% of the ultimate pile capacity. Beyond this point, the location of the minimum DoF changes in each test. In the second heating period, the location of the minimum DoF in 7 out of 10 tests remains similar to the first cycle. In the second cooling period, relatively similar behaviour is seen as in the first cooling period (see Figure 6.4). For Scenario 5 tests, the location of the minimum DoF changes in each period and for each test. In S5TM4, where the maximum restraint is applied on the pile head, the location of the minimum DoF is seen at the SP3 level for both heating and cooling periods during two cycles. As mentioned in Chapter 2, the null point is defined as the point where zero thermal displacement is observed; this is due to the high level of restraint at that point. It is stated by Murphy et al. (2014) that the location of the null point depends on the level of restraint imposed by the top and the bottom supports, the restraint caused by the soil (depending on the soil stiffness) and the distribution of shear resistance on the soil–pile interface. In Figures 6.3 and 6.4, it can be seen that the location of the null point shifts during

each heating and cooling period, and it can differ in each test based on the level of restraint caused by the surrounding soil and the applied mechanical load. Unlike the findings of Bourne-Webb et al. (2013), it seems that it is not possible to estimate an exact location for a null point in the pile set-up. Shifts in the location of the null point are more apparent in the shaft resisting pile due to the larger displacements observed at each period. Using in-situ and centrifuge tests, it is found by Ng et al. (2015), Laloui et al. (2006), Murphy and McCartney (2012) and Goode et al. (2014) that the location of the null point changes during each cycle. According to Ng et al. (2015), differences in the location of the null point – compared to Bourne-Webb et al. (2013) – are mainly due to the assumption of a uniform temperature profile and shaft resistance along the pile. For a thermal pile designer, the knowledge of the location of the null point under specific loading, end-bearing and soil conditions helps determine where the maximum induced load and stress can be expected. Based on the literature findings presented above, as well as the findings of this study, it seems that predicting the exact location of the null point depends on the specific soil and pile conditions in each test. Moreover, parameters such as the magnitude of thermal loading, duration of thermal loading and the thermal pile operational mode can affect the prediction.



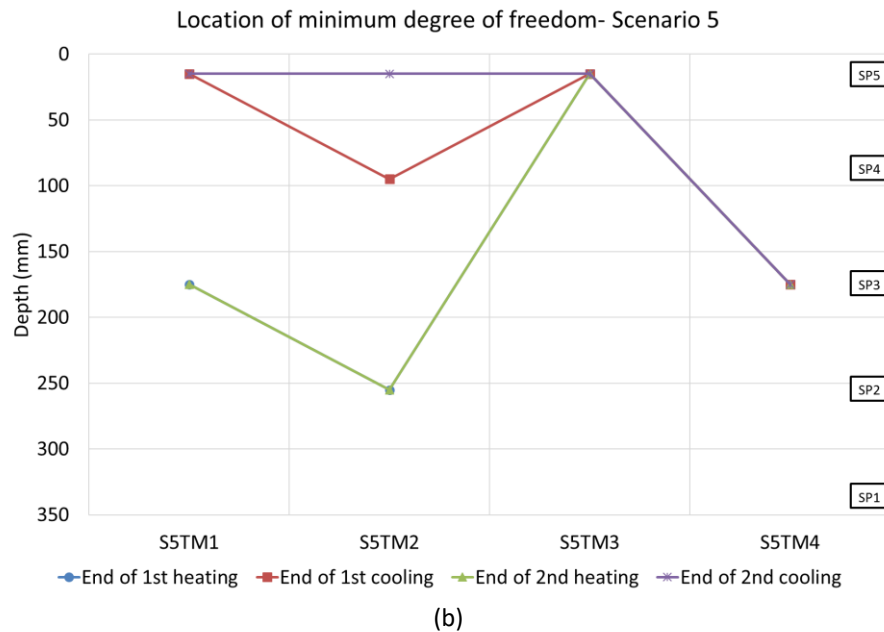


Figure 6-4. Location of the minimum DoF – (a) Scenarios 3 and 4 and (b) Scenario 5

6.5 Thermally induced axial load and stress in the pile

For the design of a shaft and base resisting pile, it is assumed that the maximum and the minimum loads are carried by the pile head and toe respectively, unless a stiff base exists beneath the soil (resulting in a base resisting pile). This assumption does not seem to be applicable for thermal piles, as the pile toe could carry a load as large as the pile head or the mid-depth of the pile, or even a larger load. The magnitude of thermal load at each depth along the pile depends on the restraint level at that depth and the magnitude of temperature changes. In Scenario 3, the maximum load carried at the SP1 level is equal to 155N, which is 61% of the maximum induced thermal load on the pile (see Figure 6.5). In Scenario 4 tests, the maximum induced load applied on the pile toe is equal to 198N, which is 68.4% of the maximum induced thermal load on the pile. In Scenario 5, this value is reduced to 129N (seen in S5TM4), which is 44% of the maximum induced load caused by thermal loading. This means that the maximum induced thermal load at the SP1 level for the shaft resisting pile is 1.53 times the same for the shaft and base resisting pile. For various soil conditions, considerable induced load is seen at the pile toe (Stewart and McCartney, 2014; Goode et al., 2014; Laloui et al., 2006; Sutman et al., 2015).

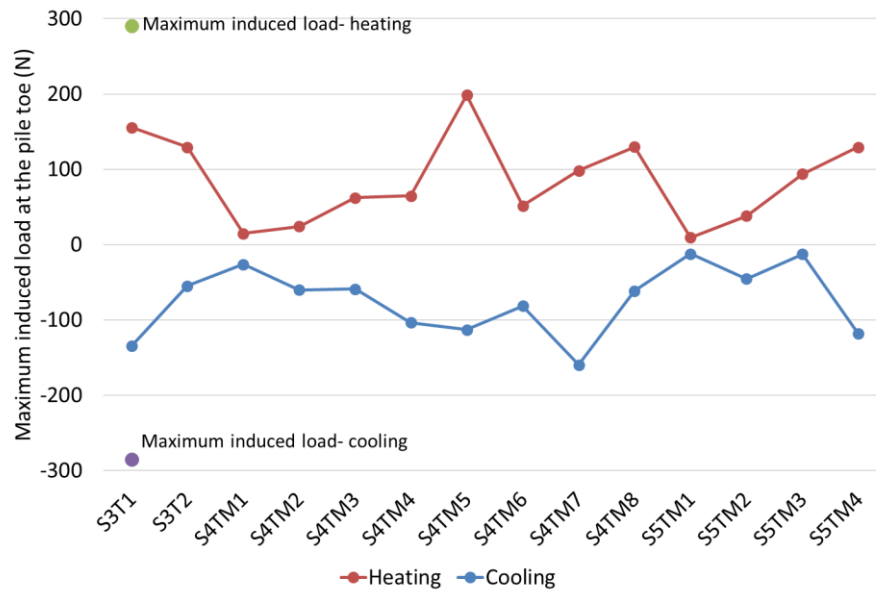


Figure 6-5. Maximum induced thermal load at the pile toe compared to the maximum induced load along the pile during the two heating-cooling cycles

The maximum induced thermal load in Scenarios 3, 4 and 5 are equal to 256N, 285N and 290N respectively (see Figure 6.6). For Scenarios 3 and 4, the maximum induced load is 1.55 and 1.72 times the ultimate shaft capacity, while in Scenario 5, the maximum induced load is 0.9 times the ultimate capacity of the pile at 320N. The maximum induced thermal load is 2 and 1.7 times the structural weight applied on the pile head in Laloui et al. (2006) and Bourne-Webb et al. (2009) respectively. The greater ratios achieved for these two in-situ studies are mainly due to the existence of a stiff soil layer beneath the pile, as well as a larger degree of restraint caused by the surrounding soil and mechanical loading on the pile head. The location of the maximum induced axial load caused by thermal loading depends on the stiffness of the soil and the level of friction between the pile and soil. As shown in Figure 6.6, the location of the maximum induced thermal load varies in each test and each thermal loading period. In Scenario 3 tests, it is seen that the location of the maximum axial load is at the SP5 level during the cooling periods. It remains at the SP5 level in S3T2, S4TM1 and S4TM2, which carry up to 33% of the ultimate pile capacity. With an increase in the magnitude of mechanical loading, less predictability in the location of the maximum induced thermal load is mainly observed in the shaft resistant pile. This could be mainly due to the considerable initial settlement under initial mechanical loading before applying the heating-cooling cycles. In S5TM1 and S5TM2, more induced load is seen during the cooling period compared to the heating period. This means that the heating period behaves as recovery for the cooling period. The effect of the magnitude of mechanical loading on the induced thermal load can be observed in Scenario 5 test because they have not experienced a pile displacement as large as S4TM3-S4TM5 tests in Scenario 4. In S5TM3, where the mechanical load equal to 46% of the ultimate pile capacity is applied on the pile, more restriction is seen for pile expansion and

contraction. This is then followed by shifting the location of maximum induced thermal load to SP3 in S5TM4. In a 1g physical model study done by Yavari et al. (2014), for the model pile embedded in dry sand with $D_r = 50\%$ and $D_{50} = 0.23\text{mm}$, it is seen that the magnitude of mechanical loading applied on the pile during the cooling period is higher than the induced load during the heating period. This is in agreement with the observations made for S5TM1 and S5TM2.

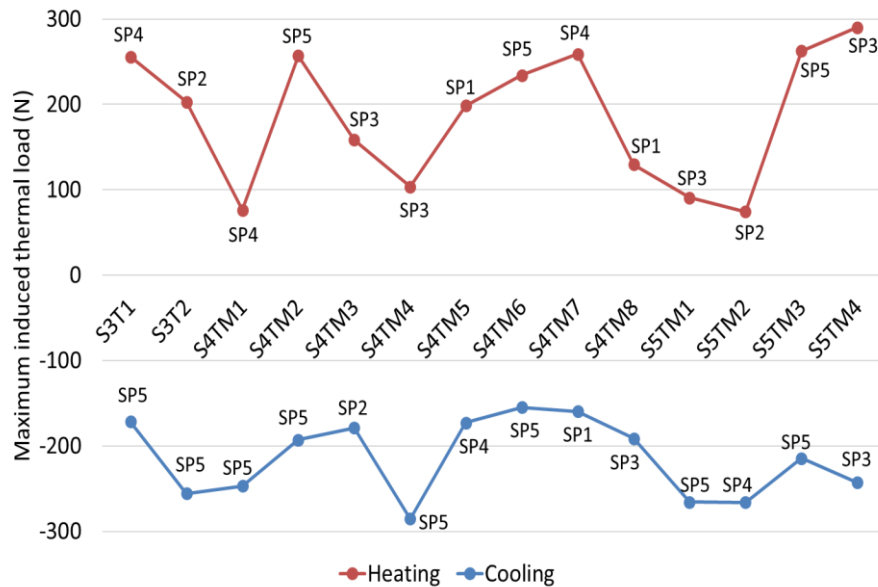


Figure 6-6. The location and magnitude of the maximum induced thermal load during the two cycles of heating and cooling

The maximum induced stresses in Scenarios 3 to 5 are equal to 2.05MPa, 2.29MPa and 2.32MPa, which are only 3.26%, 3.63% and 3.69% of the maximum allowable induced stress in the model pile (see Figure 6.7). The magnitude of induced stress caused by thermal loading should be in the range specified by BS 8004:1986 (British Standards Institution, 1986). In this study, due to the use of stainless steel, the allowable compressive strength for the pile material needs to be below 30% of yield stress, which is 63MPa. The maximum induced stress in Scenarios 3 to 5 is only 3.69% of the allowable stress, which is mainly due to the high compressive strength of stainless steel at 210MPa. For in-situ installations, the maximum allowable stress in the concrete is equal to 25% of the 28-day concrete cube compression strength at 30MPa. For instance, Bourne-Webb et al. (2009) observes that the stress ratio in the pile increases from 0.14 for mechanical-only loading to 0.24 after the heating period, which is close to the 0.25 limit given by BS 8004:1986 (British Standards Institution, 1986). Higher magnitudes of temperature changes in Bourne-Webb et al. (2009) or the presence of stiffer soil could result in crossing the safety limit given by BS 8004:1986 (British Standards Institution, 1986). The closeness of the maximum induced stress after thermal loading to the threshold given by BS 8004:1986 (British Standards Institution, 1986) shows the importance of considering the increased induced stress caused by thermal loading in

pile design. The maximum stress caused by thermal loading is seen in S5TM4 and is 1.17 times larger than the axial stress caused by 225N of mechanical loading in S5TM4.

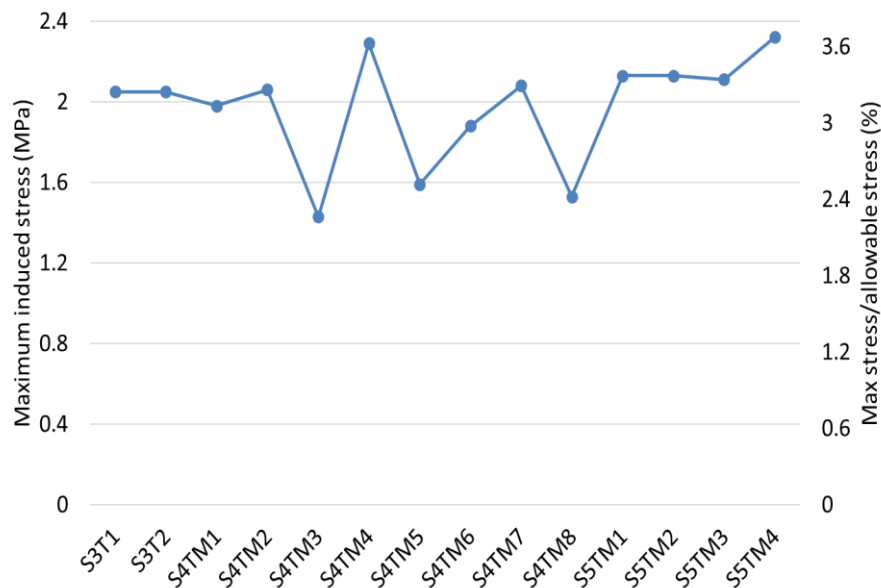


Figure 6-7. Rate of induced stress per degree change in temperature vs maximum induced stress over allowable stress – Scenarios 3 to 5

The ratio of maximum induced stress per degree change in temperature for the cooling and heating periods is shown in Figure 6.8. This ratio is achieved by dividing the maximum induced stress at the end of each heating and cooling period by the ΔT observed at that level. The maximum is 85.27kPa/°C and 78.97kPa/°C for the heating and cooling periods respectively. In Scenario 5, for mechanical loadings beyond 31% of the ultimate pile capacity, the ratio of induced stress increases from 20.56kPa/°C in S5TM2 to 75.54kPa/°C and 85.27kPa/°C in S5TM3 and S5TM4 respectively. A comparison between the literature and results found in this study for induced stress per degree change in temperature is presented in Figure 6.8. It shows that, during the heating period, the values range from 104kPa/°C (Laloui et al., 2003; 2006) to 329kPa/°C (Bourne-Webb et al., 2009). Differences in the values given in the literature are mainly due to the different levels of restraints. In this study, a much lower level of restraint exists compared to the studies given in Table 2.4, but the high elastic modulus of the pile and higher ΔT values have resulted in values not far from the low range of the in-situ installations (104kPa/°C) given in Table 2.4.

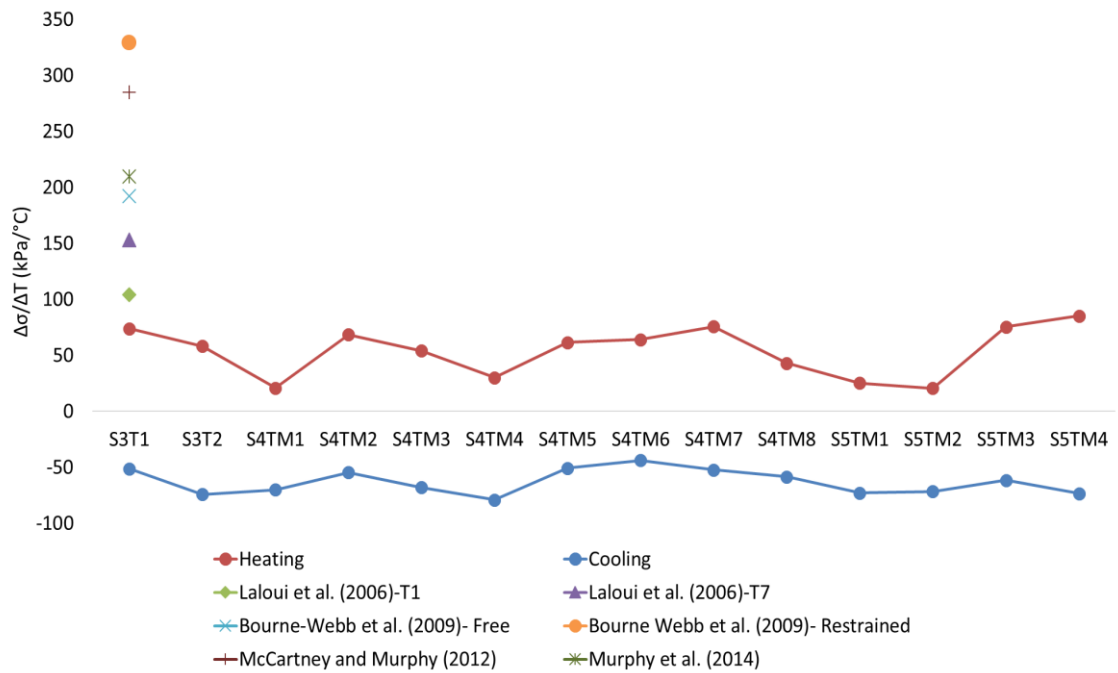


Figure 6-8. The rate of induced stress per degree change in temperature during the heating and cooling periods – Comparison between the results from Scenarios 3 to 5 and the literature

Table 6-2. Maximum induced stress per degree change in temperature (kPa/°C) – Scenarios 3 to 5

	$\Delta\sigma/\Delta T$ (kPa/°C)		Maximum induced axial load at the end of two heating-cooling periods (N)				$\sigma_{Max.}$ (MPa)	$\sigma_{Max.}/$ $\sigma_{Allowable}$ (%)
	Heating	Cooling	Heating	Location	Cooling	Location	Heating & cooling	
S3T1	74	-51.19	255.98	SP4	-171.77	SP5	2.05	3.26
S3T2	58.28	-74.10	202.88	SP2	-255.59	SP5	2.05	3.25
S4TM1	20.84	-69.91	76.31	SP4	-246.91	SP5	1.98	3.14
S4TM2	68.62	-54.53	257.07	SP5	-192.97	SP5	2.06	3.27
S4TM3	54.08	-68.04	158.66	SP3	-178.66	SP2	1.43	2.27
S4TM4	30.15	-78.97	103.74	SP3	-285.30	SP5	2.29	3.63
S4TM5	61.46	-50.70	198.48	SP1	-172.85	SP4	1.59	2.52
S4TM6	64.04	-43.68	234.16	SP5	-154.85	SP5	1.88	2.98
S4TM7	75.68	-52.21	259.21	SP4	-159.46	SP1	2.08	3.30
S4TM8	42.94	-58.36	129.80	SP1	-191.11	SP3	1.53	2.43
S5TM1	25.21	-72.90	90.82	SP3	-265.85	SP5	2.13	3.38
S5TM2	20.56	-71.47	74.35	SP2	-265.97	SP4	2.13	3.38
S5TM3	75.54	-61.43	262.78	SP5	-214.52	SP5	2.11	3.34
S5TM4	85.27	-73.34	290.15	SP3	-242.95	SP3	2.32	3.69

6.6 Pile head displacement

Due to the high stiffness of the model pile, the pile can be assumed as incompressible. For Scenario 5, the maximum pile compression under 320N is equal to 0.0044mm determined using Equation 2.10 and by considering the elastic response of the pile. In Scenarios 3 and 4, this value is equal to 0.0025mm under 165N of mechanical loading. Values obtained for both types of piles

are negligible compared to the values achieved for pile displacement under mechanical, thermal and thermo-mechanical loading. This means that the measured pile head displacement in Scenarios 3 to 5 represents the pile toe displacement, and the compression of the pile can be ignored. A similar observation is made by Kalantidou et al. (2012) despite having a model pile with an even lower stiffness.

Irreversible settlements are seen in S3T1, S4TM1–S4TM5 and Scenario 5 tests (see Figure 6.9). Normalised pile head displacements with regard to the pile diameter for S3T1, S4TM1–S4TM3 and S5TM1–S5TM4 are shown in Figure 6.9-a. For the shaft and base resistant piles, it is observed that the maximum pile head settlement (seen in S5TM4) is approximately 6% of the pile diameter, which is below the maximum allowable settlement of 10% of the pile diameter. It is also seen in Figure 6.9-a that, with an increase in the magnitude of mechanical loading, the normalised pile head displacement increases. It is also observed that two heating-cooling cycles result in an increase in the ratio of normalised pile head displacement. For instance, in S5TM4, the ratio of the settlement over the pile diameter is approximately 4% at the end of mechanical loading, but it has increased to 5.95% after two heating-cooling cycles, which is approximately 1.5 times the normalised settlement observed at the end of mechanical loading under a mechanical load equivalent to 70% of the ultimate pile capacity. For the shaft resisting piles, the minimum normalised settlement is observed in S3T1 (where no mechanical load exists) and is equal to 0.42%, which is slightly greater than the 0.41% in S5TM1 for the shaft and base resisting pile (see Figure 6.9-a). This means that, in the absence of mechanical loading on the pile head, approximately similar behaviour is observed for both types of piles after two heating-cooling cycles. For the shaft resisting piles, it is observed that an increase in the magnitude of mechanical loading results in an increase in the magnitude of normalised pile head displacement. In S4TM2, where mechanical loading on the pile head is equal to approximately one-third of the ultimate pile capacity, normalised pile head displacement for the shaft resisting pile is 2.75%. This is 1.14 times the normalised pile head displacement for the shaft and base resisting pile with similar loading conditions (S5TM2). Thus, if the magnitude of mechanical loading on the pile head remains equal to or below the working limit state, the ratio of normalised pile settlement between these two types of piles ranges between 1 and 1.15.

For applied mechanical loading equivalent to approximately 70% of the ultimate pile capacity, the maximum normalised pile head displacement reaches 5.95% for S5TM4, while failure occurs in the second cooling period for S4TM4 (see Figure 6.9-a). This shows the significant effect of second cyclic loading on the shaft resisting pile (compared to the shaft and base resisting pile) when a large magnitude of mechanical loading is applied on the pile head. Similar observations are made when the normalised pile head displacement over the pile length is compared for these two types of piles (see Figure 6.9-b).

The maximum allowable pile head settlement is equal to 10% of the pile diameter for the shaft and base resisting pile. In all Scenario 5 tests, magnitude of pile head displacement remains below the allowable 10% limit, with the maximum settlement at approximately 6% for S5TM4. Despite remaining in the allowable limit, only 40% of the total settlement is recovered in S5TM2 to S5TM4 tests, which means that cumulative irreversible settlement happens during the heating-cooling cycles. A similar observation is made by Yavari et al. (2014), where irreversible settlements are seen under thermo-mechanical loading.

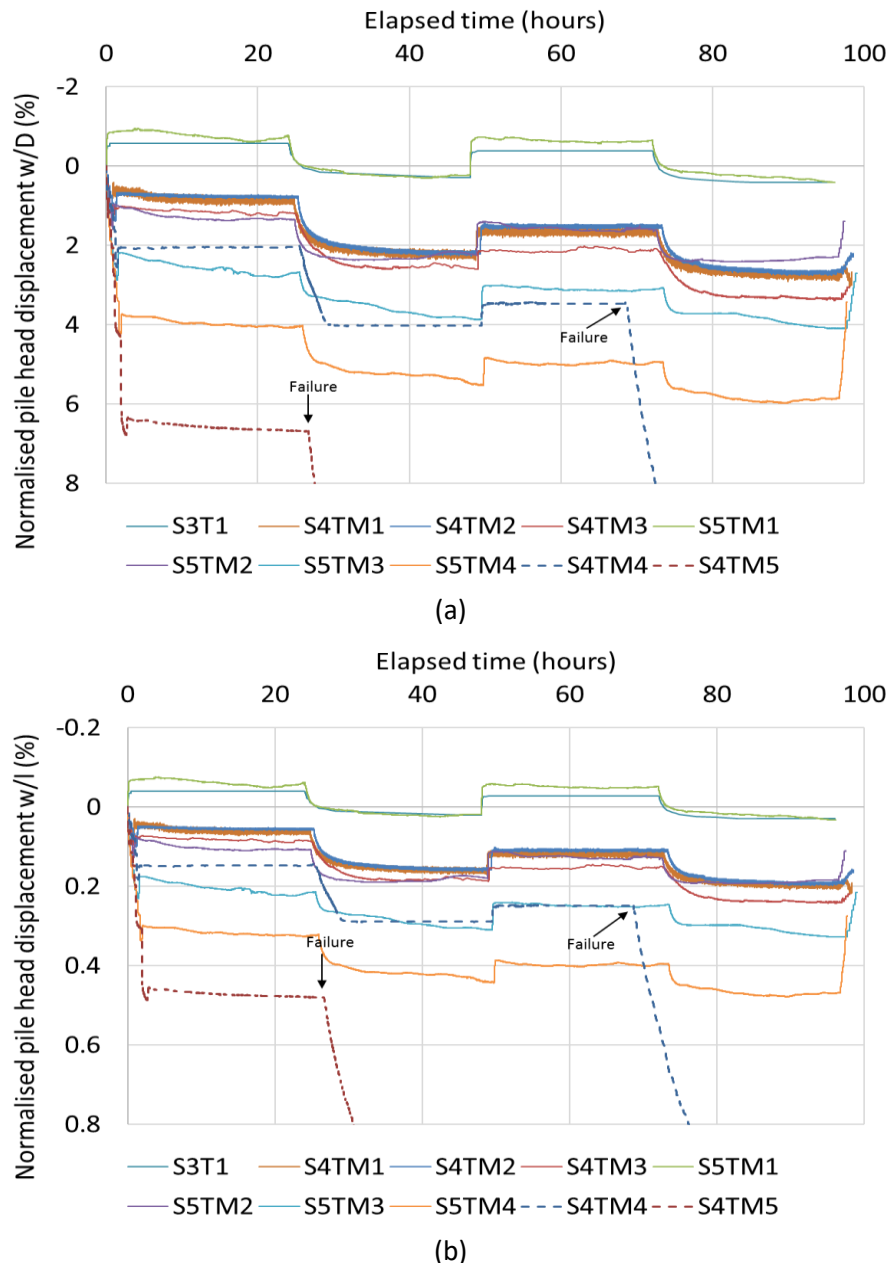


Figure 6-9. Normalised pile head displacement – Scenarios 3 to 5

The rate of pile settlement and heave per degree change in temperature is shown in Figure 6.10. Values given for S4TM4 are only for the first cycle, as failure is observed in the second cycle.

For the shaft and base resistant pile, increase in the magnitude of mechanical loading results in an increase and decrease in the rate of pile settlement and heave respectively. Similar behaviour is observed for the rate of pile heave in the shaft resistant pile, while the settlement rate does not follow this trend in all five tests. For the shaft resisting pile, the maximum rate of pile settlement ranges between 0.009–0.018mm/°C compared to 0.011–0.017mm/°C for the shaft and base resisting pile. For in-situ installations, the maximum ratio of pile settlement over temperature change ranges between 0.10–0.16mm/°C (Di Donna and Laloui, 2014), which is approximately 10 times greater than the values achieved for the base and shaft resistant piles. Soil properties are crucial in determining the rate of pile settlement. Thus, by multiplying the rate of pile settlement achieved in this study by 10, an approximate pile settlement rate for in-situ installations with soil similar to those mentioned by Di Donna and Laloui (2014) can be achieved.

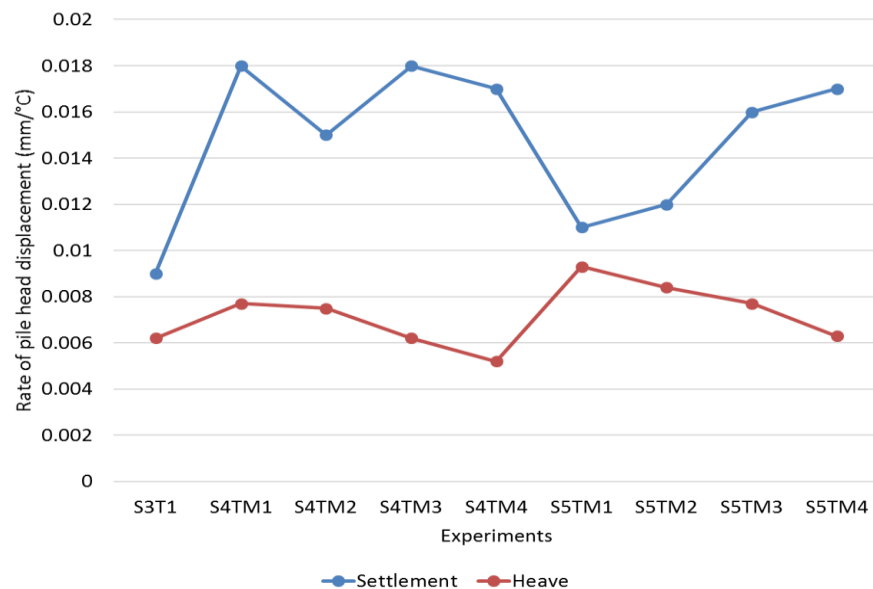


Figure 6-10. Rate of pile head displacement – Scenarios 3 to 5

In S4TM1–S4TM3 (where mechanical loadings below the 50% ultimate shaft resistance are applied), the ratios of the settlement at the end of the two cycles to the settlement before any thermal loading are 2.63, 1.98 and 2.51 respectively. For the shaft resisting pile, the magnitudes of settlement after the two heating-cooling cycles are equivalent to the settlement under a mechanical load of 120–130N for all three tests. In S4TM4 and S4TM5, failure is observed during the second cooling period. In Scenario 5, for initial mechanical loading (up to 50% of the ultimate capacity of the pile), the cumulative settlement after two heating-cooling cycles is equivalent to the settlement caused by an additional 50N of mechanical loading. This value is reduced to 30–40N when the magnitude of initial mechanical loading is increased to 70% of the ultimate pile capacity. The reduction in the equivalent load in S5TM4 is mainly due to the larger settlement seen under the initial mechanical loading of 225N. This is equivalent to the reduction of the safety

factor in S5TM2 to S5TM4 from 3.2, 2.13 and 1.42 to 2.13, 1.6 and 1.28 respectively (see Figure 6.11). In S5TM4, it is seen that the safety factor reaches close to 1, which shows the significant impact of thermal cycles when there is a large magnitude of mechanical loading (70% of the ultimate pile capacity) on the pile head. In the shaft resisting pile, it is observed that the safety factor is reduced from 5.5, 3 and 2.2 for S4TM1 to S4TM3 respectively to approximately 1.3 for all three tests (see Figure 6.11). A larger magnitude of reduction in the safety factor is seen in the shaft resisting pile, mainly due to the larger amount of displacement and the lower ultimate capacity.

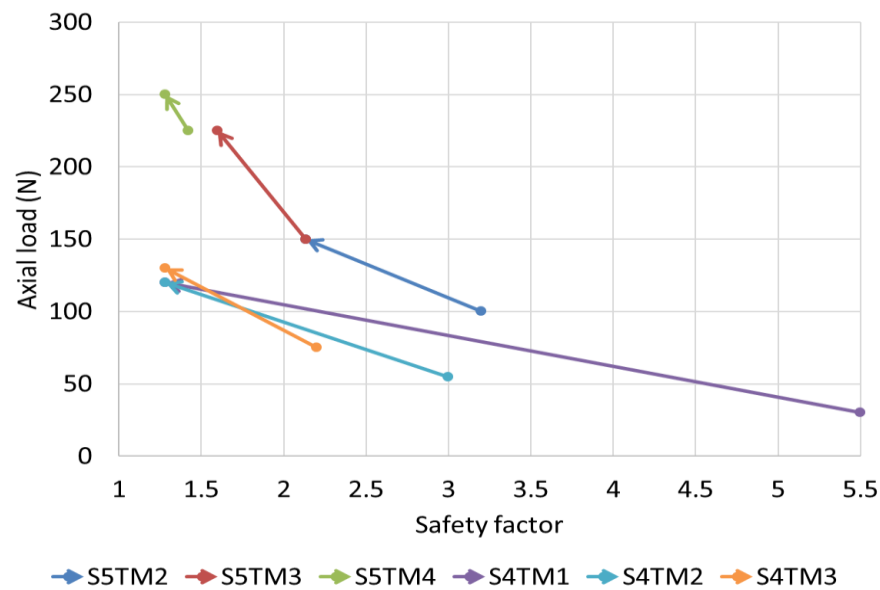


Figure 6-11. Changes in the safety factor due to two heating-cooling cycles – Scenarios 4 and 5

A comparison between normalised pile displacement and the findings in the literature is presented in Figure 6.12. The minimum and the maximum normalised pile settlements are observed in S5TM1 and S4TM5 respectively. For in-situ installations, maximum settlement is observed by Sutman et al. (2015), which is mainly due to the lower level of support offered by the sandy soil used in their study. Moreover, Sutman et al. (2015) use a smaller pile, which helps to further increase the pile settlement compared to other installations. The main reason for the small normalised settlement in Laloui et al. (2006) and Bourne-Webb et al. (2009) is the much lower DoF in these two studies, resulting in more friction at the soil–pile interface. Results found in this study are more directly comparable with the results found by Yavari et al. (2014) and Kalantidou et al. (2012). This is mainly due to the use of medium-dense sand in these studies. The maximum rate of pile settlement found by Kalantidou et al. (2012) is equal to 6.5 for the mechanical loading of 95% of the ultimate pile capacity for the shaft and base resisting pile. In S4TM5, where the failure occurs under the mechanical loading of 96% of the ultimate pile capacity, rate of pile head displacement before the failure is 6.78. Comparing the rate of pile head displacement in this study

with the in-situ installations, it is found that the laboratory results for the thermal-only condition approximately represent the level of restraint caused by mechanical loading on the pile head and the surrounding soil in Laloui et al. (2006) and Bourne-Webb et al. (2009).

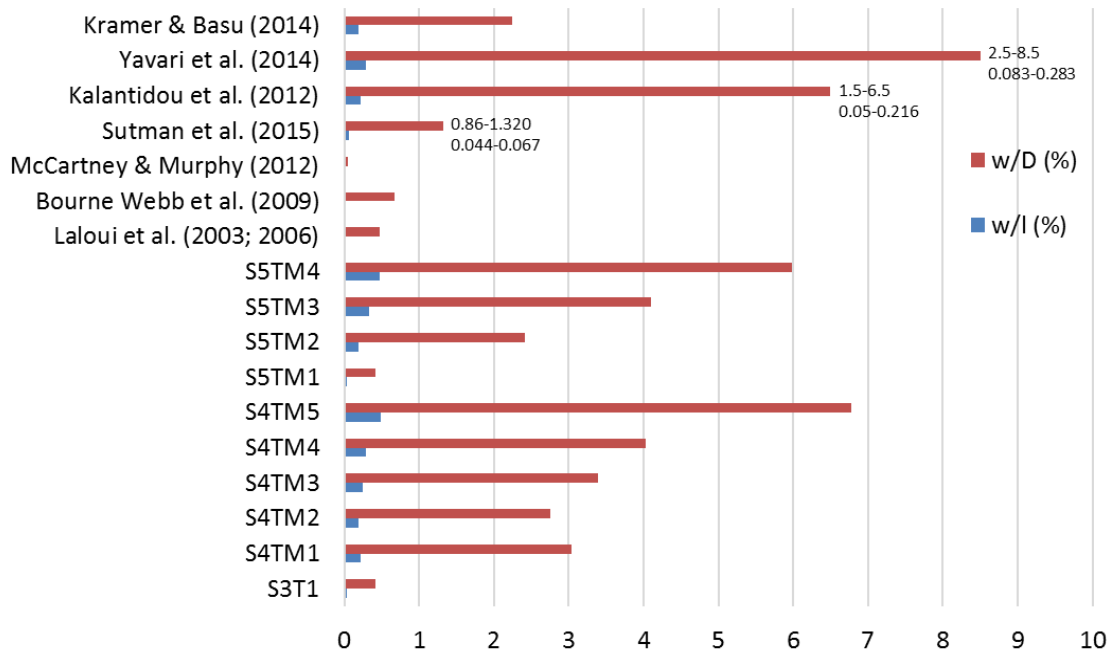


Figure 6-12. Normalised pile head displacement – Comparison between Scenarios 3 to 5 with the literature

6.7 Mobilised friction at the soil–pile interface

6.7.1 Observed response

It is observed for both types of piles that, with an increase in the magnitude of mechanical loading, the mobilised friction increases. The maximum mobilised friction for the shaft resisting pile under mechanical-only loading is equal to 11.78kPa (seen at S4TM4 with 120N on the pile head). The maximum mobilised friction under thermal-only loading for the shaft resistant pile is seen at S3T1 equal to 9.11kPa, which is 77% of the maximum friction mobilised under the mechanical loading of 160N. The maximum mobilised friction under thermo-mechanical loading for the shaft resistant pile (S4TM1–S4TM5) is equal to 17.47kPa, which is 1.48 times the maximum ultimate mobilised friction caused by mechanical loading for the shaft resistant pile. For the shaft and base resisting pile, the maximum mobilised friction under mechanical loading is equal to 14.15kPa. The maximum mobilised friction under thermo-mechanical loading for Scenario 5 tests is seen at the end of the first heating period in S5MT3 and is equal to 18.68kPa, which is 1.32 times the maximum mobilised friction under the mechanical loading of 320N (seen in S5TM4).

Different mobilised friction responses are seen in the literature for thermal piles under heating-only and piles under heating-cooling cycles. It is found by McCartney and Rosenberg (2011) that heating increases pile friction by 40% compared to the mobilised friction under mechanical

loading. It is believed that the differential expansion of the foundation and the surrounding soil due to the relative movement of the pile and soil could be the main reason. A reverse process is observed when the pile is under a heating-cooling cycle (as opposed to a single-mode heating period). Heating results in an increase in the lateral stress and friction between the soil and pile, and contraction results in the reduction of pile volume, lateral stress and a reduction in side friction is expected (McCartney and Rosenberg, 2011). For heating-cooling cycles, it is stated by McCartney and Rosenberg (2011) that the cumulative decrease in side friction could happen at the soil–pile interface if the friction at the soil–pile interface does not return to its initial value before thermal loading. Using the load settlement figures discussed in Section 6.6, this behaviour is clearly observed alongside cumulative settlements, with failure occurring in the second cooling period of S4TM4 and S4TM5.

In all Scenario 5 tests, it is seen that the mobilised friction increases at the end of the first heating period in three zones, and there is negative friction in one zone. At the end of the second heating period, the mobilised friction increases in all four zones compared to the previous cooling period. It is then followed by a decrease in all four zones in all four tests at the end of the second cooling period, except in Zones 1 and 2 in S5TM4. According to Mimouni (2014), heating the pile results in an increase in the mobilised friction at the pile head (Zone 4) due to heaving. At the upper half of the pile (Zone 3), decrease in the mobilised friction is expected due to the upward movement of the pile, which can lead to negative skin friction. Mobilised friction is expected to increase at the lower half of the pile (Zones 1 and 2) due to the downward displacement of the pile, and ultimate friction is achievable depending on the magnitude of thermal loading. Additionally, an increase in the mobilised base resistance is expected due to the downward movement of the base. A reverse procedure is expected to be seen during the cooling period. It is also stated by Murphy et al. (2014) that, during the heating period, an increase in the magnitude of mobilised friction is expected due to the radial expansion of the pile, resulting in an increase in the contact surface between the pile and the soil. In another study, done by Tang et al. (2013), the maximum mobilised friction under mechanical loading is seen at the bottom of the pile. The addition of heating-cooling cycles has entirely changed the mobilised friction profile, and the direction of the mobilised friction at the upper half of the pile is reversed in Tang et al. (2013). In the laboratory study done by Yavari et al. (2014) on a model thermal pile in sand, irregular behaviour is observed where mobilised friction is increased and decreased due to heating and cooling respectively in only one zone.

6.7.2 Sand–pile interface

The irreversibility of pile displacement in the absence of mechanical loading for the shaft resisting pile could be due to the inability of the pile to reach the initial friction level with sand. For the shaft resistant pile during the cooling process, it seems that friction is lost with pile contraction

and the friction angle cannot return to its original position, as observed by Uesugi et al. (1989) for a sand–steel surface. This can be considered an explanation for an irreversible displacement in the shaft resistant pile. It is observed in Scenario 5 tests that a lower magnitude of pile heave is observed compared to pile settlement, which means that the behaviour of the pile is thermo-plastic and irreversible settlements are seen. In order to understand sand behaviour at the pile surface, the radiography technique is used by Robinsky and Morrison (1964). The metal pile is pushed into the sand sample, which is a softer process than driving but more exaggerated than pile displacement due to heating and cooling. Both polished and roughened surfaces are tested:

- At the tip of the pile, sand particles are compacted and potentially crushed, which could improve the capacity of the pile depending on the soil–pile interface response. At the soil–pile interface adjacent to the pile wall, the drag-down effect of the pile wall on the surrounding sand is seen, with the pile’s downward movement resulting in sand displacement, the reduction of sand density and an increase in the void ratio in a thin layer of sand to accommodate sand arching. It is stated by Robinsky and Morrison (1964) that this can be the main cause for the low load transfer capacity of the shaft, which justifies the significant pile displacement in S4TM4 and S4TM5. A similar stress transfer path is adopted by Loukidis and Salgado (2008) for a pile under mechanical loading, where the stress is transferred to the lower sand layers in a conical shape (the so-called arching phenomenon). An arching load transfer can be applied for the shaft resisting pile but only at a much lower extent, due to the absence of pushing or driving the pile into the sand.
- Sand movement can result in the reduction of the angle of internal friction for a thin layer of soil in the so-called shear bond zone adjacent to the pile wall. The peak and critical angles of friction are determined as 35° and 27.8° respectively (see Section 3.5.4), but these could be reduced due to sand displacement at the soil–pile surface. This process is described by Uesugi et al. (1989) below.
- Robinsky and Morrison (1964) have shown that inconsistent variations in the sand’s relative density are seen due to compaction at the tip of the pile and sand displacement at the soil–pile interface. This produces both low and high relative density zones of 14.2% and 50%, compared to the initial relative density of 37%. Applied load on the pile head is carried by a complex pattern of arching. It is suggested that the stress level could be high at some points along the pile, but that it rapidly dissipates towards the limits of the displacement envelope.
- The degree of sand movement at the pile tip and pile wall is mainly dependent on the initial state of the sand. For medium-dense sand with $D_r = 37\%$, Robinsky and Morrison (1964) observe that sand particles are moved 4.5 to 5.5 times the pile diameter at the pile wall, while there is a lower extent of sand movement at 3 to 4.5 times the pile diameter at the pile tip.

The sand bed in this model has a higher relative density, and less movement among sand particles is expected.

- The coordination number – i.e. the average number of contacts per particle (Zhao, 2009) – is considered an important parameter to study particle movement and arrangement, as well as to understand the changes in the void ratio of the sample. It is found by O’Sullivan et al. (2004) that a decrease in the coordination number will result in a decrease in specimen strength. Generally, increase and decrease in the coordination number will result in specimen contraction and dilation respectively (Zhao, 2009). This means that higher relative density will result in a higher coordination number. When sand particles are displaced at the soil–pile interface, the formation of voids can cause a reduction in the coordination number and, consequently, soil strength is reduced. This behaviour can be used to justify the large displacements observed during S4TM4 and S4TM5. This is considered microstructure behaviour of thermal piles, and it needs to be verified using various techniques for modelling the granular materials (such as the discrete element method).

Using Figure 6.9 for Scenarios 4 and 5 (particularly for the shaft resistant pile), it can be concluded that the friction between the stainless steel pile surface and the sand is reduced with an increase in thermal loading and thermal cycles. This behaviour seems to reflect an initial sliding between the pile and sand, resulting in a reduction in friction and not returning to the original contact level between the pile and sand. It could also be considered as a degradation of skin friction after the first cycle, particularly in S4TM3–S4TM5. The findings can be compared with Uesugi et al. (1989), where the behaviour of the sand–steel interface under repeated loading is investigated using shear box tests. For a dry dense Toyoura sand with $D_{50} = 0.19$, it is seen that:

- Under two-way repeated loading, interface sliding is noticeable in the reloading stage, resulting in inelastic deformation of the shear zone under stress reversal that cannot be ignored. In contrast, in one-way cyclic loading, the sliding displacement is found to be negligible. The compaction rate used in this study is approximately 57% and a higher rate of inelastic deformation is expected. Based on the observed pile displacement, interface sliding in two-way cyclic loading seems to be applicable for this study.
- After sliding occurs at the sand–steel interface, the coefficient of friction at the restart of the sliding becomes smaller than the peak value of the previous loading. In fact, it is found that, after a few cycles, the coefficient value of friction converges towards the residual shear stress of the sand mass. The formation of the shear zone along the sand–steel interface is considered the main reason for the decrease in the upper limit of the value of the friction angle. This could also be a reason for the reduction of soil–pile friction in the second cycle in Scenarios 4 and 5.

- Uesugi et al. (1989) show that most of the inelastic deformation happens in the first three cycles and, from the fourth cycle onwards, the deformation profile becomes similar to monotonic loading. Similarly, it is stated by Polous (1989) that most of the deformation under cyclic loading is expected to be seen in the first few cycles. Reduction in the magnitude of the pile head settlement in the second cooling period (compared to the first cooling period) in S5TM2–S5TM4 is in line with these findings. Tests with more cyclic heating and cooling could justify this assumption.
- It is also stated by Chakraborty and Salgado (2010) that sand dilates with shearing, where dilation is directly related to relative density and has an inverse relationship with confining pressure. According to the findings by Robinsky and Morrison (1964) regarding inconsistent changes in the relative density of the sand sample after shearing, both an increase and a decrease in dilation are expected to be seen with the possible reduction of sand dilation in areas adjacent to the container wall. Dilation of sand particles at the sand–steel interface is also dependent on the roughness of the pile: smooth surfaces are not expected to see considerable dilation and particles are considered as sliding instead of rolling over (Lings and Dietz, 2005). A similar observation is made by Tehrani et al. (2016) for a non-displacement pile installed in sand. The shear band, formed adjacent to the pile wall, is found to have a thickness of 3.9 to 5.2 times that of medium-dense sand D_{50} for a roughened pile surface. There is no shear band next to a smoothed pile surface. It seems that the behaviour of the model pile in this study – particularly the shaft resistant pile – is closer to the sliding observed in the interaction between sand and a smooth steel surface (rather than the particles rolling over). This is mainly due to the smooth pile surface used for the model pile.
- It is stated by Suryatriyastuti et al. (2013) that the soil will not be affected by thermal volumetric variations and the ground temperature equilibrium will remain constant in two soil conditions. The first situation is where sandy soil exists and the groundwater flows away quickly. The second situation is where a significant groundwater flow exists (>35m/year). If these two cases are present, the pile will only undergo thermal variations and the analysis is limited to soil–pile interaction. Moreover, it is suggested by Poulos (1989) that the effects of sand modulus degradation are not significant and can be ignored compared to the significant impact caused by clay modulus degradation.

6.7.3 Assessing the assumption of cyclic compression-tension for thermal piles

Cyclic expansion and contraction of thermal piles under seasonal heating and cooling cycles have been considered as a two-way cyclic compression and tension response under heating and cooling periods respectively. This assumption can be assessed by comparing the results found in this study with the expected response for one-way and two-way cyclic loadings given in Section 2.3:

- In terms of the failure mechanism proposed by Poulos (1989) for a pile under cyclic mechanical loading, both mechanisms given for one-way and two-way cyclic loading are observed. These include the accumulation of settlement and the degradation of skin friction. Accumulation of settlement is observed in the shaft resistant pile and the shaft and base resistant pile, whereas skin degradation can be mainly seen in the shaft resistant pile (S4TM3–S4TM5) (see Figure 6.9).
- In addition to the two above-mentioned failure mechanisms for piles, the ‘sudden failure’ mechanism for a micropile under cyclic axial loading is observed by Lee (2004) and depends on the magnitude of cyclic loading. This response is observed in S4TM4 and S5TM5, whereas the sudden failure occurs during the cooling periods.

Based on the above-mentioned parameters for both regular piles and micropiles, the thermal pile response for a model pile under cyclic heating-cooling cycles can be considered two-way cyclic loading with the detrimental effects of both one-way and two-way cyclic loading.

6.8 Comparison with the framework

The results of Scenarios 3 to 5 are compared with the proposed framework given by Bourne-Webb et al. (2013) (and that has also been adopted by the Thermal Pile Standard (2012)). Differences and similarities are observed between the laboratory profiles and the framework profiles. In some cases, a perfect agreement is seen between the framework and the laboratory results. For the shaft and base resisting piles, comparison with the framework for the restrained strain and the mobilised friction is provided in Section 5.9. For instance, in S5TM4, where the maximum mechanical load is applied on the pile head, the maximum restrained strain is observed at the mid-depth of the pile with a reduction towards both ends. On the other hand, differences are observed in the mobilised friction profiles. In this section, restrained strain profiles for the shaft resistant pile in Scenarios 3 and 4 are compared with the framework profiles, where no base support (sand or base support) is provided. Similar to Scenario 5, differences are observed between the framework profiles and the attained profiles in this study. Part of the observed difference lies within the six assumptions made by Bourne-Webb et al. (2013) given in Section 2.2.1, which are not perfectly applicable to this study:

- Assumption 1 – The pile load will be resisted by the shaft alone. In S3T1 and S4TM1–S4TM5, the pile load is carried by the shaft alone, but in Scenario 5 tests, part of the load is also carried by the pile base. In practice, the type of load-bearing is mainly dependent on the soil beneath and surrounding the pile, and the level of pile base resistance is mainly dependent on the stiffness of the soil layer beneath the pile. This assumption can justify part of the difference between the Scenario 5 profiles and the framework.

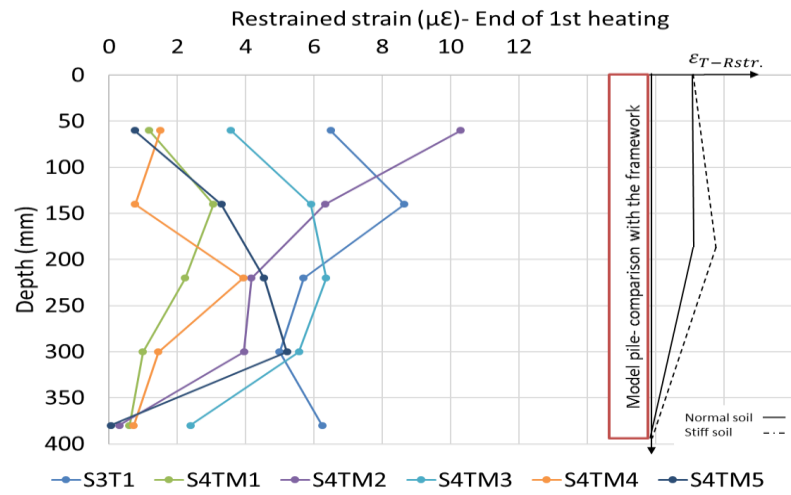
- Assumption 2 – The resistance generated is uniform along the length of the shaft. This means that there is a constant rate of change in strain with depth, which is mainly due to the perfectly homogenous soil sample considered in the framework. In numerical modelling, this can be easily achieved. However, even with the repetitive sampling method used in this study, it is difficult to consider the sample as perfectly homogenous. This results in a relatively constant strain profile along the pile with minor differences, mainly due to the differences in the soil–pile friction at a specific point.
- Assumption 3 – There is an idealised soil profile with uniform strength made of one soil type. The perfectly uniform soil is impossible to achieve, either in the laboratory or in-situ, but this should not be considered a main source of difference in this study due to the application of a repetitive sampling technique. Moreover, similar to the framework, one type of soil is used in this laboratory model. For in-situ installations, the soil profile usually comprises several soil types with different stiffness and friction levels.
- Assumption 4 – There is a linear elastic pile with a constant cross-sectional area. This assumption is applicable to the stainless steel model pile used in this study, with possibly negligible differences in the internal pile diameter along the pile.
- Assumption 5 – Temperature variations are uniform over the length of the pile. This assumption is not perfectly applicable in this study. This is mainly due to the drop in temperature towards the pile bottom. It is also stated by Ng et al. (2015) that the assumption of a uniform temperature profile and uniform shaft resistance along the pile surface could be one of the sources of the difference between the proposed framework by Bourne-Webb et al. (2013) and findings in other studies.
- Assumption 6 – The null point is located at the mid-depth of the pile. This assumption is not seen to be applicable in the study, as the location of the null point changes during the heating and cooling periods.

It seems that the framework idealises the soil condition and uses extreme cases of mechanical loading and end restraints. On the other hand, in in-situ studies, there is mostly a combination of soils in the soil profile along the pile and a homogenous sample does not seem to be applicable to all in-situ installations. An imperfect level of restraint is observed for the pile base support and mechanical loading on the pile head, which differs from the assumption of a perfectly free/fixed end in the framework. The magnitude of restrained strain is also dependent on the soil type, soil stiffness and the magnitude of changes in temperature (Amatya et al., 2012). From what has been observed and discussed in this study and the findings in the literature, it can be concluded that, for in-situ installations, the framework needs to be used cautiously, considering soil and pile conditions for each site to avoid overprediction or underprediction of restrained strain, induced load and mobilised friction. Moreover, it is concluded that the proposed framework cannot be

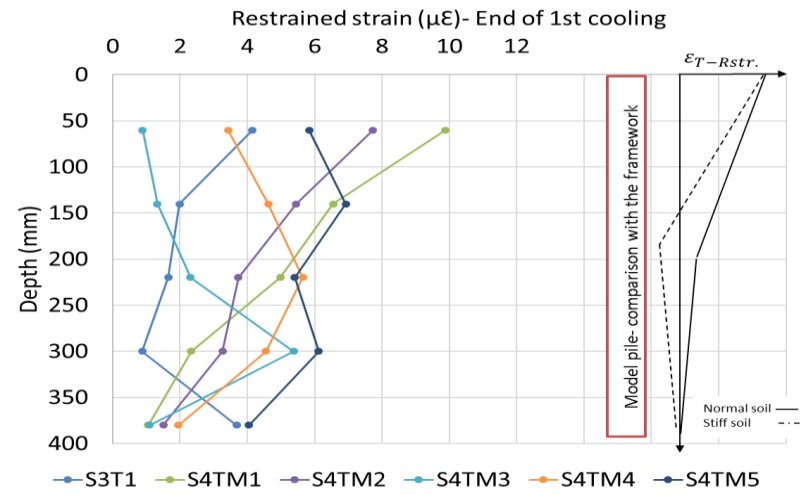
directly applied to a model thermal pile embedded in dry sand and the assumptions of the proposed framework need to be considered in the analysis if adopted.

6.9 Error analysis

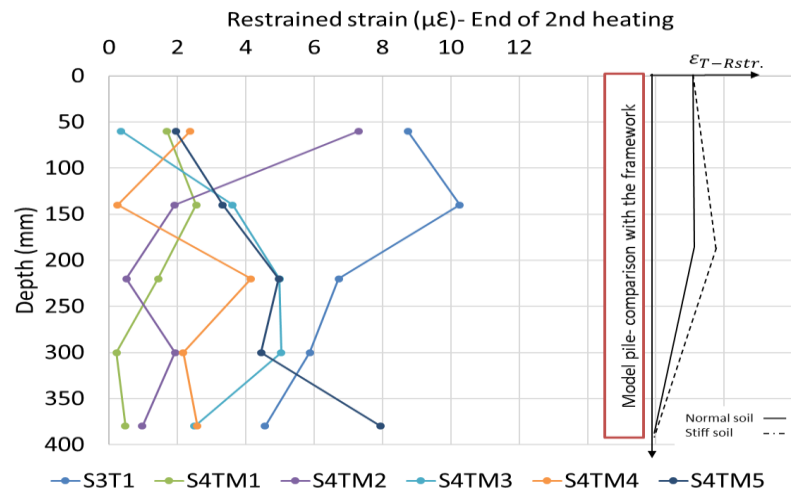
Similar to any other monitoring equipment, it is expected to achieve a certain level of error from FBG measurements. For strain monitoring, one of the main advantages of using FBGs instead of conventional strain gauges is the accuracy of FBGs. For the FBGs used in this study, strain and temperature resolution are equal to $1\mu\epsilon$ and $0.1K$ respectively. The main reason for the high accuracy of the sensors is the working mechanism of FBGs. A specific wavelength is defined for each FBG where the light is reflected at that wavelength. FBGs measure the absolute wavelength that will be changed due to an external effect such as temperature variations or loading on the FBG's host body. Shift in the wavelength will be used to determine the changes in the strain or temperature values based on the strain and temperature sensitivity values found using test S1T1. This has resulted in negligible level of error in the FBG measurements. It is shown by Tang & Wang (2010) using experimental results that error caused by strain and temperature FBGs is approximately $\pm 6\mu\epsilon$ and $\pm 0.13^\circ C$ respectively. This error can potentially happen if a FBG sensor is used to determine strain and temperature simultaneously but in this study, a set of temperature only FBGs were used along the pile surface which is used for the temperature compensation. Following this procedure will result in errors up to the resolution of FBGs which are $1\mu\epsilon$ and $0.1K$ for strain and temperature measurements which is negligible.



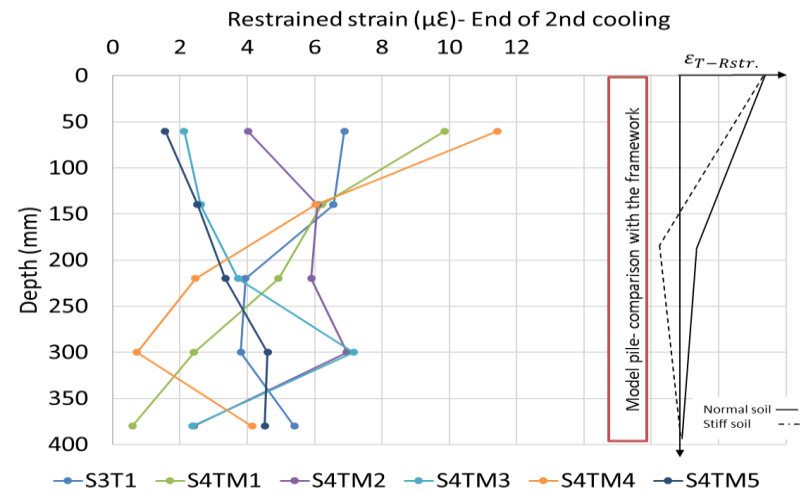
(a)



(b)



(c)



(d)

Figure 6-13. Comparison between restrained strain profiles for the shaft resistance pile and the proposed framework

Chapter 7. Conclusions and recommendations for future works

7.1 Conclusions

A 1g physical model was used to investigate the behaviour of a thermal pile under thermo-mechanical loading. Experiments were divided into Scenarios 1 to 5 based on the framework proposed by Bourne-Webb et al. (2013). A summary of the outcomes and conclusions is given below.

- Using Scenario 1 test, it was found that the thermal expansion of the stainless steel model pile was in the range of 15.79 to 17.98 (10^{-6} m/m.K) when obtained at different depths. This means that applying a constant thermal expansion coefficient value along the pile resulted in an error in the analysis. The captured coefficients were found to be greater than the value recommended by EN 1993-1-4:2006 (British Standards Institution, 2006), 16 (10^{-6} m/m.K).
- The temperature sensitivity of FBGs was found to be a function of the host body material. For FBGs installed on a stainless steel pile and covered by epoxy resin, the temperature sensitivity of the FBGs was found to be in the range of 29.7pm/°C to 32.5pm/°C, which was more than 2.5 times the temperature sensitivity of a bare FBG fibre.
- The strain sensitivity of FBGs was found to be in the range of 0.001204nm/με to 0.001221nm/με, which is in close agreement with the strain sensitivity of 0.0012nm/με commonly used for bare FBG fibres.
- Relatively uniform observed strain profiles were obtained along the pile surface under thermal loading for both type of piles, which shows that the sand deposition technique used in this study resulted in a relatively homogenous sample with minor differences of friction between soil and pile at different levels.
- In Scenarios 3 to 5, the pile temperature was raised to 50°C during the heating period, but it did not return to the original position after 24 hours of cooling. This shows that the sand surrounding the pile works as an insulator and retains a small amount of the generated heat.
- The maximum applied load threshold used to observe the thermo-elastic response was noted as 31% of the ultimate load-bearing capacity for the shaft and base resisting pile. This value decreased to 18% of the ultimate pile capacity for the shaft resisting pile. The thresholds were obtained by ignoring the approximately 0.1mm displacement due to the weight of the pile itself and ignoring minor changes in the strain values due to temperature differences.
- For both the shaft resisting pile and shaft and base resisting pile, which were embedded in the sand with a mechanical load on the pile head, it was observed that the location of the maximum observed strain during two heating-cooling cycles was not constant, and changed after a period of heating or cooling. It was also detected that the strain during the heating period was only slightly changed from the maximum value achieved after one hour of heating.

This is unlike the cooling period, where the observed strain seemed to be time-dependent until the steady-state being achieved (after 20 hours).

- For the shaft resisting pile, the maximum restrained strain during the heating period was observed in the upper half of the pile for mechanical loadings from 0 to 33% of the shaft capacity. It then shifted to pile mid-depth for mechanical loadings higher than 33% of the ultimate capacity. Similarly, the maximum restrained strain was observed at the pile head for Scenario 5 tests with mechanical loading of up to 47% of the ultimate capacity, and then it shifted to the pile mid-depth for higher magnitudes of mechanical loading.
- For the shaft and base resisting pile, the time at which the maximum restrained strain was observed seemed to be dependent on the extent of the mechanical loading. The maximum restrained strain was observed during cooling periods for mechanical loadings of up to 31% of the ultimate pile capacity, while for mechanical loads higher than 46% of the ultimate pile capacity, the maximum restrained strain was during heating periods.
- The effect of end restraints was observed in S4TM6–S4TM7, where higher magnitudes of restrained strain were detected for the pile with base support compared to other Scenario 4 tests with no base support. This shows the importance of the stiffness of the soil/support beneath the pile on the amount of load carried by the pile toe.
- For Scenarios 3 to 5, the magnitude of the degree of freedom was observed as being in the range of 0.97 to 1. This means that the level of restraint imposed by the surrounding sand at an approximate relative density of 57% with low level of vertical stresses, and the restraint caused by mechanical loading on the pile head was rather limited.
- The shift in the position of the null point was observed during heating-cooling cycles, and determining a fixed position for the null point was not possible.
- It was witnessed that the conventional load transfer mechanism used for shaft bearing piles under mechanical loading, cannot be applied to the pile under either thermal or thermo-mechanical loading. The pile toe carries a considerable load—up to 68.4% of the maximum induced thermal load—compared to nearly zero loads carried by the pile toe under mechanical loading only. The additional load carried by the pile toe needs to be considered for thermal pile design.
- For the shaft resisting pile in Scenarios 3 and 4, the maximum induced thermal load was observed as being equal to 1.55 and 1.72 times the ultimate shaft capacity respectively. The maximum induced thermal load for the shaft and base resisting pile was 90% of the ultimate bearing capacity of the pile.
- Despite the considerable induced thermal load observed in Scenarios 3 to 5, the maximum induced stress was observed as being 3.26%, 3.63% and 3.69% of the BS 8004:1986 (British Standards Institution, 1986) maximum allowable stress for a stainless steel pile respectively.

The main reason for the small ratios seemed to be the high compressive strength of stainless steel, which is approximately seven times greater than the compressive strength of a 28-day concrete sample. This means that where concrete piles are used for in-situ installation, this could become close to the allowable limit, as noted by Bourne-Webb et al. (2009).

- The maximum stress produced by thermal loading was observed as being 1.17 times the maximum stress caused by a mechanical load equal to 70% of the ultimate capacity of the pile.
- For the shaft and base resisting pile, when the mechanical loading was up to 31% of the ultimate pile capacity, the more induced load was seen during the cooling periods, and the heating periods were acting as partial recovery. This was reversed when the mechanical loading was increased to 47% or more.
- The maximum induced stress per degree change in temperature was 74kPa/°C, 78.97kPa/°C and 85.7kPa/°C for Scenarios 3 to 5 respectively. These values are less than the observed range for in-situ installations given in the literature in the range of 104kPa/°C to 329kPa/°C. The main reason for this seemed to be the decrease in restraint caused by the surrounding soil, the pile head and also the absence of overburden pressure.
- The effect of end restraints on the magnitude of induced load was observed at high magnitudes of mechanical loading. Consistently lower strain values were recorded in S5TM4 for the shaft and base resisting pile under the mechanical load equivalent to 70% of ultimate pile capacity.
- An irreversible settlement was observed for both types of piles under both thermal and thermo-mechanical loading. In the absence of mechanical loading, irreversible settlements were detected equal to 0.41% of the pile diameter for Scenarios 3 and 5.
- For both types of piles, the rate of pile settlement with a 1°C decrease in the temperature varied between 0.009mm/°C and 0.0186mm/°C pre-failure of the pile. The rate of settlement in the shaft and base resisting pile was lower compared to the shaft resisting pile due to the presence of sand beneath the pile in the shaft and base resisting pile. It was observed that, with an increase in the magnitude of the mechanical load, the rate of settlement per degree decrease in the temperature increased.
- For both types of piles, the rate of upward movement per degree increase in the temperature varied between 0.0042mm/°C and 0.0093mm/°C. The rate of pile upward movement for the shaft and base resisting pile was higher than the shaft resisting pile. An inverse relationship was observed between the magnitude of the initial mechanical load on the pile head and the rate of pile heave.
- For both types of piles, the ratio of pile settlement over pile heave was observed as being higher than 1, with minimum and maximum values equal to 1.18 and 2.90 respectively,

excluding S4TM4 and S4TM5, where the failure happened. This ratio increased with an increase in the magnitude of the initial mechanical load.

- The effect of thermal cycles on the cumulative settlement of piles was investigated. It was observed that, for the shaft resisting pile, the ratio of pile settlement after and before thermal loading was 2.63, 1.98 and 2.51 for S4TM1 to S4TM3 respectively. Moreover, failure occurred in S4TM4 and S4TM5, showing the considerable impact of thermal cycles on the behaviour of the shaft resisting pile. This ratio was observed as being 1.81, 1.79 and 1.27 for the shaft and base resisting pile in S5TM2 to S5TM4 respectively, which shows less impact compared to the shaft resisting pile.
- In terms of the shaft and base resisting pile, for mechanical loads up to 47% of the ultimate pile capacity, the cumulative settlement under two thermal cycles was observed as being equivalent to the settlement caused by an additional 50N of mechanical loading. It was reduced to 30N–40N when the initial mechanical load on the pile head was increased to 70% of the ultimate capacity. Similarly, for the shaft resisting tests of S4TM1–S4TM3, this value was observed as being in the range of 45N–100N, with the higher values in S4TM4–S4TM5 resulting in the pile failure. This shows that thermal cycles had a greater impact on the shaft resisting model pile than the shaft and base resisting pile.
- Based on the above-mentioned equivalent additional loads, the factor of safety for the shaft and base resisting pile was observed as being reduced from 3.2, 2.13, 1.42 before the thermal cycles to 2.13, 1.6 and 1.28 after the thermal cycles for S5TM2 to S5TM4 respectively. Likewise, for the shaft resisting pile, the factor of safety was reduced from 5.5, 3 and 2.2 to approximately 1.3 for S4TM1 to S4TM3 respectively. This shows that there were larger reductions in the factor of safety for the shaft resisting pile than the base and shaft resisting pile.
- It was found that, for the shaft and base resisting pile tests, cumulative settlement after the thermal cycles remained below 10% of the pile diameter, which means none reached the ultimate limit state after a thermal cycle.
- For the shaft resisting pile, the ratio of a cumulative settlement over pile length was observed as being in the range of 0.029 to 0.487, while this value was observed as being 0.033 to 0.478 for the shaft and base resisting pile.
- It was observed that a direct relationship exists between the magnitude of mechanical loading and mobilised friction. For the shaft resisting pile in the absence of mechanical loading, it was observed that the maximum mobilised friction under thermal loading was 77% of the maximum mobilised friction under the ultimate shaft capacity of the pile. In S4TM1 to S4TM5, the maximum mobilised friction was observed as being 1.48 times the ultimate friction mobilised under the load of 160N.

- For the shaft and base resisting pile, the maximum mobilised friction under thermo-mechanical loading was observed as being 1.32 times the ultimate friction mobilised under ultimate mechanical loading. This means that the mobilised friction under a thermal cycle increased up to 32% compared to the friction mobilised under 320N.
- For the shaft and base resisting pile, it was observed that heating increased the friction at the soil–pile interface, and cooling resulted in a reduction of friction. On the other hand, a relatively irregular behaviour was seen for the shaft resisting pile. It can be concluded that, despite an increase in the mobilised friction during the heating period, cumulative friction after two heating-cooling cycles was reduced—particularly for the shaft resisting pile.
- Two main processes seemed to be driving forces in the additional settlement observed during the cooling periods. Firstly, the friction at the soil–pile interface seemed to be reduced for both types of piles. Secondly, the additional induced load in the cooling periods seemed to be coupled with the axial load on the pile from the mechanical loading, resulting in larger settlements.
- It was observed that the assumption of two-way cyclic loading could be applied to thermal piles undergoing seasonal heating and cooling.
- A comparison between laboratory results and the framework proposed by Bourne-Webb et al. (2013), which has been adopted by the Thermal Pile Standard (GSHPA, 2012), was made. It was found that the framework could not be directly applied for a model pile embedded in dry sand. Whether this conclusion can be expanded to other soil types and pile scales needs further investigation. The main reason is found to be the assumptions used by the proposed framework which has considered an idealised situation that can lead to overprediction or underprediction of restrained strain, induced load and mobilised friction. For thermal pile design, the proposed framework needs to be applied along with the site specific information for soil and mechanical load on the pile head.

7.2 Recommendations for future works

In this study, a set of observational data was gathered that could be used later to compare with future numerical models and laboratory data. The following recommendations could be applied to future investigations in this field:

- Apply mechanical loading at the end of thermal cycles to capture the differences made in the pile response. Moreover, alternative loading mechanisms such as a hydraulic jack or the use of a water tank can be adopted to determine the effect of a loading mechanism on the pile response.
- Quantify the effects of intermediate temperature levels by heating up the pile in 3°C to 5°C temperature increments. This procedure will help to quantify the intermediate levels of

induced load imposed by thermal loading and will also help to compare the results with the quick heating procedure used in this study.

- Investigating the heat transfer process in sand was not considered in the scope of this study but the data collected from FBGs (See Appendix J) can be used as a comparison mean for future studies in this area.
- Use fluids applied for the in-situ installations, such as glycol-water as the circulating fluid. In addition, different shapes of pipes could be installed inside the model pile to investigate the efficiency of each configuration. Also, lower temperature ranges close to the freezing point could be tested using heat pumps.
- Examine the effects of groundwater on the soil and pile behaviour by using moist sand or another type of soil with a specific level of water content. Other properties of the sand, such as relative density and the size of the particles, could be altered to understand their effect on soil and pile responses.
- Compare the restraint level with the in-situ conditions. This could be done by taking the following actions:
 - Use a more compacted sand with a higher relative density.
 - Use clay or another type of soil that would restrict the pile more than sand.
 - Roughen the pile surface to potentially increase soil–pile friction.
 - Apply an overburden pressure on the soil to increase the confinement in the soil and, consequently, increase the restraint level caused by the soil. This is achievable either by using centrifuge modelling with various g-levels, or in the laboratory 1g models by applying a distributed pressure on the soil with methods such as surcharged air pressure using a rubber membrane, which was adopted by Ergun and Akbulut (1995).
- In this study, insulation jackets were used to insulate the container and sand surface, but there was some heat loss, which could have resulted in minor temperature differences along the pile. Future models could be designed to be completely sealed units.
- In this study, axial strain along the pile was monitored. An extension to this work would be to collect the radial strain in the soil using FBGs to understand the effect of heating-cooling cycles on soil behaviour.
- In this study, two heating-cooling cycles were applied to the pile to represent two years of thermal pile operation. More heating-cooling cycles, 10 cycles or more, can be applied to simulate the thermal pile behaviour for longer periods.
- In this study, the focus was on the macro-scale response of thermal piles. Investigating the microstructure behaviour of the model pile, especially with regard to the soil–pile interface, would help to better understand the thermal pile response. Several techniques could be used,

such as using thermography and transparent soils in the laboratory or using numerical modelling techniques such as the discrete element method.

- Determine the most detrimental parameters affecting the cyclic thermal loading, such as the amplitude of cyclic loading, the number of cycles, the type of soil and the pile material.
- The proposed framework by Bourne-Webb et al. (2013) is based on idealised conditions where both ends are either completely free or completely fixed. Using completely rigid end restraints would make it possible to have end conditions close to those in the framework.
- The results found in this study should not be used directly to interpret the behaviour of thermal piles in the field, but, based on observations made in this study, the following recommendations could be used for design purposes:
 - If FBGs are used for strain monitoring, a set of FBG sensors also needs to be used to determine the temperature variations for temperature compensation. Without the knowledge of wavelength variations under thermal loading, the strain caused by thermal and mechanical loading cannot be decoupled.
 - It is better for the thermal expansion coefficient of the pile to be accurately determined rather than a constant value assumed, as this can result in noticeable over- or under-prediction of strain values and affect the analysis.
 - Consider making the pile toe carry a large magnitude of the thermal load.
 - Make sure that the induced thermal load and stress are within the limits recommended for the pile under compression and tension.
 - The thermal pile response seemed to be mainly dependent on the initial magnitude of mechanical loading. If the applied mechanical load is up to the working limit state, the need for large safety factors is reduced.
 - The pile response under thermal loading also seemed to be dependent on the surrounding soil, and a comprehensive knowledge of the ground conditions could help to avoid the application of larger than conventional safety factors.

References

- Al-Mhaidib, A. and Edil, T. 1998. Model Tests for Uplift Resistance of Piles in Sand. *Geotechnical Testing Journal*, 21(3), pp. 213-221, <http://dx.doi.org/10.1520/GTJ10895J>.
- Altaee, A. & Fellenius, B., H. 1994. Physical modelling in sand. *Canadian Geotechnical Journal*. 31(3), pp. 420-431.
- Amatya, B., Soga, K., Bourne-Webb, P., Amis, T. And Laloui, L. 2012. Thermo-mechanical behaviour of energy piles. *Géotechnique*, 62(6), pp. 503-519.
- American Petroleum Institute. 2005. RP 2A-WSD. Recommended Practice for Planning, Designing and Constructing Fixed Offshore Platforms—Working Stress Design. Washington DC: API.
- American Society for Testing and Materials. 1993. MNL12-4TH. *Manual on the Use of Thermocouples in Temperature Measurement: 4th Edition*. West Conshohocken, Pennsylvania, United States, ASTM International.
- Amis, T., Bourne-Webb, P., Davidson, C., Amatya, B. & Soga, K. 2008. An investigation into the effects of heating and cooling energy piles whilst under working load at Lambeth College, UK. *Proceedings of the 33rd Annual and 11th International Conference of the Deep Foundations Institute*, New York, USA, 10 pages.
- Ansari, F. 2007. Practical Implementation of Optical Fiber Sensors in Civil Structural Health Monitoring. *Journal of Intelligent Material Systems and Structures*, 18(8), pp. 879-889.
- Atkinson, J. 2007. *The mechanics of soils and foundations*. London: Taylor & Francis.
- Baker, P., Matian, M., Peacock, a. D., Sudtharalingam, S., Staffell, I., Barton, J., Infield, D., et al., 2009. UK microgeneration. Part I: policy and behavioural aspects. *Proceedings of the ICE - Energy*, 162(1), pp. 23-36.
- Banks, D. 2008. *An Introduction to Thermogeology: Ground Source Heating and Cooling*. Chichester, West Sussex: Wiley-Blackwell.
- Batchelor, T. 2005. Geothermal energy: a major renewable energy resource. *Proceedings of the Institution of Civil Engineers: Civil Engineering*, 158(6), pp. 40–44.
- Batini, N., Rotta Loria, A., Conti, P., Testi, D., Grassi, W. and Laloui, L. 2015. Energy and geotechnical behaviour of energy piles for different design solutions. *Applied Thermal Engineering*, 86, pp.199-213.
- Berezantsev, V., G., Khristoforov, V., Golubkov, V. 1961. Load-bearing capacity and deformation of piled foundations. *Proceedings of the 5th International Conference (ISSMFE)*, Paris, Vol. 2, pp. 11–15.
- Blomberg, T., 1996. *Heat conduction in two and three dimensions: computer modelling of building physics applications*. PhD. Lund University.

- Bourne-Webb, P., Amatya, B. and Soga, K. 2013. A framework for understanding energy pile behaviour, *Proceedings of the Institution of Civil Engineers - Geotechnical Engineering*, 166(2), pp. 170-177. doi: 10.1680/geng.10.00098.
- Bourne-Webb, P., Amatya, B., Soga, K., Amis, T., Davidson, C. and Payne, P. 2009. Energy pile test at Lambeth College, London: geotechnical and thermodynamic aspects of pile response to heat cycles. *Géotechnique*, 59(3), pp. 237-248.
- Bradshaw, A. S. 2012. Framework for Scaling 1g Model Pile Tests for Offshore Wind Structures. *Proceedings of ASCE GeoCongress 2012*, Oakland, CA, USA, March, ASCE, Reston, VA, pp. 336-345.
- Brandl, H., 2006. Energy foundations and other thermo-active ground structures. *Géotechnique*, 56(2), pp. 81-122.
- British Standards Institution, 1986. BS 8004:1986. *Code of Practice for foundations*. Milton Keynes: BSI.
- British Standards Institution, 1990. BS 1337-7: 1990. *Methods of test for Soils for civil Engineering purposes - Part 7: Shear strength tests (total stress)*. Milton Keynes: BSI.
- British Standards Institution, 1990. BS 1377-2:1990. *Methods of test for Soils for civil Engineering purposes - Part2: Classification tests*. Milton Keynes: BSI.
- British Standards Institution, 2002. BS 1337-4:1990. *Methods of test for Soils for civil engineering purposes - Part 4: Compaction-related tests*. Milton Keynes: BSI.
- British Standards Institution, 2004. BS EN 10025-1:2004. *Hot rolled products of structural steels. General technical delivery conditions*. Milton Keynes: BSI.
- British Standards Institution, 2005. BS EN 10088-1:2005. *Stainless steels. List of stainless steels*. Milton Keynes: BSI.
- British Standards Institution, 2006. BS EN 1993-1-4:2006. *Design of steel structures. General rules. Supplementary rules for stainless steels*. Milton Keynes: BSI.
- Buckingham, E. 1914. On Physically Similar Systems; Illustrations of the Use of Dimensional Equations. *Phys. Rev.*, 4(4), pp. 345-376.
- Bustamante, M., Gianceselli, L., Bertero, M. & Paviani, A. 1991. Study of the load-bearing capacity of a pile of considerable length bored using bentonite mud. *Proceedings of 4th International DFI Conference*, Balkema, pp. 535- 542.
- Butterfield, R. 1999. Dimensional analysis for geotechnical engineers. *Géotechnique*, 49(3), pp. 357-366.
- Chakraborty, T. and Salgado, R., 2010. Dilatancy and Shear Strength of Sand at Low Confining Pressures. *J. Geotech. Geoenviron. Eng.*, 136(3), pp. 527-532.
- Correia, R. 2008. *Development of a Pore Pressure Sensor Employing Fibre Bragg Gratings*. PhD. Cranfield University.

- de Moel, M., Bach, P., Bouazza, A., Singh, R. and Sun, J. 2010. Technological advances and applications of geothermal energy pile foundations and their feasibility in Australia. *Renewable and Sustainable Energy Reviews*, 14(9), pp.2683-2696.
- Department for Business, Energy & Industrial Strategy. 2016. *UK Energy in Brief*. National Statistics, London.
- Department of Energy & Climate Change. 2013. *UK Renewable Energy Roadmap Update*. Department of Energy & Climate Change, London.
- Di Donna, A. and Laloui, L. 2014. Numerical analysis of the geotechnical behaviour of energy piles. *Int. J. Numer. Anal. Meth. Geomech.*, 39(8), pp. 861-888.
- Dickson, M. and Fanelli, M. 2004. *What Is Geothermal Energy?*. [online] CNR-Instituto di Geoscience e Georisorse. Available at: <<http://users.metu.edu.tr/mahmut/pete450/Dickson.pdf>> [Accessed 5 Aug. 2016].
- Doyle, C. 2003. *Fibre Bragg Grating Sensors: An Introduction to Bragg gratings and interrogation techniques*. Smart Fibres Ltd. Available at: <https://smartfibres.com/Attachments/Smart%20Fibres%20Technology%20Introduction.pdf> [Accessed 25 Oct. 2013].
- Dunnicliff, J. and Green, G. 1988. *Geotechnical instrumentation for monitoring field performance*. New York: Wiley.
- El Naggar, M. and Wei, J. 2000. Cyclic Response of Axially Loaded Tapered Piles. *Geotechnical Testing Journal*, 23(1), pp. 100-115.
- Ergun, M. and Akbulut, H. 1995. Bearing capacity of shaft-expanded driven model piles in sand. *Géotechnique*, 45(4), pp. 715-718.
- Farahi, F., Webb, D., Jones, J. and Jackson, D. 1990. Simultaneous measurement of temperature and strain: cross-sensitivity considerations. *Journal of Lightwave Technology*, 8(2), pp.138-142.
- Fioravante, V. 2002. On the Shaft Friction Modelling of Non-Displacement Piles in Sand. *Soils and Foundations*, 42(2), pp. 23-33.
- Franke, E. & Muth, G. 1985. Scale effect in 1g model tests on horizontally loaded piles. *Proceedings of the 11th International Conference of Soil Mechanics and Foundation Engineering*, San Francisco, Calif. Vol. 2, pp. 1011–1014.
- Gao, J., Zhang, X., Liu, J., Li, K. and Yang, J. 2008. Thermal performance and ground temperature of vertical pile-foundation heat exchangers: A case study. *Applied Thermal Engineering*, 28(17-18), pp. 2295-2304.
- Garnier, J. & Konig, D. 1998. Scale effects in piles and nail loading tests in sand. *Proceedings of the international conference centrifuge 98*, Tokyo, vol. 1, Balkema, Amsterdam, pp. 205-210.
- Ghasemi-Fare, O. and Basu, P. 2013. A practical heat transfer model for geothermal piles. *Energy and Buildings*, 66, pp. 470-479.

- Glišić, B. and Inaudi, D. 2007. *Fibre optic methods for structural health monitoring*. Chichester, England: John Wiley & Sons.
- Goode, J.C., III, Zhang, M. and McCartney, J.S. 2014. Centrifuge Modeling of energy foundations in sand. *Proceedings of the 8th International Conference on Physical Modelling in Geotechnics(ICPMG2014)*. C. Gaudin and D. White, eds. Perth, Australia, Taylor and Francis. London. pp. 729– 736.
- Ground Source Heat Pump Association, 2012. Thermal Pile Design, Installation & Materials Standards Issue 1.0. Milton Keynes. GSHPA.
- Habel, W. and Krebber, K. 2011. Fiber-optic sensor applications in civil and geotechnical engineering. *Photonic Sens*, 1(3), pp. 268-280.
- Hamada, Y., Saitoh, H., Nakamura, M., Kubota, H. and Ochifuji, K. 2007. Field performance of an energy pile system for space heating. *Energy and Buildings*, 39(5), pp.517-524.
- Hamdhan, I., and Clarke, B. 2010. Determination of thermal conductivity of coarse and fine sand soils. *Proceedings of World Geothermal Congress, volume 7*, Bali, Indonesia, 25-29 April 2010. 7 pages.
- Head, K. 2006. *Manual of Soil Laboratory Testing: Volume 1: Soil classification and compaction tests*. 3rd ed. Caithness: Whittles.
- Head, K. and Epps, R. 2011. *Manual of Soil Laboratory Testing*. Dunbeath: Whittles Publishing.
- Iten, M. 2011. *Novel applications of distributed fibre optic sensing in geotechnical engineering*. PhD. ETH Zurich.
- Jalaluddin, Miyara, A., Tsubaki, K., Inoue, S. and Yoshida, K. 2011. Experimental study of several types of ground heat exchanger using a steel pile foundation. *Renewable Energy*, 36(2), pp.764-771.
- Kalantidou, A., Tang, A., Pereira, J. And Hassen, G. 2012. Preliminary study on the mechanical behaviour of heat exchanger pile in physical model. *Géotechnique*, 62(11), pp.1047-1051.
- Kaniraj, S. 1988. *Design aids in soil mechanics and foundation engineering*. New Delhi: Tata McGraw-Hill Pub. Co.
- King, G.J.W., Dickin, E.A., and Lyndon, A. 1985. The development of a medium size centrifugal testing facilities. *Proceedings of Symposium on Application of Centrifuge Modelling in Geotechnical Design*, Manchester, UK, W. H. Craig, ed., A. A. Balkema, Rotterdam, The Netherlands 25-46.
- Kister, G., Winter, D., Gebremichael, Y., Leighton, J., Badcock, R., Tester, P., Krishnamurthy, S., Boyle, W., Grattan, K. and Fernando, G. 2007. Methodology and integrity monitoring of foundation concrete piles using Bragg grating optical fibre sensors. *Engineering Structures*, 29(9), pp. 2048-2055.

- Klar, A., Bennett, P., Soga, K., Mair, R., Tester, P., Fernie, R., St John, H. and Torp-Peterson, G. 2006. Distributed strain measurement for pile foundations. *Proceedings of the Institution of Civil Engineers - Geotechnical Engineering*, 159(3), pp. 135-144.
- Knellwolf, C., Peron, H. and Laloui, L. 2011. Geotechnical Analysis of Heat Exchanger Piles, *J. Geotech. Geoenviron. Eng.*, 137(10), pp. 890-902. doi: 10.1061/(asce)gt.1943-5606.0000513.
- Kong, L. and Zhang, L. 2008. Experimental study of interaction and coupling effects in pile groups subjected to torsion. *Canadian Geotechnical Journal*, 45(7), pp.1006-1017.
- Kouroussis, G., Kinet, D., Moeyaert, V., Dupuy, J. and Caucheteur, C. 2016. Railway structure monitoring solutions using fibre Bragg grating sensors. *International Journal of Rail Transportation*, 4(3), pp. 135-150.
- Kraft, L. 1991. Performance of Axially Loaded Pipe Piles in Sand. *Journal of Geotechnical Engineering*, 117(2), pp.272-296.
- Kramer, A. C. and Basu, P. 2014. Performance of a model geothermal pile in sand. *Proceedings of the 8th International Conference on Physical Modelling in Geotechnics(ICPMG2014)*. C. Gaudin and D. White, eds. Perth, Australia, Taylor and Francis. London. pp. 771–777.
- Kramer, C., Ghasemi-Fare, O. and Basu, P. 2014. Laboratory Thermal Performance Tests on a Model Heat Exchanger Pile in Sand. *Geotechnical and Geological Engineering*, 33(2), pp.253-271.
- Kulhawy, F., H., 1984. Limiting tip and side resistance, fact or fallacy, Symposium on Analysis and Design of Pile Foundations. *Proceedings of the American Society of Civil Engineers, ASCE, Symposium on Analysis and Design of Pile Foundations*, R. J. Meyer, Ed., Sanfrancisco, pp. 80-98.
- Kulhawy, F., H., Traumann, C., H., Beech, J., F., O'Rourke, T. D. & McGuire, W. 1983. Transmission Line Structure Foundations For Uplift-Compression Loading, Report Number EL2870, EPRI, Palo Alto, CA.
- Laloui, L. & Nuth, M. 2009. Investigations on the mechanical behaviour of a Heat Exchanger Pile. *Proceedings of the 5th international symposium on deep foundations on bored and auger piles, University of Ghent, Belgium*, Taylor and Francis, London, pp. 343-347.
- Laloui, L. 2011. In-situ testing of a heat exchanger pile. *Proceedings of GeoFrontiers 2011 (GSP 211)*, J. Han and D. E. Alzamora, eds., ASCE, Reston, VA, pp. 410-419.
- Laloui, L. and Di Donna, A. 2011. Understanding the behaviour of energy geo-structures. *Proceedings of the Institution of Civil Engineers - Civil Engineering*, 164(4), pp. 184-191.
- Laloui, L., and Nuth, M. 2006. Numerical modeling of some features of heat exchanger pile. *Foundation analysis and design: Innovative methods (GSP 153)*, R. L. Parsons, L. Zhang, W. D. Guo, K. K. Phoon, and M. Yang, eds., ASCE, Reston, VA, pp. 189–195.
- Laloui, L., Moreni, M. and Vulliet, L. 2003. Comportement d'un pieu bi-fonction, fondation et échangeur de chaleur. *Canadian Geotechnical Journal*, 40(2), pp. 388-402.

- Laloui, L., Nuth, M. and Vulliet, L. 2006. Experimental and numerical investigations of the behaviour of a heat exchanger pile, *Int. J. Numer. Anal. Meth. Geomech.*, 30(8), pp. 763-781. doi: 10.1002/nag.499.
- Lee, C. and Lam, H. 2013. A simplified model of energy pile for ground-source heat pump systems. *Energy*, 55, pp. 838-845.
- Lee, J., Kim, T. and Leigh, S. 2013. Thermal performance analysis of a ground-coupled heat pump integrated with building foundation in summer. *Energy and Buildings*, 59, pp. 37-43.
- Lee, S., 2004. *Behaviour of a single micropile in sand under cyclic axial loads*. PhD. University of Illinois at Urbana-Champaign.
- Lennon, D. J., Watt, E., Suckling, T.P. 2009. Energy piles in Scotland. *Proceedings of the 5th international symposium on deep foundations on bored and auger piles, University of Ghent, Belgium*, Taylor and Francis, London, pp. 349-355.
- Leung, C., Wan, K., Inaudi, D., Bao, X., Habel, W., Zhou, Z., Ou, J., Ghandehari, M., Wu, H. and Imai, M. 2013. Review: optical fiber sensors for civil engineering applications. *Materials and Structures*, 48(4), pp. 871-906.
- Li, J., Correia, R., Chehura, E., Staines, S., James, S., W., Tatam, R., P., Butcher, A., P., and Fuentes, R. 2009. Field monitoring of static, dynamic and statnamic pile loading tests using fiber Bragg grating strain sensors. *Proceedings of SPIE- The International Society for Optical Engineering*, volume 7503, pp. 75034O-1–75034O-4.
- Li, Z., Bolton, M. and Haigh, S. 2012. Cyclic axial behaviour of piles and pile groups in sand. *Canadian Geotechnical Journal*, 49(9), pp. 1074-1087.
- Lings, M. And Dietz, M. 2005. The peak strength of sand–steel interfaces and the role of dilation. *Soils and Foundations*, 45(6), pp. 1-14.
- Loukidis, D. and Salgado, R. 2008. Analysis of the shaft resistance of non-displacement piles in sand. *Géotechnique*, 58(4), pp. 283-296.
- Loveridge, F. and Powrie, W. 2013. Pile heat exchangers: thermal behaviour and interactions. *Proceedings of the Institution of Civil Engineers - Geotechnical Engineering*, 166(2), pp. 178-196.
- Man, Y., Yang, H., Diao, N., Liu, J. and Fang, Z., 2010. A new model and analytical solutions for borehole and pile ground heat exchangers. *International Journal of Heat and Mass Transfer*, 53(13-14), pp. 2593-2601.
- Mayne, P.W., Springman, S., Coop, M.R., Huang, A.B., and Zornberg, J. 2009. State-of-the-Art Paper (SOA-1): GeoMaterial Behavior and Testing. Proceeding of 17th *International Conference on Soil Mechanics & Geotechnical Engineering*, Vol. 4 (ICSMGE), Alexandria, Egypt, Millpress/IOS Press, Amsterdam, pp. 2777-2872.

- McCartney, J. S., and Rosenberg, J. E. 2011. Impact of heat exchange on side shear in thermoactive foundations. *Proceedings of GeoFrontiers 2011 (GSP 211)*, J. Han and D. E. Alzamora, eds., ASCE, Reston, VA, pp. 488–498.
- Mimouni, T. 2014. *hermomechanical Characterization of Energy Geostructures with Emphasis on Energy Piles*. PhD. École Polytechnique Fédérale De Lausanne.
- Mimouni, T. and Laloui, L., 2015. Behaviour of a group of energy piles. *Canadian Geotechnical Journal*, 52(12), pp. 1913-1929.
- Mishra, V., Lohar, M. and Amphawan, A. 2016. Improvement in temperature sensitivity of FBG by coating of different materials. *Optik - International Journal for Light and Electron Optics*, 127(2), pp. 825-828.
- Mohamad, H. 2012. Temperature and strain sensing techniques using Brillouin Optical Time Domain Reflectometry. *Proceedings of Smart Sensor Phenomena, Technology, Networks, and Systems Integration (SPIE)*, volume 8346, San Diego, California. T. E. Matikas, K. J. Peters, W. Ecke, eds. Vol. 8346, pp. 83461M1-13.
- Morino, K. and Oka, T. 1994. Study on heat exchanged in soil by circulating water in a steel pile. *Energy and Buildings*, 21(1), pp. 65-78.
- Muir Wood, D., 2004. *Geotechnical modelling*. London: Spon Press.
- Murphy, K. and McCartney, J. 2014. Seasonal Response of Energy Foundations During Building Operation. *Geotechnical and Geological Engineering*, 33(2), pp. 343-356.
- Murphy, K., McCartney, J. and Henry, K. 2014. Evaluation of thermo-mechanical and thermal behavior of full-scale energy foundations. *Acta Geotechnica*, 10(2), pp. 179-195.
- Murphy, K.D. and McCartney, J.S. 2012. Behavior of Full-Scale Energy Foundations in Denver, Colorado. *Proceedings of GeoChallenges: Rising to the Geotechnical Challenges of Colorado (GPP 7)*, Denver, Colorado. C. M. Goss, J. A. Stricklan, R. L. Wiltshire, eds., ASCE, Reston, VA, pp. 217-229.
- Ng, C., Shi, C., Gunawan, A., Laloui, L. and Liu, H. 2015. Centrifuge modelling of heating effects on energy pile performance in saturated sand, *Canadian Geotechnical Journal*, 52(8), pp. 1045-1057. doi: 10.1139/cgj-2014-0301.
- Nicholson, D., 2012. *Thermal pile guide: ground source support for this growing technology*. Ecobuild, London.
- O’Sullivan, C., Bray, J. and Riemer, M. 2004. Examination of the Response of Regularly Packed Specimens of Spherical Particles Using Physical Tests and Discrete Element Simulations. *J. Eng. Mech.*, 130(10), pp. 1140-1150.
- Oh, J. H., Lee, W., J., Lee, S., B., Lee, W., J. 2000. Analysis of Pile Load Transfer using Optical Fiber Sensor. *Proceedings of Smart Structures and Materials: Smart Systems for Bridges, Structures, and Highways (SPIE)*, Vol. 3988, S. C. Liu. Ed., pp. 349-358.

- Olgun, C. and McCartney, J. 2014. Outcomes from international workshop on thermoactive geotechnical systems for near-surface geothermal energy: from research to practice. *DFI Journal - The Journal of the Deep Foundations Institute*, 8(2), pp. 59-73.
- Othonos, A. and Kalli, K. 1999. *Fiber Bragg Gratings: Fundamentals and Applications in Telecommunications and Sensing*. London: Artech House Publishers.
- Ozudogru, T., Brettmann, T., Olgun, G., Martin, J. and Senol, A. 2012. Thermal conductivity testing of energy piles: field testing and numerical modelling, *Proceedings of ASCE GeoCongress 2012*, Oakland, CA, USA, March, ASCE, Reston, VA, pp. 4436-4445.
- Paik, K. and Salgado, R. 2004. Effect of Pile Installation Method on Pipe Pile Behavior in Sands. *Geotech. Test. J.*, 27(1), pp. 1-11.
- Patel, G., P. & Bull, J., W. 2011. Selection of material used for thermopiles for recycling heat within a building. *Proceedings of GeoFrontiers 2011 (GSP 211)*, J. Han and D. E. Alzamora, eds., ASCE, Reston, VA, pp. 400-409.
- Poulos, H. 1989. Cyclic Axial Loading Analysis of Piles in Sand. *Journal of Geotechnical Engineering*, 115(6), pp. 836-852.
- Preene, M. and Powrie, W. 2009. Ground energy systems: delivering the potential. *Proceedings of the Institution of Civil Engineers - Energy*, 162(2), pp. 77-84.
- Randolph, M. F. & Wroth, C. P. 1978. Analysis of deformation of Vertical Loaded Piles. *Journal of the Geotechnical Engineering Division*, 104(12), pp. 1465-1488
- Rao, Y. 1997. In-fibre Bragg grating sensors. *Measurement Science and Technology*, 8(4), pp. 355-375.
- Rees, S., Adjali, M., Zhou, Z., Davies, M. and Thomas, H. 2000. Ground heat transfer effects on the thermal performance of earth-contact structures. *Renewable and Sustainable Energy Reviews*, 4(3), pp. 213-265.
- Ren, L., Li, H., Sun, L., Li, D., and Song, G. 2004. Application of FBG Sensors to Ground Heat Pump System. *Proceedings of Engineering, Construction, and Operations in Challenging Environments*. Houston, Texas, United States, March 7-10. pp. 554-558. doi: 10.1061/40722(153)77
- Robinsky, E.I., and Morrison, C.F. 1964. Sand displacement and compaction around model friction piles. *Canadian Geotechnical Journal*, 1(2): 81-93. doi:10.1139/t64-002.
- Rotta Loria, A., Donna, A. and Laloui, L. 2015. Numerical Study on the Suitability of Centrifuge Testing for Capturing the Thermal-Induced Mechanical Behavior of Energy Piles. *J. Geotech. Geoenviron. Eng.*, 141(10), p. 04015042.
- Sadrekarami, J., Gouhari, M.B., and Roohimehr, A. 2009. Surface roughness effects on the bearing capacity of piles in dry sand. *The Electronic Journal of Geotechnical Engineering*, Vol. 14A. Available at: <http://www.ejge.com/2009/Ppr0910.pdf>

- Schwamb, T., 2010. *Comparative study of fibre optic sensors for structural health monitoring in civil engineering*. MRes. University of Cambridge and University College London.
- Sekine, K., Ooka, R., Hwang, S., Nam, Y. & Shiba, Y. 2006. Development of a ground source heat pump system with ground heat exchanger utilizing the cast in place concrete pile foundations of a building, *Proceedings of the 10th International Conference on Thermal Energy Storage ECOSTOCK 2006*, May 31 – June 2, New Jersey, US, The Richard Stockton College of New Jersey. [Online]. Available from: https://intraweb.stockton.edu/eyos/energy_studies/content/docs/FINAL_PAPERS/11A-3.pdf[Accessed 10 August 2013].
- Stewart, M. and McCartney, J. 2014. Centrifuge Modeling of Soil-Structure Interaction in Energy Foundations. *J. Geotech. Geoenviron. Eng.*, 140(4), p. 04013044.
- Suryatriyastuti, M. E., Mroueh, H. and Burlon, S. 2013. Numerical Analysis of the Bearing Capacity of Thermoactive Piles Under Cyclic Axial Loading, in *Energy Geostructures* (eds L. Laloui and A. Di Donna), John Wiley & Sons, Inc., Hoboken, NJ USA. doi: 10.1002/9781118761809.ch7
- Suryatriyastuti, M., Burlon, S. and Mroueh, H. 2015. On the understanding of cyclic interaction mechanisms in an energy pile group. *Int. J. Numer. Anal. Meth. Geomech.*, 40(1), pp. 3-24.
- Suryatriyastuti, M., Mroueh, H. and Burlon, S. 2012. Understanding the temperature-induced mechanical behaviour of energy pile foundations. *Renewable and Sustainable Energy Reviews*, 16(5), pp. 3344-3354.
- Sutman, M., Olgun, C.G. and Brettmann, T. 2015. Full-Scale Field Testing of Energy Piles. *Proceedings of the International Foundations Congress and Equipment Expo (IFCEE)*, San Antonio, Texas, March 17-21, 2015. pp. 1638-1647.
- Tang, A. M., Pereira, J.-M., Hassen, G. and Yavari, N. 2013. Behavior of Heat-Exchanger Piles from Physical Modeling, in *Energy Geostructures* (eds L. Laloui and A. Di Donna), John Wiley & Sons, Inc., Hoboken, NJ USA. doi: 10.1002/9781118761809.ch4
- Tang, J., L & Wang, J., N. 2010. Error Analysis and Measurement Uncertainty for a Fiber Grating Strain-Temperature Sensor. *Sensors (Basel, Switzerland)*. 10(7), pp. 6582-6593.
- Tehrani, F., Han, F., Salgado, R., Prezzi, M., Tovar, R. and Castro, A. 2016. Effect of surface roughness on the shaft resistance of non-displacement piles embedded in sand. *Géotechnique*, 66(5), pp. 386-400.
- Tomlinson, M. and Woodward, J. 2008. *Pile design and construction practice*. 5th ed. Abingdon: Taylor & Francis.
- Uesugi, M., Kishida, H. and Tsubakihara, Y. 1989. Friction between sand and steel under repeated loading. *SOILS AND FOUNDATIONS*, 29(3), pp.127-137.
- Vesic, A., 1977. Design of Pile Foundation. Synthesis of Highway Practice No. 42, TRB, 1977, 68 p.

- Vulliet, L. and Meyer, A. 1999. The Vigner tunnel: determining contact laws from static load tests on Piles. *Proceedings of Twelfth European Conference on Soil Mechanics and Geotechnical Engineering*, Balkema, Rotterdam, pp. 1175-1181.
- Wang, B., Bouazza, A., and Haberfield, C. 2011. Preliminary observations from laboratory scale model geothermal pile subjected to thermalmechanical loading. *Proceedings of GeoFrontiers 2011 (GSP 211)*, J. Han and D. E. Alzamora, eds., ASCE, Reston, VA, pp. 430-439.
- Wang, B., Bouazza, A., Barry-Macaulay, D., Singh, M., Webster, M., Haberfield, C., Chapman, G., and Baycan, S. 2012. Field and Laboratory Investigation of a Heat Exchanger Pile. *Proceedings of GeoCongress 2012*, Oakland, CA, USA, March, ASCE, Reston, VA, pp. 4396-4405.
- Wang, B., Bouazza, A., Singh, R.M., Barry-Macaulay, D., Haberfield, C, Chapman, G. & Baycan, S. 2013. Field investigation of a geothermal energy pile: Initial observations. *Proceedings of the 18th International Conference on Soil Mechanics and Geotechnical Engineering, Paris, September 2-6*. pp. 3415-3418.
- Weinstein, G. 2008. *Long term behaviour of micropiles subject to cyclic axial loading*. PhD. Polytechnic University.
- Weng, X., Chen, J. and Wang, J. 2014. Fiber Bragg Grating-Based Performance Monitoring of Piles Fiber in a Geotechnical Centrifugal Model Test. *Advances in Materials Science and Engineering*, 2014, pp. 1-8.
- Wood, C., Liu, H. and Riffat, S. 2009. Use of energy piles in a residential building, and effects on ground temperature and heat pump efficiency. *Géotechnique*, 59(3), pp. 287-290.
- Yasufuku, N. and Hyde, A. 1995. Pile end-bearing capacity in crushable sands. *Géotechnique*, 45(4), pp. 663-676.
- Yavari, N., Tang, A., Pereira, J. and Hassen, G. 2014. Experimental study on the mechanical behaviour of a heat exchanger pile using physical modelling. *Acta Geotechnica*, 9(3), pp. 385-398.
- Yu, K., Singh, R., Bouazza, A. and Bui, H., 2015. Determining Soil Thermal Conductivity Through Numerical Simulation of a Heating Test on a Heat Exchanger Pile. *Geotechnical and Geological Engineering*, 33(2), pp.239-252.
- Zhao, J., 2001. *An Object-oriented Simulation Program for Fibre Bragg Gratings*. Rand Afrikaans University, Johannesburg.
- Zhao, X., 2009. *A Numerical Investigation of the Effects of Loading Conditions on Soil Response*. PhD. North Carolina State University.

Appendices

Appendix A. Numerical model

The governing partial differential equation (PDE) for two-dimensional heat conduction at temperature $T(x, y, t)$ is presented by Blomberg (1996):

$$\lambda_x \frac{\partial^2 T}{\partial x^2} + \lambda_y \frac{\partial^2 T}{\partial y^2} + I(x, y, t) = C \frac{\partial T}{\partial t} \quad (A.1)$$

Where:

$I(x, y, t)$: Rate of internal heat generation (W/m^3)

λ_x and λ_y : Thermal conductivities in x and y directions respectively ($W/m.K$)

C : Volumetric heat capacity ($J/m^3.K$)

At the steady-state, there is no heat gradient, and therefore the right-hand side of the equation is equal to zero and Laplace Equation applies:

$$\lambda_x \frac{\partial^2 T}{\partial x^2} + \lambda_y \frac{\partial^2 T}{\partial y^2} = 0 \quad (A.2)$$

In this study, transient state heat transfer model is applied with two assumptions to simplify the analysis:

- The rate of internal heat generation is zero.
- Thermal conductivities in x and y directions are equal: $\lambda_x = \lambda_y$.

Applying the above assumptions into equation mentioned above results in a 2D transient heat conduction equation:

$$\frac{\partial T}{\partial t} = \alpha \left(\frac{\partial^2 T}{\partial x^2} + \frac{\partial^2 T}{\partial y^2} \right) \quad (A.3)$$

Where α is the thermal diffusivity of the material (m^2/s). It is rearranged in the following format which shows an elliptic PDE:

$$\frac{\partial^2 T}{\partial x^2} + \frac{\partial^2 T}{\partial y^2} = q'''(x, y) \quad (A.4)$$

Where q''' is the volumetric heat source.

To solve this PDE, finite difference method is used. The finite difference code uses an explicit solution scheme where it can be computed forward in time using quantities from previous steps.

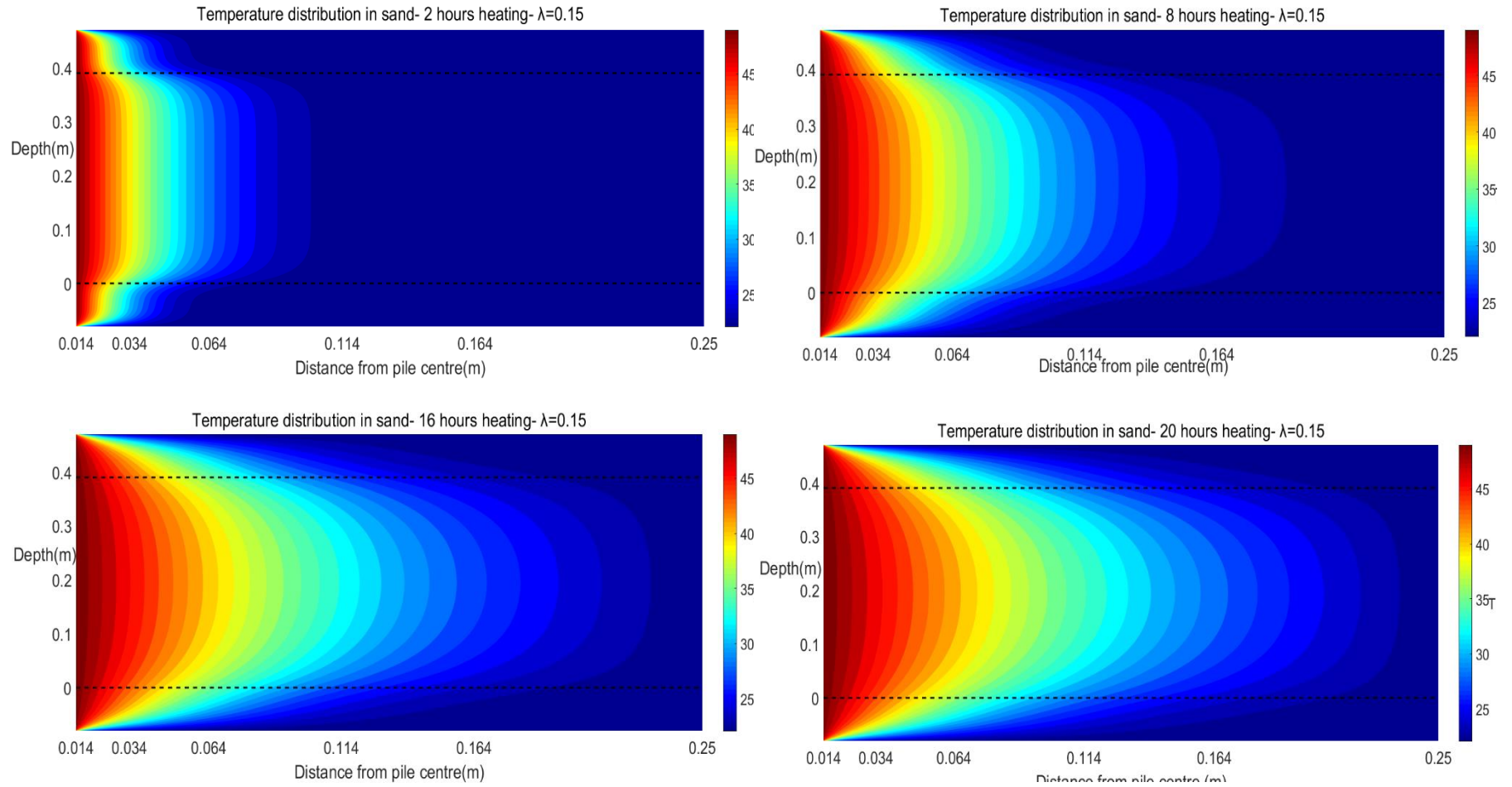
For a 2D model in both x and y directions:

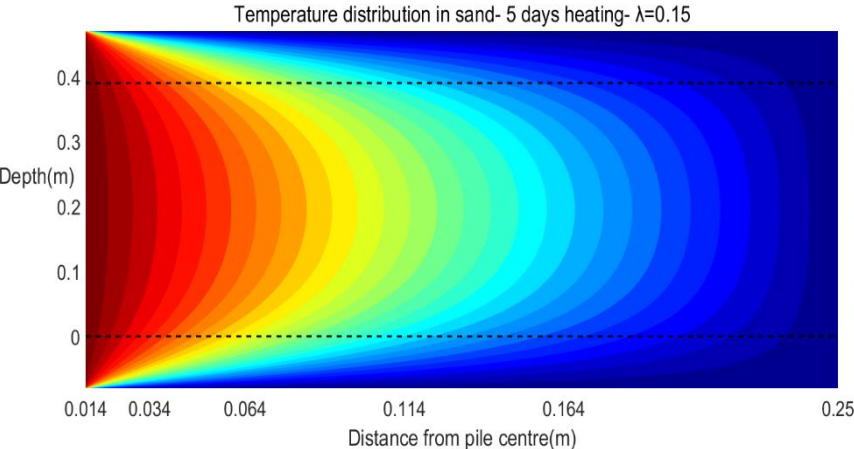
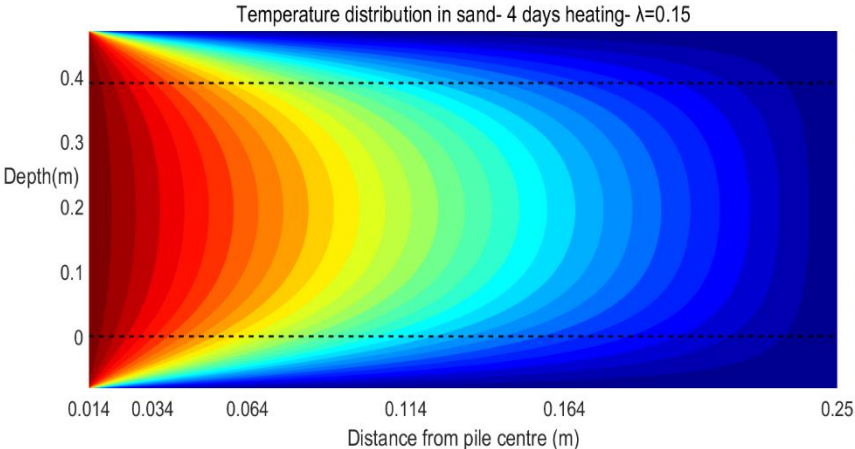
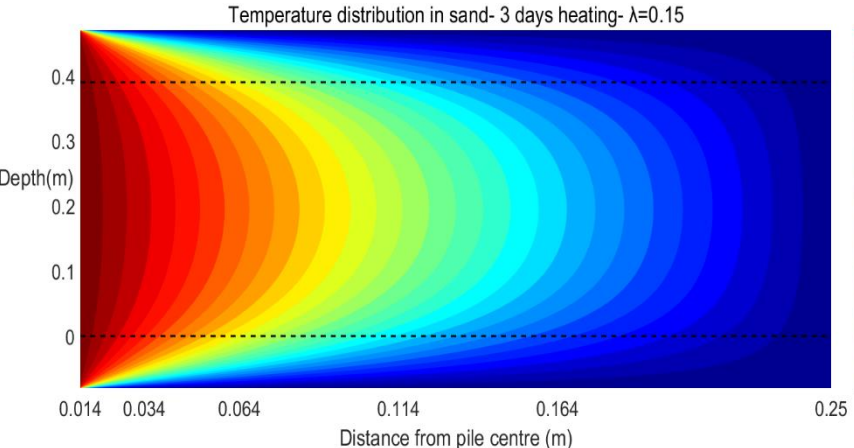
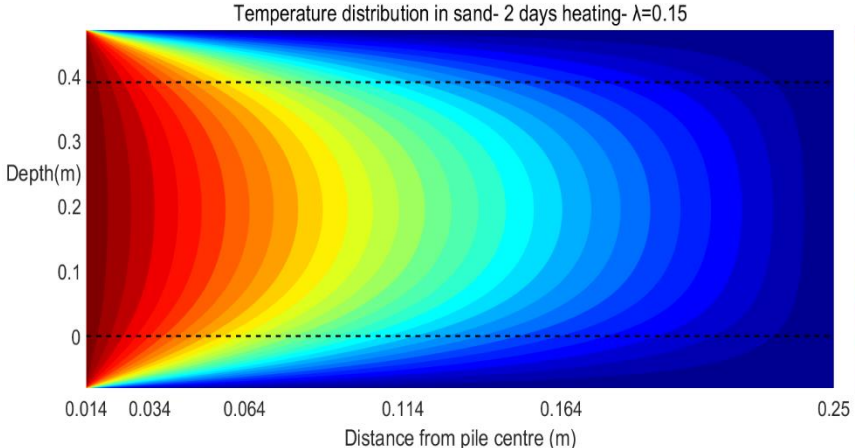
$$T_{i,j}^{n+1} = T_{i,j}^n + \frac{\alpha \Delta t}{(\Delta x)^2} (T_{i,j+1}^n - 2T_{i,j}^n + T_{i,j-1}^n) + \frac{\alpha \Delta t}{(\Delta y)^2} (T_{i+1,j}^n - 2T_{i,j}^n + T_{i-1,j}^n) \quad (A.5)$$

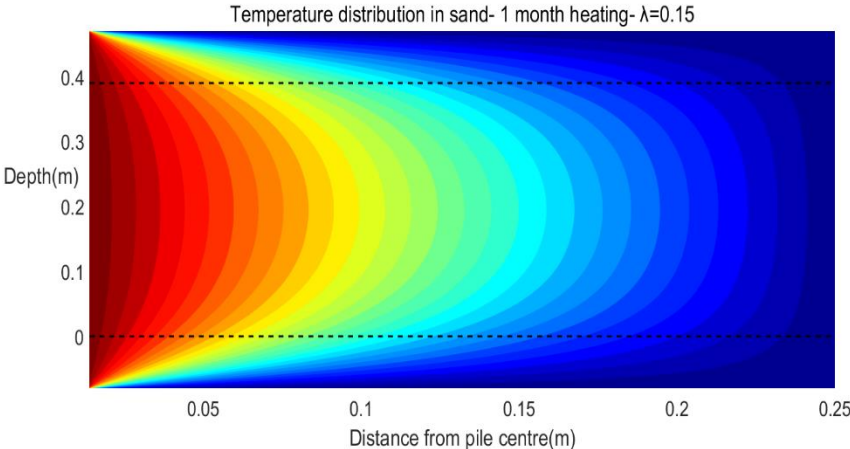
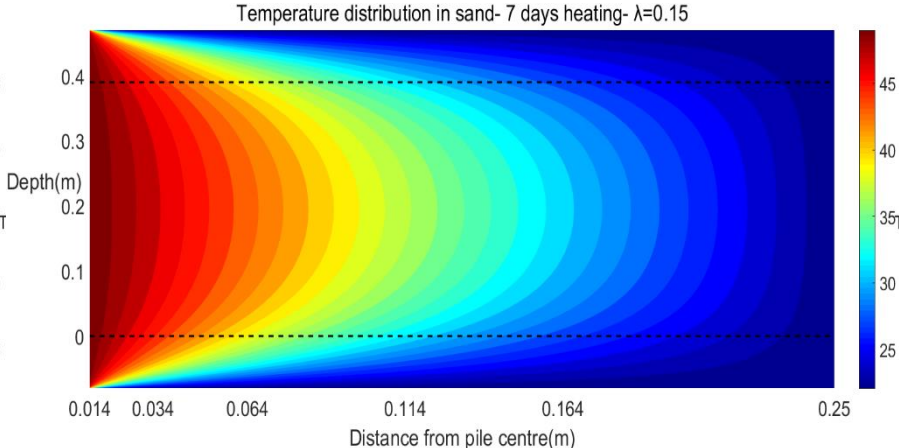
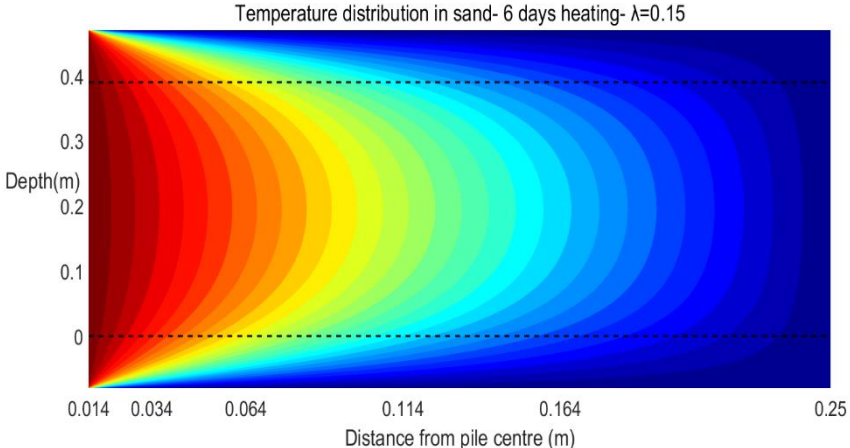
Table A.1. Thermo-elastic properties of sand and insulator

Thermal conductivity in x direction	0.15 (<i>W/m.K</i>)
Thermal conductivity in y direction	0.15 (<i>W/m.K</i>)
Thermal conductivity of fibreglass insulation	0.04 (<i>W/m.K</i>)
Sand dry density	1510 (<i>Mg/m³</i>)
Fibreglass dry density	2000 (<i>Mg/m³</i>)
Specific heat capacity of dry sand	800 (<i>J/kg.K</i>)
Specific heat capacity of fibreglass insulation	750 (<i>J/kg.K</i>)

Appendix B. Temperature profiles







Appendix C. Matlab code

```
clear all
close all
clc
f1 = figure();
set(f1,'Visible','off');
hold on
f2 = figure();
set(f2,'Visible','off');
hold on

% SYSTEM SIZE
D = 0.5; % soil diameter (m)
H = 0.39; % soil height (m)
d = 0.028; % pipe outer diameter (m)
insulation_top = 0.08; % (m)
insulation_bottom = 0.08; % (m)

% MATERIAL PARAMETERS
lambda_x = 0.15; % thermal conductivity (W/mK)
lambda_y = 0.15; % thermal conductivity (W/mK)
lambda_insulation = 0.04; % thermal conductivity of fibreglass(W/mK)

rho_soil = 1510; % dry sand density (kg/m^3)
rho_insulation = 2000; % Fibreglass density (kg/m^3)

cp_soil = 800; % specific heat capacity of dry sand (J/kg.K)
cp_insulation = 670; % specific heat capacity Fibreglass (J/kg.K)

alpha_soil_x = lambda_x/(rho_soil*cp_soil); % thermal diffusivity
(m^2/s)
alpha_soil_y = lambda_y/(rho_soil*cp_soil); % thermal diffusivity
(m^2/s)
alpha_insulation = (lambda_insulation)/(rho_insulation*cp_insulation);
% thermal diffusivity (m^2/s)

% NUMERICAL RESOLUTION
nx = 400;
```

Appendix

```
ny = 400;
dt = 1.0;
t_max = 4*3600; % (s)

% BOUNDARY CONDITIONS
T_pipe = 47.7;
T_inside = 19.4;
T_outside = 19.4;

% Go..
t = 0.; % set initial time
t_list = linspace(0.,t_max,11); % when to save
x = linspace(d/2.,D/2.,nx); % x coordinate
y = linspace(-insulation_bottom,H+insulation_top,ny); % y coordinate
dx = x(2) - x(1); % grid spacing horizontal (m)
dy = y(2) - y(1); % grid spacing vertical (m)

T = T_inside*ones(ny+2,nx+2); % temperature
T(:,1) = T_pipe; % left BC
T(:,end) = T_outside; % right BC
T(1,:) = T_outside; % bottom BC
T(end,:) = T_outside; % top BC

insulation_bottom_rows = sum(y<=0.); % how many rows of insulation in
bottom of the container
insulation_top_rows = sum(y>=H); % how many rows of insulation on top
of the container

% Constant thermal conductivity in x direction for both soil and
insulator
L_x = alpha_soil_x*ones(ny,nx); % thermal conductivity in x direction
for sand and insulation
L_x(1:insulation_bottom_rows,:) = alpha_insulation;
L_x(end-insulation_top_rows:end,:) = alpha_insulation;

% Constant thermal conductivity in y direction for both soil and
insulator
L_y = alpha_soil_y*ones(ny,nx); % thermal conductivity in y direction
for sand and insulation
L_y(1:insulation_bottom_rows,:) = alpha_insulation;
```

```

L_y(end-insulation_top_rows:end,:) = alpha_insulation;

while t <= t_max
    if any(abs(t-t_list)<(dt/100))
        f1;
        plot(x,T(int32(ny/2),2:end-1),'k-')
        f2;
        plot(x,T(int32(ny/3),2:end-1),'k-')
    end

    T(2:end-1,2:end-1) = T(2:end-1,2:end-1) + ...
L_x.*dt.*(T(2:end-1,3:end) - T(2:end-1,2:end-1)*2 + T(2:end-1,1:end-
2))/(dx^2) + ...
L_y.*dt.*(T(3:end,2:end-1) - T(2:end-1,2:end-1)*2 + T(1:end-2,2:end-
1))/(dy^2);
    t = t + dt;

end

f1;
xlabel('x')
ylabel('T','rot',0)
print(gcf,'-dpng','T_center.png')
f2;
xlabel('x')
ylabel('T','rot',0)
print(gcf,'-dpng','T_third.png')
figure(3)
hold on
contourf(x,y,T(2:end-1,2:end-1))
plot(x,zeros(nx),'k--','linewidth',2)
plot(x,H*ones(nx),'k--','linewidth',2)
xlabel('x(m)')
ylabel('y(m)','rot',0)
c = colorbar();
ylabel(c,'T','rot',0)
print(gcf,'-dpng','T_contour.png')

```

Appendix D. Sieve analysis test results

Table A.2. Sieve analysis test: datasheet and results

Grain size analysis							
Date tested	22.03.2013						
Tested by	Amin Rafiei						
Test method	BS 1377-2:1990:9.3						
Test number	Test 1						
Soil description	Leighton Buzzard Sand						
Wight of container (gr)	352.42						
Weight of container+ dry soil (gr)	452.42						
Weight of dry sample (gr)	100						
Sieve no.	Opening diameter (mm)	Sieve Weight (gr)	Mass of Sieve+ Soil Retained (gr)	Soil Retained (gr)	Percent Retained (%)	Cumulative mass retained %	Percent Passing (%)
16	1.18	487.85	487.85	0	0.0	0.0	100
30	0.6	498.13	498.17	0.04	0.04	0.04	99.96
40	0.425	463.05	463.11	0.06	0.06	0.10	99.9
50	0.3	455.6	455.9	0.3	0.3	0.40	99.6
70	0.212	420.05	450.85	30.8	30.8	31.2	68.8
100	0.15	434.35	473.72	39.37	39.37	70.57	29.43
230	0.063	397.05	426.47	29.42	29.42	99.99	0.01
Pan	0.01	377.43	377.43	0	0.0	0.0	0.0
Findings							
D_{10}	D_{30}	D_{60}	C_u	C_c			
0.086	0.16	0.2	2.32	1.48			
Soil classification: Uniform fine sand							

Appendix E. Specific gravity test results

Table A.3. Specific gravity test: datasheet and results

Particle Density (Small pycnometer)						
Date tested	25.04.2013					
Tested by	Amin Rafiei					
Test Method	BS 1377-2:1990:8.3					
Test number	Test 1					
Soil Description	Leighton Buzzard Sand- Uniform fine sand					
Pyknometer number						
	Notation	unit	A	B	1	2
Mass of pycnometer+ soil+ water	m_3	gr	91.73	93.89	93.25	94.58
Mass of pycnometer+ Dry soil	m_2	gr	45.21	46.58	47.33	47.7
Mass of pycnometer+ water	m_4	gr	85.56	87.59	86.78	88.35
Mass of empty, clean pycnometer	m_1	gr	35.25	36.46	36.92	37.65
Mass of soil	m_2-m_1	gr	9.96	10.12	10.41	10.05
Mass of water in full bottle	m_4-m_1	gr	50.31	51.13	49.86	50.7
Mass of water used	m_3-m_2	gr	46.52	47.31	45.92	46.88
Volume of soil particles	$(m_4-m_1)-m_3-m_2$	mL	3.79	3.82	3.94	3.82
Specific Gravity	G_s	-	2.627	2.649	2.642	2.630
Average Specific Gravity	G_s	-	2.640			
Particle Density	ρ_s	Mg/m ³	2.627	2.649	2.642	2.630
Average value	ρ_s	Mg/m ³	2.640			

Appendix F. Limiting densities test results

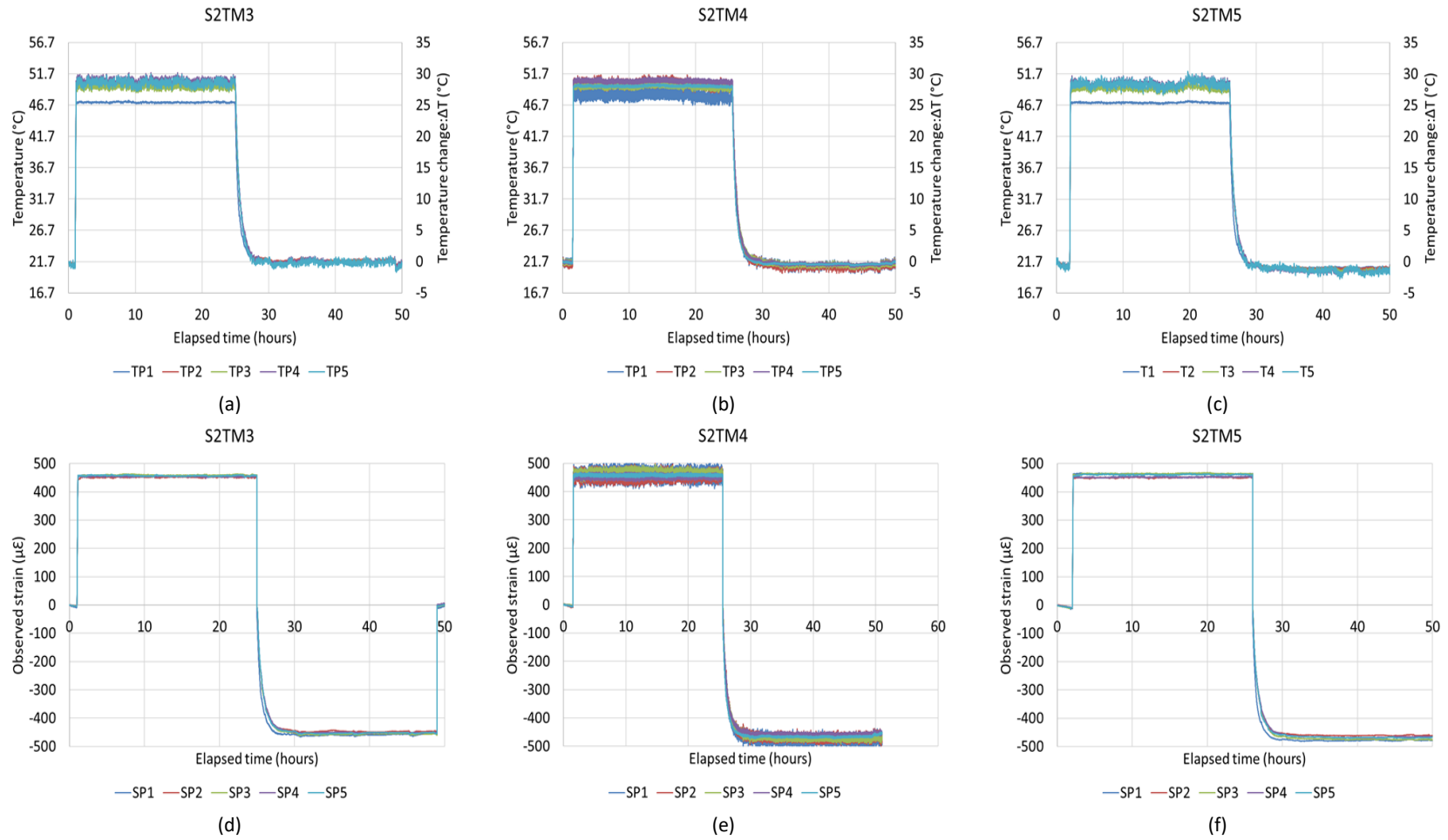
Table A.4. Maximum density test: datasheet and results

Soil Description	Leighton Buzzard Sand	
Test Method	BS 1377-4:1990	
Date	02.05.2013	
Weight of Dry sand+ tray	gr	2025.5
Weight of tray	gr	366.5
Weight of Dry sand	gr	1659
Diameter of Mould	mm	105
Height of Mould	mm	115.5
Volume of Mould	cm ³	1000.11
Maximum Density $\rho_{d,max}$	gr/cm ³	1.658

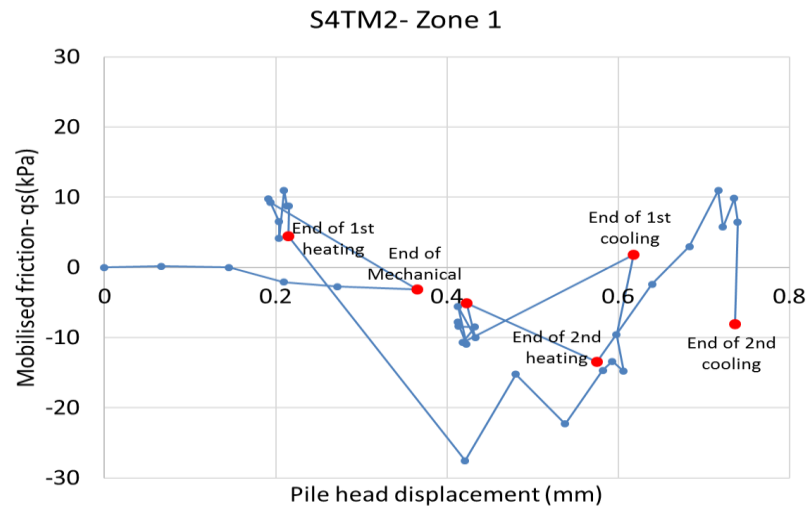
Table A.5. Minimum density test: datasheet and results

Soil Description	Leighton Buzzard Sand	
Test Method	BS 1377-4:1990	
Date	30.04.2013	
	Test No.	Volume (cm ²)
	1	725
	2	731
	3	735
	4	740
	5	741
	6	732
	7	725
	8	735
	9	720
	10	740
	unit	
Weight of sand	gr	1000
Maximum volume	cm ³	741
$\rho_{d,min}$	gr/cm ³	1.349

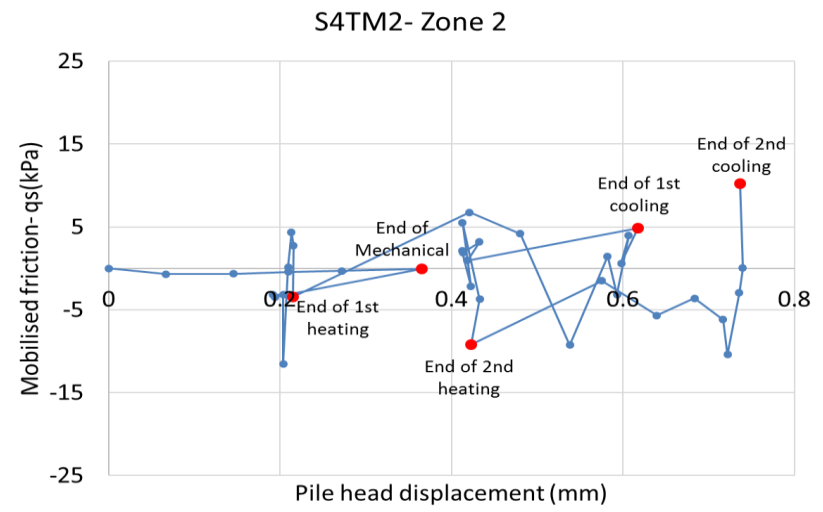
Appendix G. Scenario 2- Temperature and strain profiles



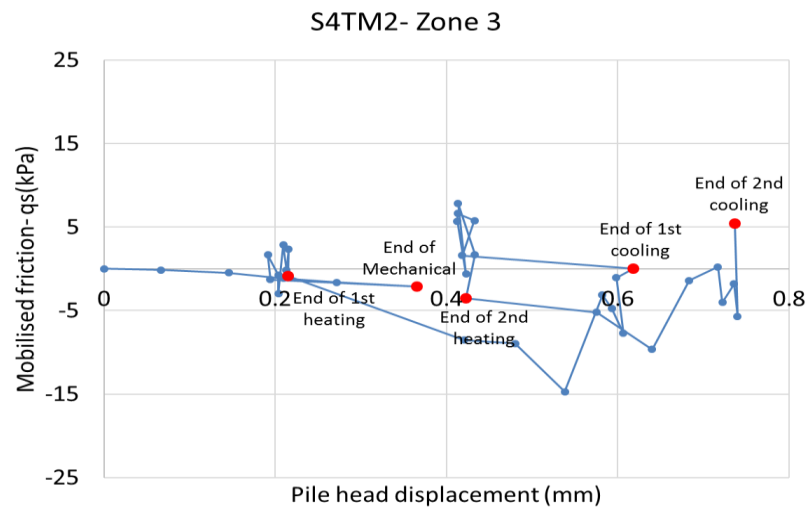
Appendix H. Mobilised shaft friction- Scenario 4



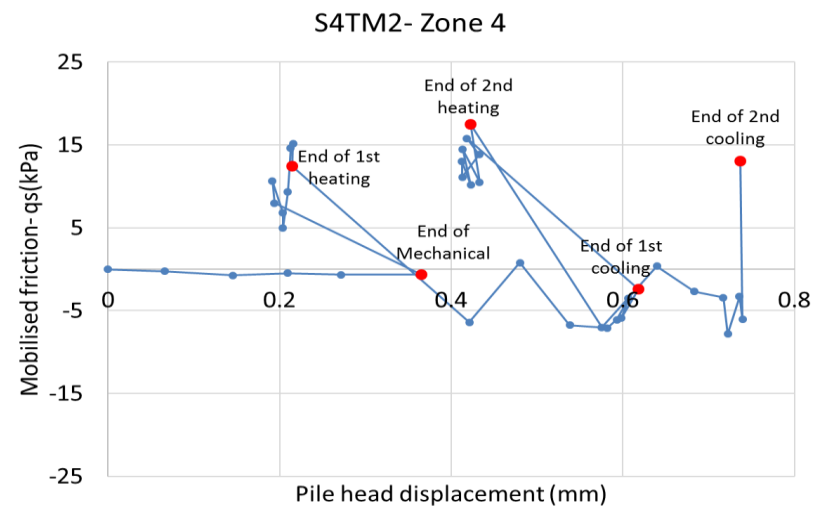
(a)



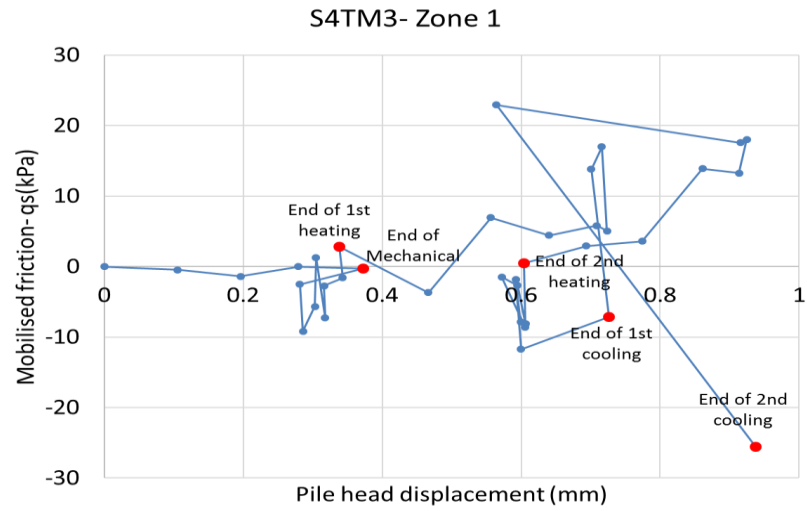
(b)



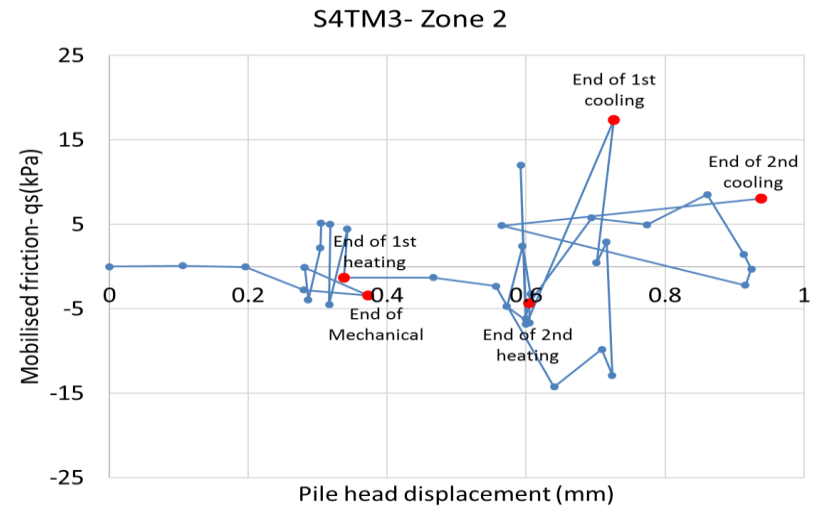
(c)



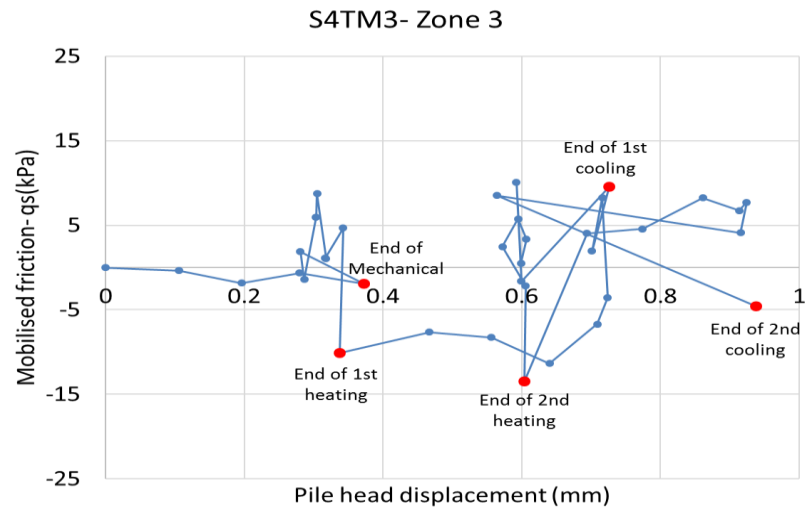
(d)



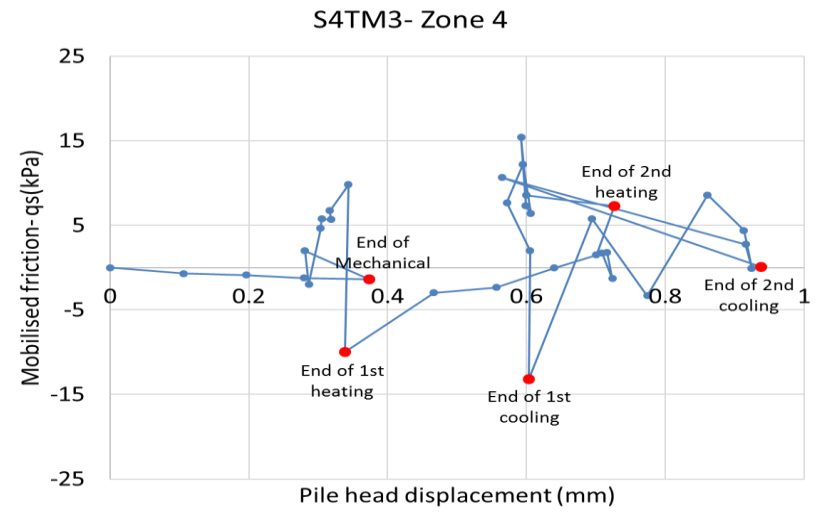
(a)



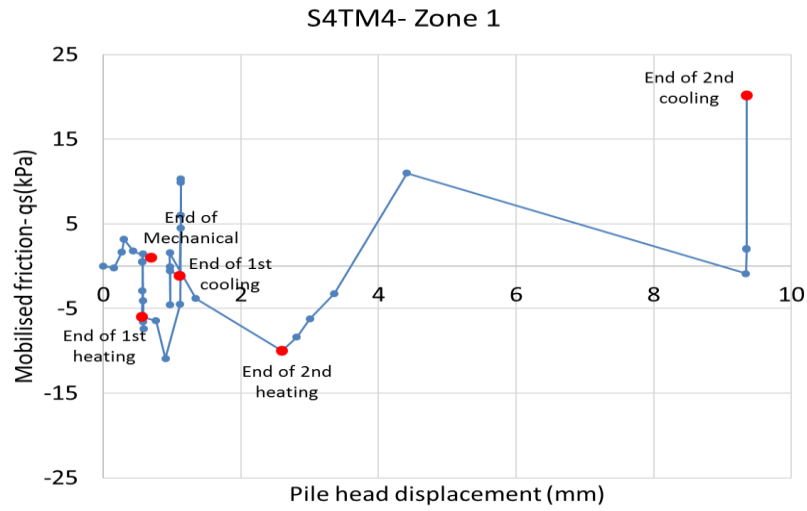
(b)



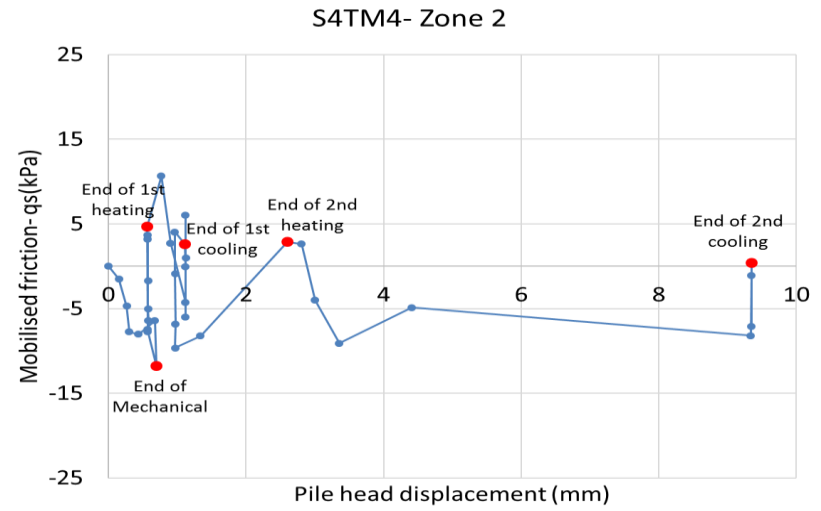
(c)



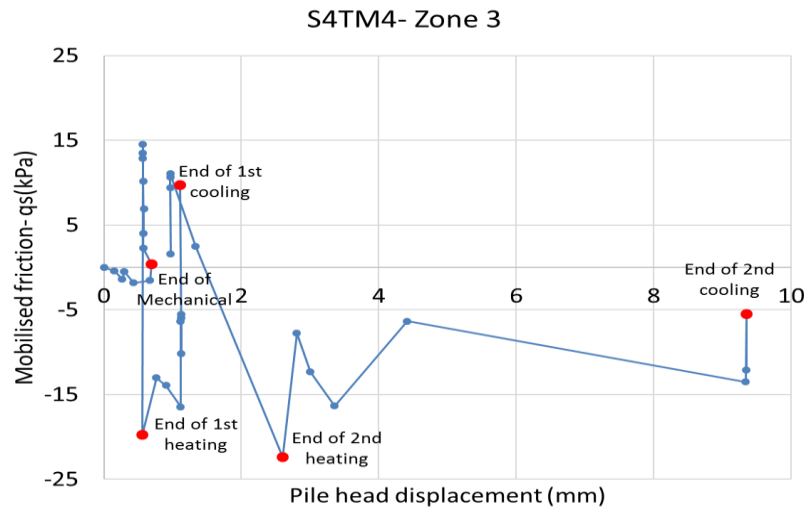
(d)



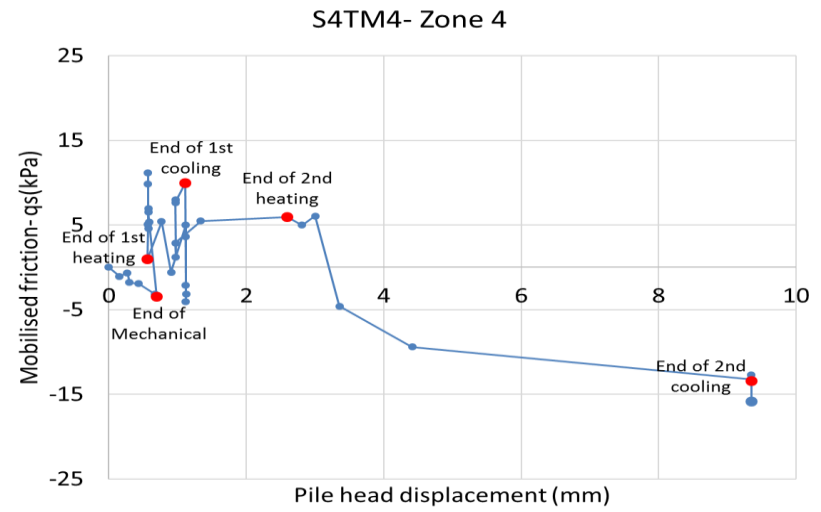
(a)



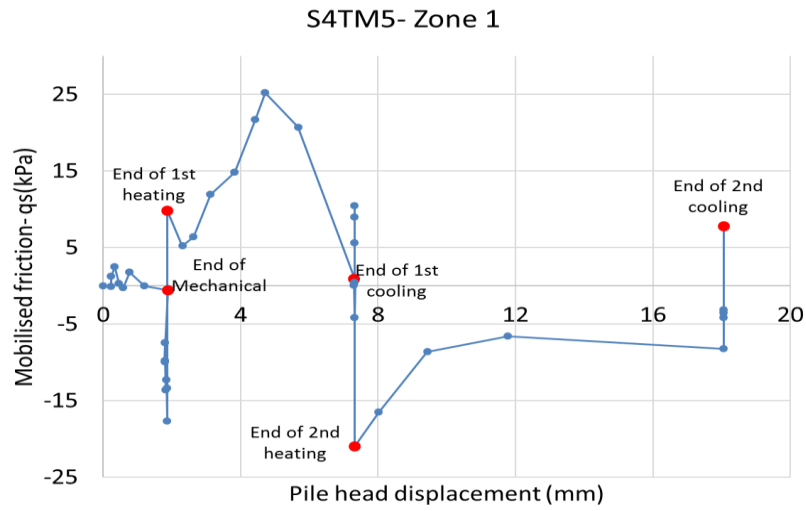
(b)



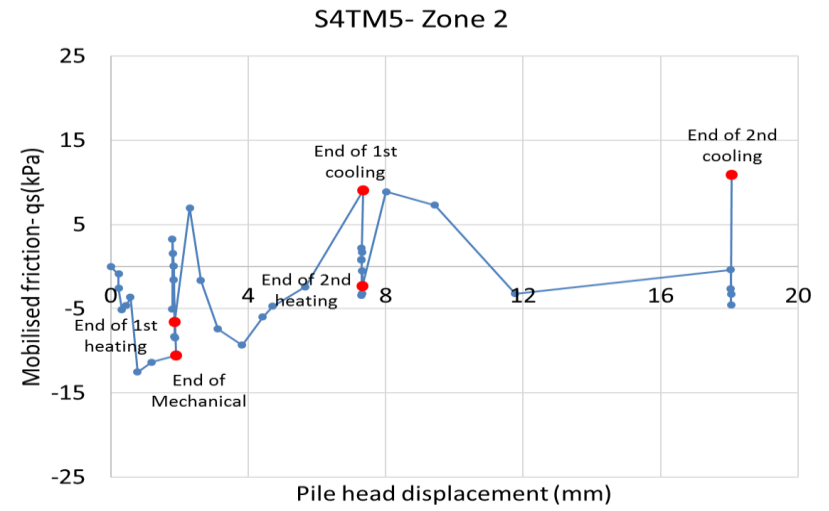
(c)



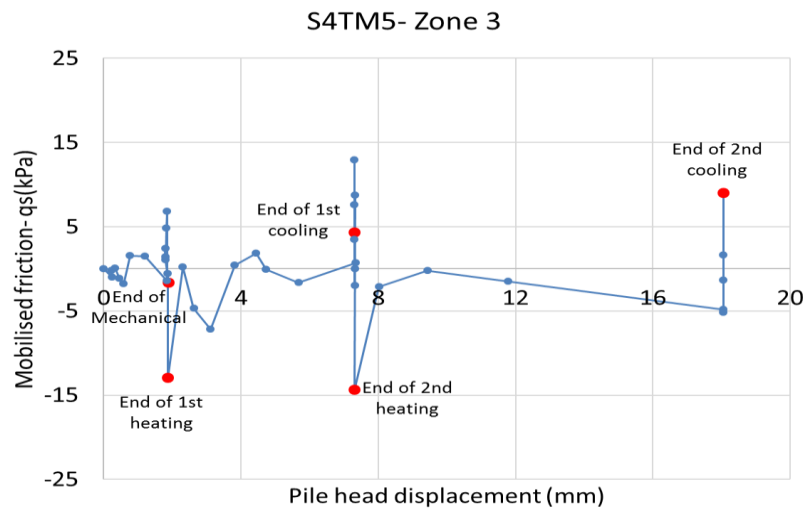
(d)



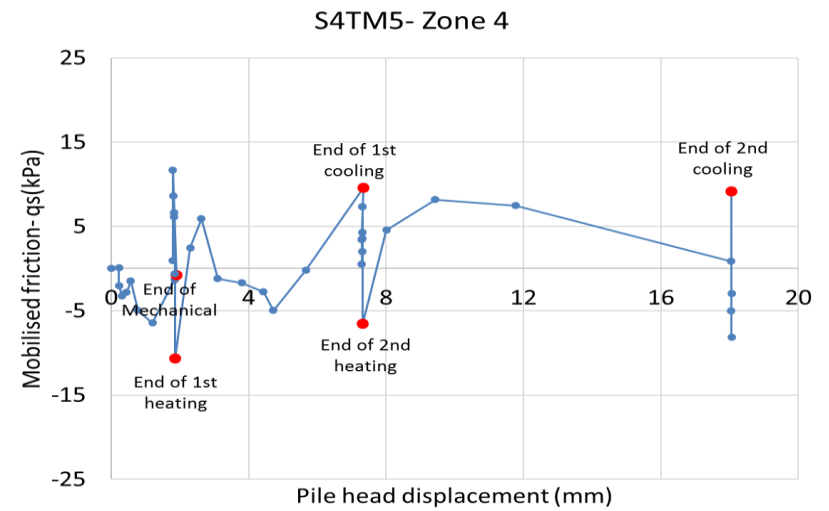
(a)



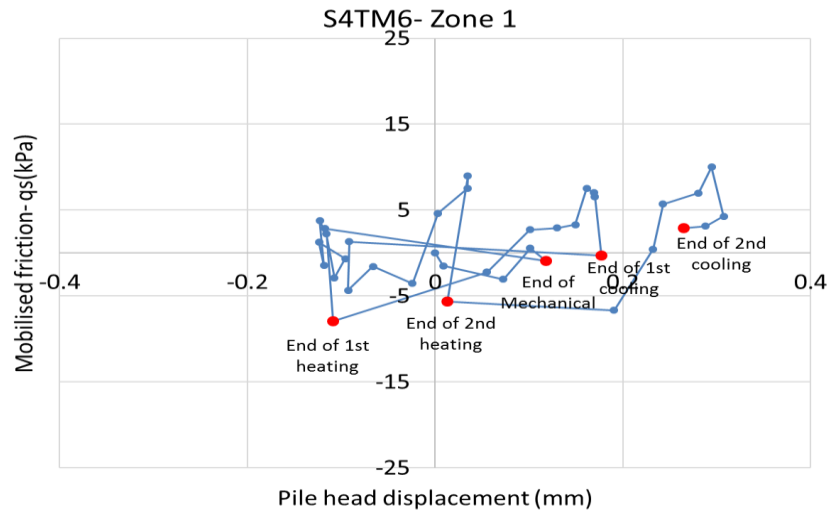
(b)



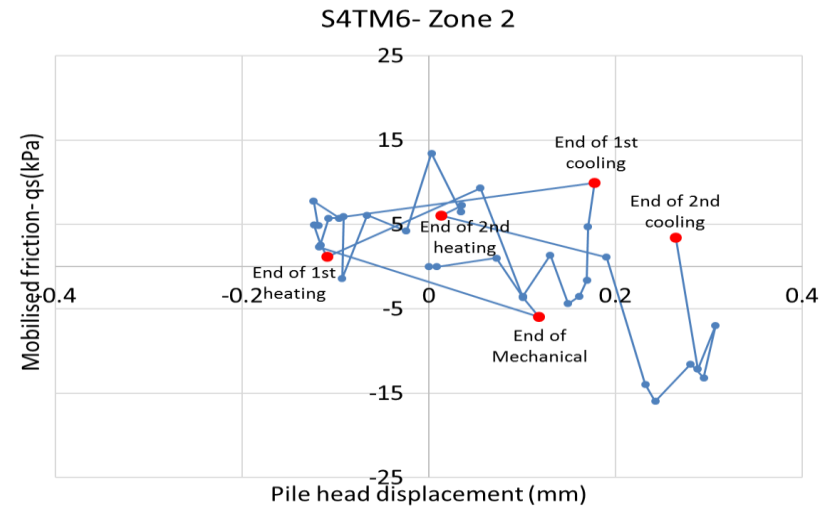
(c)



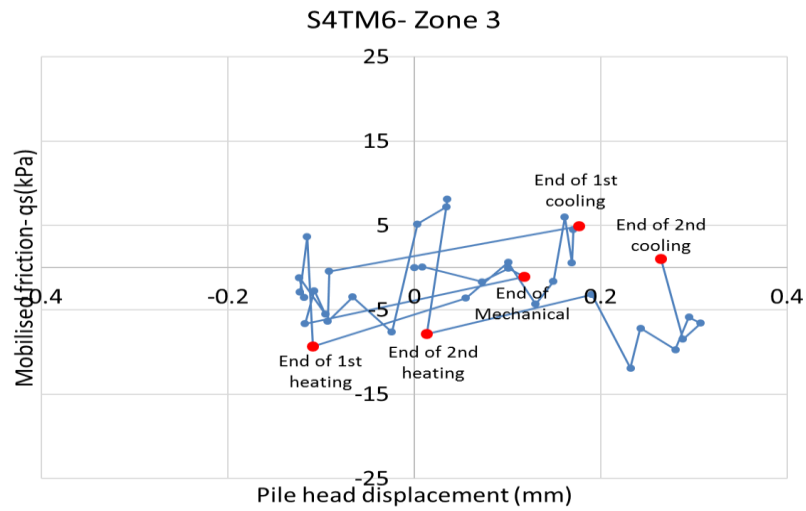
(d)



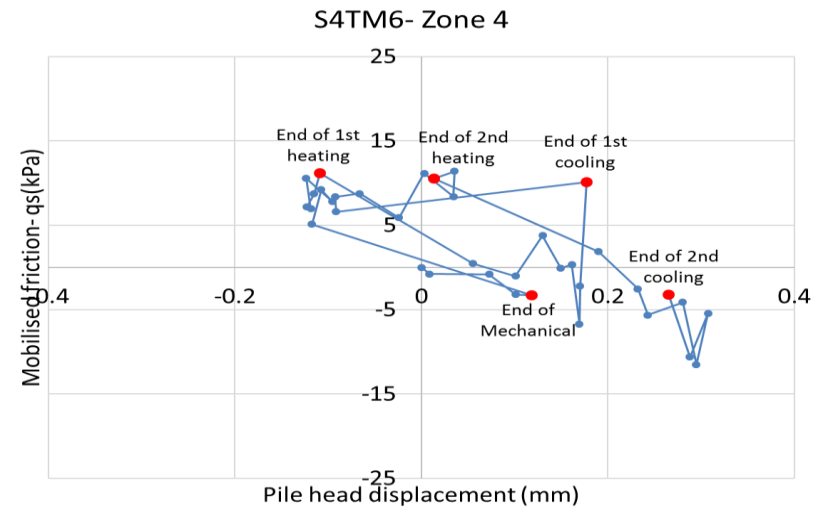
(a)



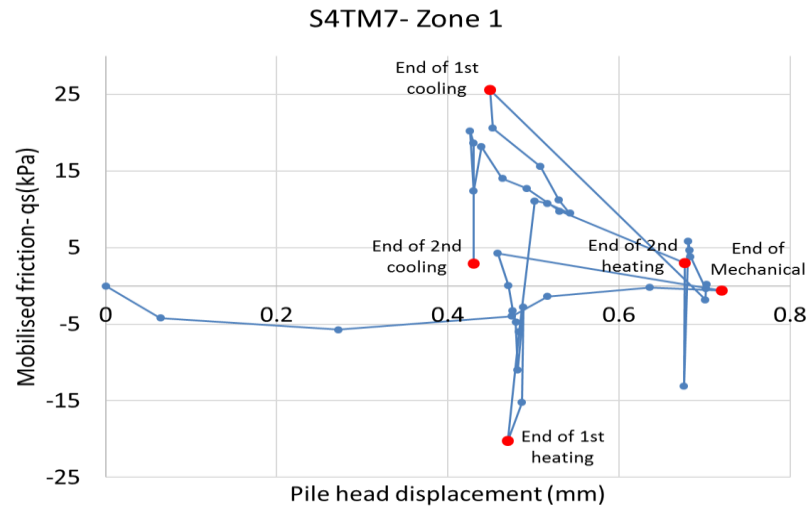
(b)



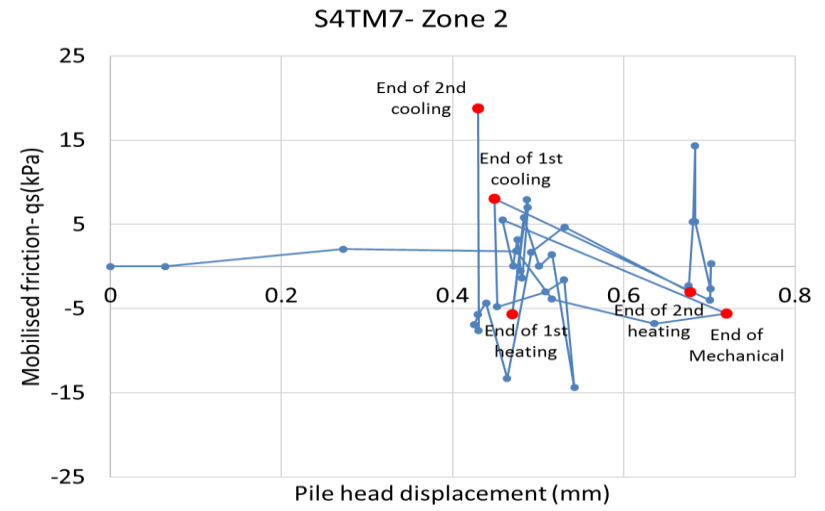
(c)



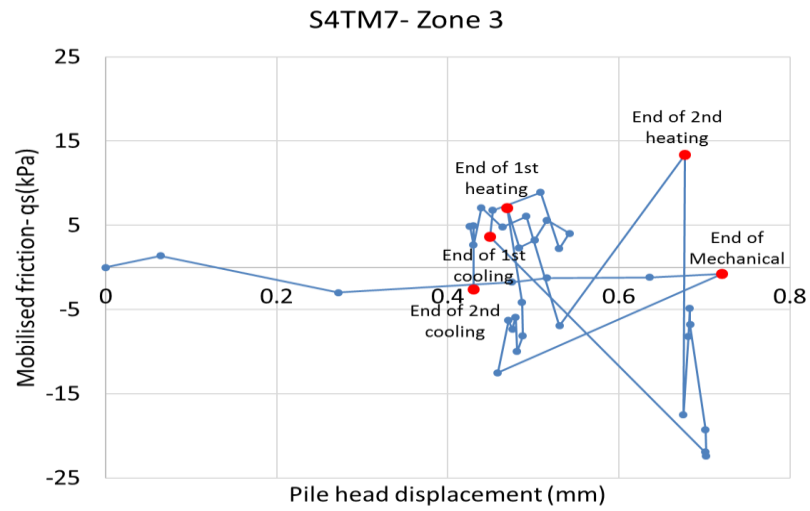
(d)



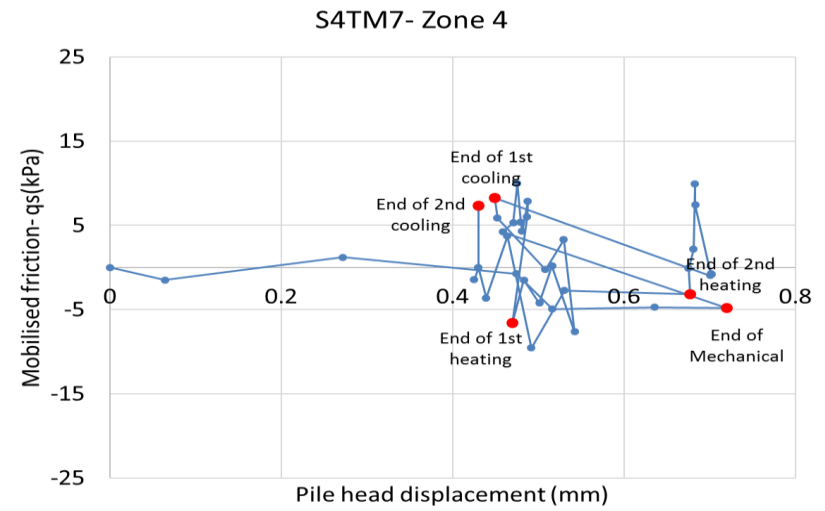
(a)



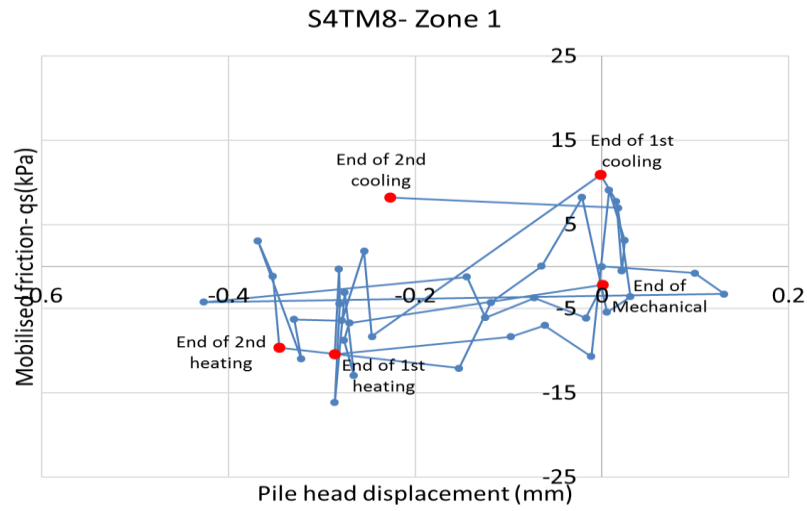
(b)



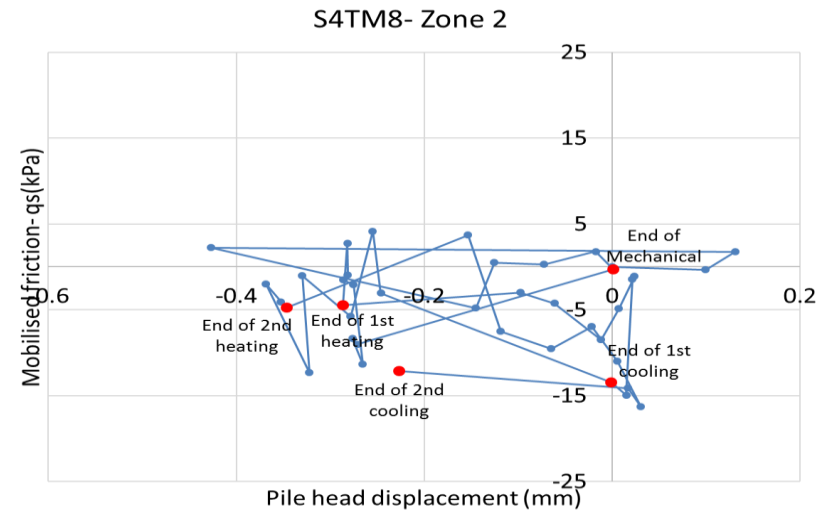
(c)



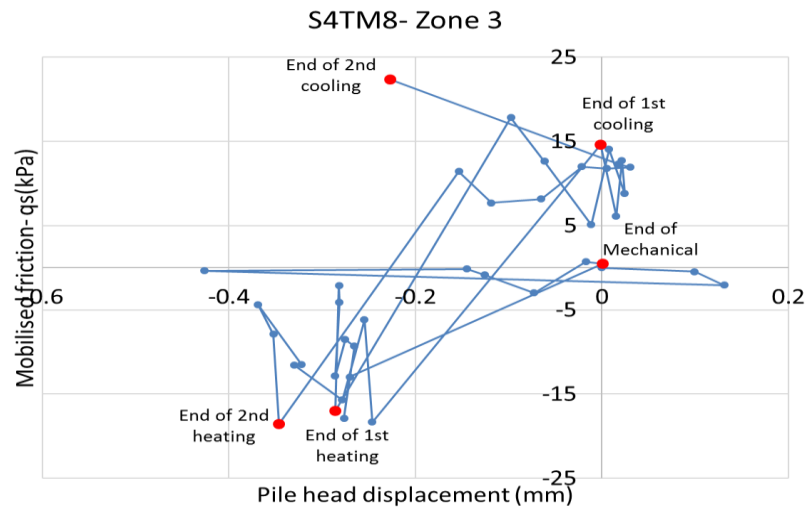
(d)



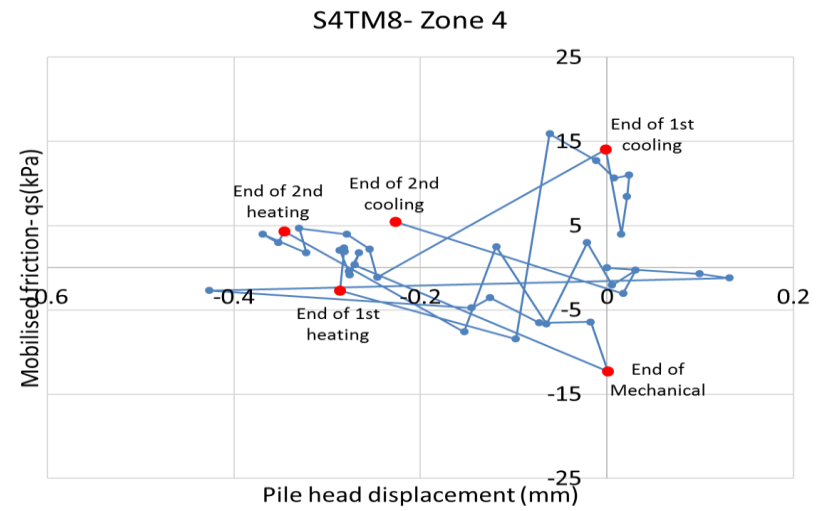
(a)



(b)



(c)



(d)

Appendix I. Load-bearing capacity of piles

Ultimate bearing capacity of a pile is estimated using the following equation (API, 2005):

$$Q_{ult} = Q_s + Q_b \pm W_p \quad (A.6)$$

Where:

Q_{ult} : Ultimate bearing capacity of pile

Q_s : Shaft resistance

Q_b : Base (tip) resistance

W_p : Pile weight

Pile weight is usually much smaller than ' Q_{ult} ' and it is generally ignored in calculations. For a shaft resistant pile, by assuming that the base bearing capacity is negligible, Equation A.6 is simplified into the following equation:

$$Q_{ult} = Q_s = A_s \times f_s \quad (A.7)$$

Where:

A_s : Area of the shaft in contact with soil

f_s : Local side friction between the pile and the surrounding soil

The most common method to determine ' f_s ' is the American Petroleum Institute (API) recommended practice. The local side friction between the pile and the surrounding soil is calculated using the following formula (API, 2005):

$$f_s = K p_o \tan \delta \quad (A.8)$$

Where:

K = coefficient of lateral earth pressure

p_o = effective overburden pressure

δ = friction angle between the soil and pile wall

Similar approach is used by Kulhawy (1984) to predict unit skin friction resistance:

$$f_s = \sigma'_h \cdot \tan \delta \quad (A.9)$$

Where,

σ'_h : Horizontal effective stress = $K_h \cdot \sigma'_{vo}$

K_h : Coefficient of horizontal earth pressure

σ'_{vo} : Vertical effective overburden pressure

δ : Coefficient of friction between pile and soil

A theoretical approach is proposed by Vesic (1977) to estimate the base resistance of a single pile which based on effective stress parameters:

$$Q_p = A_p q_p = A_p (\sigma'_0 N_\sigma) \quad (A.10)$$

Where:

σ'_0 : mean normal ground effective stress at the pile base level

N_σ : bearing capacity factor

Kulhawy et al. (1983) proposed the following formula for the net unit end bearing capacity:

$$q'_p = B\gamma N_\gamma + \sigma'_{zD} N_q \quad (A.11)$$

Where:

B : pile diameter

σ'_{zD} : vertical effective stress at the pile tip

N_q is a bearing capacity factor than can be calculated as a function of effective angle of internal friction (Φ') and rigidity index (I_r).

For a base resistant pile, Equation A.6 is simplified into the following equation:

$$Q_b = A_b \cdot N_q \sigma'_{v0} \quad (A.12)$$

The value of N_q is estimated using the relationship developed by Berezantsev et al. (1961) which is a relationship between the drained angle of shearing resistance of the soil at the pile base (Φ') and the penetration depth of the pile.

Appendix J. Temperature variations in sand

